



IntechOpen

Neuroimaging  
Structure, Function and Mind

*Edited by Sanja Josef Golubic*





---

# Neuroimaging - Structure, Function and Mind

*Edited by Sanja Josef Golubic*

Published in London, United Kingdom

---



## IntechOpen







*Supporting open minds since 2005*



Neuroimaging – Structure, Function and Mind  
<http://dx.doi.org/10.5772/intechopen.76733>  
Edited by Sanja Josef Golubic

#### Contributors

Atsushi Kawaguchi, Leon Petchkovsky, Michael Petchkovsky, Philip Morris, Paul Dickson, Danielle Montgomery, Jonathan Dwyer, Patrick Burnett, Kirstin Robertson-Gillam, Agnieszka Reid, Toshinori Kato, Juan Carlos Gutiérrez Franchi, Yongxia Zhou, Mitsuo Tonoike, Takuyo Hayashi

#### © The Editor(s) and the Author(s) 2019

The rights of the editor(s) and the author(s) have been asserted in accordance with the Copyright, Designs and Patents Act 1988. All rights to the book as a whole are reserved by INTECHOPEN LIMITED. The book as a whole (compilation) cannot be reproduced, distributed or used for commercial or non-commercial purposes without INTECHOPEN LIMITED's written permission. Enquiries concerning the use of the book should be directed to INTECHOPEN LIMITED rights and permissions department ([permissions@intechopen.com](mailto:permissions@intechopen.com)).

Violations are liable to prosecution under the governing Copyright Law.



Individual chapters of this publication are distributed under the terms of the Creative Commons Attribution 3.0 Unported License which permits commercial use, distribution and reproduction of the individual chapters, provided the original author(s) and source publication are appropriately acknowledged. If so indicated, certain images may not be included under the Creative Commons license. In such cases users will need to obtain permission from the license holder to reproduce the material. More details and guidelines concerning content reuse and adaptation can be found at <http://www.intechopen.com/copyright-policy.html>.

#### Notice

Statements and opinions expressed in the chapters are those of the individual contributors and not necessarily those of the editors or publisher. No responsibility is accepted for the accuracy of information contained in the published chapters. The publisher assumes no responsibility for any damage or injury to persons or property arising out of the use of any materials, instructions, methods or ideas contained in the book.

First published in London, United Kingdom, 2019 by IntechOpen  
eBook (PDF) Published by IntechOpen, 2019

IntechOpen is the global imprint of INTECHOPEN LIMITED, registered in England and Wales, registration number: 11086078, The Shard, 25th floor, 32 London Bridge Street  
London, SE19SG – United Kingdom  
Printed in Croatia

#### British Library Cataloguing-in-Publication Data

A catalogue record for this book is available from the British Library

Additional hard and PDF copies can be obtained from [orders@intechopen.com](mailto:orders@intechopen.com)

Neuroimaging – Structure, Function and Mind

Edited by Sanja Josef Golubic

p. cm.

Print ISBN 978-1-78985-805-1

Online ISBN 978-1-78985-806-8

eBook (PDF) ISBN 978-1-83962-108-6

# We are IntechOpen, the world's leading publisher of Open Access books Built by scientists, for scientists

4,100+

Open access books available

116,000+

International authors and editors

120M+

Downloads

151

Countries delivered to

Our authors are among the  
Top 1%

most cited scientists

12.2%

Contributors from top 500 universities



WEB OF SCIENCE™

Selection of our books indexed in the Book Citation Index  
in Web of Science™ Core Collection (BKCI)

Interested in publishing with us?  
Contact [book.department@intechopen.com](mailto:book.department@intechopen.com)

Numbers displayed above are based on latest data collected.  
For more information visit [www.intechopen.com](http://www.intechopen.com)







# Meet the editor



Sanja Josef Golubic is a senior research and teaching assistant (postdoctoral fellow) at the Department of Physics, Faculty of Science, University of Zagreb. Her academic qualifications include a PhD in cognitive neurodynamics and an MSc in theoretical physics. Despite a short scientific career, she has made outstanding achievements in the field of neuroscience. Her first scientific publication was nominated for the Nightingale Prize for Best Medical and Biological Engineering and Computing Paper in 2011. Other notable contributions to the field include a significant role in resolving the 30-year-long enigma of the neural network underlying auditory sensory gating; revealing the functional role of neural generators involved in the sensory gating processing; and proposing the neural mechanism of sensory gating phenomena. Notably, her major scientific achievements are finding a new, fast cortical pathway, a gating stream that links the prefrontal cortex to primary sensory areas along with well-established ventral and dorsal sensory pathways, and particularly the discovery of a discrete individual biomarker of Alzheimer's disease with the potential to detect the disease in its preclinical stage. The high translational potential of the discovery is emphasized by its selection in the top 100 best spin-offs in 2018.



# Contents

<b>Preface</b>	<b>XIII</b>
<b>Section 1</b> Analysis of Brain Imaging Data	<b>1</b>
<b>Chapter 1</b> Supervised Sparse Components Analysis with Application to Brain Imaging Data <i>by Atsushi Kawaguchi</i>	<b>3</b>
<b>Chapter 2</b> Vector-Based Approach for the Detection of Initial Dips Using Functional Near-Infrared Spectroscopy <i>by Toshinori Kato</i>	<b>23</b>
<b>Chapter 3</b> Application of ICA and Dynamic Mixture Model to Identify Microvasculature Activation in fMRI <i>by Yongxia Zhou</i>	<b>51</b>
<b>Section 2</b> Functional Brain Imaging	<b>69</b>
<b>Chapter 4</b> Simultaneous Smelling an Incense Outdoor and Putting the Hands Together Activate Specific Brain Areas <i>by Mitsuo Tonoike and Takuto Hayashi</i>	<b>71</b>
<b>Chapter 5</b> Neuroimaging Reveals Heterogeneous Neural Correlates of Reading Deficit in Individuals with Dyslexia Consistent with a Multiple Deficit Model <i>by Agnieszka A. Reid</i>	<b>101</b>
<b>Section 3</b> Structural Imaging	<b>129</b>
<b>Chapter 6</b> Imaging Tests for Predicting the Presence of Difficult Airway in Head and Neck Cancer Patients Undergoing Otorhinolaryngological Surgery <i>by Juan Gutiérrez Franchi, S. Merino, P. de la Calle, C. Perrino, M. Represa and P. Moral</i>	<b>131</b>

**Section 4**

Mind and Brain

145

**Chapter 7**

Functional Brain Imagery and Jungian Analytical Psychology: An Interesting Dance?

147

*by Leon Petchkovsky, Michael Petchkovsky, Philip Morris, Paul Dickson, Danielle T. Montgomery, Jonathan Dwyer, Patrick Burnett and Kristin Robertson-Gillam*

# Preface

Modern neuroimaging technologies allow not only for the visualization of anatomical structures but also for reaching their functional characteristics and monitoring their dynamics. Both structural and functional imaging have a long tradition in neuroscience and are widely used in basic research and clinical settings. The novel generations of neuroimaging tools include innovative methods in computed tomography (CT), magnetic resonance imaging (MRI), positron emission tomography, near-infrared spectroscopy (NIRS), electroencephalography, and magnetoencephalography (MEG). Both scientists and technologists are joining forces to find a way to improve technology, data analysis, and the application of neuroimaging in the wide spectra of scientific and clinical research, including the study of topography and dynamics of neural networks, sensory processing, and investigations of neurodevelopment, neurological diseases, neuropsychological disorders, and aging. Recent achievements of neuroimaging techniques suggest that they are essential for the identification of biological markers of the earliest stages of neurodiseases and the development of new therapies.

This book does not intend to provide the reader with a comprehensive overview of neuroimaging techniques and methods, but offers a narrow overview of processing and application advances in the current state-of-the-art imaging modalities and their utility. The first part of the book addresses the current advances of methods for analyzing brain imaging data. In the chapter “Supervised Sparse Component Analysis with Application to Brain Imaging Data,” the author provides strong evidence that supervised multiblock sparse component analysis identifies the association between brain areas at the voxel level, enabling more reliable interpretation of neuroimaging results. The chapter “Vector-Based Approach for the Detection of Initial Dips Using Functional Near-Infrared Spectroscopy” follows the progress in functional NIRS detection of local brain dynamics from its beginnings, discusses problems with single index analysis, and introduces a novel vector-based method, which could provide information on neural dynamics with a better temporal resolution. Finally, the chapter “Application of ICA and Dynamic Mixture Model to Identify Microvasculature Activation in fMRI” provides a comprehensive description of a novel method for improving the quality of the functional MRI signal, which comprises a complex mixture of neuronal, metabolic, and vascular process signals, and is additionally corrupted by multiple nonneuronal artifacts of instrumental, physiological, or subject-specific origin. The author presents both simulations and experimental testing of the novel method, pointing out the advantages and limitations of the proposed approach.

The second part of the book focuses on functional brain imaging, essential for understanding spontaneous neural activity and brain mechanisms engaged in the processing of external inputs, memory formation, and cognition. The chapter “Simultaneous Smelling an Incense Odor and Putting the Hands Together to Activate Specific Brain Areas” provides an example of the usefulness of MEG, a high temporal and spatial resolution neuroimaging technique, for investigating the changes in topology and dynamics of sensory processing evoked by multimodal inputs. In the chapter “Neuroimaging Reveals the Heterogeneous Neural Correlates

of Reading Deficit in Individuals with Developmental Dyslexia,” the author presents a unique approach utilizing the functional MRI technique and multiple case approach for testing the prediction of the main dyslexia theories, including the Phonological Deficit Theory, Magnocellular Deficit Theory, and Cerebral Deficit Theory.

The third part of the book focuses on the role of structural imaging techniques as diagnostic tools in the evaluation of disease processes that affect the airway. The advanced imaging modalities, including CT, ultrasonography, and MRI, are discussed as indispensable tools in head and neck cancer evaluation. The fourth part of the book provides an example of the possible synergy between psychology, art (music), and neuroimaging in an attempt to reach the integrated mind and brain constructs.

**Dr. Sanja Josef Golubić**  
Department of Physics,  
Faculty of Science,  
University of Zagreb,  
Croatia



---

Section 1

# Analysis of Brain Imaging Data

---



# Supervised Sparse Components Analysis with Application to Brain Imaging Data<sup>†</sup>

*Atsushi Kawaguchi*

## Abstract

We propose a dimension-reduction method using supervised (multi-block) sparse (principal) component analysis. The method is first implemented through basis expansion of spatial brain images, and the scores are then reduced through regularized matrix decomposition to produce simultaneous data-driven selections of related brain regions, supervised by univariate composite scores representing linear combinations of covariates. Two advantages of the proposed method are that it identifies the associations between brain regions at the voxel level and that supervision is helpful for interpretation. The proposed method was applied to a study on Alzheimer's disease (AD) that involved using multimodal whole-brain magnetic resonance imaging (MRI) and positron emission tomography (PET). For illustrative purposes, we demonstrate cases of both single- and multimodal brain imaging and longitudinal measurements.

**Keywords:** data-driven approach, dimension reduction, principal component analysis, multimodal, multi-measurement

## 1. Introduction

Recently, multiple neuroimaging data sets per subject have become obtainable due to the remarkable development of imaging techniques such as magnetic resonance imaging (MRI) and positron emission tomography (PET), as well as computer resources and technologies. Vandenberghe and Marsden [1] provide a review on the use of PET and MRI integration technology, such as integrated scanning devices, rather than data analysis. Other modalities such as diffusion MRIs (dMRIs) and functional MRIs (fMRIs) are also useful in collecting brain-related information. These multimodal imaging data sets have the potential to provide rich information about human health and behavior, such as brain function and structure, from different perspectives. From multiple measurements of a single-modal (or multimodal) technique, longitudinal changes in the status and combination of neuro

---

<sup>†</sup>Data used in preparation of this article were obtained from the Alzheimer's Disease Neuroimaging Initiative (ADNI) database ([adni.loni.usc.edu](http://adni.loni.usc.edu)). As such, the investigators within the ADNI contributed to the design and implementation of ADNI and/or provided data but did not participate in analysis or writing of this report. A complete listing of ADNI investigators can be found at: [http://adni.loni.usc.edu/wp-content/uploads/how\\_to\\_apply/ADNI\\_Acknowledgement\\_List.pdf](http://adni.loni.usc.edu/wp-content/uploads/how_to_apply/ADNI_Acknowledgement_List.pdf)

biomarkers can be observed to support the prediction and early diagnosis of disease and the classification of disease subtypes.

Multimodal brain imaging analysis is important in brain-related disease studies. Arbabshirani et al. [2] provide many reviews on the subject. Imaging data analysis makes a substantial contribution to the study of mental disorders. Most single-modal or multimodal imaging studies concern dementia leading to Alzheimer's disease (AD) [3] (around 300 of the AD imaging studies searched in Ref. [2]). Modalities considered in there are structural MRIs (sMRIs), fMRIs, dMRIs, fluorodeoxyglucose PETs, and Amyloid/Tau PETs. In a recent study, Ref. [4] examined sMRI and cerebrospinal fluid (CSF) markers. Magnetoencephalography (MEG) is also useful as AD biomarker, and its localization using sMRI has high accuracy [5]. Schizophrenia is the second most studied disorder after dementia. Shah et al. [6] provide an example of multimodal meta-analysis. For Huntington's disease, white matter is evaluated using dMRI [7]. For mood disorders (depressive disorder and bipolar disorder), Refs. [8, 9] provide a review of the machine learning method. Moeller and Paulus [10] studied the longitudinal prediction of relapse for substance-related disorders using MRI, fMRI, EEG, and PET. Moser et al. [11] studied schizophrenia and bipolar disorder using multimodal imaging data analysis. dMRI is also effective for analyzing these conditions [12]. For developmental disabilities, Ref. [13] investigated volume reductions in attention-deficit hyperactivity disorder (ADHD) with 1713 participants. Aoki et al. [14] reviewed dMRI studies and conducted meta-analysis for ADHD. Li et al. [15] provide a review of imaging studies in autism spectrum disorder. For anxiety disorder, Ref. [16] applied support vector machine (SVM) to multimodal data. They used clinical questionnaires and measured cortisol release, and gray and white matter volumes in subjects with generalized anxiety disorder and major depression and in healthy subjects. Steiger et al. [17] investigated cortical volume, diffusion tensor imaging, and network-based statistics using multimodal analysis for social anxiety disorder. For borderline personality disorder, Ref. [18] conducted an imaging-based meta-analysis of 10 studies. In cancer research, especially that on glioblastoma multiforme, multimodal imaging analysis is useful for identifying some types of tumors and evaluating patient prognosis (for more details, see [19]). Genome-related data can be regarded as a modality and called imaging genetics when analyzed in combination with imaging data [20].

One important technique for single- and multimodal imaging analysis is prediction, which is useful for the support of disease diagnosis and the selection of treatments [21]. SVM is the most used method not only in neuroimaging but also in the life sciences in high-dimensional data analysis. The random forest method is also useful due to their capability for complex interactions based on the tree model [22, 23]. For multimodal analysis, multiple kernel learning [24] and (multimodal) deep learning [25, 26] have been developed. Janssen et al. [27] reviewed machine learning methods for psychiatric prognosis. Related statistical methodology appeared as multi-omics in bioinformatics, and Ref. [28] reviewed these methods while introducing an R package, mixOmics.

Analysis for such discovery and evaluation is based on the detection of the buried signal in the noise (irrelevant information). Statistical analysis is useful for this purpose; however, it suffers from the ultrahigh dimensional and complex structure of this data, and appropriate dimension reduction is therefore required. Even if a machine learning method is used, appropriate input (feature) should be specified to obtain interpretable results because the method is feasible for high-dimensional procedures but not ultrahigh dimensional ones. A region-of-interest-based analysis was the leading approach. In contrast, whole-brain analysis is more informative, and if it is combined with a data-driven approach, it can potentially

obtain undiscovered knowledge. In [29], by using ReliefF [30], features such as the fractional amplitude of low-frequency fluctuations from resting-state fMRIs, segmented gray matter from sMRIs, and fractional anisotropy from dMRIs were extracted. Component analysis based on low-rank approximation is a successful data-driven approach in the fields of not only neuroimaging but also other biological and medical big data analyses, including principal component analysis, partial least squares, canonical correlation analysis (CCA), independent component analysis (ICA), and nonnegative matrix factorization. These methods are organized into a matrix decomposition framework consisting of score and loading (weight) matrices. The score matrix, with same row length as the number of subjects, is regarded as dimension-reduced data and is suitable for application to statistical models. The weight matrix, with the same column length as the number of features in the imaging data, is regarded as the basis images. All these methods, except for ICA, have a derivation sparse approach with a regularized matrix decomposition to pose small weights to zeros, which helps estimation by avoiding irrelevant information. In addition, the resulting weights can be interpreted to mean that the corresponding features with nonzero weights contribute to the basis image, specifically to produce data-driven selections of brain regions related to that component.

These methods also consider another direction in which the application of multimodal imaging data can be extended. Supplementary information from another data set can also be useful for the interpretation of the output. For this purpose, appropriate data fusion or integration techniques are required and are useful for multisite studies. In neuroimaging data analysis, multimodal CCA (mCCA) [31] and mCCA + joint ICA [32] have been developed on the schizophrenia study. Multivariate data fusion approaches were categorized by [33] into asymmetric or symmetric data and blind or semi-blind data in symmetric approach. The asymmetric approach is a regression-type approach and includes specific modalities such as dMRI and electroencephalography. The symmetric approach is a correlation-type approach and allows relationships in both directions. Kawaguchi [19] constructed a risk score for glioblastomas based on MRI data and proposed a two-step dimension-reduction method using a radial basis function-supervised multi-block sparse principal component analysis (SMS-PCA) method. Kawaguchi and Yamashita [34] proposed a more general case including a PLS or CCA framework and applied it to MRI, PET, and SNP data sets. Yoshida et al. [4] analyze imaging and non-imaging data with network structure by using the PLS.

In this chapter, we applied SMS-PCA to MRI and PET data sets and a longitudinal MRI data set. One of the key features in the analysis is a multi-block technique which can achieve structural dimension reduction with interpretable parameters (weights for each data set and the possibility of combining them). Although it is not the focus of this chapter, the dimension reduction prior to SMS-PCA is conducted using 3D basis functions. Specifically, our dimension reduction takes place in two steps, and, as described in [35] which applied these techniques to longitudinal study, this two-step approach yields a composite basis function expression with a flexible shape. The organization of this chapter is as follows. Section 2 describes the methodology of the SMS-PCA, which is applied to real data in Section 3. The characteristics of the method, found through its application, are discussed in Section 4.

## 2. Methods

We describe the proposed method in this section. The contents are similar to Ref. [19].

## 2.1 Priory dimension reduction

$\mathbf{S} = \{\mathbf{s}_\alpha\}_{\alpha=1, \dots, n}$  is the  $n \times N$  matrix whose column corresponds to the vectorized original image data. As the dimensions for each  $m$ th image are the same, we use the same basis function to reduce the dimension from  $N$  to  $q$ .  $\mathbf{X} = \mathbf{S}\mathbf{B}$  is the  $n \times q$  matrix, where  $\mathbf{B}$  is the  $N \times q$  matrix whose  $j$ th column corresponds to the vectorized basis function with the  $j$ th knot being the center. Note that knots are pre-specified to span the space equally, as shown in **Figure 1**. In this example, four-pixel equal spanning knots are applied.

## 2.2 Objective function

Dimension reduction using the basis function is then followed by the SMS-PCA method, considering (sample) correlations based on data values. We consider score  $\mathbf{t}$  for  $n \times q$  matrices  $\mathbf{X}_m$ , where  $m = 1, 2, \dots, M$  with the following multi-block structure:

$$\mathbf{t} = \sum_{m=1}^M b_m \mathbf{X}_m \mathbf{w}_m = \sum_{m=1}^M b_m \mathbf{t}_m, \quad (1)$$

where  $\mathbf{w}_m$  is the weight vector for the  $m$ th sub-block  $\mathbf{X}_m$  and  $b_m$  is the weight for the superblock. Here, it should be noted that the scores in Eq. (1) are referred to as the super scores, whereas  $\mathbf{t}_m = \mathbf{X}_m \mathbf{w}_m$  is referred to as the block score. **Figure 2** schematically describes the score structure for the case of  $M = 2$ .

Thus, the super score has a hierarchical structure for each individual and can be used in an application such as the construction of a diagnosis score.

When matrix  $\mathbf{X}_m$  is normalized by its columns, the weights  $\mathbf{w} = (w_1, w_2, \dots, w_M)^\top$  and  $\mathbf{b} = (b_1, b_2, \dots, b_M)^\top$  are estimated by maximizing the function

$$L(\mathbf{b}, \mathbf{w}) = (1 - \mu) \mathbf{t}^\top \mathbf{t} + \mu \mathbf{t}^\top \mathbf{Z} - \sum_{m=1}^M P_{\lambda_m}(\mathbf{w}_m) \quad (2)$$

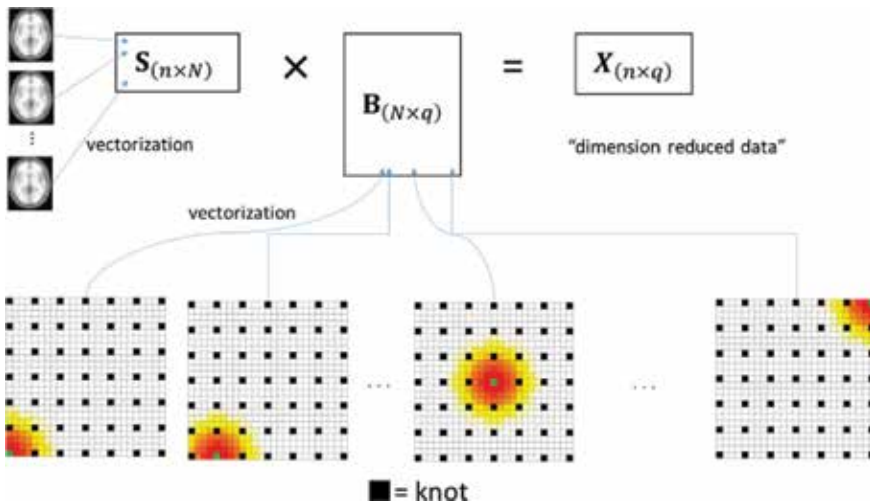


**Figure 1.**  
Dimension reduction via basis function.



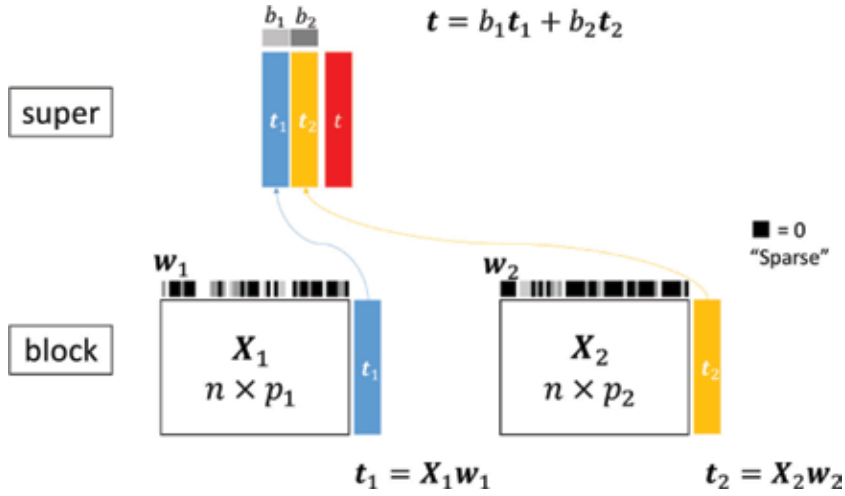


**Figure 2.**  
Score structure.

1. Initialize  $\mathbf{t}$  with  $\|\mathbf{t}\|_2 = 1$ .
2. Repeat until convergence:
  - 2.1. Set  $\tilde{\mathbf{w}}_m = h_{\lambda_m}(b_m \mathbf{X}_m^T \{(1 - \mu)\mathbf{t} + \mu \mathbf{Z}\})$ , where  $h_\lambda(y) = \text{sign}(y) (|y| > \lambda)_+$ , and normalize as  $\hat{\mathbf{w}}_m = \tilde{\mathbf{w}}_m / \|\tilde{\mathbf{w}}_m\|_2$  ( $m = 1, 2, \dots, M$ ).
  - 2.2. Set  $\mathbf{t}_m = \mathbf{X}_m \hat{\mathbf{w}}_m$  and  $\tilde{b}_m = \mathbf{t}_m^T \{(1 - \mu)\mathbf{t} + \mu \mathbf{Z}\}$ ; then set  $\tilde{\mathbf{b}} = (\tilde{b}_1, \tilde{b}_2, \dots, \tilde{b}_M)^T$  and normalize as  $\hat{\mathbf{b}} = \tilde{\mathbf{b}} / \|\tilde{\mathbf{b}}\|_2$ .
  - 2.3. Set  $\mathbf{t} = \sum_{m=1}^M \hat{b}_m \mathbf{X}_m \hat{\mathbf{w}}_m$ .
3. (Deflation step) Set  $\mathbf{p}_m = \mathbf{X}_m^T \mathbf{t}_m / \mathbf{t}_m^T \mathbf{t}_m$  and  $\hat{\mathbf{X}}_m = \mathbf{t}_m \mathbf{p}_m^T$ , and  $\mathbf{X}_m \leftarrow \mathbf{X}_m - \hat{\mathbf{X}}_m$ .

**Table 1.**  
Algorithm for SMS-PCA method.

subject to  $\|\mathbf{w}_m\|_2^2 = 1$  and  $\|\mathbf{b}\|_2^2 = 1$  with  $\|\cdot\|_2$  as the L2 norm, where  $0 \leq \mu \leq 1$  is the proportion of the supervision,  $P_\lambda(x)$  is the penalty function,  $[P_\lambda(x) = 2\lambda|x|]$  is used in this study], and  $\lambda > 0$  is the regularized parameter that is used to control the sparsity. The larger value of the regularization parameter  $\lambda_m$  has many nonzero elements in  $\mathbf{w}_m$ .

### 2.3 Optimization

The algorithm given in **Table 1** is used to estimate the weights in Eq. (1) by maximizing L in Eq. (2). The rationality behind this approach is provided in [19].

Note that the deflation step yields multiple components and has several alternatives; that is, through  $K$  time iteration for step. 1 to 3 of the algorithm, we can obtain  $K$  component super scores  $\mathbf{t}^{(1)}, \dots, \mathbf{t}^{(K)}$  with  $\mathbf{t}^{(k)} = (\mathbf{t}_1^{(k)}, \dots, \mathbf{t}_M^{(k)})^T$ .

### 2.4 Parameter selection

The optimal value for  $\lambda = (\lambda_1, \dots, \lambda_M)^T$  is selected by minimizing the Bayesian information criterion (BIC):

$$\text{BIC}(\lambda) = \log \left( \frac{\sum_{m=1}^M \|\hat{\mathbf{X}}_m^{(r)} - \mathbf{X}_m\|^2}{nMq} \right) + \frac{\log(nMq)}{nMq} (\# \text{ nonzero elements in } \mathbf{w}_m),$$

where  $\hat{\mathbf{X}}_m^{(r)} = \mathbf{T}_m^{(r)} \mathbf{P}_m^{(r)}$  with  $\mathbf{T}_m^{(r)} = [\mathbf{t}_m^{(1)}, \dots, \mathbf{t}_m^{(r)}]$  and  $\mathbf{P}_m^{(r)} = [\mathbf{p}_m^{(1)}, \dots, \mathbf{p}_m^{(r)}]$  is obtained from  $r$  deflation steps (the projection of  $\mathbf{X}_m$  onto the  $r$ -dimensional subspace). There are several search strategies for optimization, and these are introduced in the software options below.

## 2.5 Software

The statistical software R package `msma` is provided to implement the method described in Ref. [34] where the SMS-PCA method is a part of the package and the PLS type can also be implemented. The package is available from the Comprehensive R Archive Network (CRAN) at <http://CRAN.R-project.org/package=msma>. Four-parameter search methods are available. Here, the parameters are  $\lambda_m$  and the number of components. The “simultaneous” method identifies the number of components by searching the regularized parameters in each component. The “`regpara1st`” method identifies the regularized parameters by fixing the number of components and then searching for the number of components with the selected regularized parameters. The “`ncomp1st`” method identifies the number of components with a regularized parameter of 0 and then searches for the regularized parameters with the selected number of components. The “`regparaonly`” method searches for the regularized parameters with a fixed number of components.

In this chapter, the “`ncomp1st`” method was applied with nonzero sparsity when the number of components was selected because, in our experience, the BIC value suffered from the high dimensionality of the data. The basic R code for this method is as follows:

```
tuneparams = optparasearch(X=X, Z=Z, search.method="ncomp1st",
maxpct4ncomp=0.5, muX=0.5)
```

where the argument `maxpct4ncomp = 0.5` means that  $0.5 \lambda_{\max}$  is used as the regularized parameter when the number of components is searched and where  $\lambda_{\max}$  is the maximum of the regularized parameters among the possible candidates. In order to obtain the final fit result with optimized parameters, the following code should be implemented:

```
fit1 = msma(X=X, Z=Z, comp=tuneparams$optncomp, lambdaX=tuneparams
$optlambdaX, lambdaY=tuneparams$optlambdaY, muX = 0.5)
```

For more details, please see the package manual.

## 3. Application

In this section, we apply the SMS-PCA described in the previous section to real data. The data used in the preparation of this article were obtained from the Alzheimer’s Disease Neuroimaging Initiative (ADNI) database ([adni.loni.usc.edu](http://adni.loni.usc.edu)). The ADNI was launched in 2003 as a public-private partnership, led by Principal Investigator Michael W. Weiner, MD. The primary goal of ADNI has been to test whether serial magnetic resonance imaging (MRI), positron emission tomography (PET), other biological markers, and clinical and neuropsychological assessment can be combined to measure the progression of mild cognitive impairment (MCI) and

early Alzheimer’s disease (AD). We use two types of data set: baseline measurement with multimodal MRI and PET images and repeated measuring MRI images.

### 3.1 Multimodality

#### 3.1.1 Data

Baseline imaging data were collected from 106 subjects with mean ages of 75.2 years for the 54 normal cognitive subjects and 72.9 years for the 27 patients with dementia. This data set was somewhat larger than that of [34] because in this study single-nucleotide polymorphism (SNP) was not considered and subjects with missing SNP data were included. **Table 2** summarizes the characteristics of these patients.

We consider imaging data from two modalities, MRI  $\mathbf{X}_1$  and PET  $\mathbf{X}_2$ , namely,  $M = 2$ . The preprocessing method is the same as that used in [34]. For the basis function, we used four-voxel (therefore,  $h = \sqrt{3 \times 4^2} = 6.93$ ) equal spacing knots because of the results of our simulation study. The clinical outcome to supervise is given by  $Z = 3.17 \times CDR + 0.11 \times ADAS13 - 0.57 \times MMSE$  where CDR is the clinical dementia rating score, ADAS13 is the Alzheimer’s disease assessment scale-cognitive subscale, and MMSE is the mini-mental state examination score. These coefficients were the same as in [34]. The SMSMA method was applied to the data  $(\mathbf{X}_1, \mathbf{X}_2, \mathbf{Z})$  with parameters  $\mu = 0, 0.25, 0.5, \text{ and } 0.75$ .

#### 3.1.2 Results

The original data with dimensions of 2,122,945 ( $= 121 \times 145 \times 121$ ) was reduced to 7,162 using the basis functions for each imaging data set. The number of components were selected as 8 for all  $\mu = 0, 0.25, 0.5, 0.75, 1$ . **Figure 3** shows the correlation matrix from the dataset with the binary outcome, AD or Normal, and the resulting super scores for each  $\mu$ .

The correlations between the super scores were small except for  $\mu = 1$ , and for  $\mu = 0$ , the second component had a high correlation with the outcome. In contrast, for  $\mu > 0$ , the first component had the highest correlation with the outcome.

**Table 3** shows the results for the multiple logistic regression model with AD or normal as the outcomes and the super scores as predictors for each  $\mu$ . The numbers

	Dementia	Normal	P
n	52	54	
Age (mean [sd])	75.41 (7.18)	74.93 (4.89)	0.684
PTGENDER = Male (%)	31 (59.6)	36 (66.7)	0.582
APOE4 (%)			<0.001
0	17 (32.7)	39 (72.2)	
1	29 (55.8)	13 (24.1)	
2	6 (11.5)	2 (3.7)	
PTEDUCAT (mean [sd])	14.19 (3.04)	15.89 (2.99)	0.005
CDRSB (mean [sd])	4.54 (1.73)	0.03 (0.12)	<0.001
ADAS11 (mean [sd])	18.70 (5.63)	6.56 (3.28)	<0.001
ADAS13 (mean [sd])	28.94 (6.30)	10.08 (4.30)	<0.001
MMSE (mean [sd])	23.38 (2.07)	28.87 (1.24)	<0.001

**Table 2.**  
 Characteristic for data set 1.

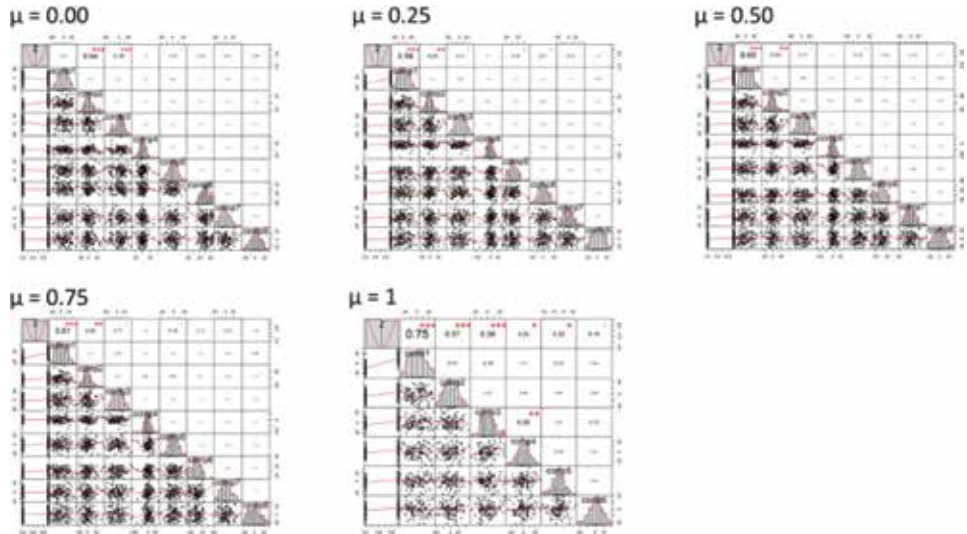


**Figure 3.**  
Correlations between super scores.

of 5% statistically significant components were 3, 4, 3, 3, and 0 for  $\mu = 0, 0.25, 0.5, 0.75,$  and 1, respectively. The minimum numbers of nonzero subweights were 552, 581, 574, 523, and 1075, respectively.

**Figure 4** shows the reconstructed subweights  $Bw_1$  and  $Bw_2$  for the MRI and PET data, respectively, overlying a structural brain image shown for the most correlated components with the binary outcome from each of  $\mu = 0, 0.5, 0.75,$  and 1. The images for  $\mu = 0.25$  were similar to those of  $\mu = 0.5, 0.75$  and are not shown here.

**Figure 5** shows the reconstructed subweights  $Bw_1$  and  $Bw_2$  overlying a structural brain image and bar plots for the super-weights (right bottom) in the case of  $\mu = 0.5$  for all components.

In each component, the negative and positive sides are represented. These can be interpreted by looking at the sign of the super-weight. Most cases remain on one side of 0 (positive or negative), except for components 5 to 8. The super-weights are similar between MRI and PET.

A 10-fold cross validated ROC analysis (**Figure 6A**) was conducted to evaluate the diagnostic probabilities estimated from the multivariable logistic regression mode whose coefficients and p-values are shown in **Table 3**. For comparison, the single modalities, MRI (**Figure 6B**) and PET (**Figure 6C**), were also analyzed.

In the case of the multimodal MRI and PET (**Figure 6A**),  $\mu = 1$  had the highest AUC value (0.984) following by  $\mu = 0.75$  (AUC = 0.880). In the case of the single-modal MRI (**Figure 6B**), all values were below the AUC values of the multimodal case. In the case of the single-modal PET (**Figure 6C**),  $\mu = 1$  and 0.75 outperformed the multimodal case, and the other values ( $\mu = 0, 0.25,$  and 0.5) did not.

## 3.2 Multi-measurements

### 3.2.1 Data

The second data set was a collection of repeated measured imaging data from 68 patients with mild cognitive impairment (MCI). There were two groups, the conversion to dementia MCI (cMCI) group and the stable MCI (not converted to dementia, sMCI) group. MRI data measured at four time points were used. For the cMCI group, the four time points were just before diagnosis of conversion.

	$\mu = 0.00$		$\mu = 0.25$		$\mu = 0.50$		$\mu = 0.75$		$\mu = 1$	
	Estimate	$\Pr(> z )$	Estimate	$\Pr(> z )$	Estimate	$\Pr(> z )$	Estimate	$\Pr(> z )$	Estimate	$\Pr(> z )$
comp1	-0.0210	0.0615	0.0827	<0.0001	0.0832	<0.0001	0.0857	<0.0001	4.287	0.9982
comp2	0.0882	<0.0001	0.0460	0.0030	0.0458	0.0031	0.0451	0.0039	2.555	0.9989
comp3	-0.0621	0.0001	0.0180	0.0923	0.0180	0.0920	0.0181	0.0952	4.633	0.9995
comp4	-0.0072	0.6126	0.0037	0.7953	0.0044	0.7583	0.0064	0.6574	1.827	0.9987
comp5	-0.0424	0.0228	0.0452	0.0432	0.0430	0.0203	0.0431	0.0206	3.905	0.9988
comp6	-0.0364	0.0900	0.0396	0.0320	0.0403	0.0715	0.0425	0.0658	4.994	0.9984
comp7	0.0446	0.0891	0.0505	0.0636	0.0510	0.0619	0.0535	0.0549		
comp8	0.0336	0.2517	-0.0228	0.3804	-0.0226	0.3816	-0.0218	0.3904		

**Table 3.**  
 Results for multivariable logistic regression analysis.

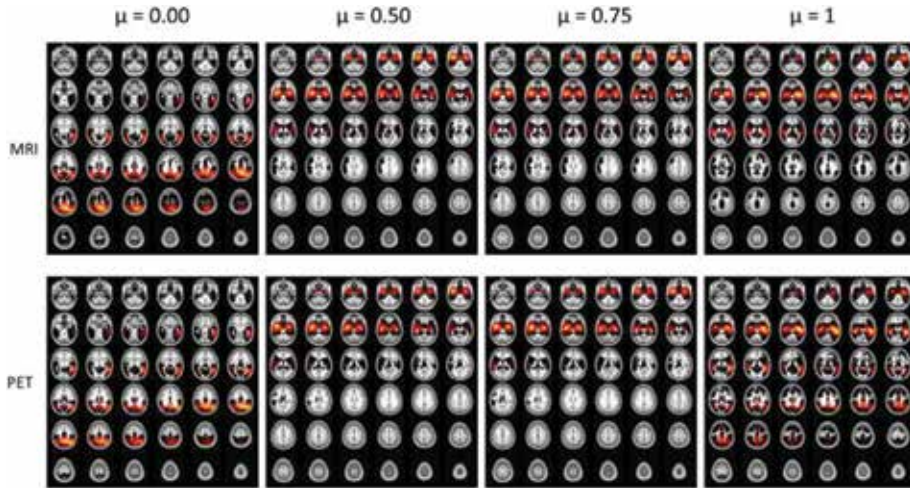


Figure 4.  
Subweights.

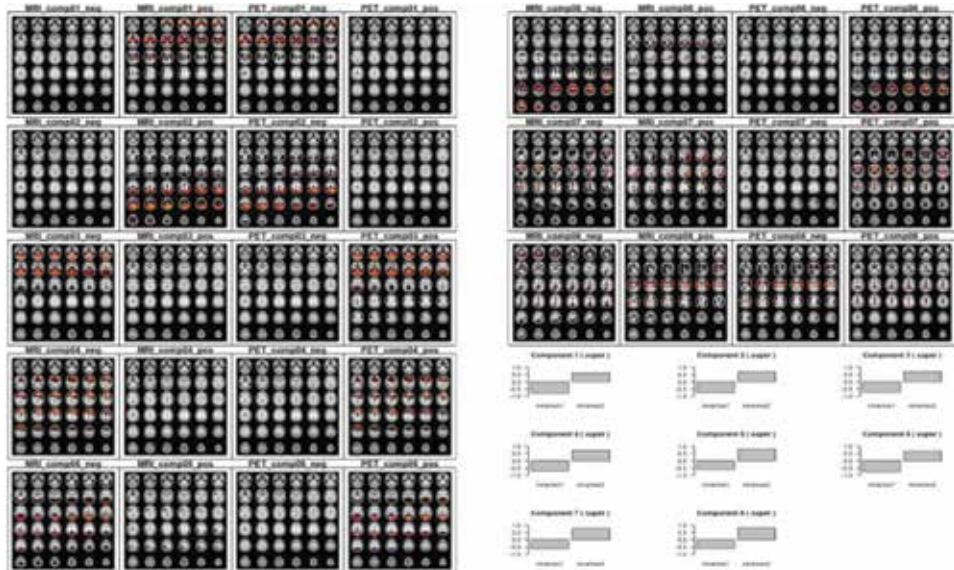


Figure 5.  
Sub- and super-weights for all components of  $\mu = 0.5$ .

For the sMCI group, the four time points were from the baseline for the entire period of the study. Groups were matched for age, gender, and intracranial volume. **Table 4** summarizes the characteristics of these patients at baseline (at the first image observation).

For imaging data processing, we used the VBM8 toolbox. For the basis function, we used four-voxel equal spacing knots, as in the first study in the previous section. The clinical outcome is given by  $Z = 0.44 \times CDR + 0.12 \times ADAS13 - 0.11 \times MMSE$ . The coefficients were different from those in the first study because the target population was different.

### 3.2.2 Results

The original data with dimensions of 2,122,945 ( $=121 \times 145 \times 121$ ) was reduced to 7162 using basis functions for each imaging data set. The number of components



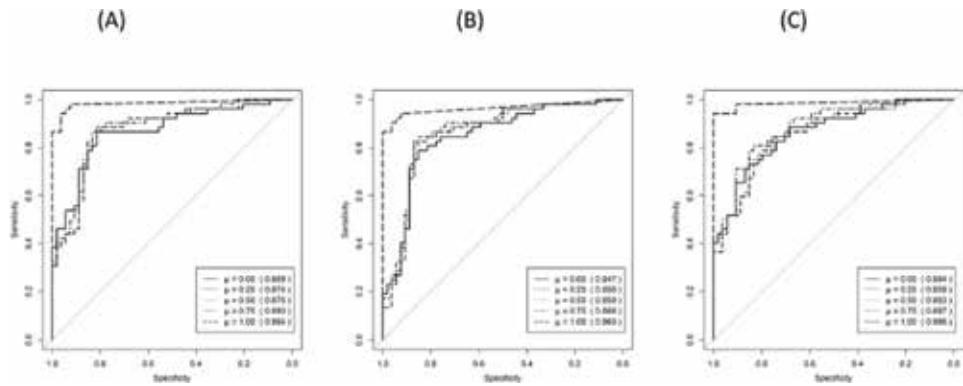


**Figure 6.** Results for cross-validated ROC analysis for (A) MRI and PET, (B) MRI, and (C) PET.

	cMCI	sMCI	p
n	34	34	
Age (mean [sd])	76.06 (5.94)	75.91 (5.90)	0.922
PTGENDER = 2 (%)	10 (29.4)	10 (29.4)	1.000
APOE4 (%)			0.040
0	12 (35.3)	22 (64.7)	
1	18 (52.9)	11 (32.4)	
2	4 (11.8)	1 (2.9)	
PTEDUCAT (mean [sd])	16.15 (3.06)	15.50 (2.86)	0.371
CDRSB (mean [sd])	1.76 (1.07)	1.32 (0.73)	0.051
ADAS11 (mean [sd])	12.09 (3.49)	9.40 (4.08)	0.005
ADAS13 (mean [sd])	19.65 (4.31)	15.93 (6.10)	0.005
MMSE (mean [sd])	26.71 (1.71)	27.88 (1.70)	0.006

**Table 4.** Characteristic for data set 2.

selected was 6 for  $\mu = 0, 0.25, 0.5, 0.75$  and 4 for  $\mu = 1$ . **Table 5** shows the results for the multiple logistic regression model with cMCI or sMCI as the outcomes and the super scores as the predictors for each  $\mu$ . The numbers of 5% statistically significant components were 2, 3, 3, 3, and 2 for  $\mu = 0, 0.25, 0.5, 0.75, 1$ , respectively. The minimum numbers of nonzero subweights were 724, 736, 749, 753, and 852, respectively.

A tenfold cross validated ROC analysis (**Figure 7**) was conducted to evaluate the diagnostic probabilities estimated from the multivariable logistic regression mode whose coefficients and p-values are shown in **Table 5**.

For comparison, the single-modal analysis for each time point was conducted. The fourth time point (MRI4), which is closest to the MCI conversion diagnosis time, had the highest AUC values, and these were higher than the multimodal values (**Figure 8**).

**Figure 9** shows the first component subweights,  $Bw_m$  ( $m = 1, 2, 3, 4$ ), for the four time points for  $\mu = 0$  and 0.5. In the case of  $\mu = 0.5$ , the hippocampus area was related to the components, and in the case of  $\mu = 0$ , the parietal lobe was.

	$\mu = 0.00$		$\mu = 0.25$		$\mu = 0.50$		$\mu = 0.75$		$\mu = 1$	
	Estimate	$\Pr(> z )$	Estimate	$\Pr(> z )$	Estimate	$\Pr(> z )$	Estimate	$\Pr(> z )$	Estimate	$\Pr(> z )$
comp1	-0.0132	0.0139	0.0142	0.0215	0.0142	0.0212	0.0143	0.0204	0.0331	0.0018
comp2	0.0083	0.1714	0.0198	0.0199	0.0095	0.1298	0.0097	0.1240	0.0359	0.0049
comp3	-0.0125	0.1481	-0.0093	0.1410	0.0195	0.0215	0.0196	0.0214	0.0172	0.2833
comp4	-0.0333	0.0042	-0.0073	0.4505	-0.0073	0.4490	-0.0070	0.4709	-0.0157	0.5288
comp5	0.0001	0.9963	0.0458	0.0022	0.0460	0.0021	0.0469	0.0019		
comp6	-0.0203	0.1617	0.0077	0.6205	0.0074	0.6313	0.0078	0.6139		

**Table 5.**  
Results for multivariable logistic regression analysis.

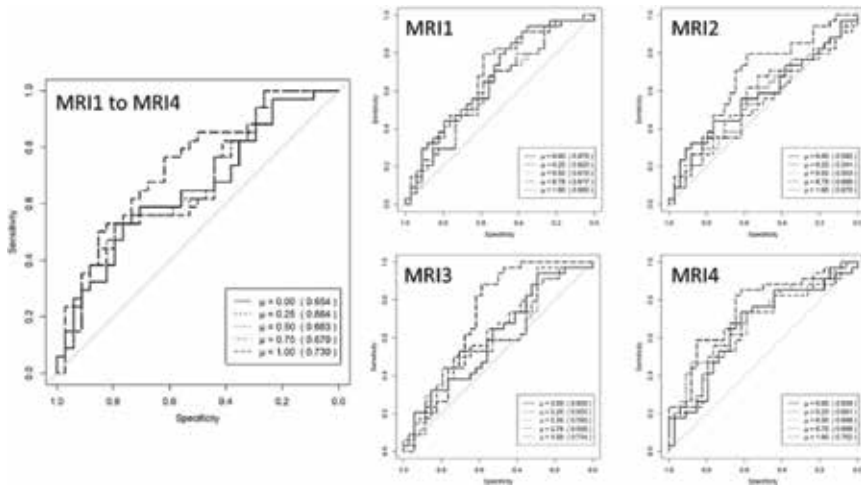


**Figure 7.**  
 Results for cross validated ROC analysis.

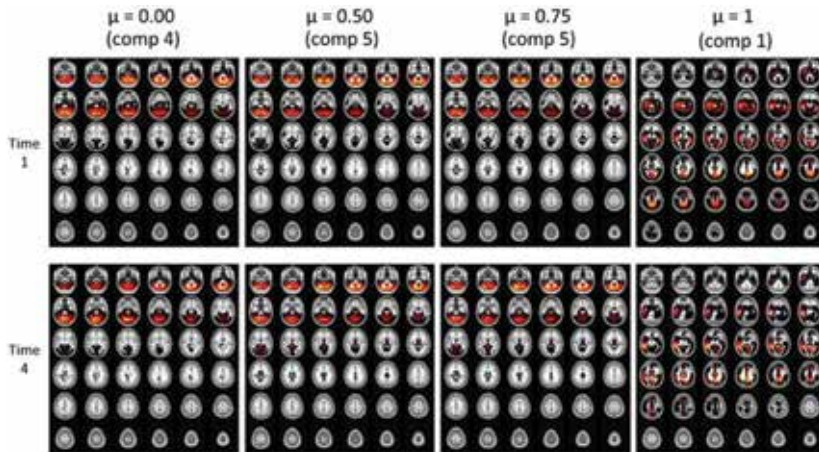


**Figure 8.**  
 Subweights for times 1 and 4.

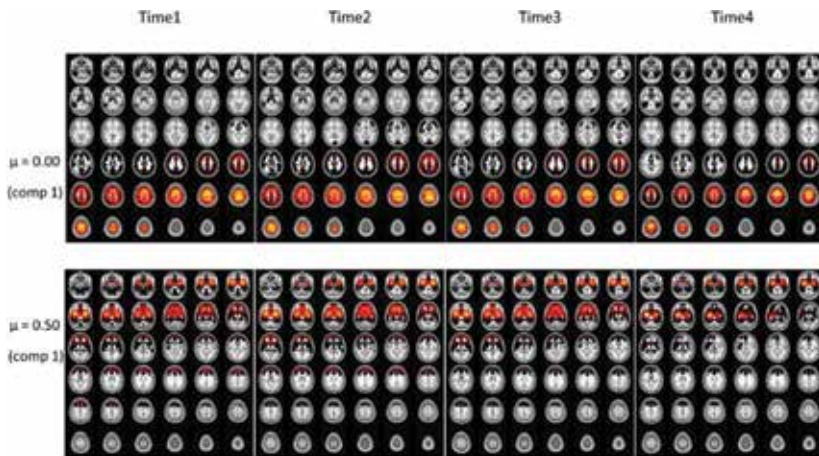


**Figure 9.**  
 Subweights for all time points for  $\mu = 0$  and  $0.5$ .

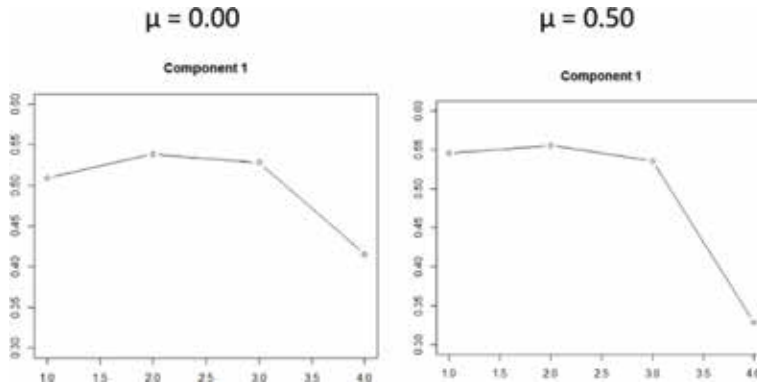


**Figure 10.**  
Super-weights.

**Figure 10** shows the corresponding super-weights. This result should be carefully interpreted. For time 4, the sparsest block weights were obtained, and thus the weight values were larger than those of times 1 to 3, which were balanced by the small super-weight. As a result, the super score for this component has the mean value of the block scores.

#### 4. Discussion

In this chapter, the SMS-PCA method was introduced and applied to multiple measured neuroimaging data sets. The first data set consisted of two different types of images, MRI and PET. The second data set consisted of repeated MRI measurements (the same type of image). These imaging data have many voxels per person which were reduced using the basis function prior to conducting the SMS-PCA. The multi-block feature of the SMS-PCA also caused further reduction in each block, and their summary was obtained in the super level where the weights were the relationship and the scores were used in the prediction model.

One of the key features in the SMS-PCA is that it is supervised and its proportion to (self) variance is parametrized by  $\mu$ . In each study, the impact of  $\mu$  was studied. The case of  $\mu = 1$  resulted in only supervision, that is, only the correlation between the score and the outcome, without the variance of the score. As in an original PCA, maximizing the variance of the score corresponds to  $\mu = 0$ , and the correlated variables (voxels) have relatively high weights for each component. Thus, the messy maps for the block weights overlaying the brain in the case of  $\mu = 1$  were reasonable. In both applications, because  $\mu = 0.25, 0.5$ , and  $0.75$  had similar results, a possible large value in  $\mu < 1$ , or the median value  $\mu = 0.5$  with a trade-off, can be selected as optimal.

Repeated measured imaging data analysis was studied in [35] which reduced the imaging dimensions using basis functions but did this independent for each image. In contrast, in this study, the correlation between measurements at different time points is considered. That is, simultaneous temporal and spatial correlation was considered. This approach was limited by the need that the number of images for each individual be the same, and this will be improved in future work. In addition, the method introduced in this chapter can incorporate modalities such as network models which would need to summarize the information into the component. This research is in progress.

## **5. Conclusion**

Although there is room for improvement in this method, this study showed reasonable results when the method was applied to the dementia study. In conclusion, this data-driven approach would be helpful for exploratory neuroimaging data analysis.

## **Acknowledgements**

This study was supported in part by the Intramural Research Grant (27-8) for Neurological and Psychiatric Disorders of NCNP. For this research work, we used the supercomputer of ACCMS, Kyoto University. Data collection and sharing for this project were funded by the Alzheimer's Disease Neuroimaging Initiative (ADNI) (National Institutes of Health Grant U01 AG024904) and DOD ADNI (Department of Defense Award Number W81XWH-12-2-0012). ADNI is funded by the National Institute on Aging, the National Institute of Biomedical Imaging and Bioengineering, and through generous contributions from the following: AbbVie, Alzheimer's Association; Alzheimer's Drug Discovery Foundation; Araclon Biotech; BioClinica, Inc.; Biogen; Bristol-Myers Squibb Company; CereSpir, Inc.; Cogstate; Eisai Inc.; Elan Pharmaceuticals, Inc.; Eli Lilly and Company; EuroImmun; F. Hoffmann-La Roche Ltd. and its affiliated company Genentech, Inc.; Fujirebio; GE Healthcare; IXICO Ltd.; Janssen Alzheimer Immunotherapy Research & Development, LLC.; Johnson & Johnson Pharmaceutical Research & Development LLC.; Lumosity; Lundbeck; Merck & Co., Inc.; Meso Scale Diagnostics, LLC.; NeuroRx Research; Neurotrack Technologies; Novartis Pharmaceuticals Corporation; Pfizer Inc.; Piramal Imaging; Servier; Takeda Pharmaceutical Company; and Transition Therapeutics. The Canadian Institutes of Health Research is providing funds to support ADNI clinical sites in Canada. Private sector contributions are facilitated by the Foundation for the National Institutes of Health ([www.fnih.org](http://www.fnih.org)). The grantee organization is the Northern California Institute for Research and Education, and the study is coordinated by the Alzheimer's Therapeutic Research Institute at the University of Southern California. ADNI data are disseminated by the Laboratory of Neuro Imaging at the University of Southern California.

## **Conflict of interest**

None declared.

## **Author details**


Atsushi Kawaguchi<sup>†</sup>  
Faculty of Medicine, Saga University, Saga, Japan

\*Address all correspondence to: akawa@cc.saga-u.ac.jp

<sup>†</sup>For the Alzheimer's Disease Neuroimaging Initiative

## **IntechOpen**

---

© 2018 The Author(s). Licensee IntechOpen. This chapter is distributed under the terms of the Creative Commons Attribution License (<http://creativecommons.org/licenses/by/3.0>), which permits unrestricted use, distribution, and reproduction in any medium, provided the original work is properly cited. 

## References

- [1] Vandenberghe S, Marsden PK. PET-MRI: A review of challenges and solutions in the development of integrated multimodality imaging. *Physics in Medicine and Biology*. 2015; **60**:R115-R154
- [2] Arbabshirani MR, Plis S, Sui J, Calhoun VD. Single subject prediction of brain disorders in neuroimaging: Promises and pitfalls. *NeuroImage*. 2017; **145**:137-165
- [3] Rondina JM, Ferreira LK, De Souza Duran FL, et al. Selecting the most relevant brain regions to discriminate Alzheimer's disease patients from healthy controls using multiple kernel learning: A comparison across functional and structural imaging modalities and atlases. *NeuroImage: Clinical*. 2018; **17**:628-641
- [4] Yoshida H, Kawaguchi A, Yamashita F, Tsuruya K. The utility of a network-based clustering method for dimension reduction of imaging and non-imaging biomarkers predictive of Alzheimer's disease. *Scientific Reports*. 2018; **8**:2807
- [5] Josef Golubic S, Aine CJ, Stephen JM, Adair JC, Knoefel JE, Supek S. MEG biomarker of Alzheimer's disease: Absence of a prefrontal generator during auditory sensory gating. *Human Brain Mapping*. 2017; **38**:5180-5194
- [6] Shah C, Zhang W, Xiao Y, et al. Common pattern of gray-matter abnormalities in drug-naive and medicated first-episode schizophrenia: A multimodal meta-analysis. *Psychological Medicine*. 2017; **47**: 401-413
- [7] Liu W, Yang J, Burgunder J, Cheng B, Shang H. Diffusion imaging studies of Huntington's disease: A meta-analysis. *Parkinsonism & Related Disorders*. 2016; **32**:94-101
- [8] Kim YK, Na KS. Application of machine learning classification for structural brain MRI in mood disorders: Critical review from a clinical perspective. *Progress in Neuro-Psychopharmacology & Biological Psychiatry*. 2018; **80**:71-80
- [9] Librenza-Garcia D, Kotzian BJ, Yang J, et al. The impact of machine learning techniques in the study of bipolar disorder: A systematic review. *Neuroscience & Biobehavioral Reviews*. 2017; **80**:538-554
- [10] Moeller SJ, Paulus MP. Toward biomarkers of the addicted human brain: Using neuroimaging to predict relapse and sustained abstinence in substance use disorder. *Progress in Neuro-Psychopharmacology & Biological Psychiatry*. 2018; **80**:143-154
- [11] Moser DA, Doucet GE, Lee WH, et al. Multivariate associations among behavioral, clinical, and multimodal imaging phenotypes in patients with psychosis. *JAMA Psychiatry*. 2018; **75**: 386-395
- [12] O'Donoghue S, Holleran L, Cannon DM, McDonald C. Anatomical dysconnectivity in bipolar disorder compared with schizophrenia: A selective review of structural network analyses using diffusion MRI. *Journal of Affective Disorders*. 2017; **209**:217-228
- [13] Hoogman M, Bralten J, Hibar DP, et al. Subcortical brain volume differences in participants with attention deficit hyperactivity disorder in children and adults: A cross-sectional mega-analysis. *Lancet Psychiatry*. 2017; **4**:310-319
- [14] Aoki Y, Cortese S, Castellanos FX. Research review: Diffusion tensor imaging studies of attention-deficit/hyperactivity disorder: Meta-analyses

and reflections on head motion. *Journal of Child Psychology and Psychiatry*. 2018;**59**:193-202

[15] Li D, Karnath HO, Xu X. Candidate biomarkers in children with autism spectrum disorder: A review of MRI studies. *Neuroscience Bulletin*. 2017;**33**: 219-237

[16] Hilbert K, Lueken U, Muehlhan M, Beesdo-Baum K. Separating generalized anxiety disorder from major depression using clinical, hormonal, and structural MRI data: A multimodal machine learning study. *Brain and Behavior: A Cognitive Neuroscience Perspective*. 2017;**7**:e00633

[17] Steiger VR, Brühl AB, Weidt S, et al. Pattern of structural brain changes in social anxiety disorder after cognitive behavioral group therapy: A longitudinal multimodal MRI study. *Molecular Psychiatry*. 2017;**22**:1164-1171

[18] Schulze L, Schmahl C, Niedtfeld I. Neural correlates of disturbed emotion processing in borderline personality disorder: A multimodal meta-analysis. *Biological Psychiatry*. 2016;**79**:97-106

[19] Kawaguchi A. Supervised dimension reduction methods for brain tumor image data analysis. In: Matsui S, Crowley J, editors. *Frontiers of Biostatistical Methods and Applications in Clinical Oncology*. Singapore: Springer; 2017. pp. 401-412

[20] Shen L, Thompson PM, Potkin SG, et al. Genetic analysis of quantitative phenotypes in AD and MCI: Imaging, cognition and biomarkers. *Brain Imaging and Behavior*. 2014;**8**:183-207

[21] Stephan KE, Schlagenhaut F, Huys QJM, et al. Computational neuroimaging strategies for single patient predictions. *NeuroImage*. 2017;**145**:180-199

[22] Sarica A, Cerasa A, Quattrone A. Random forest algorithm for the

classification of neuroimaging data in Alzheimer's disease: A systematic review. *Frontiers in Aging Neuroscience*. 2017;**9**:329

[23] Dimitriadis SI, Liparas D. How random is the random forest? Random forest algorithm on the service of structural imaging biomarkers for Alzheimer's disease: From Alzheimer's disease neuroimaging initiative (ADNI) database. *Neural Regeneration Research*. 2018;**13**:962-970

[24] Ahmed OB, Benois-Pineau J, Allard M, et al. Recognition of Alzheimer's disease and mild cognitive impairment with multimodal image-derived biomarkers and multiple kernel learning. *Neurocomputing*. 2017;**220**: 98-110

[25] Vieira S, Pinaya WH, Mechelli A. Using deep learning to investigate the neuroimaging correlates of psychiatric and neurological disorders: Methods and applications. *Neuroscience & Biobehavioral Reviews*. 2017;**74**:58-75

[26] Shen D, Wu G, Suk HI. Deep learning in medical image analysis. *Annual Review of Biomedical Engineering*. 2017;**19**:221-248

[27] Janssen RJ, Mourão-miranda J, Schnack HG. Making individual prognoses in psychiatry using neuroimaging and machine learning. *Biological Psychiatry: Cognitive Neuroscience and Neuroimaging*. 2018

[28] Rohart F, Gautier B, Singh A, Lê Cao KA. mixOmics: An R package for 'omics feature selection and multiple data integration. *PLoS Computational Biology*. 2017;**13**:e1005752

[29] Meng X, Jiang R, Lin D, et al. Predicting individualized clinical measures by a generalized prediction framework and multimodal fusion of MRI data. *NeuroImage*. 2017;**145**: 218-229



- [30] Stokes ME, Visweswaran S. Application of a spatially-weighted relief algorithm for ranking genetic predictors of disease. *BioData Mining*. 2012;5:20
- [31] Correa NM, Adali T, Li YO, Calhoun VD. Canonical correlation analysis for data fusion and group inferences: Examining applications of medical imaging data. *IEEE Signal Processing Magazine*. 2010;27:39-50
- [32] Sui J, He H, Pearlson GD, et al. Three-way (N-way) fusion of brain imaging data based on mCCA+jICA and its application to discriminating schizophrenia. *NeuroImage*. 2013;66: 119-132
- [33] Calhoun VD, Sui J. Multimodal fusion of brain imaging data: A key to finding the missing link(s) in complex mental illness. *Biological Psychiatry: Cognitive Neuroscience and Neuroimaging*. 2016;1:230-244
- [34] Kawaguchi A, Yamashita F. Supervised multiblock sparse multivariable analysis with application to multimodal brain imaging genetics. *Biostatistics*. 2017;18:651-665
- [35] Kawaguchi A. Diagnostic probability modeling for longitudinal structural brain MRI data analysis. In: Truong KY, editor. *Statistical Techniques for Neuroscientists*. Boca Raton, Florida: CRC Press; 2016. pp. 361-374



# Vector-Based Approach for the Detection of Initial Dips Using Functional Near-Infrared Spectroscopy

*Toshinori Kato*

## Abstract

Functional near-infrared spectroscopy (fNIRS) is a non-invasive method for the detection of local brain activity using changes in the local levels of oxyhemoglobin (oxyHb) and deoxyhemoglobin (deoxyHb). Simultaneous measurement of the levels of oxyHb and deoxyHb is an advantage of fNIRS over other modalities. This review provides a historical description of the physiological problems involved in the accurate identification of local brain activity using fNIRS. The need for improved spatial and temporal identification of local brain activity is described in terms of the physiological challenges of task selection and placement of probes. In addition, this review discusses challenges with data analysis based on a single index, advantages of the simultaneous analysis of multiple indicators, and recently established composite indicators. The vector-based approach provides quantitative imaging of the phase and intensity contrast for oxygen exchange responses in a time series and may detect initial dips related to neuronal activity in the skull. The vector plane model consists of orthogonal vectors of oxyHb and deoxyHb. Initial dips are hemodynamic reactions of oxyHb and deoxyHb induced by increased oxygen consumption in the early tasks of approximately 2–3 seconds. The new analytical concept of fNIRS, able to effectively detect initial dips, may extend further the clinical and social applications of fNIRS.

**Keywords:** functional near-infrared spectroscopy, fNIRS, initial dip, phase, vector-based analysis, cerebral oxygen exchange, COE, oxyhemoglobin, deoxyhemoglobin

## 1. Introduction

Functional near-infrared spectroscopy (fNIRS) is a non-invasive method for the detection of brain activity using changes in the local levels of oxyhemoglobin (oxyHb), deoxyhemoglobin (deoxyHb), and total hemoglobin (total Hb) [1]. fNIRS imposes fewer physical restrictions on patients compared with positron emission tomography (PET) or functional magnetic resonance imaging (fMRI), allowing investigators to measure and analyze cerebral circulation and metabolism while the patient walks or moves his/her upper body. Recently, studies showed that brain activity during rehabilitation [2] and car driving [3–6] may also be measured using fNIRS. In 1991, the first study of fNIRS utilizing localized changes in the levels

of oxyHb and deoxyHb was conducted by Kato and his colleagues at the National Center of Neurology and Psychiatry, Tokyo, Japan [1].

This study was the first to demonstrate that the activation of Hb in the human brain during photic stimuli was associated with increased levels of oxyHb, deoxyHb, and total Hb in the visual cortex. Of note, the measurements in the prefrontal cortex did not show clinically meaningful changes in the levels of these three indices. The original fNIRS technique was able to detect local activation of the brain during a task that is stronger than the signals during rest, by placing pairs of probes 2.5 cm apart on the scalp over the targeted cortex [7–9].

Thus, fNIRS solved the problem of oxygenation monitoring in NIRS [10, 11]. The measurement of targeted temporal changes in task-related activation markedly reduced data noise from the blood flow in the scalp at rest and from artifact-related bodily movement. Nowadays, more than 25 years later, statistical processing and mapping of changes in the levels of hemoglobin measured by fNIRS are used for the evaluation of brain activity.

The advantage of fNIRS over fMRI and other modalities is the ability to simultaneously and independently measure the levels of oxyHb and deoxyHb. Combined, these data may be used as indices reflecting changes in both blood volume and oxygenation.

However, the temporal resolution of fNIRS is fairly low on a 40–100 ms scale, compared with the underlying neural activity which is spanning from 1 to 3 ms of action potential firing and can be recorded extracranially using magnetoencephalography (MEG). MEG can be sensitive on subcortical activity in a case of large extent of activated neuronal assembly and spatial extent of activated cortical assembly [12, 13].

In slow voluntary movements of the self-paced index finger, the activity of the sensorimotor area was detected before 4.5 seconds of the pre-movement using electroencephalography (EEG) [14]. Consistent with the findings of EEG, early deoxygenation of 3–4 seconds prior to the movement of the finger was observed in the sensorimotor area using fNIRS [15]. Presently, research on simultaneous measurements using fNIRS and EEG is becoming an effective means of brain-computer interface [16].

In addition, a disadvantage of fNIRS is the low spatial resolution (5–10 mm) of the activation mapping of the cortical surface compared with those obtained from fMRI and PET. Research combining the use of fNIRS, fMRI, and MEG for source localization is currently ongoing [17]. These combination studies have advantages in temporal and spatial mapping of brain function.

A response involving increased and decreased levels of oxyHb and deoxyHb, respectively, has been considered the model of canonical activation in numerous studies utilizing fNIRS. However, the actual frequency of the occurrence of canonical activation, the most suitable index or indices for the differentiation between the center of activation and the surrounding area, and the associated degree of probability remain to be investigated. Following canonical activation, the rates of change in the levels of oxyHb and deoxyHb are not constant and may differ according to the task. Wylie et al. [18] performed a qualitative differentiation between two types of canonical activation according to the increase/decrease in the levels of total Hb. The investigators of that study identified four additional patterns of increase and decrease in the levels of oxyHb, deoxyHb, and total Hb that do not correspond to canonical activation.

Presently, the detection of the spatiotemporal characteristics of brain activity using fNIRS remains suboptimal. This fundamental limitation in evaluating brain activity may lead to misdiagnosis. fNIRS research is particularly challenging in the prefrontal cortex, responsible for complex higher functions. In areas of the brain

with clear localization of cerebral function (i.e., primary motor or visual cortices), it is possible to verify the accuracy of fNIRS data. However, in the human prefrontal cortex, there is currently no clear understanding of the localization of the more complex functions, and thus, the verification of the reliability of fNIRS data in this area remains a challenge.

Studies have attempted to bolster the reliability of fNIRS in the prefrontal cortex by comparing data obtained from fNIRS and fMRI [19, 20]. However, because the mechanisms differ between the two modalities [21–24], even if conformity is found between fMRI and fNIRS data, the reliability of the results is not necessarily increased. Several problems have been pointed out. Considerable attention is required when analyzing with the index of oxyHb alone. In the prefrontal region, task-dependent data noise in the oxyHb response (increased levels) resulting from skin blood flow has been reported [25, 26]. In 2011, an article criticized the use of NIRS in the clinical diagnosis of psychiatric disorders as being insufficiently supported by scientific evidence [27]. In mental illness studies, the actual localization of increases in the levels of oxyHb is not clear [28], and therefore, measurements of oxyHb levels cannot be linked to a specific brain activity.

Furthermore, analytical challenges in the field of fNIRS have been reported. This review introduces new composite functional indices incorporating ratios of changes in the levels of oxyHb and deoxyHb, along with a novel vector-based fNIRS method [29, 30]. This vector-based approach can be used to visually and quantitatively evaluate combinations of changes in the levels of oxyHb and deoxyHb as new indices. It was useful to classify variations in the levels of hemoglobin in response to neural activity, using combinations of changes in the levels of hemoglobin. It was effective especially when the signal change is small such as initial dips. Initial dips are the hemodynamic reactions of oxyHb and deoxyHb induced by increased oxygen consumption in the early tasks of approximately 2–3 seconds [31, 32]. The vector-based approach could improve the sensitivity of fNIRS in the detection of brain activity both temporally and spatially through recognition of the initial dips from the skull to hemodynamic responses [33–36].

In addition, this review discusses challenges with data analysis based on a single index, advantages of the simultaneous analysis of multiple indicators, and recently established composite indicators.

## **2. NIRS until 1990**

Prior to the development of fNIRS, NIRS was used mainly for monitoring cerebral oxygenation. Changes in tissue oxygen saturation are accompanied by simultaneous changes in cerebral blood volume. Using NIRS, Jöbsis [37] reported hypocapnia and a reduction in cerebral blood volume during human hyperventilation. In addition, NIRS was used to prevent hypoxia through monitoring newborn and premature infants [10, 11]. Of note, NIRS had also been used to investigate the brains of animals [38–40].

In 1990, Takashima et al. [41] used NIRS to examine patients with probes placed 5 cm apart from each other. This study was based on the original concept of the research conducted by Jöbsis [29]. The results of this study showed reductions in the levels of oxyHb, deoxyHb, and total Hb in the prefrontal area during hyperventilation. Until 1990, research on NIRS did not target the specific localized brain function of the cerebral cortex. The technique was merely used to observe changes in the levels of hemoglobin (task-related and at rest), without specific spatial identification.

Hypocapnia is known to cause global changes in the scalp and the entire brain. Hence, the changes reported during hyperventilation did not constitute proof of

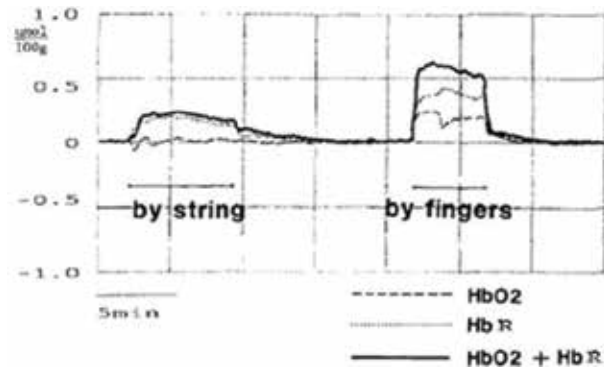


**Figure 1.**

*Changes in the levels of HbO<sub>2</sub> (oxyhemoglobin, oxyHb), HbR (deoxyhemoglobin, deoxyHb), and HbO<sub>2</sub> + HbR (total hemoglobin, total Hb) with neck compression [40]. Comparisons between tasks had been reported at that time, unlike responses derived from specific cortical activity.*

functional local brain activity. These early studies of hyperventilation suggested that blood volume was reduced in the region supplied by the external carotid artery, which distributes blood mainly to the scalp and muscles outside the skull. In brain death, in spite of the absence of blood flow through the internal carotid artery, the blood flow distribution through the external carotid artery remains unimpaired—an observation known as “the finding of the hollow skull” [42]. Early data obtained using NIRS data were affected by this blood flow from areas of the scalp supplied by the external carotid artery and the veins.

In addition, probes placed in the prefrontal area of seven healthy patients in a task of pressure for 1 minute on the jugular vein reported increases in the levels of oxyHb, deoxyHb, and total Hb [41]. These results were consistent with those obtained from an animal study (**Figure 1** [40]), indicating task-related hemodynamic changes prior to 1990. Importantly, the presence of a task does not differentiate fNIRS from NIRS.

Until 1990, NIRS had not been considered a tool for the identification of specific cortical activity. In the usage of NIRS at the time, there was no technique that data could be obtained selectively from a site on the cortex located directly under a site sandwiched between irradiation and detection probes, let alone evidence of brain activity. The near-infrared light paths and the range and depth of irradiation were unknown. Moreover, the influence of factors such as the external carotid artery was undeniable. Early NIRS did not associate changes in the levels of Hb with localized brain activity and was unable to clearly distinguish between signals derived from the external carotid artery or the veins and those derived from the cortex.

### 3. Conception and first experiment of fNIRS in 1991

fNIRS was developed in 1991 [1, 7–9, 31] as a functional imaging method using NIRS to detect local brain activity accurately. This was achieved by identifying changes in the levels of Hb in different areas of the brain at rest and during a task. It was necessary to initially demonstrate that NIRS was able to detect localized brain activity to establish fNIRS. The selection of an experimental task and the settings of the probe were the key factors in this process. In the search for a task, lesion studies and PET studies were reviewed to identify a small part of the brain that could be clearly stimulated and measured from the frontal lobe. A multifocal increase in regional cerebral blood flow (CBF) had been reported in a mental arithmetic task in the frontal lobe [43]. Furthermore, mental arithmetic tasks to induce an autonomic

nerve stimulus had been used to show the possibility of blood volume changes in the region supplied by the external carotid artery [44, 45]. Dyscalculia was not sufficiently localized, because it occurs in multiple sites of the frontal and temporal lobes from injury, etc. [46].

The cerebral metabolic rate of oxygen (CMRO<sub>2</sub>) was shown to increase by approximately 10% in a study using thinking tasks [47]. However, when compared with that observed at rest, this change in regional cerebral blood volume (CBV) was not significant. Exercise tasks produced side effects from movement of the probes and systemic circulation. In addition, a PET study had shown that blood flow increased in both the primary motor area of the frontal lobe and the nearby supplementary motor areas [48]. Overall, the confirmation of localization in the frontal lobe was challenging. The primary auditory cortex is located inside the Sylvian fissure, and there was no certainty that near-infrared light would be able to reach the site and reflect back to produce meaningful data.

In summary, an experiment designed to confirm that localization was possible using fNIRS required a task meeting the following conditions:

1. It should not stimulate the autonomous nervous system.
2. It should not induce global activation of the brain.
3. It should avoid the region supplied by the external carotid artery (possibility of changes in the volume of blood).
4. It should not involve pressure on the carotid artery.
5. It should not require bodily motion.
6. It should not target brain activity from the frontal or temporal lobes (possibility of movement of the scalp or muscles).
7. It should induce brain activity within a well-defined site.

According to these conditions, a suitable task would be one that stimulates the primary visual cortex, located in the occipital lobe and supplied with blood mostly from the posterior cerebral artery. An earlier study had reported an increase in CBF in the visual cortex with a task of 7.8 Hz photic stimulation [49]. A major question at that point was the following: "What kind of response in terms of local Hb levels would be obtained in a photic stimulation experiment using NIRS?" Other, more practical problems included the use of external light with the NIRS equipment and the irradiation of the stimulus light to the patient wearing the probes. However, these problems were resolved during the experiment. As shown by PC darkness in **Figure 2**, the influence of extraneous light could be eliminated in actual experiments.

In 1991, the time course of responses arising from changes in the local levels of oxyHb, deoxyHb, and total Hb remained unknown. Therefore, it was necessary to perform measurements on different sites that would demonstrate brain activity and a null response. It was thought that the detection of varied responses from different sites in response to a given stimulus could demonstrate the localization of function.

In the actual experiment, photic stimulation (8 Hz) was delivered using a photosonic stimulator (Nihon Kohden Co., Japan) from the front and at the height of the patient's line of sight for 5 minutes. As **Figure 2** shows, the activation observed in the visual cortex during the photic stimulus was associated with increased levels of oxyHb, deoxyHb (slightly), and total Hb. No changes were observed in the

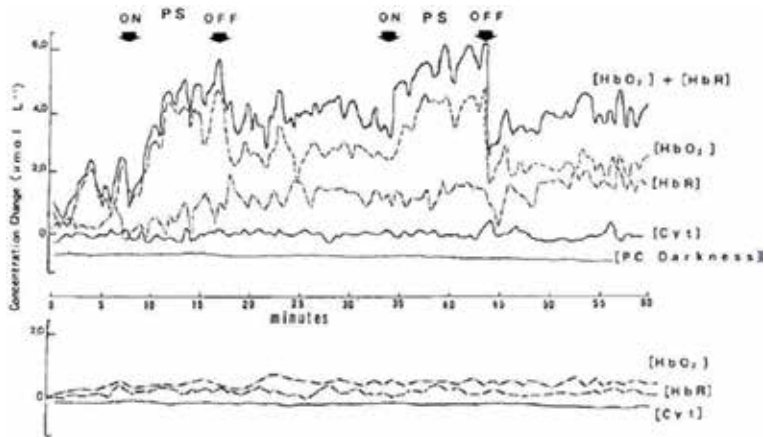


**Figure 2.**

Changes in the levels of oxyhemoglobin (oxyHb), deoxyhemoglobin (deoxyHb), total hemoglobin (total Hb), Cyt (Cytochrome $a_2$ ), and PC darkness (photon counting darkness) measured over the occipital surface (above) and the frontal surface (below) prior to, during, and after photic stimulation in a healthy adult. Background noise from extraneous light was monitored as PC darkness. The data show spatial (site-dependent) and temporal (task on/off) differences in response [7, 8].

prefrontal cortex following photic stimulation. These findings demonstrated that fNIRS is able to detect spatial and temporal information (i.e., different hemodynamic responses), depending on the site and the presence or absence of stimulation.

Today, fNIRS is widely used for tasks or in environments difficult for other modalities. Although the above list of requirements for task selection may seem outdated, the first four conditions are still required to distinguish between local activity and global change. The difference between local activity and global changes is still determined by the presence or absence of a response, limitation to a specific site, and dependence on the duration of the task.

#### 4. Probe placement on the skull

A fundamental part for fNIRS is probe placement. As **Figure 3A** shows, Jöbsis [37] used infrared transillumination and optical computed tomography (CT) to create images of blood flow distribution at rest corresponding to brain structures. He estimated the optical path length of the human head to be 13.3 cm [37]. In addition, he stated that an interprobe distance of  $\geq 4.25$  cm would allow the detection of data from the brain tissue rather than the scalp (**Figure 3B** [50]). Although the diffused and reflected light used today had already replaced infrared transillumination, subsequent research on cerebral oxygenation monitoring [41] continued to use this setting (distance between probes  $\geq 4.25$  cm).

During the design of the first investigation using fNIRS, MRI showed that the distance between the scalp and the primary visual cortex was  $< 1$  cm in neonates and  $< 2$  cm in adults and demonstrated the gentle curvature of the skull [51]. The shape of the skull permitted further reduction in the distance between the probes (**Figure 3C**) and improved the detection of activity in the cerebral cortex.

In the study, placement of the probes 5 cm apart revealed only a slight increase in the levels of oxyHb. When the distance between the probes was shortened to 4 cm, the increase in the levels of oxyHb became more pronounced. At an interprobe distance of 2.5 cm, a transient dip in the levels of oxyHb was observed. This effect occurred simultaneously with the initiation of the stimulus, followed promptly by an



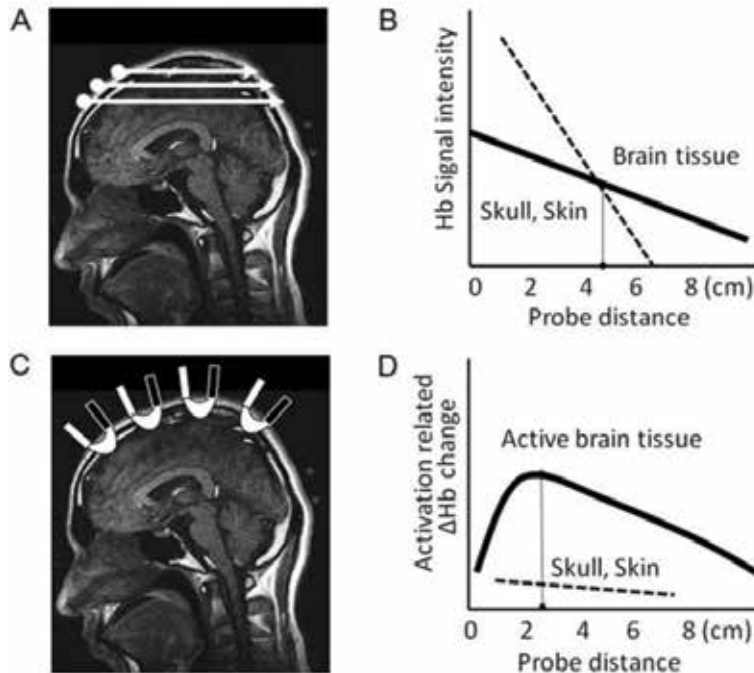


**Figure 3.** (A) Conceptual schema of optical computed tomography performed by Jöbsis illustrated on a magnetic resonance imaging (MRI) image (revision from [37]). (B) Relationship between the signal intensity of hemoglobin and the distance between the light entry and exit locations, using the reflectance technique according to the origin of the reflected light (revision from [50]). (C) Conceptual schema of functional near-infrared spectroscopy illustrated on the same MRI image. (D) Relationship between the activation-related change in the levels of hemoglobin and the distance between the light source and detector [31].

increase in the levels of oxyHb, faster peak latency, and a post-stimulus undershoot in oxyHb. At an interprobe distance of 1.0–1.5 cm, there was either no response at all or the total amounts of Hb remained unchanged while small mirror-image changes were observed, namely an increase and decrease in the levels of oxyHb and deoxyHb, respectively. These mirror-image changes may have been derived from either the scalp (where metabolism does not increase) or from vascular changes in the veins on the surface of the brain. From these findings, it was established that an interprobe distance of 2.5 cm provided the most robust results (**Figure 3D**).

Based on this empirical hypothesis, the area on the scalp corresponding to the visual cortex that can be covered with two probes was considered to be  $1.0 \times 2.5$  cm, as identified through sagittal MRI. Each pair of emitter and receptor probes was placed 2.5 cm apart vertically to prevent data noise from activity in the secondary visual cortex and the large vein running vertically through the sagittal sinus.

The movement of the probes outward by 1.0 cm impaired the detection of response in the pilot study. Thus, pairs of probes (channels) were placed within 1.0 cm of the target in the horizontal direction to ensure accuracy. This adjustment permitted the investigators to develop the concept of functional resolution (in this case  $1.0 \times 2.5$  cm) for the identification of the precise area of response. The original NIRS apparatus used (NIRO 1000, Hamamatsu Photonics K.K., Japan), shown in **Figure 4**, had only two channels and 5-mm diameter optical fibers for the emission and reception of light with  $8 \times 8$  mm contact surfaces.

The concept that the spatial resolution of fNIRS should be determined by the anatomy of the cerebral cortex and the range in which a response occurs was developed from this early research. To establish the desired resolution, the distance

between the probes and the distance between the channels should be controlled independently. The more recently available multichannel fNIRS devices have become essential for the localization of brain activity. Unless the interchannel distance is changed depending on whether the measurement target is deep or wide from the scalp, the likelihood of detecting a localized response is reduced. In newborns, the distance between the brain and the surface of the cortex is <1 cm [51, 52]. Thus, in infants, the distance between probes should be shortened to 1–2 cm [53], rather than being set at 2.5 cm apart [7–9, 54]. The 3-cm apart matrix array of probes commonly used in recent years [55, 56] cannot necessarily provide results corresponding to the actual distribution of brain function in usage not considering age and head size. Spatial identification may not be performed effectively when a probe “hat” with probes arranged without reference to the anatomy of the brain/scalp is used. Registration markers and MRI should be used to determine the localization of probe placement for each individual.

In late 1992, Hoshi and Tamura [57] reported findings from research using task-related NIRS. The investigators reported a calculation task which stimulated the autonomic nervous system with an interprobe distance of 4 cm. This protocol did not meet the requirements for either task selection or probe settings described earlier in this review, and thus, the method is not considered fNIRS. Villringer et al. [58] selected probe positions on the scalp with interprobe distances ranging from 4 to 7 cm. In 1993, Chance et al. [59] also performed the task-related NIRS experiments from the frontal skull. However, they were unable to demonstrate localization. Advances in techniques for the improvement of spatial resolution continued. The spatial resolution of the 3 cm<sup>2</sup> probe arrangement failed to provide detailed information regarding responses in the cortex [60]. Highly selective probe arrangements for establishing high-density measurement points have been reported (e.g., one with 10-mm channel interval and 25-mm probe interval [31, 32], and one with a center probe and surrounding probes [61]). Structural MRI has been used to evaluate the distance between the brain and the scalp [62]. Moreover, a method using diffuse optical tomography for removing signals on the scalp has been reported [63–65].

Of note, fNIRS has also been used in animal studies. The results have shown that measurement of fNIRS indices from the scalp with an interprobe distance of 4 and 8 mm was possible in the brain of rats [66] and cats, respectively. As **Figure 5** shows, using fNIRS (ETG-100, Hitachi Medical Co., Tokyo, Japan), an initial dip was able to



**Figure 4.** The NIRO 1000 (Hamamatsu Photonics K.K., Japan) used in the first functional near-infrared spectroscopy experiment [7–9].

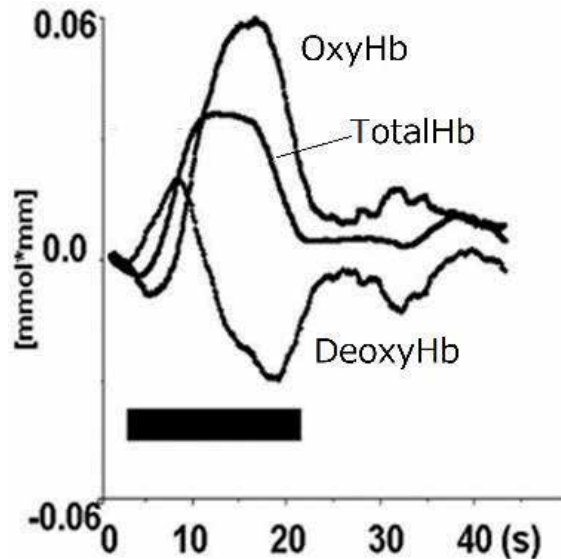


**Figure 5.**  
*Time series data of hemodynamic response showing an initial dip in the levels of total hemoglobin decreased through stimulation using light in the cat brain. A thick black line indicates stimulation using light.*

measure hemoglobin indices in the visual cortex during photic stimulation from outside the skull of a cat. In particular, the fNIRS response pattern to photic stimulation was identical between the cat and the human brains [67, 68]. These animal studies suggested that it was possible to use fNIRS for the detection of activity in a 1–2 mm region of the targeting cortex from the scalp.

## 5. Brain function indices and oxygen responses in capillaries

Numerous current fNIRS devices measure the levels of oxyHb, deoxyHb, and total Hb independently. A new challenge is that spatiotemporal characteristics may vary in functional brain imaging depending on the index used, and this problem has not been widely recognized or studied. In 1991, Kato et al. reported increases in the levels of oxyHb, deoxyHb (slight), and total Hb in the primary visual cortex during photic stimulation. Subsequent studies using fMRI and fNIRS reported increases and decreases in the levels of oxyHb and deoxyHb, respectively, in motor and visual tasks [69–71]. These results were accepted as typical fNIRS responses and have been corroborated by numerous fNIRS studies [1].

Nowadays, atypical responses are mostly ignored and left unexplained. There is a widespread tendency, hypothesized patterns of hemoglobin reaction in advance and those that are not hypothesized reaction types tend to be statistically excluded from the analysis data without being insufficiently examined [72]. In response to this trend, recent studies also have processed statistically and mapped independently the observed increase and decrease in the levels of oxyHb [73, 74] and deoxyHb [75, 76], respectively. Even in studies using rats, their analysis may be performed using only oxyHb [77].

However, evaluation of brain activity using a single hemoglobin index is contrary to the physiological mechanisms involved, ignoring the fact that hemodynamic responses include both blood volume and oxygenation. The distinction between blood volume and oxygenation, applying to fNIRS and fMRI [23, 24], has

been a subject of controversy. This remains an unresolved problem common to all brain functional imaging research based on hemodynamic responses. The beginning of this argument can be traced back to Roy and Sherrington, who in 1890 proposed neurovascular coupling. Changes in oxygenation and blood volume in the capillaries reflect neuronal activity. However, as Roy and Sherrington noted, these data were not derived from the capillaries [78].

The first to report the quantification of CBF using Fick's law (i.e., subtracting the value of the veins from that of arteries, in units of per 100 g per minute) were Kety et al. [79]. Increases in CBF, calculated without taking the capillaries into account, show a positive correlation with increasing  $CMRO_2$  [80]. Based on slight increases in  $CMRO_2$  observed following an increase in CBF [81], a coupling model of a positive correlation between CBF and  $CMRO_2$  [82, 83] was used widely to evaluate vascular response. Changes in CBF were used as a substitute for changes in oxygen metabolism. It is likely that this trend also affected fNIRS and led to the independent analysis of the levels of oxyHb, as performed today. Recent waveforms of increases in the levels of oxyHb closely resemble the waveforms of increases in blood flow reported by Roy and Sherrington in 1890. After more than 120 years, the interpretation of neurovascular coupling has not advanced considerably. Roy and Sherrington had foresight in their interpretation related to blood flow, but they did not observe cerebral oxygen metabolism.

Although the capillary transit time in humans is reported to be <10 seconds [84], PET sampling times are markedly longer. For this reason, PET data include changes in CBF in the capillaries related to oxygen exchange, coupled with the additional component of the delayed increase in CBF in the veins not accompanied by oxygen exchange. Using PET, a dissociation between  $CMRO_2$  and CBF has been reported [85, 86]. Using fMRI, signals have been shown to remain unaltered during

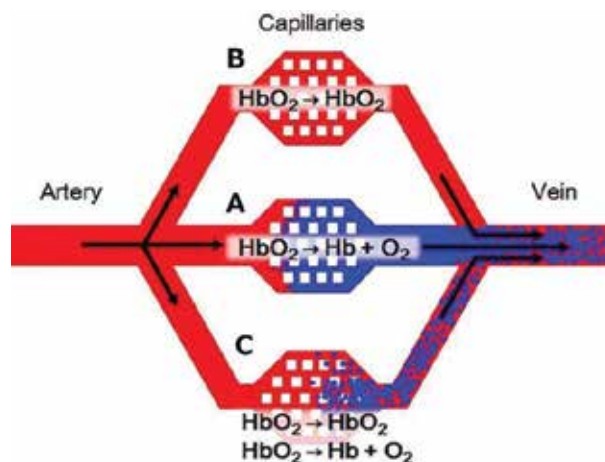


**Figure 6.**

*Schematic diagram of the possible hemodynamic responses occurring simultaneously with neural activity (revision from [31]). In (A), oxygen demand is increased by neural activity, and consequently, transient deoxygenation increases in the capillaries (oxyhemoglobin [ $HbO_2$ ] → hemoglobin [ $Hb$ ] + oxygen [ $O_2$ ]). In a site with little neural activity (B), minimal amounts of oxygen enter the cells and even during a task, increased levels of oxyHb from the artery pass through the capillaries, bypassing the cells ( $HbO_2 \rightarrow HbO_2$ ). This response—increased and decreased levels of oxyHb and deoxyHb, respectively—has been recognized as typical activation. In actuality, according to the variation in the amount of oxygen exchange due to neural activity (C), a mixed response combining these two responses must also be present. These responses, differing according to the strength of oxygen exchange, are likely to be distributed among different sites, depending on the strength of neural activity at each site. Because the blood flows from (A), (B), and (C) are further mixed in the large veins, the data may not provide specific spatial information if responses are measured at longer sampling times than the capillary transit time.*

the capillary transit time [87]. In other words, there is a need to move beyond the simplistic interpretation of neurovascular coupling, which predicts an increase in the levels of oxyHb and blood flow in response to neural activity. **Figure 6** shows the relationship between neural activity and hemodynamic response schematically.

fNIRS is able to measure the levels of oxyHb and deoxyHb at the same time. Therefore, it is a useful tool to solve this serious problem of simultaneously measuring cerebral blood flow and cerebral oxygen metabolism which are faced by brain researchers for over 120 years. Future fNIRS research should distinguish between changes in blood volume and oxygenation occurring simultaneously with brain activity in the analysis of hemodynamic responses. In addition, it is necessary to re-evaluate activity-based hemodynamic responses using modalities such as EEG and MEG.

Research involving event-related optical signals [87] and invasive optical measurements [88, 89] has been unable to distinguish between oxygenation and blood volume. OxyHb and deoxyHb are involved in both oxygenation and blood volume. Thus, it may not be possible to evaluate brain activity based exclusively on the measurement of the levels of oxyHb.

## 6. Detection of initial dipoles

Currently, an experimental protocol termed block task design, employing tasks that continue for  $\geq 10$  seconds (longer than the capillary transit time), is being used in many fNIRS studies. The reason for this is that the peak latency of oxyHb is generally 10 seconds (occasionally longer) from the initiation of a task. The use of this method in fNIRS studies has followed from its use in fMRI and PET research, where the low temporal resolution of the modality justifies the use of a block design. When a task requires a longer period of time corresponding to a block design or the task requires a certain amount of time to elapse for observation, the selection of a block design protocol in research using fNIRS, providing higher temporal resolution, is appropriate. With fNIRS, there is no need to repeat cognitive tasks involving factors such as perception, recognition, or judgment for prolonged time to obtain a sufficiently strong peak response in oxyHb levels. A block design including many task components does not clarify the correspondence between each task component and spatiotemporal local brain activity. Studies have also analyzed post-task time periods [90, 91]. However, the data from these studies lacked simultaneity with local brain activity and were unable to temporally and spatially identify local brain activity. Although EEG shows high simultaneity between data and brain activity, it is characterized by poor spatial resolution. In this respect, if the spatial resolution of fNIRS can be set from the standpoint of functional resolution as described earlier, its high temporal resolution may be valuable for event-related measurements.

The initial dip, which is early deoxygenation in event-related experiments, is a highly accurate spatial indicator of neural activity [92]. In studies using optical intrinsic signals (OIS), increase in the levels of deoxyHb occurring prior to slow increases in the levels of oxyHb or total Hb has also been considered to be an index of increased oxygen metabolism [88, 93–97]. The absence of a correspondence (spatial or temporal) between increases in early deoxygenation and blood volume was also shown in a human study using invasive optical imaging [98]. Kato et al. [67, 68, 99, 100] conducted the first fNIRS study measuring initial dipoles appearing in fNIRS signals from the motor, visual, and language areas. Subsequently, the initial dip was observed in several fNIRS studies [18, 32–36, 101].

It has been suggested that this early increase in the levels of deoxyHb may arise from a transient increase in the consumption of oxygen in tissues [102, 103]. It has been obvious that this deoxyHb increase is useful as a precise indicator of brain

activity, but against the background that this increase in deoxyHb has been difficult to detect. For example, there is the case of less likely early deoxyHb increase depend on factors such as the type of task or the use of anesthesia [92]. A minimal and very localized increase may be attributed to imprecise fNIRS probe settings (i.e., missing the center of activity) or masking due to a strong increase in blood flow in the veins compromising detection.

With fMRI, what was reported previously as an early increase in the levels of deoxyHb was observed as an “initial dip” [21, 104, 105]. However, fMRI does not differentiate between oxyHb and deoxyHb. In addition, the relationship between increases or decreases in the levels of oxyHb and the increase in the levels of deoxyHb has not been investigated.

The more recently developed vector-based NIRS method [29, 30] is able to measure initial dips characterized by the canonical dip pattern showing increased deoxyhemoglobin, as well as several different hemoglobin patterns corresponding to differences in the degree of oxygen metabolism [32]. This method has permitted the reproducible measurement of hypoxic–ischemic initial dips (i.e., decreased levels of oxyHb) [34–36]. The initial dip at which the level of deoxyHb increases and the reaction where oxyHb increases after 2–3 seconds do not necessarily occur at the same site. Moreover, research on the intersection of these responses is limited, leading investigators to select one of the two responses (i.e., the typical oxyHb response or the initial dip) for the evaluation of brain activity. This serious problem may arise from the lack of quantification of brain activity. Indeed, the results of the evaluation of laterality in the language area [106, 107] may differ depending on the index used [108]. In addition, investigation of the relationship between event-related oxyHb and deoxyHb responses, especially those within seconds from neural activity, in previous fNIRS studies has been limited.

## 7. Composite indices derived from vector analysis

An advantage of fNIRS over other modalities is the simultaneous measurement of the levels of oxyHb and deoxyHb. However, this advantage leads to the following question: What do the various possible combinations of oxyHb, deoxyHb, and total Hb mean? Early fNIRS lacked a quantitative integrated theory for the interpretation of combinations of hemoglobin indices from multiple channels. Kato [29, 30] developed a quantitative method of analysis of the ratios between changes in the levels of oxyHb ( $\Delta O$ ) and deoxyHb ( $\Delta D$ ) to differentiate between oxygenation and blood volume.

This technique uses a two-dimensional vector plane on which vector tracks generated by task-related changes in cerebral blood volume ( $\Delta CBV$ ) and change in cerebral oxygen exchange ( $\Delta COE$ ) are quantitatively classified into eight “phases.” This provides a visible graphical display of information concerning hemodynamic responses (**Figure 7**). This vector-based approach is able to calculate the angle  $k$ , determining the phase of the response, and the intensity of response  $L$ . Subsequently, these may be used as indices of vector-based brain activity.

**Figure 7** shows an orthogonal vector coordinate plane defined by the  $\Delta O$  and  $\Delta D$  axes. Rotating this vector plane 45° counterclockwise results in an orthogonal vector coordinate plane defined by the  $\Delta CBV$  and  $\Delta COE$  axes. For  $\Delta COE$ , a positive value indicates hypoxic change from  $\Delta COE = 0$ , whereas a negative value indicates hyperoxic change. The relationships among these four axes are described by the following square matrix:

$$\begin{pmatrix} \Delta O + \Delta D \\ -\Delta O + \Delta D \end{pmatrix} = \begin{pmatrix} 1 & 1 \\ -1 & 1 \end{pmatrix} \begin{pmatrix} \Delta O \\ \Delta D \end{pmatrix} = \begin{pmatrix} \Delta CBV \\ \Delta COE \end{pmatrix} \quad (1)$$

$$\begin{pmatrix} \Delta O \\ \Delta D \end{pmatrix} = \frac{1}{2} \begin{pmatrix} 1 & -1 \\ 1 & 1 \end{pmatrix} \begin{pmatrix} \Delta CBV \\ \Delta COE \end{pmatrix} \quad (2)$$

Expansion of these shows  $\Delta CBV$  and  $\Delta COE$  representing blood volume and oxygenation, respectively:

$$\Delta CBV = \frac{1}{\sqrt{2}} (\Delta D + \Delta O) \quad (3)$$

$$\Delta COE = \frac{1}{\sqrt{2}} (\Delta D - \Delta O) \quad (4)$$

The scalar  $L$ , drawn from the origin to the coordinates of an arbitrary point on the vector plane, indicates the amplitude of a vector, reflecting the amount of change in Hb.  $L$  can be described by the following equation:

$$\begin{aligned} L &= \sqrt{(\Delta O)^2 + (\Delta D)^2} = \frac{1}{\sqrt{2}} \sqrt{(\Delta D - \Delta O)^2 + (\Delta D + \Delta O)^2} \\ &= \frac{1}{\sqrt{2}} \sqrt{(\Delta COE)^2 + (\Delta CBV)^2} \end{aligned} \quad (5)$$

The angle  $k$ , indicating the phase, is defined by the following equation:

$$k = \text{Arc tan} \left( \frac{\Delta D}{\Delta O} \right) = \text{Arc tan} \left( \frac{\Delta COE}{\Delta CBV} \right) + 45^\circ \quad (-135^\circ \leq k \leq 225^\circ) \quad (6)$$

A vector on the polar coordinate plane contains the four Hb indices (i.e.,  $\Delta O$ ,  $\Delta D$ ,  $\Delta CBV$ , and  $\Delta COE$ ). The relationships between the four Hb vectors (**Figure 7**) are defined by the equations shown earlier in this section: Eqs. (1) and (2) define hemoglobin changes; Eq. (5) defines the scalar  $L$ ; and Eq. (6) defines the angle  $k$ , which determines the phase of a vector. Earlier evaluations of brain activity were

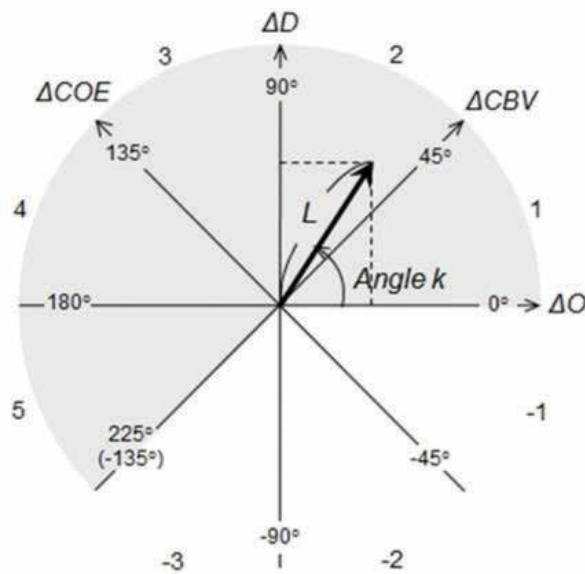


**Figure 7.** Functional near-infrared spectroscopy vector plane. Revised from [29, 30].



based on signal intensity, without the concept of a phase. However, this method describes all the possible combinations of responses through eight phases on the vector plane. In addition, particular patterns of physiological responses are presented in a highly visual manner. This method provides a quantitative measure of oxygen metabolism, offering the advantage of measurements expressed in units of degrees. Moreover, measurements are determined from ratios of change rather than the actual extent of change in the levels of Hb.

## 8. Interpretation of initial dips using the vector-based approach

The angle  $k$  shows a positive value in the phases of initial dip occurrence. Previously, the initial dip was regarded as an indication of increased oxygen consumption. However, it was not possible to evaluate the strength of the initial dip or the possibility of different kinds of initial dips. Yoshino and Kato [32] classified initial dips in the language area by phase according to their particular combinations of  $\Delta O$ ,  $\Delta D$ ,  $\Delta CBV$ , and  $\Delta COE$ .

- Phases 1 through 5 on the vector plane were dip phases, showing increases in  $\Delta D$  or  $\Delta COE$ ; the presence of an event-related vector in these phases defined an initial dip.
- Phase 1 ( $0 < \Delta D < \Delta O$ ,  $\Delta COE < 0 < \Delta CBV$ ) and Phase 2 ( $0 < \Delta O < \Delta D$ ,  $0 < \Delta COE < \Delta CBV$ ) are canonical dips [79], in which both  $\Delta D$  and  $\Delta O$  increase.
- Phase 3 ( $\Delta O < 0 < \Delta D$ ,  $0 < \Delta CBV < \Delta COE$ ) is a hypoxic-hyperemic dip, in which  $\Delta O$  decreases and  $\Delta CBV$  increases.
- Phase 4 ( $\Delta O < 0 < \Delta D$ ,  $\Delta CBV < 0 < \Delta COE$ ) and Phase 5 ( $\Delta O < \Delta D < 0$ ,  $\Delta CBV < 0 < \Delta COE$ ) are hypoxic-ischemic dips, in which  $\Delta COE$  increases and  $\Delta CBV$  decreases.
- Phases  $-1$  through  $-3$  are non-dip phases, in which  $\Delta D$  and  $\Delta COE$  decrease.

Regarding oxygen metabolism, responses in the dip phases may indicate stronger brain activity than those in the non-dip phases. It is necessary to verify the strongest dip phases during the evaluation of the regulation between the oxygenation axis ( $\Delta COE$ ) and the blood volume axis ( $\Delta CBV$ ) in the vector plane. The typical response corresponds to Phases  $-1$  and  $-2$ , interpreted as brain activity with a low degree of oxygen exchange. The responses in other phases should be evaluated in the same manner and the frequency of their occurrence should be investigated based on phase classifications. The percentage of dips in Wernicke's area in Phases 1 and 2 was low (total: 15–21%). However, in Phases 4 and 5, this percentage was higher (total: 62–68%) [32]. Differences in the frequency of phase depending on the brain site and the task may have different physiological implications. The ratio between the decrease and increase in the levels of deoxyHb and oxyHb, respectively, in a typical response is not constant. The quantitative values of the phase angle  $k$  may be used to investigate such differences in typical responses.

In **Figure 8**, time course data for previously reported initial dips are reproduced on a vector plane using the vector-based technique. **Figure 8A** and **8B** show two different types of dip in different phases, depending on the observed change in the  $\Delta CBV$ . In both fMRI and OIS, the canonical initial dip has been considered to be a response



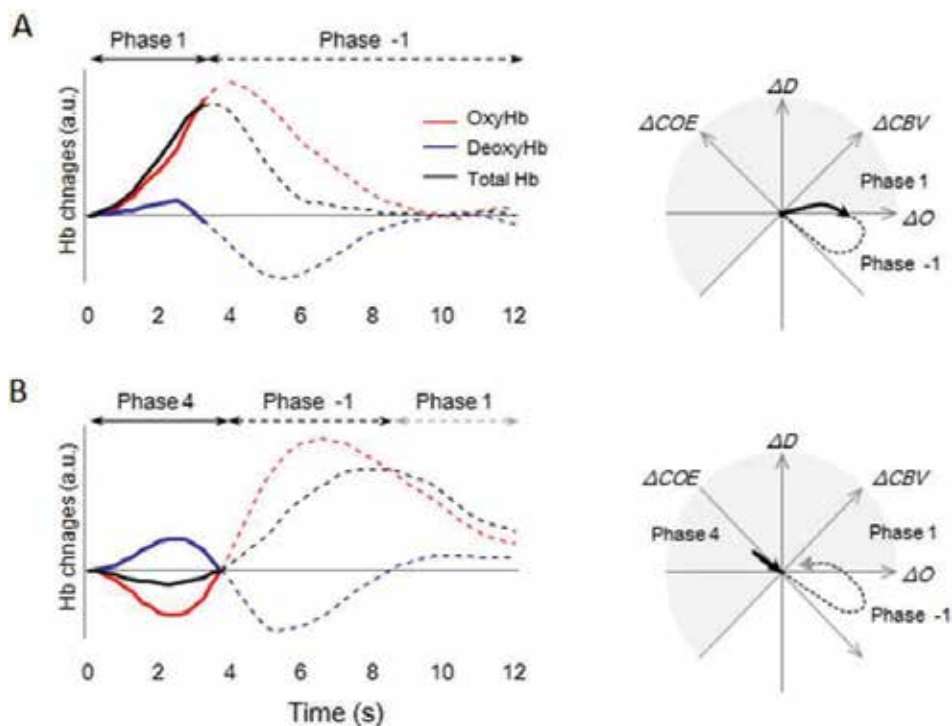


**Figure 8.** Two kinds of initial dips [32]. Representative patterns of two types of initial dips when data from (A) and (B) were converted into vectors on a vector plane. (A) In a study using optical intrinsic signals,  $\Delta D$  increased during the early part of a task [94]. The vector in this time course is in Phase 1 during the initial dip and subsequently progresses into Phase -1, indicating a typical response. (A) Initially, the vector is in Phase 1 and subsequently rotates in a clockwise direction into Phase -2. (B) The vector initially rotates in a clockwise direction into Phase 4, followed by rotation in a counterclockwise direction into Phase -1 and subsequently into Phase 1.

induced by increased levels of deoxyHb. **Figure 8B** shows an fNIRS initial dip (an increased  $\Delta D$  accompanying a decreased  $\Delta O$ ), indicating Phase 4 [18, 32, 67, 68]. Recently, fNIRS was used to observe this new type of initial dip in primates [109].

As shown in **Figure 8A**, if this canonical initial dip detected by Malonek and Grinvald using OIS [94] corresponds to that of fMRI [95, 104], this would mean that the a blood oxygenation level-dependent (BOLD) signal from fMRI was able to differentiate between Phase 1, as a signal decrease, and Phase -1, as a signal increase. However, Phase 1 is an increased  $\Delta CBV$  dip, in which  $\Delta COE$  decreases while the levels of deoxyHb increase. Thus, there is a discrepancy between the results from the two modalities. A theory bridging fNIRS and fMRI has been proposed, suggesting that a BOLD signal influenced by changes in  $\Delta CBV$  closely resembles an increase in the levels of oxyHb [24]. In this model, the fMRI signal in the increased  $\Delta CBV$  phase depends on the observed change in  $\Delta O$  (not  $\Delta D$ ). Theoretically, this change may be considered to be a BOLD signal increase rather than a dip. Indeed, the use of the vector plane may explain the fact that the OIS initial dip does not correspond to that of fMRI.

In present, initial dips could be reliably detected with OIS [92–97] and fNIRS [31–36, 109]. On the other hand, the occurrence of the initial dip in fMRI has been doubted and its mechanism is still controversial [21–24, 105]. Logothetis et al. [86] reported a period of latency, when the increase in the BOLD signal was flat for a few seconds at the beginning of the task. This shows the difficulty in detecting changes in phases during passage through the capillaries from those in the BOLD

signal. Of note, the sensitivity of fMRI declines at detecting activities with high oxygen consumption. During early research on the combination of fMRI and fNIRS [9, 110], the concept of phases had not been introduced and the differences between these methods were not understood clearly.

Collectively, research has shown that these two modalities are physiologically inconsistent in their sensitivity to the initial dip, with significant differences between them. Moreover, animal studies have demonstrated the variation of ratios between changes in the levels of deoxyHb and oxyHb occurring simultaneously with neural activity (i.e., diversity of phase) [103, 109]. Using the concept of phases, it is also possible to re-evaluate the results of a previous fNIRS study [8] (**Figure 2**) and confirm that the results indicate Phase 1 in areas where oxygen consumption is high or in the time zone. The vector-based evaluation was able to show a short initial dip and sustained oxygen metabolism because the period of the task was long in this study. On the other hand, investigations that followed this previous study [8] may have evaluated the intensity of brain activity only (similar to  $L$ ) in the Phase  $-1$  and  $-2$  typical responses.

## 9. Quantification of brain activity in time series

Local brain activity was quantified for the first time in 1993 using continuous-wave fNIRS, by substituting optical differential path length factors [8]. At that time,  $\text{mmol}\cdot\text{mm}$  (or  $\text{mmol}\cdot\text{cm}$ ) was commonly used as the unit expressing the degree of change in the levels of Hb, taking the differential path length factor as 1 [111, 112]. The phase angle  $k$  expresses oxygen metabolism quantitatively in degrees. This offers the advantage of being independent of the actual levels of Hb. **Figure 9** shows image displays from a verbal task [29, 30]. Local increases in the angle  $k$  were detected in Broca's area (channel 4) and the surrounding area during the task, with almost no change observed in  $\Delta\text{CBV}$ . Thus, the use of the angle  $k$  may permit the high-sensitivity detection of local brain activity occurring simultaneously with a task (regardless of the duration of the task) that has been undetected in previous studies against the background of slow hemodynamic change. On the other hand, intensity ( $L$ ) is strongest in channels 4 and 5 during and after the task, respectively. After the task, the angle  $k$  decreases approaching zero. These findings indicate the variable behavior of different indices in spatiotemporal imaging. In the past, the differences in spatiotemporal imaging had been largely ignored, with researchers focusing exclusively on typical responses. The differences in local brain activity of this kind were equally ignored, particularly when they occurred simultaneously with short tasks.

It has been shown that vector-based NIRS is able to quantitatively evaluate differences in the oxygen load in the prefrontal cortex arising from different breathing routes (**Figure 10** [113]). In that study, although there were no significant differences in  $L$ , differences in the time series of the angle  $k$  were apparent between nasal and mouth breathing. This may have potentially useful practical applications, such as the provision of an earlier and more reliable diagnosis of a patient's habitual breathing route compared with a patient interview. The use of an index combining both deoxyHb and oxyHb may lead to new interpretations of previous fNIRS data. Previous brain imaging studies have been based on the intensity of response.

In usage of this vector-based approach, it may not be possible to obtain the correct phase value by conventional data processing. For example, if the deoxyHb and oxyHb data are processed independently (e.g., when normalization or statistical parametric mapping has been performed on only the oxyHb data) [114], this will change the ratios, and there is a risk that the values of  $k$  will be distorted.

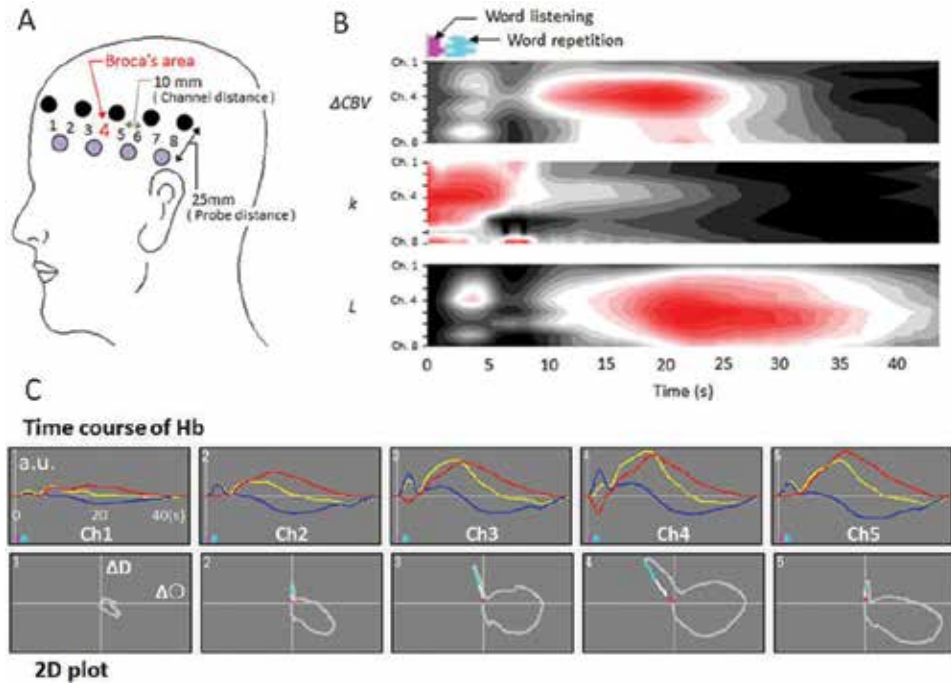


**Figure 9.** Spatiotemporal imaging of cerebral oxygen exchange for a verbal task [29, 30]. (A) Channel positions. Broca's area corresponds to channel 4. (B) Pink shows the duration of word listening (average 1.2 seconds) and blue shows the duration of word repetition (average 1.1 seconds). For  $\Delta CBV$ , red indicates positive vector changes, whereas black indicates negative vector changes. For the angle  $k$ , black indicates  $k = 0$ , whereas red indicates the maximum angle  $k$  ( $180^\circ$ ). For  $L$ , black indicates 0, whereas red indicates the peak value. (C) Time courses of hemoglobin components and their two dimensional vector coordinates. Oxyhemoglobin (OxyHb; red), deoxyhemoglobin (deoxyHb; blue), and total hemoglobin (total Hb; yellow). Arbitrary unit (a.u.).

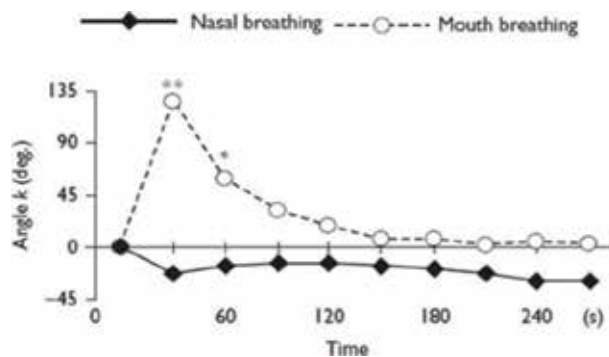


**Figure 10.** Time courses of the angle  $k$  for nasal and mouth breathing ( $**P < 0.05$ ;  $*P < 0.1$ ) [113].

In addition, a method of baseline correction, in which linear regression connecting the pre- and post-task period is used to emphasize the typical response, is available [115]. This may affect the angle  $k$  and  $L$  (intensity of response). By moving forward with quantitative analysis of this kind—designed to clarify differences between oxygenation and blood volume while taking care to avoid distortion from the initial processing of the data—fNIRS will be able to meet the challenges of quantitatively and accurately identifying localized brain activity.

## 10. Conclusion

The precise detection of local brain activity was the original purpose of fNIRS. Nowadays, because of the vector-based approach, investigators can measure initial dips from the scalp. Progress has been achieved in the quantitative detection of local brain activity and the development of spatiotemporal imaging. However, some fNIRS studies are actually task-related studies using NIRS, never intended for the spatial localization of brain function. This together with other factors has introduced doubts regarding the validity of fNIRS. The historical background described earlier in this review may be useful as we attempt to erase these doubts and improve the spatial and temporal accuracy of fNIRS. Studies are warranted to examine the physiological significance of the different combinations of changes in the levels of the different Hb and changes in the characteristics of mapping depending on the selection of indices.

Local brain activity induces local oxygen consumption and demand for oxygen supply. Further research is required to investigate the relationship between the consumption of oxygen and the spatial distribution of oxygen supply accompanying local brain activity. The indices angle  $k$  and  $L$ , indicating the phase of hemoglobin response and its intensity, respectively, are new indices for the detection of local brain activity. In addition, the simultaneous measurement of composite indices of this kind may improve the detection of local brain activity. The application of methods for the simultaneous evaluation of these composite indicators is one of the challenges for future research on the new fNIRS method.


### Author details

Toshinori Kato

Department of Brain Environmental Research, KatoBrain Co., Ltd., Tokyo, Japan

\*Address all correspondence to: [kato@katobrain.com](mailto:kato@katobrain.com)

### IntechOpen

© 2018 The Author(s). Licensee IntechOpen. This chapter is distributed under the terms of the Creative Commons Attribution License (<http://creativecommons.org/licenses/by/3.0>), which permits unrestricted use, distribution, and reproduction in any medium, provided the original work is properly cited. 

## References

- [1] Ferrari M, Quaresima V. A brief review on the history of human functional near-infrared spectroscopy (fNIRS) development and fields of application. *NeuroImage*. 2012;**63**:921-935. DOI: 10.1016/j.neuroimage.2012.03.049
- [2] Mihara M, Miyai I. Review of functional near-infrared spectroscopy in neurorehabilitation. *Neurophotonics*. 2016;**3**:031414. DOI: 10.1117/1.NPh.3.3.031414
- [3] Yoshino K, Oka N, Yamamoto K, Takahashi H, Kato T. Functional brain imaging using near infrared spectroscopy during actual driving on an expressway. *Frontiers in Human Neuroscience*. 2013;**7**:882. DOI: 10.3389/fnhum.2013.00882. eCollection 2013.
- [4] Yoshino K, Oka N, Yamamoto K, Takahashi H, Kato T. Correlation of prefrontal cortical activation with changing vehicle speeds in actual driving: A vector-based functional near-infrared spectroscopy study. *Frontiers in Human Neuroscience*. 2013;**7**:895. DOI: 10.3389/fnhum.2013.00895
- [5] Oka N, Yoshino K, Yamamoto K, Takahashi H, Li S, Sugimachi T, et al. Greater activity in the frontal cortex on left curves: A vector-based fNIRS study of left and right curve driving. *PLoS One*. 2015;**10**(5):e0127594. DOI: 10.1371/journal.pone.0127594
- [6] Orino Y, Yoshino K, Oka N, Yamamoto K, Takahashi H, Kato T. Brain activity involved in vehicle velocity changes in a sag vertical curve on an expressway: Vector-based functional near-infrared spectroscopy study. *Journal of the Transportation Research Board*. 2015;**2518**:18-26. DOI: 10.3141/2518-03
- [7] Takashima S, Kato T, Hirano S, Mito T. Observation of activation in local cerebral blood flow by means of near-infrared spectroscopy. *Comprehensive research report concerning medical care for children (people) with disabilities*. Japan. Ministry of Health & Welfare. 1992:179-181
- [8] Kato T, Kamei A, Takashima S, Ozaki T. Human visual cortical function during photic stimulation monitoring by means of near-infrared spectroscopy. *Journal of Cerebral Blood Flow and Metabolism*. 1993;**13**:516-520. PMID: 8478409 DOI: 10.1038/jcbfm.1993.66
- [9] Kato T, Takashima S, Kamada K, Kishibayashi J, Sunohara N, Ozaki T. Advantage of near-infrared spectroscopy in the human functional MR imaging in brain. In: 12th Annual Scientific Meeting of the Society of Magnetic Resonance in Medicine. Proceedings of the International Society for Magnetic Resonance in Medicine. New York; Aug 14-20 1993;**1993**(S3):1409. <https://onlinelibrary.wiley.com/doi/epdf/10.1002/mrmp.22419930308>
- [10] Wyatt JS, Cope M, Delpy DT, Wray S, Reynolds EO. Quantification of cerebral oxygenation and haemodynamics in sick newborn infants by near infrared spectrophotometry. *Lancet*. 1986;**2**:1063-1066
- [11] Togari H. Noninvasive cerebral blood volume monitoring in premature infants. *Journal of Clinical and Experimental Medicine*. 1987;**142**:907-909
- [12] Golubic SJ, Susac A, Grilj V, Ranken D, Huonker R, Hauelsen J, et al. Size matters: MEG empirical and simulation study on source localization of the earliest visual activity in the occipital cortex. *Medical & Biological Engineering & Computing*. 2011;**49**(5):545-554. DOI: 10.1007/s11517-011-0764-9

- [13] Hillebrand A, Barnes GR. A quantitative assessment of the sensitivity of whole-head MEG to activity in the adult human cortex. *NeuroImage*. 2002;**16**:638-650
- [14] Stancák A, Wackermann J. Spatial EEG synchronisation over sensorimotor hand areas in brisk and slow self-paced index finger movements. *Brain Topography*. 1998;**11**:23-31
- [15] Kato T, Sancak A. Distinction of regional cerebral FORCE (fast-oxygen response in capillary event) effect by unilateral and bilateral finger movements. In: 11th Annual Meeting of the Organization for Human Brain Mapping, Toronto, Ontario, Canada. Jun 12-16, 2005. Presentation No. 1582
- [16] Shin J, Kim DW, Müller KR, Hwang HJ. Improvement of information transfer rates using a hybrid EEG-NIRS brain-computer interface with a short trial length: Offline and pseudo-online analyses. *Sensors (Basel)*. 2018;**18**(6). pii: E1827. DOI: 10.3390/s18061827
- [17] Huppert T, Barker J, Schmidt B, Walls S, Ghuman A. Comparison of group-level, source localized activity for simultaneous functional near-infrared spectroscopy-magnetoencephalography and simultaneous fNIRS-fMRI during parametric median nerve stimulation. *Neurophotonics*. 2017;**4**(1):015001. DOI: 10.1117/1.NPh.4.1.015001
- [18] Wylie GR, Graber HL, Voelbel GT, Kohl AD, DeLuca J, Pei Y, et al. Using co-variations in the Hb signal to detect visual activation: A near infrared spectroscopic imaging study. *NeuroImage*. 2009;**47**:473-481
- [19] Heinzel S, Haeussinger FB, Hahn T, Ehlis AC, Plichta MM, Fallgatter AJ. Variability of functional hemodynamics as measured with simultaneous fNIRS and fMRI during intertemporal choice. *NeuroImage*. 2013;**71**:125-134
- [20] Tian F, Sharma V, Kozel FA, Liu H. Functional near-infrared spectroscopy to investigate hemodynamic responses to deception in the prefrontal cortex. *Brain Research*. 2009;**1303**:120-130
- [21] Buxton RB. The elusive initial dip. *NeuroImage*. 2001;**13**:953-958
- [22] Iadecola C. Intrinsic signals and functional brain mapping: Caution, blood vessels at work. *Cerebral Cortex*. 2002;**12**:225-233
- [23] Pouratian N, Sicotte N, Rex D, Martin NA, Becker D, Cannestra AF, et al. Spatial/temporal correlation of BOLD and optical intrinsic signals in humans. *Magnetic Resonance in Medicine*. 2002;**47**:766-776
- [24] Yamamoto T, Kato T. Paradoxical correlation between signal in functional magnetic resonance imaging and deoxygenated haemoglobin content in capillaries: A new theoretical explanation. *Physics in Medicine and Biology*. 2002;**47**:1121-1141
- [25] Takahashi T, Takikawa Y, Kawagoe R, Shibuya S, Iwano T, Kitazawa S. Influence of skin blood flow on near-infrared spectroscopy signals measured on the forehead during a verbal fluency task. *NeuroImage*. 2011;**57**:991-1002
- [26] Kirilina E, Jelzow A, Heine A, Niessing M, Wabnitz H, Bruhl R, et al. The physiological origin of task-evoked systemic artefacts in functional near infrared spectroscopy. *NeuroImage*. 2012;**61**(1):70-81
- [27] Cyranoski D. Thought experiment. *Nature*. 2011;**469**:148-149
- [28] Takizawa R, Fukuda M, Kawasaki S, Kasai K, Mimura M, Pu S, et al. Neuroimaging-aided differential

diagnosis of the depressive state. *Neuroimage*. 2014;**85**(Pt 1):498-507. DOI: 10.1016/j.neuroimage.2013.05.126

[29] Kato T. Apparatus for evaluating biological function. 2006;WO/2003/068070. Available from: <http://www.wipo.int/patentscope/search/en/WO2003068070>

[30] Kato T. Biofunction diagnosis device, biofunction diagnosis method, bioprobe, bioprobe wearing tool, bioprobe support tool, and bioprobe wearing assisting tool. 2007;WO/2006/009178. Available from: <http://www.wipo.int/patentscope/search/en/WO2006009178>

[31] Kato T. Principle and technique of NIRS imaging for human brain FORCE: Fast-oxygen response in capillary event. In: *Proceedings 15th World Congress of the International Society of Brain Electromagnetic Topography*. 2004;**1270**:88-99. by Elsevier B.V. journal ISSN: 0531-5131. DOI: 10.1016/j.ics.2004.05.052

[32] Yoshino K, Kato T. Vector-based phase classification of initial dipoles during word listening using near-infrared spectroscopy. *Neuroreport*. 2012;**23**(16):947-951. DOI: 10.1097/WNR.0b013e328359833b

[33] Akiyama T, Ohira T, Kawase T, Kato T. TMS orientation for NIRS-functional motor mapping. *Brain Topography*. 2006;**19**(1-2):1-9. DOI: 10.1007/s10548-006-0007-9

[34] Hong KS, Naseer N. Reduction of delay in detecting initial dipoles from functional near-infrared spectroscopy signals using vector-based phase analysis. *International Journal of Neural Systems*. 2016;**26**(3):1650012. DOI: 10.1142/S012906571650012X

[35] Zafar A, Hong KS. Detection and classification of three-class initial dipoles

from prefrontal cortex. *Biomedical Optics Express*. 2017;**8**(1):367-383. PMID: PMC5231305. DOI: 10.1364/BOE.8.000367

[36] Zafar A, Hong KS. Neuronal activation detection using vector phase analysis with dual threshold circles: A functional near-infrared spectroscopy study. *International Journal of Neural Systems*. 24 Jun 2018:1850031. PMID: 30045647. DOI: 10.1142/S0129065718500314

[37] Jöbsis FF. Noninvasive, infrared monitoring of cerebral and myocardial oxygen sufficiency and circulatory parameters. *Science*. 1977;**198**:1264-1267

[38] Takashima S, Ando Y. Reflectance spectrophotometry, cerebral blood flow and congestion in young rabbit brain. *Brain & Development*. 1988;**10**:20-23

[39] Koyama K, Mito T, Takashima S, Suzuki S. Effect of phenylephrine and dopamine on cerebral blood flow, blood volume, and oxygenation in young rabbits. *Pediatric Neurology*. 1990;**6**:87-90

[40] Mito T, Koyama K, Houdou S, Takashima S, Suzuki S. Response on near-infrared spectroscopy and of cerebral blood flow to hypoxemia induced by N<sub>2</sub> and CO<sub>2</sub> in young rabbits. *Brain & Development*. 1990;**12**:408-411

[41] Takashima S, Kudou H, Cho H, Houdou S, Hasegawa M. Monitoring of Oxygenation and Cerebral Blood Volume and Respiratory Abnormality of Children with Cerebral Palsy. *Comprehensive Research Report Concerning Medical Care for Children (People) with Disabilities*. Japan: Ministry of Health & Welfare; 1990. pp. 199-201

[42] Abdel-Dayem HM, Bahar RH, Sigurdsson GH, Sadek S, Olivercrona H, Ali AM. The hollow skull: A sign of

brain death in Tc-99m HM-PAO brain scintigraphy. *Clinical Nuclear Medicine*. 1989;14:912-916

[43] Roland PE, Friberg L. Localization of cortical areas activated by thinking. *Journal of Neurophysiology*. 1985;53:1219-1243

[44] Brod J, Fencel V, Hejl Z, Jirka J. Circulatory changes underlying blood pressure elevation during acute emotional stress (mental arithmetic) in normotensive and hypertensive subjects. *Clinical Science*. 1959;18:269-279

[45] Nyberg G, Graham RM, Stokes GS. The effect of mental arithmetic in normotensive and hypertensive subjects, and its modification by beta-adrenergic receptor blockade. *British Journal of Clinical Pharmacology*. 1977;4:469-474

[46] Kitagawa Y, Meyer JS, Tachibana H, Mortel KF, Rogers RL. CT-CBF correlations of cognitive deficits in multi-infarct dementia. *Stroke*. 1984;15:1000-1009

[47] Roland PE, Eriksson L, Stone-Elander S, Widen L. Does mental activity change the oxidative metabolism of the brain? *The Journal of Neuroscience*. 1987;7:2373-2389

[48] Roland PE, Skinhøj E, Lassen NA, Larsen B. Different cortical areas in man in organization of voluntary movements in extrapersonal space. *Journal of Neurophysiology*. 1980;43:137-150

[49] Fox P, Raichle M. Stimulus rate dependence of regional cerebral blood flow in human striate cortex, demonstrated by positron emission tomography. *Journal of Neurophysiology*. 1984;51:1109-1120

[50] Jöbsis FF. Method and apparatus for monitoring metabolism in body organs. U.S. Patent No.4,281,645. 1981

[51] Kato T, Okuyama K. Assessment of maturation and impairment of brain by I-123 iodoamphetamine SPECT and MR imaging in children. *Showa University Journal of Medical Sciences*. 1993;5:99-115

[52] Beauchamp MS, Beurlot MR, Fava E, Nath AR, Parikh NA, Saad SZ, et al. The developmental trajectory of brain-scalp distance from birth through childhood: Implications for functional neuroimaging. *PLoS One*. 2011;6(9):e24981. DOI: 10.1371/journal.pone.0024981

[53] Liao SM, Ferradal SL, White BR, Gregg N, Inder TE, Culver JP. High-density diffuse optical tomography of term infant visual cortex in the nursery. *Journal of Biomedical Optics*. 2012;17:081414. DOI: 10.1117/1.JBO.17.8.081414

[54] Minagawa-Kawai Y, Cristia A, Long B, Vendelin I, Hakuno Y, Dutat M, et al. Insights on NIRS sensitivity from a cross-linguistic study on the emergence of phonological grammar. *Frontiers in Psychology*. 2013;16(4):170. DOI: 10.3389/fpsyg.2013.00170 (eCollection 2013)

[55] Maki A, Yamashita Y, Ito Y, Watanabe E, Mayanagi Y, Koizumi H. Spatial and temporal analysis of human motor activity using noninvasive NIR topography. *Medical Physics*. 1995;22:1997-2005

[56] Strangman G, Franceschini MA, Boas DA. Factors affecting the accuracy of near-infrared spectroscopy concentration calculations for focal changes in oxygenation parameters. *NeuroImage*. 2003;18:865-879

[57] Hoshi Y, Tamura M. Detection of dynamic changes in cerebral oxygenation coupled to neuronal function during mental work in man. *Neuroscience Letters*. 1993;150:5-8



- [58] Villringer A, Planck J, Hock C, Schleinkofer L, Dirnagl U. Near infrared spectroscopy (NIRS): A new tool to study hemodynamic changes during activation of brain function in human adults. *Neuroscience Letters*. 1993;**154**:101-104
- [59] Chance B, Zhuang Z, UnAh C, Alter C, Lipton L. Cognition-activated low frequency modulation of light absorption in human brain. *Proceedings of the National Academy of Sciences of the United States of America*. 1993;**90**:3770-3774
- [60] Kawaguchi H, Hayashi T, Kato T, Okada E. Theoretical evaluation of accuracy in position and size of brain activity obtained by near-infrared topography. *Physics in Medicine and Biology*. 2004;**49**:2753-2765
- [61] Franceschini MA, Toronov V, Filiaci ME, Gratton E, Fantini S. On-line optical imaging of the human brain with 160-ms temporal resolution. *Optics Express*. 2000;**6**:49-57
- [62] Okamoto M, Dan H, Sakamoto K, Takeo K, Shimizu K, Kohno S, et al. Three-dimensional probabilistic anatomical cranio-cerebral correlation via the international 10-20 system oriented for transcranial functional brain mapping. *NeuroImage*. 2004;**21**:99-111
- [63] Barbour RL, Lubowsky J, Aronson R. Method of imaging a random medium. U.S. Patent No. 5,137,355. 1989
- [64] Zeff BW, White BR, Dehghani H, Schlaggar BL, Culver JP. Retinotopic mapping of adult human visual cortex with high-density diffuse optical tomography. *Proceedings of the National Academy of Sciences of the United States of America*. 2007;**104**:12169-12174
- [65] Habermehl C, Holtze S, Steinbrink J, Koch SP, Obrig H, Mehnert J, et al. Somatosensory activation of two fingers can be discriminated with ultrahigh-density diffuse optical tomography. *NeuroImage*. 2012;**59**:3201-3211
- [66] Kato T, Wang P, Kim S-G, Kamba M, Kawaguchi F, Ichikawa N. Selectivity, sensitivity and connectivity due to somatosensory stimulation in rats investigated by noninvasive subcentimeter-fNIR. *NeuroImage*. 2001;**13**:S22
- [67] Kato T, Endo A, Fukumizu M, Kato T, Takashima S, Kawaguchi F, et al. Initial cerebral metabolism due to short visual stimulation using human functional ear-infraredgraphy (fNIR): How it correlates with fMRI? In: *Proceedings of the International Society for Magnetic Resonance in Medicine, 7th Annual Meeting*. Philadelphia, Pennsylvania, USA; May 24-28 1999;**762**. Poster No. 762. <https://www.ismrm.org/99prog/program.htm>
- [68] Kato T, Endo A, Fukumizu M, Kato T, Takashima S, Kawaguchi F, et al. Real-time imaging of "initial cerebral metabolism" using human functional near-infraredgraphy (fNIR). *NeuroImage*. 1999;**9**(6):S309
- [69] Obrig H, Kleinschmidt A, Merboldt KD, Dirnagl U, Grahm J, Villringer A. Monitoring of cerebral blood oxygenation during human brain activation by simultaneous high-resolution MRI and near-infrared spectroscopy. In: *Second Meeting of the Society of Magnetic Resonance. Proceedings of the International Society for Magnetic Resonance in Medicine*. San Francisco, California USA; 6-12 August 1994;**1994**(S1):67. <https://onlinelibrary.wiley.com/doi/epdf/10.1002/mrmp.22419940103>
- [70] Nakajima T, Fujita M, Watanabe H, Kuwabara T, Takeo K, Iwamoto S, et al. Functional mapping of the human visual system with near-infrared spectroscopy and BOLD

- functional MRI. In: Second Meeting of the Society of Magnetic Resonance. Proceedings of the International Society for Magnetic Resonance in Medicine. San Francisco, California USA; Aug 6-12 1994;1994(S2):687. <https://onlinelibrary.wiley.com/doi/pdf/10.1002/mrmp.22419940204>
- [71] Kleinschmidt A, Obrig H, Requardt M, Merboldt KD, Dirnagl U, Villringer A, et al. Simultaneous recording of cerebral blood oxygenation changes during human brain activation by magnetic resonance imaging and near-infrared spectroscopy. *Journal of Cerebral Blood Flow and Metabolism*. 1996;16:817-826
- [72] Kameyama M, Fukuda M, Yamagishi Y, Sato T, Uehara T, Ito M, et al. Frontal lobe function in bipolar disorder: A multichannel near-infrared spectroscopy study. *NeuroImage*. 2006;29:172-184
- [73] Sumitani S, Tanaka T, Tayoshi S, Ota K, Kameoka N, Ueno S, et al. Activation of the prefrontal cortex during the Wisconsin card sorting test as measured by multichannel near-infrared spectroscopy. *Neuropsychobiology*. 2006;53:70-76
- [74] Hibino S, Mase M, Shirataki T, Nagano Y, Fukagawa K, Abe A, et al. Oxyhemoglobin changes during cognitive rehabilitation after traumatic brain injury using near infrared spectroscopy. *Neurologia Medico-Chirurgica (Tokyo)*. 2013;53:299-303
- [75] Telkemeyer S, Rossi S, Nierhaus T, Steinbrink J, Obrig H, Wartenburger I. Acoustic processing of temporally modulated sounds in infants: Evidence from a combined near-infrared spectroscopy and EEG study. *Frontiers in Psychology*. 2011;1:62. DOI: 10.3389/fpsyg.2011.00062 (eCollection 2011)
- [76] Leon-Dominguez U, Izzetoglu M, Leon-Carrion J, Solís-Marcos I, Garcia-Torrado FJ, Forastero-Rodríguez A, et al. Molecular concentration of deoxyHb in human prefrontal cortex predicts the emergence and suppression of consciousness. *Neuroimage*. 2014;85:616-625. DOI: 10.1016/j.neuroimage.2013.07.023
- [77] Hoshi Y, Kobayashi N, Tamura M. Interpretation of near-infrared spectroscopy signals: A study with a newly developed perfused rat brain model. *Journal of Applied Physiology*. 2001;90:1657-1662
- [78] Roy C, Sherrington C. On the regulation of the blood-supply of the brain. *The Journal of Physiology*. 1890;11:85-158
- [79] Kety SS, Schmidt CF. The determination of cerebral blood flow in man by the use of nitrous oxide in low concentrations. *The American Journal of Physiology*. 1945:153-166
- [80] Leenders KL, Perani D, Lammertsma AA, Heather JD, Buchingham P, Healy MJR, et al. Cerebral blood flow, blood volume and oxygen utilization: Normal values and effect of age. *Brain*. 1990;113:27-47
- [81] Fox PT, Raichle ME. Focal physiological uncoupling of cerebral blood flow and oxidative metabolism during somatosensory stimulation in human subjects. *Proceedings of the National Academy of Sciences*. 1986;83:1140-1144
- [82] Buxton RB, Frank LR. A model for the coupling between cerebral blood flow and oxygen metabolism during neural stimulation. *Journal of Cerebral Blood Flow and Metabolism*. 1997;17:64-72
- [83] Vafaee MS, Gjedde A. Model of blood-brain transfer of oxygen explains nonlinear flow-metabolism coupling

during stimulation of visual cortex. *Journal of Cerebral Blood Flow and Metabolism*. 2000;**20**:747-754

[84] Hudetz AG, Biswal BB, Fehér G, Kampine JP. Effects of hypoxia and hypercapnia on capillary flow velocity in the rat cerebral cortex. *Microvascular Research*. 1997;**54**:35-42

[85] Mintun MA, Lundstrom BN, Snyder AZ, Vlassenko AG, Shulman GL, Raichle ME. Blood flow and oxygen delivery to human brain during functional activity: Theoretical modeling and experimental data. *Proceedings of the National Academy of Sciences of the United States of America*. 2001;**98**:6859-6864

[86] Logothetis NK, Pauls J, Augath M, Trinath T, Oeltermann A. Neurophysiological investigation of the basis of the fMRI signal. *Nature*. 2001;**412**:150-157

[87] Gratton G, Fabiani M, Corballis PM, Hood DC, Marsha R, Wood G, et al. Fast and localized event-related optical signals (EROS) in the human occipital cortex: Comparisons with the visual evoked potential and fMRI. *NeuroImage*. 1997;**6**:168-180

[88] Sheth SA, Nemoto M, Guiou M, Walker M, Pouratian N, Toga AW. Linear and nonlinear relationships between neuronal activity, oxygen metabolism, and hemodynamic responses. *Neuron*. 2004;**42**:347-355

[89] Vanzetta I, Hildesheim R, Grinvald A. Compartment-resolved imaging of activity-dependent dynamics of cortical blood volume and oximetry. *The Journal of Neuroscience*. 2005;**25**:2233-2244

[90] Mihara M, Miyai I, Hattori N, Hatakenaka M, Yagura H, Kawano T, et al. Neurofeedback using real-time near-infrared spectroscopy enhances

motor imagery related cortical activation. *PLoS One*. 2012;**7**:e32234. DOI: 10.1371/journal.pone.0032234

[91] Lee CH, Sugiyama T, Kataoka A, Kudo A, Fujino F, Chen YW, et al. Analysis for distinctive activation patterns of pain and itchy in the human brain cortex measured using near infrared spectroscopy (NIRS). *PLoS One*. 2013;**8**:e75360. DOI: 10.1371/journal.pone.0075360

[92] Ances BM. Coupling of changes in cerebral blood flow with neural activity: What must initially dip must come back up. *Journal of Cerebral Blood Flow and Metabolism*. 2003;**24**:1-6

[93] Frostig RD, Lieke EE, Ts'ò DY, Grinvald A. Cortical functional architecture and local coupling between neuronal activity and the microcirculation revealed by in vivo high-resolution optical imaging of intrinsic signals. *Proceedings of the National Academy of Sciences of the United States of America*. 1990;**87**:6082-6086

[94] Malonek D, Grinvald A. Interactions between electrical activity and cortical microcirculation revealed by imaging spectroscopy: Implications for functional brain mapping. *Science*. 1996;**272**:551-554

[95] Vanzetta I, Grinvald A. Increased cortical oxidative metabolism due to sensory stimulation: Implications for functional brain imaging. *Science*. 1999;**286**:1555-1558

[96] Hess A, Stiller D, Kaulisch T, Heil P, Scheich H. New insights into the haemodynamic blood oxygenation level-dependent response through combination of functional magnetic resonance imaging and optical recording in gerbil barrel cortex. *The Journal of Neuroscience*. 2000;**20**:3328-3338

- [97] Jones M, Berwick J, Johnston D, Mayhew J. Concurrent optical imaging spectroscopy and laser-doppler flowmetry: The relationship between blood flow, oxygenation, and volume in rodent barrel cortex. *NeuroImage*. 2001;**13**:1002-1015
- [98] Suh M, Bahar S, Mehta A, Schwartz T. Blood volume and hemoglobin oxygenation response following electrical stimulation of human cortex. *NeuroImage*. 2006;**31**:66-75
- [99] Kato T, Endo A, Fukumizu M, Furusho J, Takashima S, Kawaguchi F, et al. Single finger movement trial using human functional near-infrared graphy (fNIR). *NeuroImage*. 1999;**9**(6):S430
- [100] Kato T, Yamashita Y, Maki A, Yamamoto T, Koizumi H. Temporal behavior of human functional near-infrared graphy (fNIR) using single-word speaking trial. *NeuroImage*. 1999;**9**(6):S1025
- [101] Jaszewski G, Strangman G, Wagner J, Kwong KK, Poldrack RA, Boas DA. Differences in the hemodynamic response to event-related motor and visual paradigms as measured by near-infrared spectroscopy. *NeuroImage*. 2003;**20**:479-488
- [102] Ances BM, Buerk DG, Greenberg JH, Detre JA. Temporal dynamics of the partial pressure of brain tissue oxygen during functional forepaw stimulation in rats. *Neuroscience Letters*. 2001;**306**:106-110
- [103] Thompson J, Peterson M, Freeman R. High-resolution neurometabolic coupling revealed by focal activation of visual neurons. *Nature Neuroscience*. 2004;**7**:919-920
- [104] Menon RS, Ogawa S, Hu X, Strupp JS, Andersen P, Ugurbil K. BOLD based functional MRI at 4 Tesla includes a capillary bed contribution: Echo-planar imaging mirrors previous optical imaging using intrinsic signals. *Magnetic Resonance in Medicine*. 1995, 1995;**33**:453-459
- [105] Hu X, Yacoub E. The story of the initial dip in fMRI. *NeuroImage*. 2012;**62**:1103-1108
- [106] Watanabe E, Maki A, Kawaguchi F, Takashiro K, Yamashita Y, Koizumi H, et al. Non-invasive assessment of language dominance with near-infrared spectroscopic mapping. *Neuroscience Letters*. 1998;**256**:49-52
- [107] Bisconti S, Di Sante G, Ferrari M, Quaresima V. Functional near-infrared spectroscopy reveals heterogeneous patterns of language lateralization over frontopolar cortex. *Neuroscience Research*. 2012;**73**:328-332
- [108] Molteni E, Contini D, Caffini M, Baselli G, Spinelli L, Cubeddu R, et al. Load-dependent brain activation assessed by time-domain functional near-infrared spectroscopy during a working memory task with graded levels of difficulty. *Journal of Biomedical Optics*. 2012;**17**:056005. DOI: 10.1117/1.JBO.17.5.056005
- [109] Zaidi AD, Birbaumer N, Fetz E, Logothetis N, Sitaram R. The hemodynamic initial-dip consists of both volumetric and oxymetric changes correlated to localized spiking activity. *bioRxiv*.2018. <https://www.biorxiv.org/content/biorxiv/early/2018/02/22/259895.full.pdf>
- [110] Kato T, Kamada K, Segawa F, Sunohara N, Takashima S, Shimizu K, et al. Effects of photo stimulation on the anisotropic diffusion of the visual fibers. In: 11th Annual Scientific Meeting of the Society of Magnetic Resonance in Medicine. Proceedings of the International Society for Magnetic Resonance in Medicine. Berlin, Germany; Aug 8-14 1992;**1992**(S3):1029. <https://>

[onlinelibrary.wiley.com/doi/epdf/10.1002/mrmp.22419920303](http://onlinelibrary.wiley.com/doi/epdf/10.1002/mrmp.22419920303)

[111] Hirano S, Hasegawa M, Kamei A, Ozaki T, Takashima S. Responses of cerebral blood volume and oxygenation to carotid ligation and hypoxia in young rabbits: Near-infrared spectroscopy study. *Journal of Child Neurology*. 1993;**8**:237-241

[112] Kamei A, Ozaki T, Takashima S. Monitoring of the intracranial hemodynamics and oxygenation during and after hyperventilation in newborn rabbits with near-infrared spectroscopy. *Pediatric Research*. 1994;**35**:334-338

[113] Sano M, Sano S, Oka N, Yoshino K, Kato T. Increased oxygen load in the prefrontal cortex from mouth breathing: A vector-based near-infrared spectroscopy study. *Neuroreport*. 2013;**24**(17):935-940. DOI: 10.1097/WNR.0000000000000008

[114] Ye JC, Tak S, Jang KE, Jung JW, Jang JD. NIRS-SPM: Statistical parametric mapping for near-infrared spectroscopy. *NeuroImage*. 2009;**44**:428-447

[115] Tsujimoto S, Yamamoto T, Kawaguchi H, Koizumi H, Sawaguchi T. Prefrontal cortical activation associated with working memory in adults and preschool children: An event-related optical topography study. *Cerebral Cortex*. 2004;**14**:703-712



# Application of ICA and Dynamic Mixture Model to Identify Microvasculature Activation in fMRI

*Yongxia Zhou*

## Abstract

The emphasis of this work is on developing novel data-processing techniques to achieve a higher spatiotemporal resolution in dynamic functional magnetic resonance imaging (fMRI). Due to partial volume effects, a pixel in fMRI may contain signals from a mixture of micro- and macrovasculature, with very different temporal characteristics. This mixture effect provides a way to separate microvasculature from macrovasculature in fMRI. A multi-component model representing a mixture of many reference functions is used to fit the time course of pixels in fMRI. The results suggest that it may be possible to separate the micro- and macrovasculature fractional contributions to pixels by this approach. Compared to the classical single-component model, the multi-component model fits the measured fMRI time course with a higher correlation coefficient and also detects voxels with low latencies more efficiently. Spatial independent component analysis (ICA) as a preprocessing step is implemented to remove major physiological noise and artifacts. The results of mixture model fitting after ICA cleaning show better results for microvasculature detection.

**Keywords:** fMRI microvasculature, ICA, dynamic mixture model, neuronal detection

## 1. Introduction

Functional magnetic resonance imaging (fMRI) is the most widely used modality to map brain function because it can be easily implemented, is noninvasive, and has a relatively high spatial resolution. The dynamic fMRI signal change is regulated by the local changes in cerebral blood flow (CBF), cerebral blood volume (CBV), and blood oxygenation. CBF studies have suggested that a local increase in oxygen delivery beyond metabolic demand occurs in active cerebral tissue, which results in a higher concentration of oxygenated blood and a decrease in deoxyhemoglobin concentration within the microvasculature of metabolically active brain regions. Due to the four unpaired electrons, deoxyhemoglobin maintains a larger observed magnetic susceptibility effect and is paramagnetic relative to oxyhemoglobin and the surrounding brain tissue. The decrement in this paramagnetic substance in the activated brain leads to an increase in the local magnetic homogeneity and reduces

dephasing of spins. This increases the  $T2^*$  contrast in the activated brain and results in increases of MR signal relative to the resting state. A fast MRI data acquisition sequence known as the echo-planar imaging (EPI) sequence is commonly used to acquire fMRI signals. The physiological contributors to the fMRI signal changes include the blood-oxygenation-level-dependent (BOLD) and in-flow effects such as the increase in local CBF and arterial oxygenation. The signal in the functional area reflects the local changes in the CBF and oxygen consumption rate due to the task or stimulus [1]. And finally, the quantitative fMRI image indicates the spatiotemporal mapping of the hemodynamic in response to a given task at specific brain areas.

The coupling between the BOLD hemodynamic effect and the underlying neuronal activity has been studied and emphasized recently [2–4]. The first question is whether the BOLD effect can reflect neuronal activation. Experiments have been done with both animals and humans to verify that the BOLD contrast directly reflects the neural responses elicited by a stimulus [5, 6]. The second question is how the BOLD signal reflects the underlying neuronal activation. The exact nature of the neurovascular coupling is not known yet. The studies by Logothetis suggest that the BOLD signal is more likely to reflect the input and local neuronal processing in a given area [5], whose weighted average of dendro-somatic components is measured as the local field potential (LFP). However, because of the slow-brain hemodynamics and the draining effects of vessels and veins, the BOLD activation detected in fMRI is temporally delayed and spatially blurred from the actual site of neuronal activation. The third question is then how to detect the neuronal activations from fMRI. Because of the unknown nature of the neurovascular coupling, how to detect neuronal activation remains an open question. Since neuronal activation originates in tissue subserved by the microvasculature, the detected microvasculature will be co-localized or at least closer to neuronal activation.

The fMRI BOLD effect originates within the microvasculature but also spreads into veins that drain blood from the activated brain tissue. And fMRI-based BOLD contrast consists mainly of activations in the microvasculature, large venules, and draining veins [7–10]. Because the BOLD signal is largely contaminated by the signals in large veins and noise, extracting earlier microvasculature activation is difficult and several issues need to be resolved. One major problem is the compounding effects from the physiological cardiac and respiratory noise, random noise, and also the contamination of head and vessel motion artifacts [11]. The percentage signal changes triggered by the stimuli typically is 1–10% in 1.5–3 T scanners [7]. Averaging scans for all events can improve signal-to-noise ratio (SNR) in fMRI by canceling random noise. Low-pass and high-pass filtering for the data can also improve SNR by removing the slow physiological processes such as subject habituation, learning or fatigue, subject motion, machine calibration drift, and scan-to-scan baseline variability [12]. However, artifacts in fMRI are often correlated with the signal of interest. Thus, classical average and filtering methods are not very effective. Noise-removing methods that are based on the intrinsic structure of the measured signals are more effective.

Another challenge is the partial volume effect (PVE) within one fMRI voxel. Because of the relatively large size of the voxel at the scale of mm compared to the size of veins and microvasculature, a mixture of micro- and macrovasculatures is present in the activated voxel with different temporal characteristics. Since the actual site of neuronal activity could be masked by signals from macrovasculature, a technique to separate micro- and macrovasculature within a voxel would be of great significance to fMRI to improve spatial specificity as well.

The vascular contributions to the BOLD signal depend on magnetic field strength as well as on data acquisition methods. Many previous works have been done to enhance the detection of microvasculature. In Chen and Ugurbil [13],



a higher field at 7 T was used to increase the relative contribution of microcomponent to the BOLD signal. In spin-echo fMRI [14], large vessel contributions were suppressed because the 180° radiofrequency (RF) pulse in spin-echo (SE) sequence refocused the dephasing effect of the static field inhomogeneity around large vessels. A fast response that may be attributed to an increased oxygen consumption had been observed [15, 16]. This fast dip might be more sensitive to microvasculature. Also, previous approaches to separate the microvasculature have relied upon post-processing techniques that utilize the fact that the phase of the MR signal often reflects the presence of larger vessels in a voxel [17, 18]. Thus, larger vessels could be removed in the frequency domain or K-space. Our group has presented a study of segmenting fMRI pixels into microvasculature, venules, and large veins using intensity, phase, and temporal delay as features [17].

Independent component analysis (ICA) was first applied to fMRI in 1998 by McKeown et al. using INFORMAX [19] and has been shown to be superior to principle component analysis (PCA) in determining the spatial and temporal extents of task-related activation. ICA can also be used to identify the nontask-related components, such as physiological noise and movement artifacts. Initially, ICA methods assumed that the sources were naturally occurring sources and mostly had a super-Gaussian probability density function. Later on, the super-Gaussian assumption was expanded to a combination of super-Gaussian and sub-Gaussian distribution assuming that the source distribution was either sub-Gaussian or super-Gaussian [20]. Recently, a mixture density model for the sources has been proposed that enables the unknown sources to have a flexible density distribution [21]. The advantages of ICA over PCA, the correlation of spatial ICA and temporal ICA to fMRI, and some other issues have been discussed in many papers for the past decade [22, 23]. In this study, ICA is implemented as an advanced preprocessing step in fMRI activation detection to remove artifacts by identifying and then removing some unrelated noisy components. ICA can also be used to identify temporally independent sources by implementing temporal ICA to fMRI signals within the region of interest (ROI). Sources identified by temporal ICA provide extra information regarding the segmentation of microvasculature and macrovasculature mixtures within one voxel.

Temporal characteristics of the BOLD response had been investigated by using a series of time-shifted reference functions [7, 24]. A better localization of the activated sites and temporal relationships among different brain regions within selected clusters of activated voxels was achieved using this dynamic correlation method. But this dynamic fitting used only a one-reference function at a time. Our method is to use a multi-component model representing a mixture of many vascular components to account for partial volume effect within one voxel [25, 26]. Because of physiological and random noises in the fMRI signal, the multiple components fitting of the dynamic mixture model can be further improved with both spatial and temporal ICA methods to improve SNR. Our purpose is to implement dynamic fitting in the proposed mixture model to account for different temporal characteristics of vascular components and to improve SNR with ICA integration for better microvasculature detections and a higher spatiotemporal resolution.

## **2. Methods**

### **2.1 Experiment**

To test the methodology, an Institutional Review Board (IRB)-approved human study was conducted with fMRI on two normal subjects aged 25 and 40 years.

A 480-volume of event-related EPI was acquired on a GE 1.5 T LX system from two continuous slices (i.e., two images per volume) through the visual cortex. The stimulus was a reversing checkerboard flashing with a 2-Hz frequency for 2 s every 20 s. The pulse repetition time TR = 275 ms, effective echo time TE = 45 ms, 45° flip angle, 64 × 128 acquisition matrix, and 20 × 40 cm field of view. A total of seven events were acquired.

## 2.2 Model

A multi-component reference function with a variable latency and a variable time separation between adjacent components was fitted to the time course of each voxel within the visual cortex, as shown in Eq. (1)

$$y(t) = \sum_{i=1}^N a_i s_i(t) + n \Rightarrow Y = SA + n, t = 1, \dots, T \quad (1)$$

where  $y$  is the normalized time course of a voxel,  $n$  is fMRI noise,  $N$  is the number of component,  $s_i$  is the  $i$ th component,  $a_i$  is the contributions or the mixture coefficient of  $s_i$  in  $y$ ,  $T$  is the number of time points in the time course.

Each vascular component is modeled by a reference function with a latency parameter (2):

$$S_{T \times N}(t; N) = [X_1(t - T_1), X_2(t - T_2), \dots, X_N(t - T_N)] \quad (2)$$

where  $X(t)$  is the reference function to best represent BOLD response, and  $T_i$  is the latency parameter for the  $i$ th component to account for delay. Since latency is the most important and influential parameter in dynamic fitting, a dual-component model was investigated in this chapter for simplicity.

## 2.3 Estimation algorithm

Assuming the noise in fMRI is Gaussian white noise and the components (or mixtures) can be explicitly modeled by a series of reference functions, there are several ways to estimate the mixture coefficient and the latency of each component.

A non-negative least square (NNLS) solver [27] can be used to estimate the contribution coefficients of each component after normalizing both the time course and the components. At each iteration, only the column of  $S$  where the associated entry of  $A > 0$  was used for least square estimation as in Eq. (3)

$$A_{NN}^{(i)} = S_J^+ Y, \quad J = \left\{ j | A_j^{(i-1)} = 0 \right\} \quad (3)$$

If the non-negative constraint is removed from the estimation, then a standard minimum norm method can be used to estimate the contribution coefficients of each component. The model falls in the general linear model (GLM) fitting problem [28]. Thus, the estimation of the coefficient and hypothesis testing for the estimation can be done using Eq. (4)

$$\begin{aligned} A_{GLM} &= (S^T S)^{-1} S^T \cdot Y \\ A_{GLM} &\sim N\left(S^+ Y, \sigma_n^2 \cdot (S^T S)^{-1}\right) \end{aligned} \quad (4)$$

Recently, a first-order Taylor approximation for the temporal derivative of the reference function is used to estimate the delay of the fMRI response and the latency difference in different regions [29, 30]. Assuming that there is a slight time delay  $T_0$  between the reference function and the measurement, the delay  $T_0$  can be estimated as listed in Eq. (5)

$$\begin{aligned}
 y(t) &= a \cdot r(t - T_0) + n(t) \\
 r(t - T_0) &\approx r(t) - T_0 \cdot \dot{r}(t) \Rightarrow y(t) = \beta_1 r(t) + \beta_2 \dot{r}(t) + n(t) \quad (5) \\
 \Rightarrow a &\approx \beta_1, T_0 \approx \beta_2 / \beta_1
 \end{aligned}$$

where  $r(t)$  is a one-reference function and  $\dot{r}(t)$  is the temporal derivative of the reference function. Both are used as two basis functions in a GLM. The beta-parameters  $\beta_1$  and  $\beta_2$  are estimated using the GLM algorithm. In case of a dual-component model, the derivative of only one component or the derivatives of both components are tested.

After the mixture coefficients are estimated for any combination of two (or more) different reference functions, the combination of the two-reference functions that has the minimum fitting error or a maximum correlation coefficient with regard to the original time course of each voxel is the estimate of the two components with different latencies.

To account for the relatively small microvasculature signal compared to veins at 1.5 T, a weighting factor can be used to estimate the relative fractions of micro- and macrovasculature inside a voxel from the fitted coefficients. For two components, assume  $\{F_m \mid m = 1,2\}$  is the estimate of fraction coefficient from each component in one voxel using NNLS method, and  $\{A_m \mid m = 1,2\}$  is the weighting factor for each component. Then, the percentage contribution of each component in this voxel is computed as in Eq. (6)

$$P_1 = 1 / \left( 1 + \frac{A_1}{A_2} \cdot \frac{F_2}{F_1} \right), P_2 = 1 - P_1 \quad (6)$$

## 2.4 Simulation

In Eq. (2), each component comes from a reference function with certain latencies. The reference function mimicking the BOLD response is represented by the convolution of the stimuli function and the hemodynamic response function (HRF), assuming that the brain response is linear to the input (7)

$$r(t) = h(t) * I(t), I(t) = \sum_{trial} \delta(t - T_{trial}) \quad (7)$$

HRF is the brain response to an impulse stimulus and is modeled as the difference between two gamma functions as in Eq. (8) [31]

$$h(t; \tau_1, \tau_2, \delta_1, \delta_2) = \left( \frac{t}{\tau_1} \right)^{\delta_1} e^{-(\delta_1/\tau_1) \cdot (t-\tau_1)} - c \cdot \left( \frac{t}{\tau_2} \right)^{\delta_2} e^{-(\delta_2/\tau_2) \cdot (t-\tau_2)} \quad (8)$$

where  $\tau_1$  controls the rising time to peak,  $\tau_2$  controls the peak time of the undershoot,  $\delta_1, \delta_2$  determine the dispersion of the two peaks, and  $c$  controls the influence of the undershoot.

Firstly, the influences of the HRF parameters  $\tau_1, \tau_2, \delta_1, \delta_2, c$  and the reference function latency parameter  $T_0$  were studied. These parameters were in the range of as listed in the study:

$\tau_1 = 3.4 : 7.4, \delta_1 = 5 : 7, \tau_2 = 12, \delta_2 = 2\delta_1, c = 0.35, T_0 = -10 : 10$  [24]. Then, the reference function with all these parameters was fitted to one time course in the activated brain. The correlation coefficient between time course and the reference function as a function of shape parameter  $\delta_1$  and delay parameter  $\tau_1$  at one latency parameter  $T_0$  is used as a criterion for optimization, similar to the dictionary-based finger-printing method. Except for the latency parameter  $T_0$ , all the other parameters of HRF are found to have a minor influence on the correlation coefficient, and thus, only the latency parameter is used as a variable for each reference function in this work. And HRF parameters are the same as in SPM software  $\tau_1 = 5.4, \tau_2 = 12, \delta_1 = 6, \delta_2 = 12, c = 0.35$  [28].

Secondly, a Monte-Carlo study was conducted to test the fitting algorithm and to study the influence of noise on the latency estimations. The simulated time course was a mixture of one- or two-reference functions at different latencies from a series of reference functions. The mixture coefficient  $W_i, i = 1, 2$  of each reference function (or component) had a uniform distribution of  $W_i \sim U[0, 1]$ . A Gaussian white noise was added to the mixed time course with different SNR. The latencies of the components were estimated by different GLM and NNLS with or without derivative algorithms. The sampling step for the reference functions was  $dt = 105$  ms in the case studied based on maximal temporal resolution that fMRI could achieve. The process of adding random Gaussian noise to the mixture of one or two components with a random uniform coefficient was repeated 1000 times for each SNR. The SNRs were tested at level from 1 to 10, 20, and infinite which is noise-free. The results were obtained for a traditional one-reference function condition and a mixture of two-reference function condition.

For the simulated time course coming from one-reference function case, the tested algorithms are GLM method for one component and one derivative (i.e., two basis functions), GLM method with only one component, and NNLS method with only one component. The results show that the estimation is unbiased for both NNLS and GLM methods for all SNRs, and the standard deviation (STD) for the estimation is relatively small (less than 100 ms) for both methods at SNR larger than 3. For the GLM plus the derivative component method, the estimation error is non-zero for larger SNR. This is because the method uses the first-order derivative as an approximation, assuming that the delay is very small and the assumption is not always valid. The result is consistent with Hensen [29]. So only, the GLM and the NNLS without derivative were tested for the mixture of two components.

For the case in which the simulated time course came from two mixed reference functions, the latency of first component and separation of the two reference functions were estimated. First, only the latency of the first component was estimated and the separation of the two reference functions was initialized and fixed. Then, the separation of the two reference functions is also set as a variable. The Monte-Carlo simulation shows that both fixed and variable separations between two reference functions give a small bias in the estimation of latency as a function of SNR in case of mixture fitting. However, the NNLS estimation algorithm produces smaller bias than GLM. Also, a variable separation gives a higher STD than a fixed separation for latency estimation. Therefore, NNLS with a fixed separation is used for this work.

## 2.5 ICA denoise preprocessing

To improve the fitting using the multi-component model, spatial ICA (SICA) was implemented first to improve SNR. Temporal ICA (TICA) had also been applied to the cleaned data within a region of interest to extract the possible intrinsic temporally independent sources. TICA has also been used on functional MRI by several groups [32, 33].

In SICA, the assumption is that all the intrinsic spatial independent components are mixed temporally and measured at different time (which has the same meaning as “channel”). In order for spatial ICA to work, the measured fMRI EPI 2D or 3D image will be transformed to 1D vector in the same order at each time. The whole fMRI data are formulated as a 2D matrix:  $X_{ij}$ ,  $i = 1, 2, \dots, N$ ;  $j = 1, 2, \dots, V$ .  $N$  is the number of EPI volumes and  $V$  is the number of voxels in each volume. Assuming  $S_{M \times V}$  are the  $M$  independent components, the independent components are mixed in the following way (9):

$$X_{N \times V} = W^{-1}_{N \times M} \cdot S_{M \times V} \Rightarrow X_i = \sum_{m=1}^M W^{-1}_{im} \cdot S_i, \quad i = 1, 2, \dots, N \quad (9)$$

$$X_i = [X_{i1}, X_{i2}, \dots, X_{iV}]'$$

where  $W^{-1}_{N \times M}$  is the mixing matrix and  $W_{N \times M}$  is called the unmixing matrix.

In order to get a good estimation of unmixing matrix and source components, the number of samples or voxel number ( $V$ ) and the number of sources ( $M$ ) should satisfy  $V \geq M^*(M+1)/2$ . The number of sources should not exceed the number of channels:  $M \leq N$  [19]. In the ICA algorithm, the number of sources by default is set to be the number of channels (time points in case of spatial ICA and voxel number in case of temporal ICA). The source numbers are usually very large and can increase the computational complexity and lead to unstable solution [21]. One way to solve this problem is to estimate the number of sources (or model order) using the probability PCA such as Bayesian information criterion (BIC) [34].

In this chapter, we used PCA to estimate the number of the sources ( $M$ ) in the data based on the eigen decomposition of the covariance matrix of the data. The number of components is estimated to maintain >95% of non-zero eigenvalues [33] to contain a majority of data information. After PCA preprocessing, the data that maintain the first  $M$  largest components were used for the spatial ICA decomposition using the ICA INFORMAX software [35]. The unmixing matrix and independent components are obtained as the output.

Three features are extracted for each independent component (IC) in order to select the artifacts components: (1) Spatial ICA map obtained by superimposing activated voxels on the anatomy for the  $i$ th IC,  $S_i$ ,  $i = 1, 2, \dots, 30$ . Each IC is scaled by the variance after removing mean:  $Z_{ij} = \frac{S_{ij} - m_i}{\sigma_i}$ ,  $i = 1, 2, \dots, 30$ ;  $j = 1, 2, \dots, 480$ . The active voxels are selected such that  $|Z| \geq 1.96$  corresponds to statistical  $p = 0.05$ . (2) The associated time course of the spatial IC. Based on Eq. (9), the contribution of the  $i$ th IC to the original data is the  $i$ th column of the mixing matrix  $W^{-1}(:, i)$ .  $W^{-1}(:, i)$  is called the associated time course for the  $i$ th IC, and it reflects the temporal pattern of this source. The correlation coefficient (CC) and the statistical P-value between the associated time course of sources and the single-shifted reference function are also calculated. (3) The power spectrum density (PSD) function for the associated time course for the  $i$ th component with sampling frequency  $f = 1/TR = 3.64$  Hz.

To clean the data, the noise independent components are removed by setting the associated columns of the noise components in the mixing matrix to be zero. Data are reconstructed from the possible signal components as shown in Eq. (10)

$$X_{V \times N} = W^{-1}_{V \times M} \cdot S_{M \times N} \Rightarrow \tilde{X}_i = \sum_{m=1}^M \tilde{W}^{-1}_{im} \cdot S_i, \quad i = 1, 2, \dots, V \quad (10)$$

$$\tilde{W}^{-1}(:,j) = 0, \quad \text{if } j \in \text{noise}; \quad \tilde{W}^{-1}(:,k) = W^{-1}(:,k), \quad \text{otherwise}$$

### 3. Results and discussion

#### 3.1 Microvasculature estimation before ICA cleaning

Microvasculature estimation based on the methods described was applied to the original data and the data after ICA cleaning. The histogram of voxels was detected as a function of latency in steps of TR = 275 ms for the single component (**Figure 1**). The histogram was fitted by a Gaussian distribution with the estimated mean and standard deviation. Since pixels containing mostly microvasculature would have a shorter latency among all detected voxels, the time separation from the peak of the Gaussian to its baseline on the left side would be a reasonable estimate of the time separation between the micro- and macrocomponents. The peak level was 22 (number of pixels) and Gaussian baseline is chosen at 10% of peak level which was 2.2. These correspond to indexes of 20 and 12, respectively, in units of TR. Therefore, a separation of  $8 \cdot \text{TR} = 2.2$  s was selected between the components of the two-component model.

**Figure 2** shows the histogram of dual-component models using separation time = 2.2 s. The histogram is a combination of two Gaussian distributions. The latency boundary of micro- and macrovascular classes is chosen based on the separation between two classes. The vertical line at  $\sim 15$  shows the separation boundary (**Figure 2**).

**Figure 3a** shows the voxels (numbering 34) localized from fitting indexes 2–15 with earlier latency (latency up to 15, **Figure 2**) and has >50% fractional

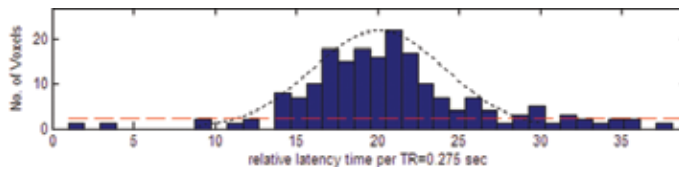


**Figure 1.** Histogram showing the number of voxels as a function of latency (each point in X-axis is 275-ms unit) for best fitting time of a one-component model.

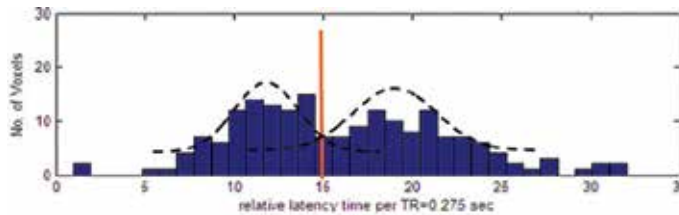


**Figure 2.** Histogram showing the number of voxels as a function of latency for best fitting time for a dual-component model.

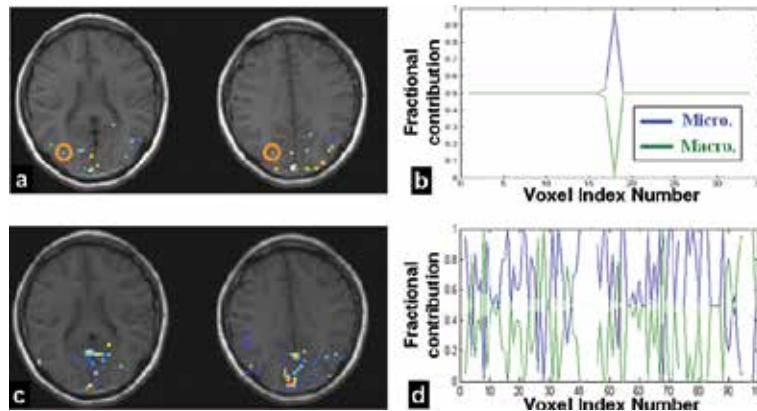


**Figure 3.** Results of mixture model for microvasculature estimation. (a) Voxels corresponding to indexes up to 15 in **Figure 2**, (b) Fractional contributions from microvasculature (blue line) and macro-vasculature (green line). (c) Voxels corresponding to indexes after 15 in **Figure 2**. (d) Fractional contributions from two components in the macrovasculature.

contribution from the earlier component. These voxels are likely to contain a microvasculature component. The relative fractional contribution of these components in the 34 voxels is shown in **Figure 3b**. **Figure 3c** shows the distribution of voxels indexed with a high latency (after 15 shown in **Figure 2**) likely to be veins. The relative contributions of the two components in these voxels are plotted in **Figure 3d**. In **Figure 3c**, a large vein structure can be seen that may contain a mixture of two macrovasculature components. In **Figure 3a**, the microvasculature estimated in the V5 region (marked by circle) is in gray matter, though a couple of pixels are likely to be macrovasculature and thus contain two vascular components as shown in **Figure 3b**. For macrovasculature voxels estimated in **Figure 3c**, since there might still be two vascular components (venules and veins) with different latencies, the fractional contributions shown in **Figure 3d** were not equally distributed as in **Figure 3b**.

### 3.2 Microvasculature estimation after ICA cleaning

To further improve the mixture model, ICA is used as a preprocessing operation for denoising. PCA was used to estimate the number of the sources, and the number of components was chosen to be 30 (**Figure 4**) that contains  $\geq 95\%$  data variation and information. After PCA preprocessing, the data that maintain the first 30 largest components were used for the spatial ICA decomposition using the ICA INFORMAX software.

**Figure 5** shows the features of a one-source component. The first row is the spatial map of the 15th IC. V1, V2, and V5, expected to be activated, can be seen in the spatial map. The second row is the associated time course and the averaged time courses of original data. The associated time course matches well with the averaged original time course. The correlation coefficient between the associated time course and the reference function is 0.4 with  $P < 0.0001$ . The third row is the PSD of the associated time course shown in the unit of Hz. Since the stimulus is presented every 20 s, the corresponding frequency is  $1/20 \text{ s} = 0.05 \text{ Hz}$ . The peak at 0.05 Hz can be seen in the PSD; however, there are also some large peaks around 0.1 Hz and lower frequencies that may come from the alias of the physiological noise. This component is mostly likely to be task-related based on the high CC of 0.4 and a distinct peak at 0.05 Hz in PSD. **Figures 6** and **7** show two examples of components

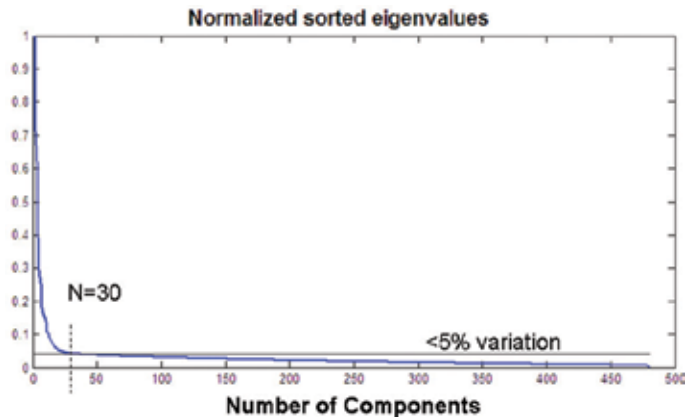


**Figure 4.** SVD decomposition of fMRI data. Cutoff horizontal line was chosen to discard less than 5% data variation with the corresponding number of components at 30.

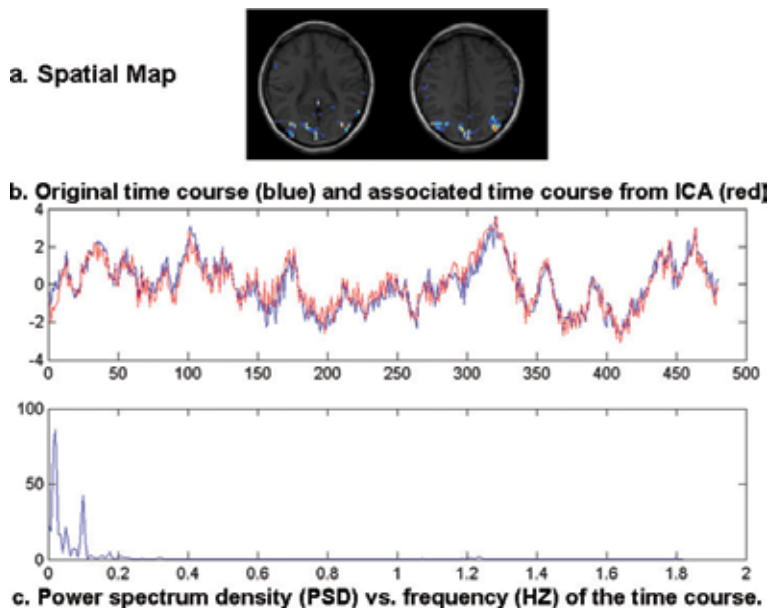


**Figure 5.** Representative result of one component from spatial ICA that is task related. (a) Spatial map of the 15th IC.  $V_1$ ,  $V_2$ , and  $V_5$ , expected to be activated, can be seen in the spatial map. (b) Associated time course (red) and the averaged time courses of original data (blue). The associated time course matches well with the averaged original time course. The correlation coefficient between the associated time course and the reference function is 0.4. (c) Power spectrum density (PSD) of the associated time course shown in the unit of Hz. Since the stimulus is presented every 20 s, the corresponding frequency is  $1/20 \text{ s} = 0.05 \text{ Hz}$  as seen with the large peak in the spectrum.

attributed to physiological noise. For instance, the source that is most likely from the heart-beating with a dominant peak in 1.2 Hz is shown in **Figure 6**, and the source that is from breathing and heart beating activation in the ventricles with distinct frequencies at 0.27 and 1.2 Hz as in **Figure 7**. **Figure 8** demonstrates an example of the motion artifact component. The associated time course shows a gradual drift along time. This component is likely to be movement-based low-frequency drift. The activations have a “ring-like” spatial distribution that is coming from head movement.



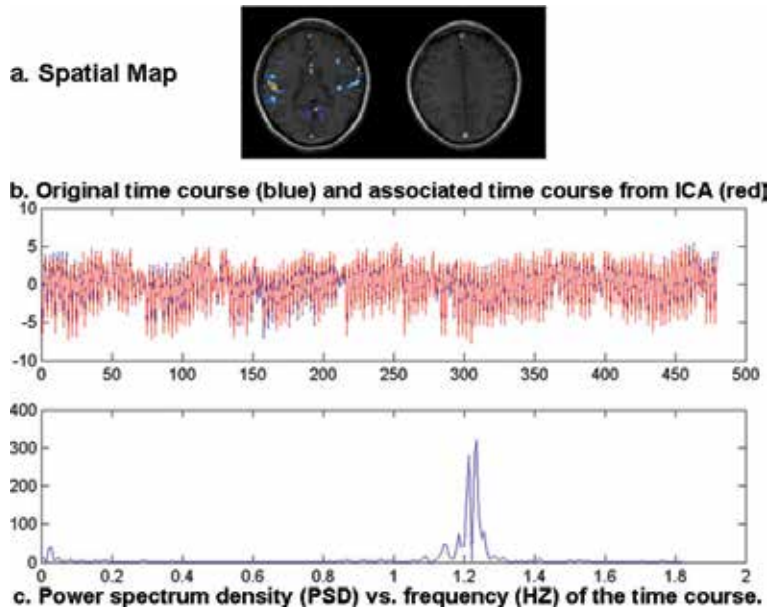


**Figure 6.**  
*One noisy component from heart beating.*

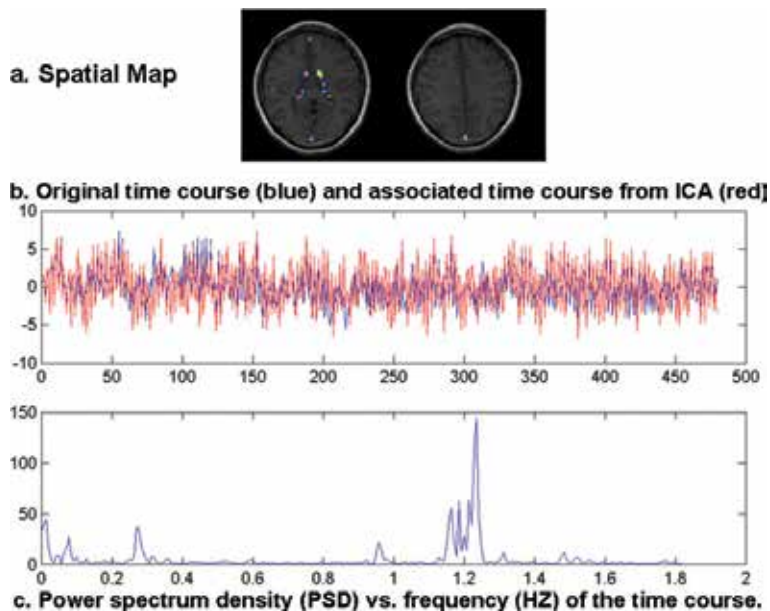


**Figure 7.**  
*Another noisy component from both breathing and heart beating with distinct frequencies at 0.27 (from breathing) and 1.2 Hz (from heart beating).*

Eight noise components were identified based on the three features, and data were reconstructed by removing these components. We applied both multi-component model and TICA to the original data and the data after ICA cleaning to the visual cortex. Dynamic mixture model was used to fit the data after ICA cleaning. The same time separation, 2.2 s, of “before ICA” was used for “after ICA” fitting.

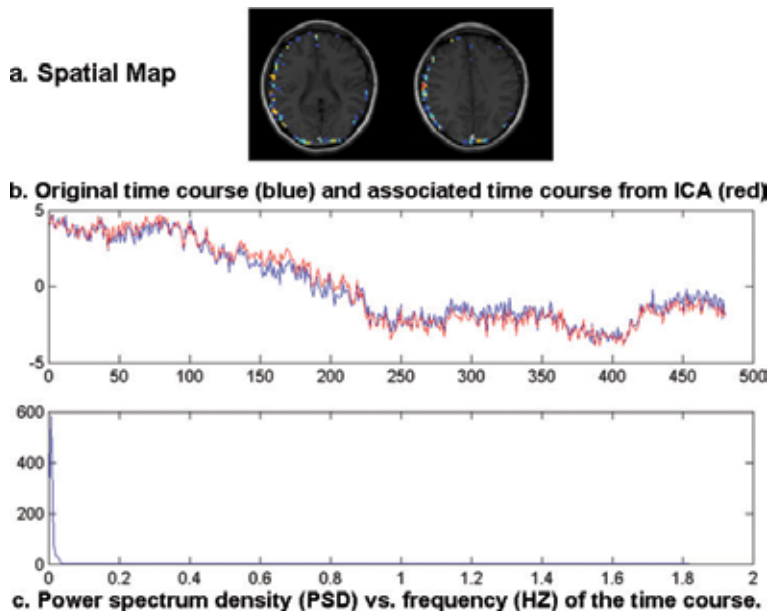


**Figure 8.**  
Result of motion artifact component from spatial ICA.

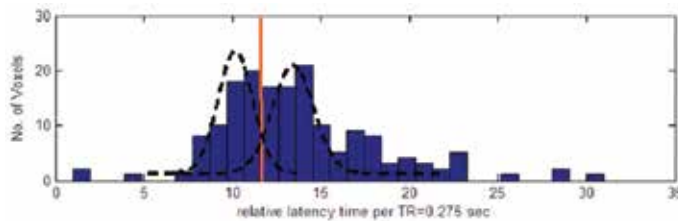


**Figure 9.**  
Histogram showing the number of voxels as a function of latency for best fitting time for a dual-component model after ICA cleaning.

**Figure 9** shows the histogram of a dual-component model using component separation time = 2.2 s after ICA cleaning. The separation of micro- and macrovascular classes was  $\sim 12$ . The shape of the Gaussian distribution is narrowed compared to **Figure 2** before ICA. This is because ICA has removed the noisy voxels and thus the distribution is less Gaussian.

**Figure 10a** shows the voxels (numbering 50) localized from low latency (up to 12, **Figure 4**) and has  $>50\%$  fractional contribution from the earlier component. These voxels are likely to contain a microvasculature component. **Figure 10b** shows the relative fractional contribution of these components. **Figure 10c** shows the distribution of voxels indexed with a high latency (after 12 in **Figure 9**) likely to be veins. The relative contributions of two components in these later voxels are plotted in **Figure 10d**.

### 3.3 Comparison of results before and after spatial ICA

The average correlation coefficient for the fitting after ICA cleaning has increased around 70% compared to the original fitting (**Figure 11**). The number of voxels at an earlier latency (up to 15 in **Figure 2** and up to 12 in **Figure 9**) also increased. The number of voxels that are most likely to be microvasculature has

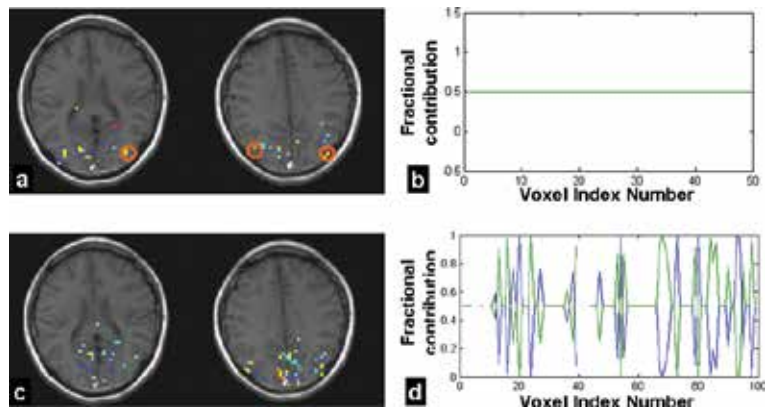


**Figure 10.** Results of microvasculature estimation after ICA cleaning. (a) Voxels corresponding to indexes up to 13 in Figure 9. (b) Fractional contributions from micro- and macrovasculature. (c) Voxels corresponding to indexes after 13 in Figure 9. (d) Fractional contributions from two components in the macrovasculature.

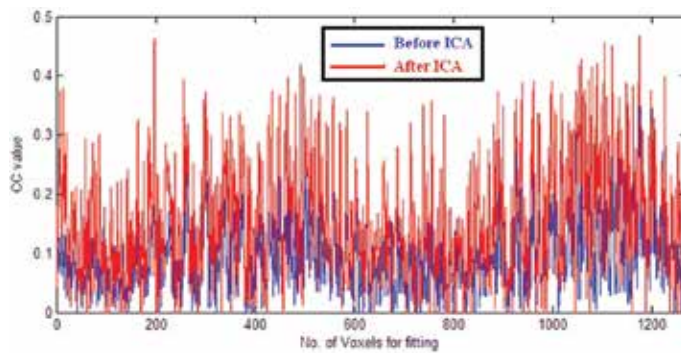


**Figure 11.** Correlation coefficient (CC) before ICA (blue) and after ICA (red). Average CC of all voxels improved 70% after ICA compared to original fitting without ICA denoising.

increased from 34 to 50 (~50%) after ICA. The regions marked by a circle in Figure 10 identified microvasculature in V5 region on the left side which was missed by the estimation before ICA.

For all the estimated microvasculature, the fractional contribution coefficients of two components after ICA (Figure 10b) are the same, suggesting all the voxels are in the microvasculature. The fractional contribution coefficients of two components in the macrovasculature are different with venules and veins.

### 3.4 Comparison microvasculature estimation with temporal ICA

We have implemented further temporal ICA to the data after spatial ICA cleaning in the cluster that has a higher correlation ( $\geq 0.3$ ) to the reference function. The assumption is that the concurrent active voxels may still be mixed with different types of temporally independent components.

The number of components was set to be 10 based on the PCA of the cleaned data within the activated cluster. There is an associated spatial map for each temporal component that reflects the spatial contribution of the component. The spatial map of each temporal IC is shown in Figure 12. Compared to the micro and macrovasculature images, temporal IC #9 and IC #1 in Figure 12 have activation patterns similar to the macrovasculature image in Figure 10c, while the spatial map

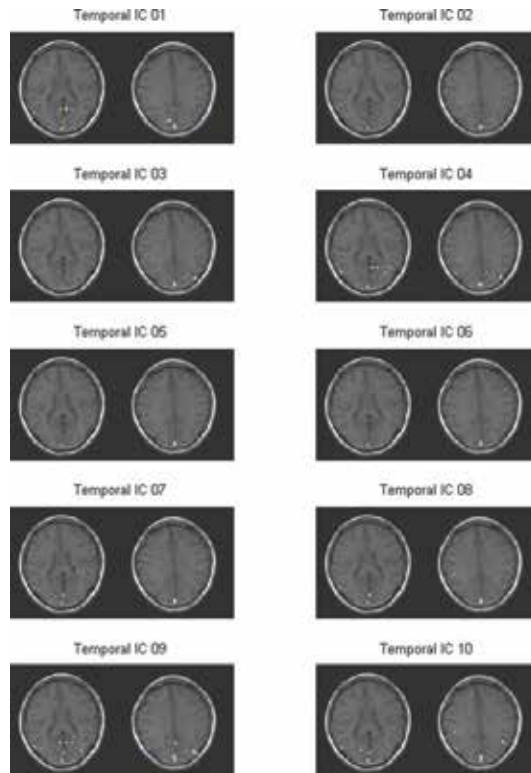


**Figure 12.**  
*Ten associated maps of temporal independent components (IC) identified by TICA.*

of temporal IC #10 and IC #4 has similar distributions with the microvasculature image in **Figure 10a**.

### 3.5 Discussion

We have described a novel multiple-component model that takes into consideration vascular mixtures in the fMRI BOLD signal and partial volume effect and developed methods to estimate the contribution of each component. Experimental studies have shown that compared to the traditional single-component model, our method achieves a better match to the original time courses of fMRI and thus reduces the fitting errors. Another advantage of the method is that it allows us to estimate microvasculature. The microvasculature is closer to the site of neuronal activation and validated with the temporal ICA method, as expected [36]. Spatial ICA has been used as a preprocessing step in the mixture model to remove noise and improve the microvasculature detection with a higher CC and more voxels with lower latencies detected. The spatial and temporal distributions of all these noisy components were consistent with the results of other studies [32, 34, 37].

We use a series of reference functions to model the brain vascular components. Compared to the classical single-component model, the multi-component model fits the measured fMRI time course with a higher correlation coefficient and also detects voxels with low latencies more efficiently. Different vascular components will have different HRF shapes. Therefore, how the brain vascular components can be modeled more accurately needs to be investigated in the future. Also, the multiple reference functions are not orthogonal to each other; some de-correlation methods can be further implemented to improve the robustness of the fitting.

Temporal ICA decomposition in the activated regions could overcome these problems with good spatial correspondence results between temporal ICA and mixture models. One limitation is that temporal independent assumption might not be fully satisfied in fMRI data since hemodynamic responses evolve with time [29].

#### **4. Conclusion**

In conclusion, we had used two new methods (i.e., ICA and dynamic mixture model) to improve microvasculature detection in fMRI that is closer to true neuronal activation and therefore improve the specificity of the fMRI microvasculature detection in both functional and structural ways [38]. Further integration and validation with other modalities such as EEG and PET are warranted in the near future. Further imaging of the full dynamic spatiotemporal multi-parametric functional and neurophysiological profile including BOLD microvasculature activation, couplings between BOLD and CBF/CBV, between BOLD, and oxygen extraction/metabolism [39] are expected in the near future [40].

#### **Acknowledgements**

The authors thank Dr. Singh and colleagues for their help on this work.

#### **Author details**

Yongxia Zhou

Departments of Radiology and Biomedical Engineering, University of Southern California and Columbia University, Los Angeles, CA, USA

Address all correspondence to: [yongxia.zhou@yahoo.com](mailto:yongxia.zhou@yahoo.com)

#### **IntechOpen**

---

© 2019 The Author(s). Licensee IntechOpen. This chapter is distributed under the terms of the Creative Commons Attribution License (<http://creativecommons.org/licenses/by/3.0>), which permits unrestricted use, distribution, and reproduction in any medium, provided the original work is properly cited. 

## References

- [1] Bandettini PA, Jesmanowicz A, Wong EC, Hyde JS. Processing strategies for time-course data sets in functional MRI of the human brain. *Magnetic Resonance in Medicine*. 1993; **30**:161-173
- [2] Arthurs OJ, Boniface S. How well do we understand the neural origins of the fMRI BOLD signal? *Trends in Neurosciences*. 2002; **25**(1):27-30
- [3] Devor A, Dunn AK, Andermann ML, Ulbert I, Boas DA, Dale AM. Coupling of total hemoglobin concentration, oxygenation and neural activity in rat somatosensory cortex. *Neuron*. 2003; **39**: 353-359
- [4] Thompson JK, Peterson MR, Freeman RD. Single-neuron activity and tissue oxygenation in the cerebral cortex. *Science*. 2003; **299**:1070-1072
- [5] Logothetis NK, Pauls J, Augath M, Trinath T, Oeltermann A. Neurophysiological investigation of the basis of the fMRI signal. *Nature*. 2001; **412**:150-157
- [6] Singh M, Kim S, Kim TS. Correlation between BOLD-fMRI and EEG signal changes in response to visual stimulus frequency in humans. *Magnetic Resonance in Medicine*. 2003; **49**: 108-144
- [7] Singh M, Sungkarat W, Jeong J, Zhou Y. Extraction of temporal information in functional MRI. *IEEE Transactions on Nuclear Science*. 2003; **49**(5):2284-2290
- [8] Gati JS, Menon RS, Ugurbil K, Rutt BK. Experimental determination of the BOLD field strength dependence in vessels and tissue. *Magnetic Resonance in Medicine*. 1997; **38**:296-302
- [9] Menon RS, Gati JS, et al. Spatial and temporal resolution of functional magnetic resonance imaging. *Biochemistry and Cell Biology*. 1998; **76**: 560-571
- [10] Turner R. How much cortex can a vein drain? Downstream dilution of activation-related cerebral blood oxygenation changes. *NeuroImage*. 2002; **16**:1062-1067
- [11] Friston KJ, Williams S, Howard R, Frackowiak RSJ, Turner R. Movement related effects in fMRI time series. *Magnetic Resonance in Medicine*. 1996; **35**:346-355
- [12] Howseman A, Josephs O, Rees G, Friston KJ, Special Issues in Functional Magnetic Resonance Imaging. SPM Short Course Notes (9). Wellcome Department of Cognitive Neurology; 1997
- [13] Chen W, Ugurbil K. High spatial resolution functional magnetic resonance imaging at very-high-magnetic field. *Topics in Magnetic Resonance Imaging*. 1999; **10**(1):63-78
- [14] Duong TQ, Yacoub E, et al. High-resolution, spin-echo BOLD, and CBF fMRI at 4 and 7T. *Magnetic Resonance in Medicine*. 2002; **48**(4):589-593
- [15] Ernst T, Hennig J. Observation of a fast response in functional MR. *Magnetic Resonance in Medicine*. 1994; **32**:146-149
- [16] Hu X, Lee T, Ugurbil K. Evaluation of the early response in fMRI in individual subjects using short stimulus duration. *Magnetic Resonance in Medicine*. 1994; **37**:877-884
- [17] Singh M, Patel P, Khosla D, Kim T. Segmentation of functional MRI by K-means clustering. *IEEE Transactions on Nuclear Science*. 1996; **43**(3):290-301

- [18] Menon RS. Postacquisition suppression of large-vessel BOLD signals in high-resolution fMRI. *Magnetic Resonance in Medicine*. 2002; **47**:1-9
- [19] McKeown MJ, Makeig S, Brown GB, Jung TB, Kindermann SS, Bell AJ, Sejnowski TJ. Analysis of fMRI data by blind separation into independent spatial components. *Human Brain Mapping*. 1998; **6**:160-188
- [20] Lee TW, Girolami M, Sejnowski TJ. Independent component analysis using an extended infomax algorithm for mixed sub-gaussian and super-gaussian sources. *Neural Computation*. 1999; **11**(2):417-441
- [21] Jeong J. Localization of brain alpha activity using independent component analysis in fMRI and EEG, Doctor of Philosophy Dissertation. USC; 2002
- [22] McKeown MJ, Hansen LK, Sejnowski TJ. Independent component analysis of functional MRI: What is signal and what is noise? *Current Opinion in Neurobiology*. 2003; **13**(5): 620-629
- [23] Calhoun V, Adali T, Hansen LK, Larsen J, Pekar J. ICA of functional MRI data: An overview. *Fourth International Symposium on Independent Component Analysis and Blind Source Separation*. 2003;281-288
- [24] Friman O, Borga M, et al. Detection of neural activity in fmri using maximum correlation modeling. *NeuroImage*. 2002; **15**:386-395
- [25] Zhou Y, Singh M, TS K, Sungkarat W. Dynamic Multiple-Component Model Applied to fMRI Data Analysis. *International Society for Magnetic Resonance in Medicine*; 2003
- [26] Singh M, Zhou Y, Sungkarat W, Kim TS. Hemodynamic response based mixture model to estimate micro- and macro-vasculature contributions in functional MRI. *IEEE Nuclear Science Symposium Conference Record*. 2004; **4**: 2473-2475
- [27] Keshava N, Mustard JF. Spectral unmixing. *IEEE Signal Processing Magazine*. 2002; **(1)**:44-57
- [28] Friston KJ, Holmes AP, Worsley KJ, Poline JP, Frith CD, Frackowiak RSJ. Statistical parametric maps in functional imaging: A general linear approach. *Human Brain Mapping*. 1995; **2**:189-210
- [29] Henson RNA, Price CJ, Rugg MD, Turner R, Friston KJ. Detecting latency differences in event-related BOLD responses: Application to words versus nonwords and initial versus repeated face presentations. *NeuroImage*. 2002; **15**:83-97
- [30] Liao CH, Worsley K, Poline JB, Aston JAD, Duncan GH, Evans AC. Estimating the delay of the response in fMRI data. *NeuroImage*. 2002; **16**: 593-606
- [31] Glover H. Deconvolution of impulse response in event-related BOLD fMRI. *NeuroImage*. 1999; **9**:416-429
- [32] Biswal BB, Ulmer JL. Blind source separation of multiple signal sources of fMRI data sets using independent component analysis. *Journal of Computer Assisted Tomography*. 1999; **23**(2):265-271
- [33] Seifritz E, Esposito F, Hennel F, Mustovic H, Neuhoff JG, Bilecen D, Tedeschi G, Scheffler K, Di Salle F. Spatiotemporal pattern of neural processing in the human auditory cortex. *Science*. 2002; **297**(5587): 1706-1708
- [34] Beckmann M, Smith SM. Probabilistic independent component analysis for functional magnetic

resonance imaging. IEEE Transactions on Medical Imaging. 2004;**23**(2):137-152

[35] Bell AJ, Sejnowski TJ. An information maximisation approach to blind separation and blind deconvolution. Neural Computation. 1995;**7**(6):1129-1159

[36] Kim TS, Zhou Y, Kim S, Singh M. EEG distributed source imaging with a realistic finite-element head model. IEEE Transactions on Nuclear Science. 2002;**49**(3):745-752

[37] Makeig S, Westerfield M, Jung TP, Enghoff S, Townsend J, Courchesne E, Sejnowski TJ. Dynamic brain sources of visual evoked responses. Science. 2002; **295**(5555):690-694

[38] Neeman M, Dafni H. Structural, functional, and molecular MR imaging of the Microvasculature. Annual Review of Biomedical Engineering. 2003;**5**:29-56

[39] Fox PT, Raichle ME. Focal physiological uncoupling of cerebral blood flow and oxidative metabolism during somatosensory stimulation in human subjects. Proceeding of National Academic Science. 1986;**83**:1140-1144

[40] Zhou Y, Functional Neuroimaging Methods and Frontiers. Nova Science Publishers. 2018





## Section 2

# Functional Brain Imaging





# Simultaneous Smelling an Incense Outdoor and Putting the Hands Together Activate Specific Brain Areas

*Mitsuo Tonoike and Takuto Hayashi*

## Abstract

Mirror neurons are involved in imitation of habitual behaviors. To increase understanding of the theory of mirror neurons and the default mode network, brain activation was explored in 11 healthy adult volunteers who did or did not have a habit of putting their hands together as if praying. Magnetoencephalography (MEG) data were recorded while the participants simultaneously smelled an odor in two kinds of incenses outdoor and/or while they moved to putting their hands together. A magnetoencephalographic contour map of the recorded findings was drawn and an estimated current dipole (ECD) was set. Regardless of a habit of putting their hands together or not, the inner lobe of the frontal area, anterior area in the temporal lobe, and F5 language area in the left frontal lobe and so on were specifically activated. We used cortisol value as an index of the stress state measured in every state (before and after smelling two different incenses outdoor). These experiments suggest that simultaneous smelling an incense outdoor and the behavior of putting their hands together increased the activity of these specific areas in the human brain due to mutual interactions and enhanced interactions.

**Keywords:** incense outdoor, putting the hands together, habit/no habit, MEG, F5 language area, mirror neuron, default mode network

## 1. Introduction

In the olfactory neural processing in humans, evoked magnetic fields by odorant synchronized with respiration and sniffing odors are found in orbito-frontal cortex (OFC) and inferior temporal lobe [1–6]. On the other hand, mirror neurons in the brain are known to activate the inner prefrontal lobe and F5 area which have the function of imitation of behavior in daily life [7–9]. Therefore, mirror neurons are considered to have the function for imitation of habit [10–12]. Super mirror neurons are concerned with determination of values, recognition of oneself and others, and reward from one's work. The inner default mode network controls the fundamental activity of daily movements and the resting state of the human brain [13–15]. Because this default mode network is strongly related to super mirror neurons, discrimination of oneself from others and the determination of social

cognition are considered important in human daily life [16, 17]. The purpose of this study is to clarify that simultaneous smelling an incense outdoor and putting the hands together activate the human brain and to show where specific areas are activated.

## **2. Materials and methods**

### **2.1 Incense sticks**

In this MEG experiment, two types of incense sticks (A: SEIUN-Violet Smokeless, and B: MAINICHI-Kou Sandalwood), which are produced by Nippon Kodo Co. Ltd. in Japan, were used as odors.

### **2.2 Subjects**

Eleven Japanese volunteer subjects (six males, five females) between the ages of 22 and 58 years (mean age  $41 \pm 11$  years) without significant smell loss or a neurologic history participated. All subjects were right-handed and were given the informed consent in accordance with guidelines set by the ethical committee on human studies in both Aino University and the Kansai center in AIST in Japan.

#### *2.2.1 Preparation of subjects*

All subjects used non-magnetic clothes, and answered no problem for the questionnaire to exclude metal artifacts. Before the MEG experiments, an individual subject was shown the essence of instructions and possible debriefing for the experiments.

All subjects were given informed consent in accordance with the acceptance for measuring MEG and individual anatomical MRI for each individual brain structure to the experiments.

Participants were requested in seated during MEG experiments, and the head of the participant was positioned in the MEG helmet under the gantry of MEG system in the magnetically shielded room.

Ten of these volunteers (except for one male) were separated into two groups, the A-group, which included individuals with a habit of putting their hands together in their daily life (similar to praying), and the B-group, which included individuals who are not in the habit of putting their hands together or who do not pray.

One person was not included in either group, because he had experience putting his hands together and sometimes prayed. In this MEG experiment, he did not use a burning incense stick and instead directly sniffed his hands, which were painted with a liquid odorant containing the same ingredients as the incense stick.

### **2.3 Experimental design**

#### *2.3.1 MEG system*

This MEG system is Neuro-magnetometer with 122 channel DC-SQUID sensors, whole-cortex type system (Neuromag-122™, Electa Co. Ltd., made in Finland).

SQUID sensor is planner DC-SQUID type. Inner helmet of the head, at the 62 points which were selected around the whole head two the first derivative DC-SQUID sensors were located individually (so, the number of total sensors are  $122 = 62 \times 2$ ). This system's version of the acquisition software is

Neuromag-Aquis122-Ver.3. Sampling frequency was used Max 600 Hz, with an analog pass-band filter of 0.01–200 Hz for acquisition filters.

As the location of the head relative to MEG sensors differ across participants, projection onto a common source space would address this issue through well-established techniques for spatial normalization [18], although realignment of the data could also be done in sensor space [19–21].

### 2.3.2 MRI system

This MRI system is 0.4T Hitachi open type MRI system (AIRIS-Light MRI system: permanent magnetic type, made in Hitachi Co. Ltd. in Japan).

1. *EOG/ECG/EMG*: EOG/ECG/EMG were measured to test for subject's seating state on the chair in MEG system before the experiments, however these data were not used in MEG experiments because no artifacts and no noise for MEG data.
2. *Head shape system*: this MEG system used Head Position Indicator (HPI) for the digital value of the own head shape for individual subjects.
3. *Head movements*: head movements of MEG were recorded continuously by using advanced HPI system, and the head movement compensation algorithm was applied [22]. The difference of between head positions before and after the run of MEG was recorrected.
4. *Position of participants*: participants were in seated in MEG experiments, and the head of the participant was positioned in the MEG helmet under the gantry of MEG system in the magnetic shielded room.
5. *External stimulation and recording devices*: this MEG system has photodiode devices to determine visual stimulus onset with respect to MEG trigger, and MEG has delays of a few msec. MEG data were corrected for these delays.
6. *Coregistration*: this MEG system has the following coregistration procedure. Anatomical MRIs were used individually to apply to individual own MEG data only by oneself. The method section is described for the preprocessing of the MEG study as the following, and the order of these preprocessing steps were carried out.
7. *Bad MEG sensors*: in this MEG system there are sometimes a few bad MEG sensors. This MEG system has tuning program for all 122 sensor's tune, and after tuning processing a few bad sensors were found, and a few bad sensors were excluded during acquisition or analysis. The signals of bad sensors were interpolated to the signal estimation by using signal estimation software.
8. *Filtering processing*: in this MEG experiments we applied the following filtering. We used the digital band-pass filtering (0.3–40 Hz) the second order forward butterworth filtering with the windows algorithms.
9. *IAC algorithms*: ICA program was applied to input data of MEG. The number of components was five for the estimation. Criteria of ICA estimation on the total five components for selecting are determined to 85% to all components of data.

10. *Trials and segments*: trials and segments were anyways applied to reject under the criteria when the external bigger noises mix the income to the MEG data and the subject's unforecasted artifacts of movements.

In this MEG experiment, each subject's head was placed in a helmet with whole-cortex type SQUID sensors (Neuromag-122™, Electa Co. Ltd.). Three-dimensional orthogonal coordinates were determined in the helmet of the neuromagnetometer. Experiments were performed in the Kansai Center in Ikeda city, National Institute of Advanced Industrial Science and Technology (AIST) in Japan.

An incense outdoor was freely presented to the subject by means of a burning incense stick on a holder that was naturally held in front of the subject while seated in a chair in a magnetically shielded room.

### *2.3.3 Experiments of the stress state using subject's saliva*

In these experiments, magnetoencephalography (MEG) was performed, and the cortisol value in the subject's saliva was measured in every state (before and after smelling two different incense outdoors (A and B)).

## **2.4 MEG experiments for four mode state**

MEG response data were measured at the following four mode states, (1): control mode, (2): simple mode of putting the hands together, (3): smelling mode with putting the hands together, (4): only smelling mode. MEG data were added with 100 times averaging with the random sampling method. The subject pushed an optical sensor button with his or her own thumb.

1. In the control mode, the subject sat quietly and naturally in a chair with his or her eyes open and freely pushed the button of the optical fiber sensor at random times with the right thumb in synchronization with active inspiration (i.e., sniffing with the nose) of his or her own respiration rate, and the average MEG brain waves were obtained from raw data collected about 100 times in the control state [23].
2. For the next mode, the simple mode for the behavior of putting the hands together was performed as the experimental task, regardless of whether the subject did or did not have the habit of putting his or her hands together or praying in daily life. During this simple mode of putting the hands together, the subject held the optical sensor between the hands and pushed the button with the right thumb at random times while putting the hands together.

By using the above two modes, we tried to measure the subject's own singular characteristic active area on the control state and to obtain the brain area activated by putting the hand together and we have examined to compare how the brain activity is different for the habit and no habit behavior of putting the hand together in daily life.

3. In the next mode that included smelling and putting the hands together, we measured the MEG response of both brain activities: smelling the odor in synchronization with active inspiration (i.e., sniffing and smelling the incense odor) and the behavior of putting the hands together [6].
4. In the last smelling mode, when the subject smelled only the incense odor without putting the hands together, the averaged MEG response was measured by adding the raw MEG data collected about 100 times by pushing the optical sensor button.

Both the control mode and simple mode of putting the hands together were recorded in the absence of the burning incense odor. After one incense odor was tested, the room air including the odor in the magnetically shielded room was exchanged completely with fresh air by using a large fan for about 10 minutes.

## 2.5 MEG and data analysis

For the purpose of observing brain activity with greater accuracy, we used a whole-head 122-sensor neuromagnetometer (a DC-SQUID device of the first order differential planar type, by Neuromag, Finland). With an attached digital band filter capable of passing only measurements in the bandwidths of 0.3–40 Hz, only valid readings were collected at an actual sampling rate of 400 Hz and converted into digital values. To observe brain functions in several experimental modes, we used a whole-head type DC-SQUID, which allowed us to detect cortical current directly and to monitor brain activities [24]. This detection method is called MEG. The analog readings detected in this manner of the brain magnetic field were digitized at a sampling rate of 400 Hz with an A/D converter, downloaded, and stored in a PC.

### 2.5.1 122-channel neuromagnetometer of the Planar Type Gradiometer

The 122-channel neuromagnetometer of the Planar Type Gradiometer can calculate the first derivative of the magnetic vector field  $B_z$  through individual SQUID sensors installed on the helmet, or it can calculate  $\{(\partial B_z/\partial x)_i, (\partial B_z/\partial y)_i\}$  about SQUID sensor  $i$ . Its dimension is  $fT/cm \sqrt{Hz}$ . The x- and y-axes represent the directions of longitude and latitude, respectively. A total of 122 sensor elements on the helmet were paired with the x- and y-axes, and each pair was assigned to measure one part of the head surface. A total of 61 sets (122 data points total) of magnetic field data can be detected, recorded at a particular interval ( $j$ ), and calculated using the formula  $\{(\partial B_z/\partial x)_{i,j}, (\partial B_z/\partial y)_{i,j}, (i = 1, 2, \dots, t; j = 1, 2, \dots, t)\}$ .

The advantage of planar gradiometer is the ability to manufacture them using standard thin-film techniques developed for the semiconductor this can reduce manufacturing costs and increase the precision with which the coils can be made since slight imperfections in the size or orientation of the two loops can reduce their ability to perfectly reject the zero-order field.

### 2.5.2 Signal Space Separation (SSS) system

Signal processing method for noise reduction to this MEG system is Signal Space Separation (SSS) which reduces environmental noise [25]. This method mathematically decomposes the magnetic field recorded from a spherically distributed array of sensors into a series expansion composed of internal and external terms that represent the proportion of the measured fields arising from inside and outside the sphere, respectively. The measured signal is reconstructed using only the internal terms to discard the environmental noise [19, 20].

### 2.5.3 Source reconstruction

In general, we use the volume conductor model of the subject's head (e.g., Sphere model, BEM, FEM) individually and the lead fields algorithms for magnetic fields [26]. Normalization procedure was also used for spatial normalization after source localization by using SPM-12 of MRI software. The coordinates of subject's brain are linked to individual subject's brain structures using the source of the lookup table (e.g., FSL atlas).

#### 2.5.4 Dipole fitting

The solutions obtained with dipole fitting approaches depend heavily on the choice that is made by the researcher. Therefore, this choice must be selected in with no intention. The reported solution for dipoles was chosen over a few alternative models. And the minimum current estimation method was used in our dipole fitting to MEG [27]. For example, the choices have to be made about the number of dipoles, time windows (single latency, multiple latencies), exact dipole models (moving, rotating, fixed dipole) for this process are shown as the following [28–32] and the fitting of the best cost function for the stability of solution [28, 33].

#### 2.5.5 Single current dipole tracing method (single sphere model)

The single current dipole tracing method is a common technique for estimating a single source of magnetic field distribution that emerges on the head surface (on the outer surface of the helmet). Given the hypothesis that the brain magnetic field is not distorted, we surmised that the influence of the distribution current (the so-called “volume current”) is balanced by spatial symmetry and that the first order approximation of reading values is not affected, based on Biot-Savart’s law. If these presumptions are valid, an equivalent current dipole, as displayed in three-dimensional vectors, should emerge in the brains.

A critical step in the use of the single sphere model is the choice of the sphere center. The flow of volume currents would be most influenced by the boundary with the largest change in conductivity, the highly resistive inner skull surface is thought to be the optimal choice for defining the sphere surface. A best-fit sphere superimposed on an individual’s structural MRI scan and obtained from performing a least-squares minimization. We can achieve a relatively good fit of a sphere to the superior and lateral aspects of the inner skull, suggesting that a single sphere model is well justified for modeling sources in the central and lateral portions of the brain.

Still, for more nonspherical portions of intracranial space, such as near the inferior frontal and temporal regions, large deviations from sphericity can introduce errors into solutions [34–36]. The distortion of volume currents should be taken in consideration. A variant of the spherical head model that is widely used in clinical MEG applications is the model of local or overlapping spheres. Instead of using a single sphere model, spheres of different curvature are fit to the various areas of the skull underlying each MEG sensor. The individual sphere centers are then used in the forward model to better model local distortions in the volume currents based on the assumption that the local curvature influences the volume currents for nearby sensors more than for distant sensors.

The current dipole can be estimated by solving the inverse problem of the magnetic field distribution as projected on the head surface. For estimation, we first drew a magnetic field contour map in reference to the measured values of  $(\partial B_z / \partial z)_{i,j}$  or in reference to the values of  $\{(\partial B_z / \partial x)_{i,j}$  and  $(\partial B_z / \partial y)_{i,j}\}$  with the inner estimation method. This magnetic field contour map allowed us to estimate a single source by following the least-squares estimation method. Using this method, the signal source can be defined as in the middle position of the extreme and the sink identified on the magnetic field. A single current dipole tracing method relies on the common notion that a higher parameter G value (goodness of fit: GOF) guarantees a higher accuracy in the least-squares estimation, and an estimated single source should therefore be closer to the actual value.



### *2.5.6 Evaluation method using statistical cost function (GOF)*

The statistical cost function measures the goodness of fit (GOF) between the magnetic field predicted by the dipole location and moment and the measured field. Typical statistical cost functions include the percent of variance unexplained (residual variance) or the corresponding chi-square statistic value [37, 38].

Most common approaches for MEG source estimation, and the dominated the field for many decades, is to specify only one or a few equivalent current dipoles (ECDs) to represent the solution. The strength (dipole moment) of ECDs ranges anywhere from  $10^{-9}$  to  $10^{-7}$  Am (or 1–100 nAm). The evoked magnetic responses, which have typical source moments ranging from 10 to 30 nAm, may involve the activation of less than 1 cm<sup>2</sup> of cortex and are therefore reasonably well modeled as a single ECD.

For highly dipolar field patterns with high SNR, such as the early components of sensory responses, ECD solutions can reach a greater than 90% goodness of fit, with good correspondence to the corresponding sensory projection areas of the brain.

### *2.5.7 Multi-current dipoles tracing method (multi source models)*

In general, the single current dipole tracing method is extremely useful if only one single cortical current is observed at a given instance as a result of brain activity. The method is not as valuable, however, if the entire brain is perceptively active and cortical current emerges at multiple points on the head surface. In such a case, use of the multi-current dipoles tracing method may provide a solution, as it presumes the appropriate number of dipoles likely to exist and estimates various current sources that may be occurring in the brain. Using this method, the parameter GOF becomes high only if the presumed number of dipoles is appropriate.

The ECD modeling approach was extended to more complex patterns of the brain activity by adding more dipole sources to the model. One solution is to keep adding dipoles until there is little or no improvement in the goodness of fit (GOF) measure or if the percent of variance obtained reaches a criterion. An alternative is to use an objective measure of signal complexity, such as the number of principal components requested to account for a criterion power.

To further stabilize the solutions, constraints can be applied (fixing the location of one source while allowing additional sources to have free parameters) such that very complex source models can sometimes be attained.

However, if it is not, the resulting estimate in the real clinical MEG is not close to the actual value. Because of the constraints in determining the propriety of the presumed number of dipoles and because of the subsequent, laborious calculations, the multi-current dipoles tracing method is usually deemed relatively unrealistic and impractical to the realistic clinical MEG.

### *2.5.8 Estimation of the current source by observing the magnetic field distribution*

Unlike an experimental observing the spontaneous control state, the task of smelling state and putting the hands together state were designed to activate brain.

As the current dipole method was not originally intended to detect such a spontaneous control state, and because dipoles of the magnetic field are expressed in rather complicated patterns by this method, we traced the variations of the magnetic field distribution by their progress over time, as well as at given intervals.

Drawing a contour map of the recorded findings, we identified extremes (maxima) and sinks (minima) found in pairs respectively on the magnetic field. We then set a virtual current vector in the middle position between each pair of extremes and sinks and traced the variations of the vector over time. Although this method has not been established for signal estimation and can only give approximations, no other available method seems more practical or acceptable for evaluation of the spontaneous control state, where neither the single dipole method nor the multi-dipole method is useful.

We observed a combination of extremes and sinks on the brain magnetic field contour map, vertically upward from the vertex. Extremes and sinks were aligned in such a way that their magnetic fields were tangential to each other. In between, the cortical current ran in the direction of the tangent vector in accordance with Biot-Savart's Law [39, 40].

We calculated the magnetic field contour map at a single time, with all three cortical currents in clear view. The test results were analyzed using the method of contrast between extreme and sink. The pattern recognition analysis of the inverse problem method is also available and more precise; however, this method was too time-consuming considering the number of cortical currents we needed to observe [41]. With respect to our test objective, we prioritized efficiency over numerical precision, which is normally preferred in localizing brain functional foci.

In order to reliable ECD fit, we must have fewer models. Another popular approach that has been used in MEG source modeling is the so-called "Spatiotemporal Dipole Fit" introduced Scherg and Von Cramon [38] in which the time-varying amplitude (time course) of each dipole is used as additional information to constrain the solutions.

### *2.5.9 Data acquisition, processing and analysis*

We traced the cortical current using the first-order differential planar type of DC-SQUID. This device enables us to detect the current source of brain activity directly under its sensor, revealing the maximum of the absolute values. This is the greatest advantage of using the differential planar type device, which has a dimension of  $fT/cm \sqrt{Hz}$ . When using neuromagnetometers of the axial type, as explained in Section 2.5.2 above (the single current dipole tracing method), we can estimate the current source as defined as the middle position between the minima and maxima of the cranial nerve magnetic field distribution [42].

Neuromagnetometers of the planar type are useful for determining where the current source of brain activity exists by detecting the maximum of absolute magnetic field values. We therefore used these readings to map the distributions of the cranial nerve magnetic field using MATLAB software, illustrating how the magnetic field varies over time [43]. Data acquisition began at the moment of the signal, although the data we actually used began 500 ms after the starting signal. Thus, we sampled the experimental activities of the brains. In the olfactory neural processing in humans, the responses of event related magnetic fields and evoked magnetic fields were obtained within about 250 ms in healthy subjects. In our MEG experiments, subjects sniff an incense odor actively by using his own nose and when starting to sniff he pushes the optical sensor button as a trigger signal. Therefore, to record the more precise changing of MEG we used the sampling interval with every 50 ms. So, measurements MEG responding data were analyzed by every 50 ms. By observing these cranial nerve magnetic field distributions on the surface of the head, we traced and recorded variations in the current source at each particular moment.

### 3. Results

#### 3.1 Result of signal source estimation of MEG in the brain obtained with the single current dipole tracing method

##### 3.1.1 Advantage of the real-time response of the brain's neural activities by analysis of millisecond-time resolution using the single current dipole tracing method of MEG

This single current dipole tracing method has the advantage of directly obtaining real-time responses of the brain's neural activities. This is different from fMRI and PET methods, which measure metabolism of physiologically active substances. We obtained changing activities of the signal source and estimated the active regions in the brain with analysis using the single current dipole tracing method. In single current dipole tracing method, the first main current dipole is the largest dipole. This current dipole was obtained in the middle position of extreme center and sink center identified on magnetic field. The second and the third current dipoles were smaller and weaker than the first main current dipole. Using this single current dipole tracing method, we can estimate only one current signal source (magnitude, direction, and location) as the most reliable neural activity in the brain.

##### 3.1.2 Mechanism of the real-time estimation method of the active area using the single current dipole tracing method of MEG data

**Figure 1** shows the real-time estimation method for obtaining the active area in the subject's brain. **Figure 1(a)** shows an example of a MEG response to random activities such as the control state before putting the hands together as assessed with the single current dipole tracing method. We could not obtain the dipole completely, and thus, we could not identify the generally active area in this control state (with no smelling odor and no putting the hands). **Figure 1(b)** shows contour mapping of MEG response at a control state.

**Figure 1(a)** shows over head vision, upper is anterior, lower is posterior of the head. Each curves show 122-channel MEG averaging response waves of duration 0.2 s time. A red vertical line shows starting time point for the inspiration of odorless air.

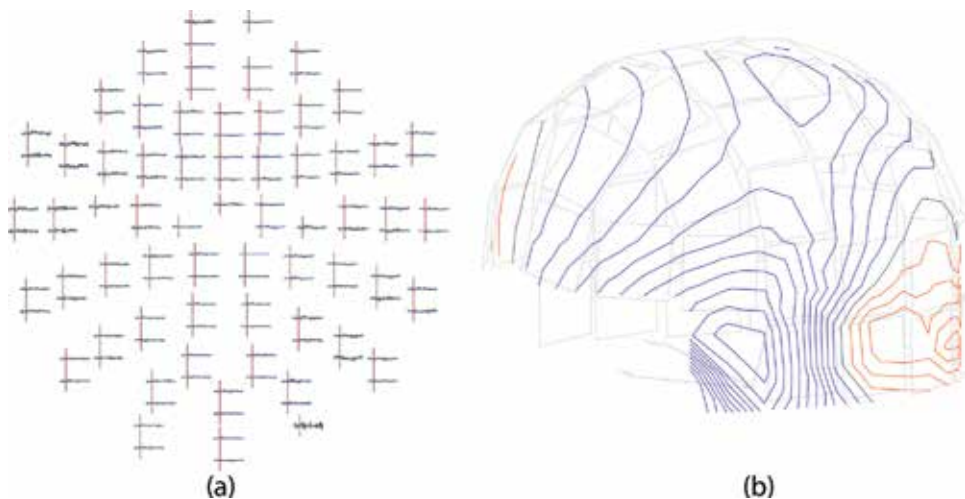


**Figure 1.**  
*Real-time active state at a control in our brain.*

**Figure 1(b)** shows the contour mapping of real time MEG response at a control state. We could not almost obtain a constricted dipole completely, then we could not find out the active brain area generally in this control state.

**(a) The simple mode of putting the hands together without smelling**

*3.1.3 The theory of mirror neurons and the default mode network*

In this experimental task, the subjects put their hands together or mimicked praying without smelling. We obtained the subject's type as an individual variation for the priority of brain laterality regarding putting the hands together or praying in daily life. **Figure 2** shows an example of the MEG response for the active area obtained with the single current dipole tracing method for this experimental condition. We analyzed estimated active areas continuously using a real-time estimation method. **Figure 2(b)** shows an MEG response on active area of left side brain as a left priority type after only putting the hands together (with no smelling odor). **Figure 2(c)** shows a vector of single current dipole estimated in the brain using 3-D coordinates.

**Figure 2(c)** shows a vector of single current dipole estimated in the brain using 3-D coordinates after putting the hands together. X-axis is the horizontal line of right to left ear, and Y-axis is the line from nasion toinion, and Z-axis is the upper to lower line of the vertical of the brain.

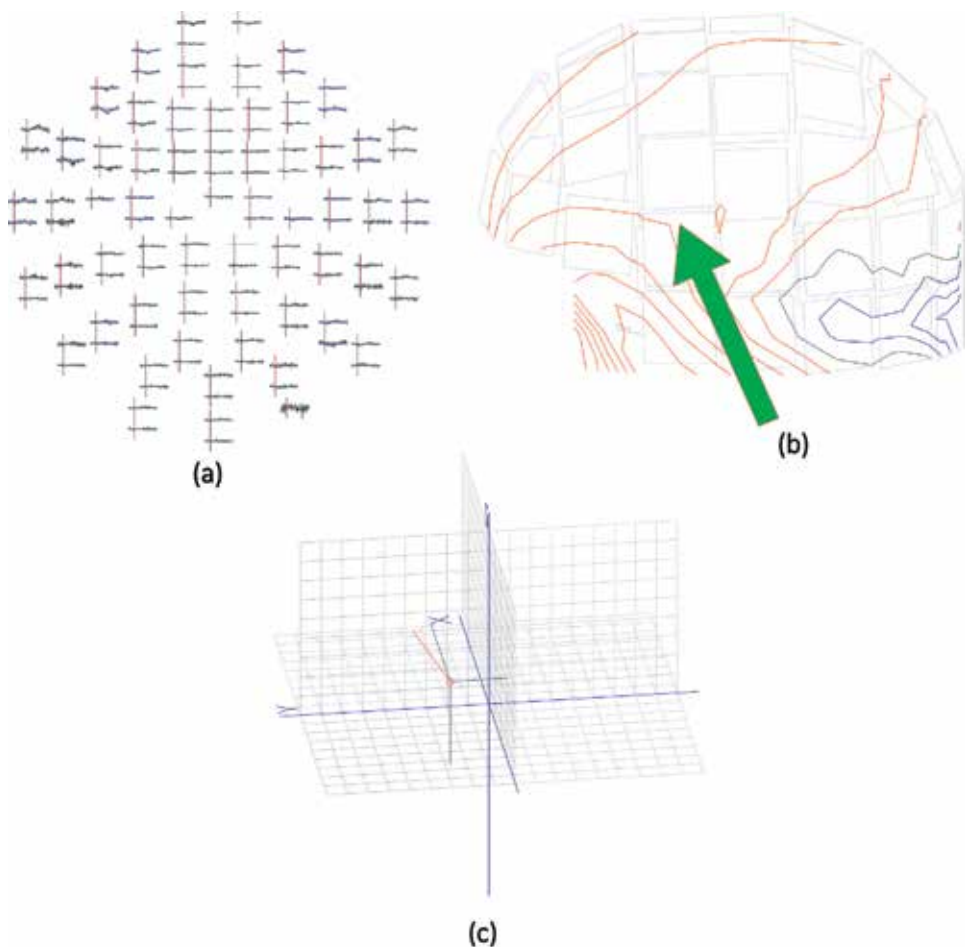


**Figure 2.**  
*Real-time estimation of the active area in our brain after only putting the hands together.*

**Table 1** shows an estimated ECD dipole each subjects for latency tie window (210–1100 ms), priority of the laterality (right or left), activated region, and GOF (statistical goodness of fit, %) for the simple mode of only putting the hands together without smelling.

*3.1.3.1 a-1. Right priority brain type*

Five of the 11 subjects had the right priority brain type for laterality. Three of these five persons regularly put their hands together in their daily life, and the other two did not.

*3.1.3.2 a-2. Left priority brain type*

Six of the 11 persons had the left priority brain type for laterality. Two of six subjects regularly put their hands together in their daily life, and the other three did not.

Only one subject of the 11 was not classified in these two groups, and this person (N1) had the left priority brain type estimated in central temporal gyrus (N1: latency 579.0 ms, GOF 32.8%) as shown in the above **Table 1**.

The priorities of brain laterality are considered important for obtaining the characteristic laterality of the active brain in daily life as described below, regardless of putting the hands together and praying or not.

*3.1.3.3 A-group: (A1–A5) habit of putting the hands together or praying*

As shown in **Table 1**, in the A-group which had the habit of putting the hands together in daily life, the main active areas in the brain were generally estimated to be on the right near the superior regions (A1: latency 309.2 ms, GOF 50.2%; A4: latency 405.6 ms, GOF 47.4%) or the left near central (A5: latency 1065.3 ms, GOF 57.6%) or left caudal regions (A2: latency 613 ms, GOF 47.9%) in the temporal gyrus. The right prefrontal area was activated in only one subject (A3: latency 974 ms, GOF 36.9%).

(a)	A-Group (Habit Group)					B-Group (No-Habit Group)					
Subject	A1	A2	A3	A4	A5	B1	B2	B3	B4	B5	N1
Latency (ms)	309.2	613	974	405.6	1065.3	215	236	303.4	419.4	366.3	579
Laterality	R	L	R	R	L	R	L	L	R	L	L
Activated region	superior temporal gyrus	caudal temporal gyrus	prefrontal lobe	superior temporal gyrus	central temporal gyrus	posterior frontal gyrus	central temporal gyrus	posterior frontal gyrus	posterior frontal gyrus	posterior frontal gyrus	central temporal gyrus
GOF (%)	50.2	47.9	36.9	47.4	57.6	28.1	68.6	30.5	19.7	27.3	32.8

**Table 1.** Results of MEG experiments for the simple modes (a) of only putting the hands together without smelling.

3.1.3.4 B-group: (B1–B5) no habit of putting the hands together or praying

As shown in **Table 1**, in the B-group, which did not have the habit of putting the hands together or praying, the main active areas in the brain were generally estimated to be the right posterior regions (B1: latency 215.0 ms, GOF 28.1%; B4: latency 419.4 ms) in the frontal gyrus and left central region (B2: latency 236.0 ms, GOF 68.6%) and left caudal regions (B3: latency 303.4 ms, GOF 30.5%; B5: latency 366.3 ms, GOF 27.3%) in the frontal gyrus.

**(b) Simultaneous smelling an incense outdoor and putting the hands together mode**

All 11 subjects were separated into two groups. The A-group had the habit of putting the hands together or praying according to the Japanese traditional conventional style of putting the hands together for a few minutes every day in their daily life. The B-group did not have this habit.

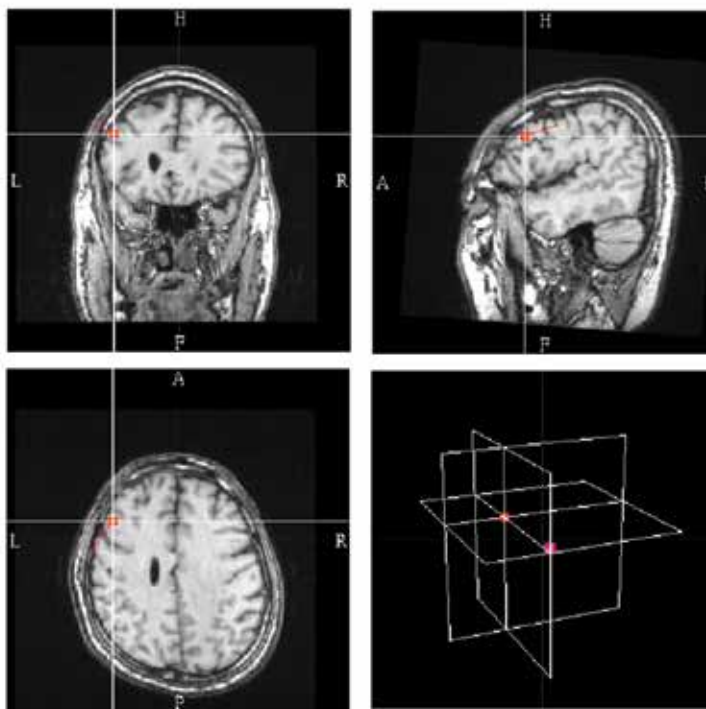
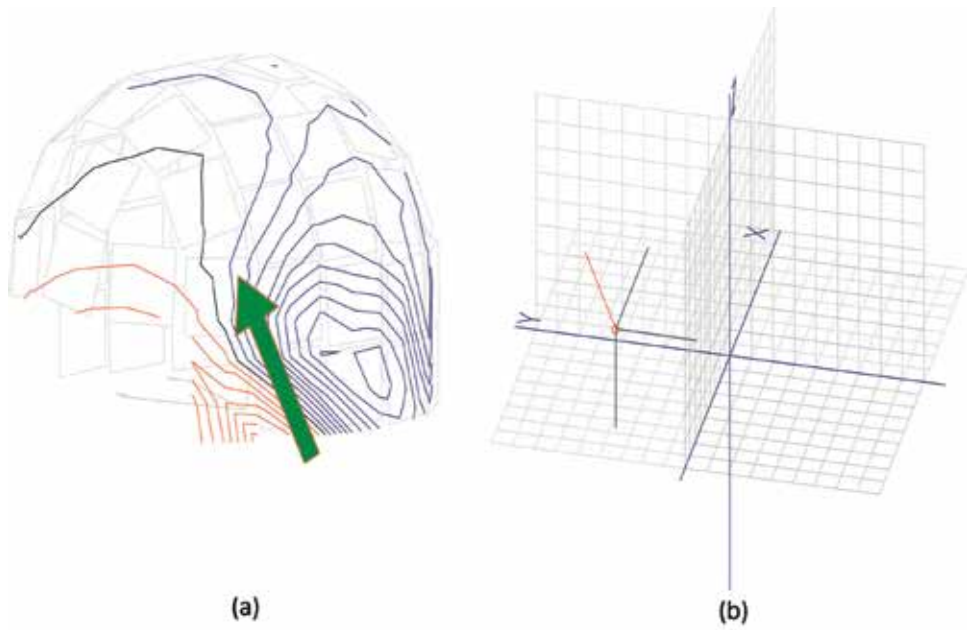
**Table 2** shows an estimated ECD dipole for each subjects for latency time (290–1900 ms), priority of the laterality (right or left), and activated region, and GOF (statistical goodness of fit, %) for simultaneous smelling an incense outdoor and putting the hands together mode.

**Figure 3** shows that the estimated current dipoles of four subjects were obtained at the F5 language area of the inner region (A5: right priority, latency 981.0 ms, GOF 68.0%; B3: left priority, latency 557.3 ms, GOF 28.3%; B4: left priority, latency 423.9 ms, GOF 58.0%; B5: left priority, latency 328.4 ms, GOF 34.5%) of the frontal gyrus in a simultaneous state of the smelling an incense outdoor and putting the hands together. These responses were presented in two subjects, one is OFC area (A3: right priority, latency 974.1 ms, GOF 33.1%) and another is F5 area (A5: left priority, latency 981.0 ms, GOF 68.0%) in the A-group and four subjects in the B-group after smelling incense odors A and B.

**Figure 4** shows that the responses of another two subjects (A2: left priority, latency 627.8 ms, GOF 55.1%; A4: right priority, latency 309.3 ms, GOF 33.7%) in the A-group were obtained at the V1 visual area in the calcarine sulcus in the right or left occipital lobe after smelling incense odors A and B with putting the hands together. These V1 responses were not found in the B-group.

(b)	A-Group (Habit Group)					B-Group (No-Habit Group)					
Subject	A1	A2	A3	A4	A5	B1	B2	B3	B4	B5	N1
Latency (ms)	443.5	627.8	974.1	309.3	981	296.1	1851	557.3	423.9	328.4	974.1
Laterality	R	L	R	R	L	R	L	L	L	L	L
Activated region	insula	V1 occipital gyrus	OFC orbito frontal gyrus	V1 occipital gyrus	F5 inner frontal gyrus	insula	insula	F5 inner frontal gyrus	F5 inner frontal gyrus	F5 inner frontal gyrus	OFC orbito frontal gyrus
GOF (%)	62.5	55.1	33.1	33.7	68	36.7	64.6	28.3	58	34.5	67.6

**Table 2.** Results of MEG experiments for simultaneous smelling an incense outdoor and putting the hands together mode.



(c)

**Figure 3.** F5 language area estimated by the simultaneous smelling an incense outdoor and putting the hands together.

Only one in the 11 subjects was classified in neither the A- nor B-group, and this only one subject (N1) was used by coating smell method. He had the left priority brain type. His estimated current dipole was obtained at the OFC orbito-frontal gyrus (**Figure 5**) (N1: left priority, latency 974.1 ms, GOF 67.6%) when he



performed the special activities of directly coating smelling both hands that were coated with the liquid incense odor A and putting his hands together.

As shown in the **Table 2**, another one subject (A1: right priority, latency 443.5 ms, GOF 62.5%) in the A-group with the habit of putting the hands together

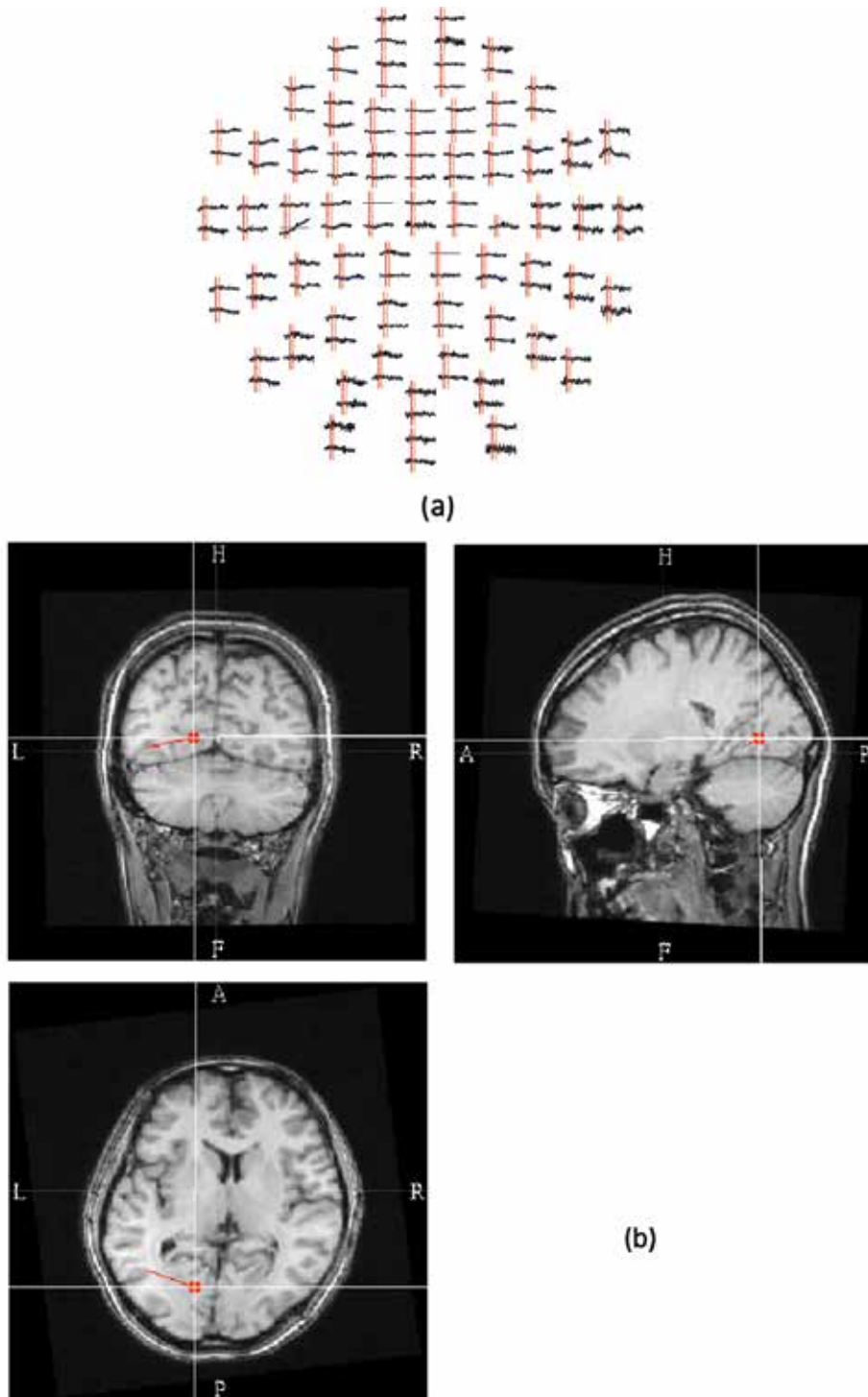


**Figure 4.** V1 visual area estimated by the simultaneous smelling an incense outdoor and putting the hands together.



or praying showed the activity in the inner central temporal area in the right insula, and two subjects (B1: right priority, latency 296.1 ms, GOF 36.7%; B2: left priority, latency 1851.0 ms, GOF 64.6%) in the B-group without this habit also showed activity in the inner area in the right and left insula.

**Figure 6** shows the estimated current dipoles of three groups obtained in insula regions in the right and left temporal gyrus in both the groups after simultaneous

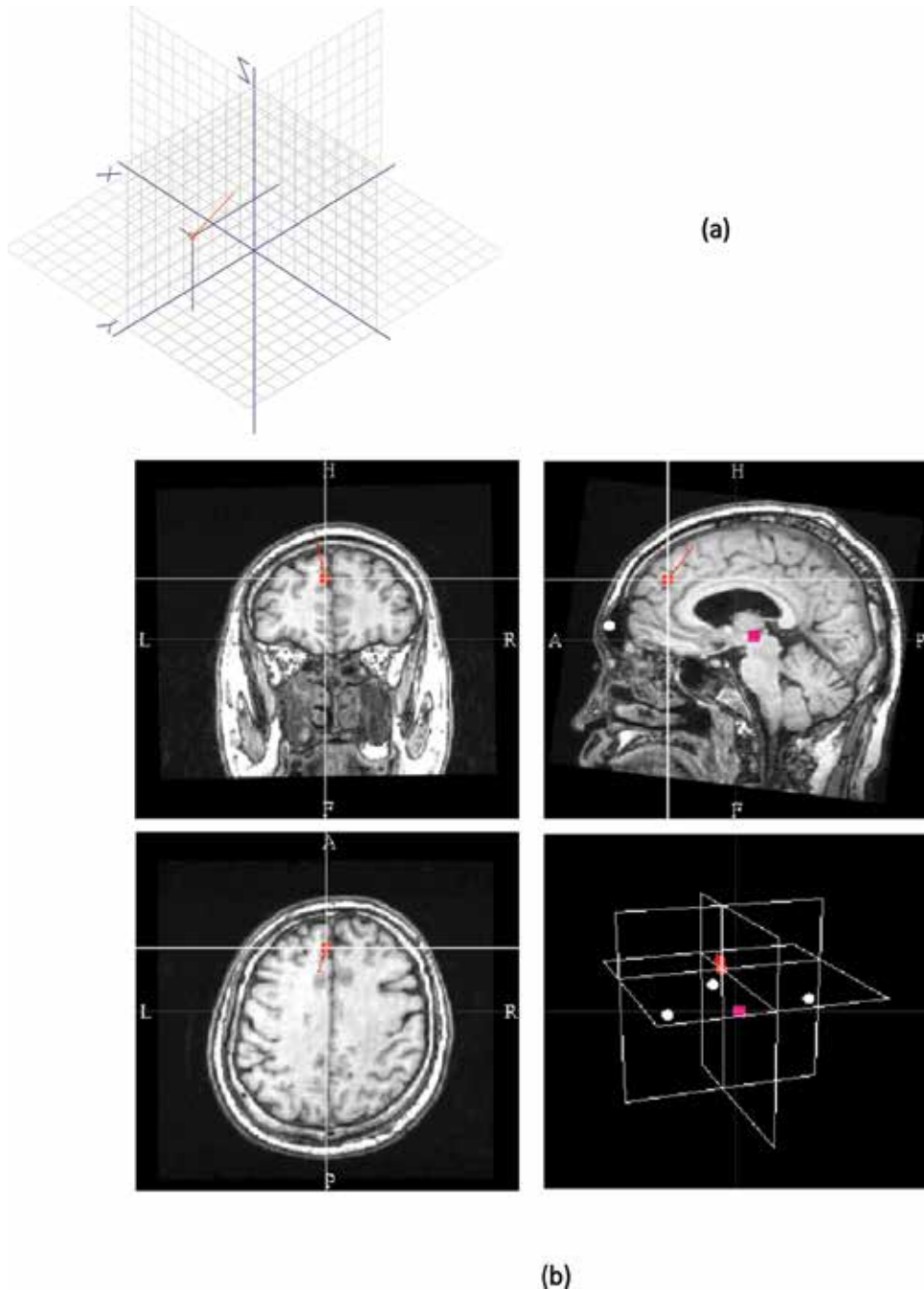


**Figure 5.** Orbito-frontal area estimated by the coating smell and putting the hands together in only one subject without A and B group.

smelling incense odors A and B outdoor and putting the hands together. In particular, the responses of almost all subjects in the B-group were found in temporal areas very close to the same regions as during the simple mode of only putting the hands together without smelling.

From the above analyses, in this task of simultaneous smelling an incense outdoor and putting the hands together mode, the brains of four subjects were activated in the F5 language area in the left frontal lobe. Two of four subjects had the right priority brain type and did not have the habit of putting the hands together in their daily life. However, their F5 language area in the left frontal lobe was activated after this task when simultaneous smelling an incense odor outdoor and putting their hands together. On the other hand, in two other persons with a habit of putting their hands together or praying in daily life, the right and left calcarine sulci of the V1 visual area in the occipital lobe were activated after the task of simultaneous smelling the odor outdoor and putting their hands together. From these all results, we consider that the F5 language area in the left frontal lobe and V1 visual area in the right and left occipital lobes were activated by the task of simultaneous smelling an incense outdoor and putting their hands together regardless of whether they had the habit of putting their hands together in their daily life. These phenomena are considered to be guided by the activation of mirror neurons and the default mode neural network's function.

#### **(c) The mode of smelling only and not putting the hands together**

**Table 3** shows an estimated ECD dipole for each subjects for latency time (230–1100 ms), priority of the laterality (right or left), activated region and GOF (statistical goodness of fit, %) for the mode (c) of smelling an incense outdoor only and not putting the hands together.

#### *3.1.4 One person (N1) not classified in the A- or B-group*

##### *3.1.4.1 c-1. Orbito-frontal lobe area*

AS shown in the above **Table 3**, only one subject was not classified in either the A- or B-group, and this person (N1: right priority, latency 414.0 ms, GOF 43.0%) had the right priority brain type. His estimated current dipole was also obtained at the left or right orbito-frontal lobe when he performed only the mode of smelling both hands, which were coated with liquid odor A or B, without putting his hands together. In this experiment, he could smell and clearly perceive the odorants on both hands.

##### *3.1.4.2 A-group: habit of putting the hands together or praying*

AS shown in **Table 3**, one female subject had the right priority brain type. Her estimated current dipole (A4: right priority, latency 473.0 ms, GOF 35.5%) were obtained in the right insula in the temporal gyrus when she performed the mode of smelling only odor A or B without putting her hands together. Also, the estimated current dipoles of a male subject (A3: left priority, latency 563.2 ms, GOF 53.7%) and another female (A5: left priority, latency 520.2 ms, GOF 58.3%) who had the left priority brain type were obtained at the left amygdala in the olfactory nervous pathway system when they performed the mode of smelling odor B without putting their hands together. Another male subject (A1: right priority, latency 1060.3 ms, GOF 28.9%) was obtained at the posterior frontal gyrus and another female subject (A2: left priority, latency 598.3 ms, GOF 21.9 5) was obtained at trigonum olfactorium in the olfactory pathway system in A-group.

They could smell and clearly perceive odor A or B, and therefore, we could obtain their nervous pathway system and active area through olfactory nerve projection regions.

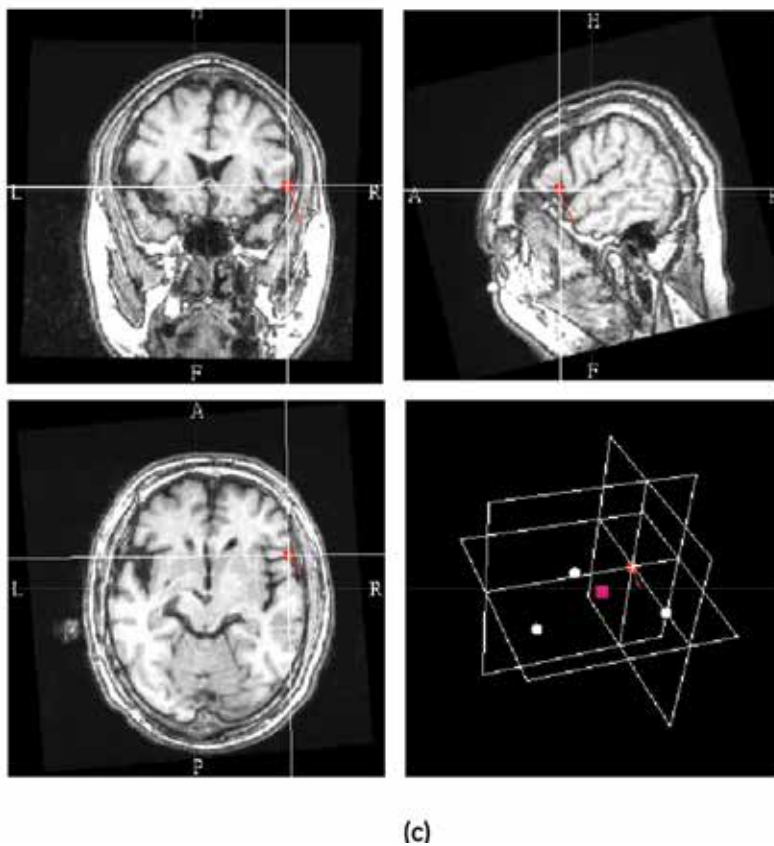
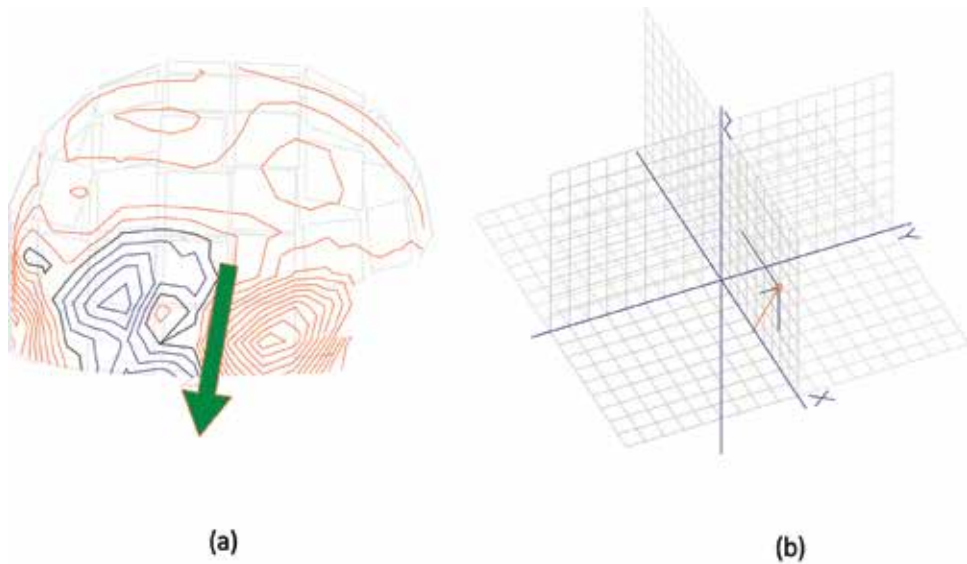


**Figure 6.** Anterior area in the temporal lobe estimated by simultaneous smelling an incense outdoor and putting the hands together in almost all B group.

(e)	A-Group (Habit Group)					B-Group (No-Habit Group)					
subject	A1	A2	A3	A4	A5	B1	B2	B3	B4	B5	N1
Latency (ms)	1060.3	598.3	563.2	473	520.2	502.5	509.7	237.1	252.2	303.4	414
Laterality	R	L	L	R	L	L	L	L	R	L	R
Activated region	posterior frontal gyrus	trigonus olfactorium	amygdala	insula	amygdala	amygdala	insula	insula	insula	amygdala	OFC orbito frontal gyrus
GOF (%)	28.9	21.9	53.7	35.5	58.3	55	38.2	57	35.2	45.3	43

**Table 3.** Results of MEG experiments for the mode (c) of smelling an incense outdoor only and not putting the hands together.

### 3.1.4.3 B-group: no habit of putting the hands together or praying

As shown in **Table 3**, two female subjects (B2: left priority, latency 509.7 ms, GOF 38.2; B4: right priority, latency 252.2 ms, GOF 35.2%) and one male subject (B3: left priority, latency 237.1 ms, GOF 57.0%) had the response at insula regions. Their estimated current dipoles were obtained in insula regions at the temporal gyrus when they performed the mode of smelling only odor B without putting their hands together.

On the other hand, other two male subjects had the left priority brain type. Their estimated current dipoles (B1: left priority, latency 502.5 ms, GOF 55.0%; B5: left priority, latency 303.4 ms, GOF 45.3%) were obtained at the left amygdala in the olfactory pathway system when they performed the mode of smelling only odor B without putting their hands together.

Although these subjects did not have the habit of putting the hands together or praying in their daily life, they could smell and clearly perceive odors A and B. Therefore, we could obtain the responses of their olfactory nervous pathway system and active areas through olfactory nerve projection regions.

## 3.2 Results of statistical analysis of the cortisol level in the saliva of each of the 11 subjects

1. Cortisol value before smelling the odor and MEG experiments
2. Cortisol value after smelling incense A
3. Cortisol value after smelling incense B

The cortisol value ( $\mu\text{g/dL}$ ) is an index of the state of stress.

**Table 4** shows the result of statistical analysis of each value, and the mean and standard deviation of the cortisol value were calculated for all 11 subjects, and for ten subjects, five subjects in the A-group and another five subjects in the B-group.

Next, statistical t-tests were performed to compare the cortisol values of each condition in all 10 subjects and each five subjects classified in the A- or B-group, respectively.

1. No significant difference was found among the mean cortisol value of the conditions 1: before smelling the odor, 2: after smelling incense odor A, and 3: after smelling incense odor B for all 10 subjects (see **Figure 7**).
2. The average cortisol value tended to decrease in the order of 1: before smelling the odor, 2: after smelling incense odor A, and 3: after smelling incense odor B in all 10 subjects and the five subjects in the A-group (see **Figure 8**).
3. A significant difference ( $p < 0.078$ ) was found between the mean cortisol value of the condition after smelling incense odor A (2) and after smelling incense odor B (3) for the five subjects in the B-group (see **Figure 9**).
4. The average cortisol value tended to decrease in the order of (1) after smelling incense odor A (2), before smelling the odor, and (3) after smelling incense odor B for the five subjects in the B-group.
5. A different tendency in the average cortisol value was observed between the A-group and B-group. In particular, an effect of stress was observed for smelling incense odor A.
6. All subjects perceived and smelled incense odor B, which had no effect regarding stress.
7. For individual subjects, the cortisol value tended to decrease in the order of 1: before smelling the incense odor, 2: after smelling incense odor A, 3: after smelling incense odor B in five subjects in the A-group.
8. For individual subjects, the cortisol value tended to decrease in the order of 1: after smelling incense odor A, 2: before smelling the odor, 3: after smelling incense odor B in three subjects in the B-group.
9. For individual subjects, especially in the one subject who was different from the other subjects in the B-group whose cortisol value tended to decrease, the cortisol value tended to decrease in the order of 1: before smelling the odor, 2: after smelling incense odor A, 3: after smelling incense odor B, similar to the A-group.

### **3.3 Relation between the impression of the subject about the incense outdoor and stress measured by the cortisol value**

#### *3.3.1 A-group: habit of putting their hands together or praying*

Almost all subjects in the A-group, except for one female, felt that incense odor B was more familiar than incense odor A in daily life. However, both incense odors were pleasant for all subjects in the A-group according to psychological inquiries. In these cases, the cortisol value for almost all subjects except this female decreased in the order of 1: before smelling the odor, 2: after smelling incense odor A, and 3: after smelling incense odor B. In other words, almost all subjects except this female reported a decrease in stress in the order 1: odor B, 2: odor A. 3: no odor.

Cortisol value ( $\mu\text{g/dL}$ )	A-group (habit group)					B-group (no-habit group)					Average	Standard deviation	
	A1	A2	A3	A4	A5	B1	B2	B3	B4	B5			N1
Before experiment	0.34	0.12	0.1	0.15	0.13	0.08	0.16	0.15	0.34	0.07	0.09	0.16	0.177
After incense A	0.32	0.07	0.08	0.1	0.1	0.12	0.16	0.25	0.15	0.23	0.06	0.15	0.184
After incense B	0.26	0.07	0.07	0.07	0.07	0.07	0.16	0.12	0.09	0.16	0.03	0.11	0.163
Average	0.31	0.09	0.08	0.11	0.1	0.09	0.16	0.17	0.19	0.15	0.06		
Standard deviation	0.057	0.035	0.021	0.057	0.042	0.007	0	0.021	0.177	0.064	0.042		

**Table 4.** Results of cortisol value ( $\mu\text{g/dL}$ ) in the saliva for each 11 subjects.

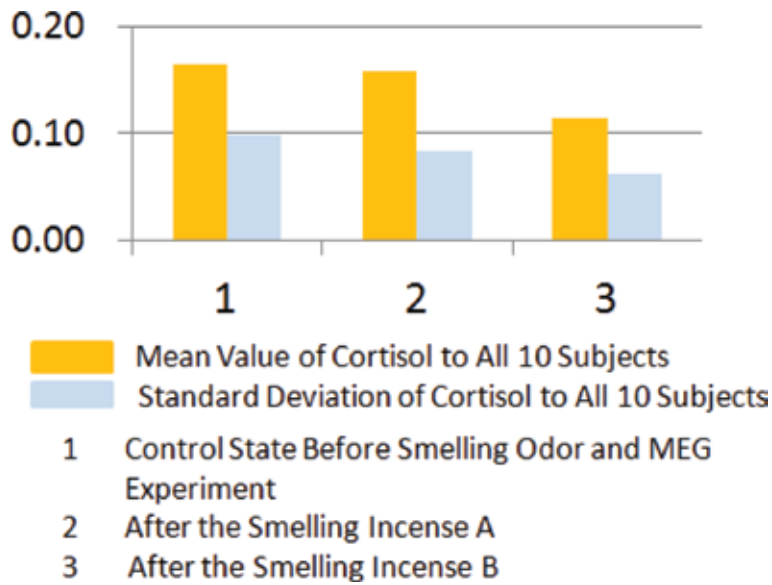


**Figure 7.**  
 Statistical analysis of cortisol value for all 10 subjects.

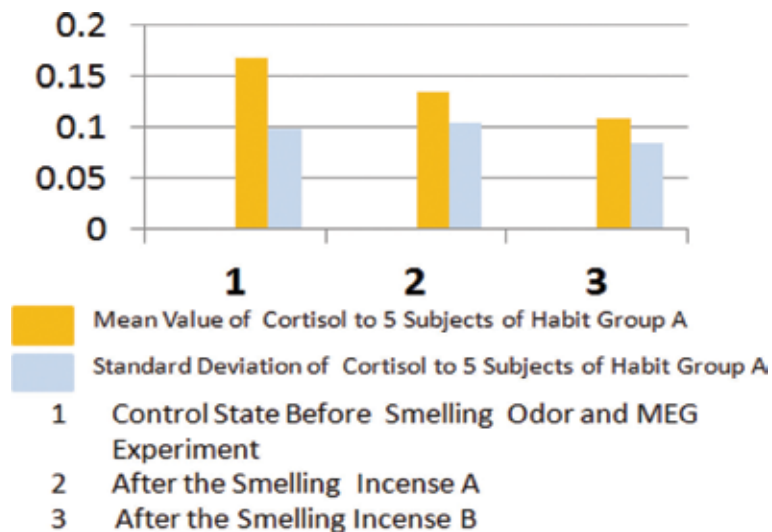


**Figure 8.**  
 Statistical analysis of cortisol value for habit group A.

Only one female subject was different from the other subjects in the A-group. She liked incense odor A more than incense odor B. Therefore, she felt not more stress from incense odor A than incense odor B. Her cortisol value decreased in the order 1: no odor, 2: odor A, odor B.

### 3.3.2 B-group: no habit of putting the hands together or praying

Almost all subjects in the B-group reported feeling more stress for incense odor A than incense odor B, because incense odor B was considered more familiar in their daily life. In contrast, almost all B-group subjects felt stress for unfamiliar odor A more than the state of no odor before smelling. Their cortisol value decreased in the order 1: incense odor A, 2: no odor, 3: incense odor B.

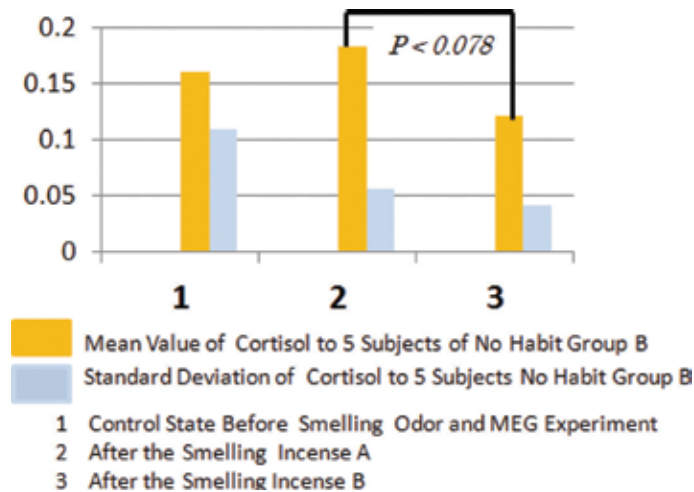


**Figure 9.**  
*Statistical analysis of cortisol value for no habit group B.*

From these analyses about the relationship between the impression of the odor and the measured cortisol value, the nature of the state of stress was different in the A-group and B-group.

### 3.4 Summary of results

#### 3.4.1 *The specific and distinct mirror neuron activities without the error activity on the hand motor system by putting the hands together*

Our MEG experiments of the above results using the methods of (1) Control mode in section 2.4 as the obtained **Figure 1(a)** and **(b)** showed the distinct and objective activities of our brain on the control state of non-motor system's activity clinically. However, in the MEG experiments of only putting the hands together without smelling using methods of (2) Simple mode of putting the hands together in section 2.4 as shown at (a) in **Figure 2(a)–(c)** we obtained the MEG local estimated signal response areas for the distinct mirror neuron activity. In our MEG experimental results for only putting the hands together without smelling an incense outdoor, 11 subject's detailed responses were obtained as **Table 1** in which A-group subjects were obtained in superior and anterior temporal gyrus or central and caudal temporal and frontal gyrus, on the other hand B-group subjects were obtained also the same temporal and frontal areas. These results show that the estimated local activated regions of B-group having the no habit of putting the hands together or praying are almost all resemble to the activated areas in brain of A-group having the habit of putting the hands together in daily lives. These results of the coincidence active areas in A-group and B-group in the behavioral action for putting the hands together show the distinct activities of mirror neurons activities as the imitation in the brain without the simple artifacts of moving error activities in moving neuronal system.

#### 3.4.2 *The simultaneous new specific stronger effects of both the distinct mirror neuron's activity putting the hands together and the activities of smelling an incense outdoor at the same time*

Our MEG experiments of the above results using the methods of (3) Smelling mode with putting the hands together in section 2.4 as the obtained (b) in **Figure 3(a–c)**



showed the distinct and objective activities of our brain on the state of simultaneous responses of putting the hands together and at the same time smelling an incense outdoor. In this simultaneous status mode of our MEG experiments, this specific active area in **Figure 3** were shown in distinct F5 language areas of the inner regions of the left frontal lobe or orbito-frontal gyrus (OFC) clinically. These responses were presented in two subjects in A-group and four subjects in B-group. These specific results show the simultaneous new distinct stronger effects of both the mirror neuronal activities as the imitation without the artifacts of the simple moving error activities and olfactory activated effects. The specific responses of another two subjects in A-group showed the simultaneous other new specific stronger effects of both the mirror neuron's activities putting the hands together and the activities of smelling an incense outdoor at the same time in V1 visual areas in the calcarine sulcus in occipital lobe clinically as the another distinct active areas as shown in **Figure 4(a)** and **(b)**. Only one person of 11 subjects in neither A- nor B-group who used by the direct coating strong smell over the hands showed the specific simultaneous activities in the orbito-frontal lobe as shown in **Figure 5(a)** and **(b)**. And the simultaneous specific activities in the brain both the putting the hands together and smelling an incense outdoor at the same time of other five subjects were obtained in anterior and posterior areas in the temporal lobes as shown in **Figure 6(a)–(c)**. These detailed MEG response data are shown in **Table 2** for simultaneous smelling an incense outdoor and putting the hands together and these results show the specific new strong effects of simultaneous responses in the relation of both the mirror neuron activities and olfactory effects at the same time.

### *3.4.3 The mode of smelling an incense outdoor only without putting the hands together (olfactory response with non-mirror neuron activity)*

The detailed responses of our MEG experiments of the above results in the mode of smelling an incense outdoor only without putting the hands together (non-mirror neuron activity) were shown in **Table 3** with almost all subject's data. From these clinical and objective MEG measurements and analysis we obtained the distinct olfactory activities clearly such as the frontal and temporal regions in the olfactory nervous projection areas and olfactory nervous pathways nevertheless A- and B-group.

## **4. Discussions**

### **4.1 The inverse problem: source estimation models**

We used dipole models for the source estimation of the recorded MEG signals. The simpler spherical model for the head is adequate for MEG source modeling in most cases. In addition, MEG benefits from very precise knowledge of the real sensor geometry, including registration of sensors to the head.

However, source modeling in MEG remains a challenging mathematical problem, especially for more complex configurations of neuronal sources associated with higher cognitive function.

As a realistic clinical tool to for the spatio-temporal localization of the evoked brain activity by simultaneous smelling an incense outdoor and putting the hands together.

A variety of methods have been applied to the MEG source estimation problem to overcome the limitations. Using the individual's MRI scan of every subjects, template can provide good approximations for realistic head modeling. For example, finite element models (FEMs) could be applied to drastic changes in tissue conductivity and can be modeled more accurately in future [44].

## **4.2 Mirror neurons and the default mode network**

The concept of mirror neurons was described by Marco Iacoboni. These neurons are located in the F5 inner area of the prefrontal lobe [7]. In general, the motion of putting the hands together and mimicking behavior are considered to activate the mirror neuron mechanism [8, 45, 46] and the default mode network in the human brain [9, 47–49]. These neural effects are considered to increase activity in the central areas of the temporal lobe and the caudal area of the frontal lobe according to the imitation principal [50–54].

The theory of these mirror neurons revealed the principal of imitation of behavior. Although these F5 areas in the left side of the human brain are in the same areas as Broca's language regions, F5 areas of both sides of the brain function to mimic motion and behavior. From anatomical research, F5 areas are connected to pre-motor areas and supplemental areas in movement regions in the brain.

Mirror neurons are thus considered to function for imitation of the habit of putting the hands together or praying, which is also performed with both hands by almost all elderly Japanese people in their daily life.

Super mirror neurons are concerned with determination of values, recognition of oneself and others, and reward from one's work. The inner default mode network controls the fundamental activity of daily movements and the resting state of the human brain. Because this default mode network is strongly related to super mirror neurons, discrimination of oneself from others and the determination of social cognition are considered important in human daily life.

## **4.3 The meaning of simultaneous smelling an incense outdoor and putting the hands together**

Odorants stimulate activity in the olfactory nervous center, orbito-frontal areas, and others in the human brain [1–4]. Neurophysiological experiments in monkeys have shown that the olfactory nervous center and olfactory pathway project to the orbitofrontal cortex [55–57]. In humans, olfactory event-related potentials and magnetic fields evoked by odorant pulses synchronized with respiration are also found in the orbitofrontal area [5, 6, 58, 59].

In this experiment, only one subject was not in the A- or B-group and smelled his hands that were coated with liquid odor. By performing this behavior, he clearly experienced strong A and B odors. We estimated that the areas activated by his sniffing of both the A and B odors were the prefrontal area and the right or left orbito-frontal area.

In habits of daily life, the brain of A-group people after smelling incense odors and putting their hands together or praying was activated at the inner lobe of the frontal area, F5 language area, anterior area in the temporal lobe, orbito-frontal area, and others.

The brain of B-group individuals who did not have the habit of smelling incense odor or putting their hands together or praying in their daily life was also activated at the inner lobe of the frontal area, anterior area in the temporal lobe, and F5 language area in the left frontal lobe, similar to the A-group.

These results suggest that mirror neurons or the super mirror neuron system and the default mode network system in the brain of B-group subjects were activated by both smelling the incense odor and their imitation of putting their hands together, although they did not have the habit of smelling incense odors or putting their hands together or praying in their daily life.

From the above analyses, in the task involving simultaneous smelling an incense outdoor and putting the hands together, four person's brains were activated in the

F5 language area in the left frontal lobe. Two of four subjects had the right priority brain type and no habit of putting their hands together in their daily life. However, their F5 language area in the left frontal lobe was activated after this task.

On the other hand, in two persons with a habit of putting their hands together or praying in their daily life, the right and left calcarine sulci of the V1 visual area in the occipital lobe were activated after the task of simultaneous smelling an incense outdoor and putting the hands together [60–63].

## 5. Conclusions

This research revealed that simultaneous smelling an incense outdoor and putting hands together increased the activity of specific brain areas, for example inner areas of the prefrontal cortex and F5 regions of the human brain. In our experiments, evoked neuronal activity was recorded by the MEG and the cortisol value in the subject's saliva was measured in every experimental stage. From a few previous researches, it is known that F5 area is activated during observation of certain actions, during action execution etc. and these results show F5 have multimodal and different type of neurons. Moreover, the F5p is also known as a hand-related area that encoded goal-directed actions, not only mimic or autonomic actions. Our results demonstrated that the sources of MEG which are postsynaptic signals synchronized activation of intracellular currents across dendrites of cortical pyramidal neurons link strongly with anatomic position of mirror neurons. Mirror neurons in our experiment case are considered to have the function for imitation of the habit of putting the hands together or praying, which almost all elderly Japanese peoples often practice in their daily life. Super mirror neurons are concerned with determination of values, recognition of oneself and others, and reward from one's work. The inner default mode network controls the fundamental activity of daily movements and the resting state of the human brain. Because this default mode network is strongly related to super mirror neurons, discrimination of oneself from others and the determination of social cognition are considered important in human daily life. From these mirror neuron theories and the above summary of our results (1). We can conclude the distinct activities as follows. From these concerns and the above summary results (2) and (3), it can be considered that the specific regions in the brain such as the F5 language area in the left frontal lobe and the V1 visual area in the right and left occipital lobes were distinctly activated by the simultaneous new stronger effects increased with the task of smelling an odor and putting their hands together regardless of the habit in daily lives. These results show that the sources of MEG strongly link with the anatomic positions of mirror neurons and their types. Especially, these phenomena are considered to be guided by the simultaneous new stronger effects increased by both the olfactory activities of smelling an incense outdoor accompanied with the activation of mirror neurons and the default mode neural network [64–66] for the imitation behavior of putting hands together. From the above results, we consider that the F5 language area in the left frontal lobe and V1 visual area in the right and left occipital lobes and other specific brain areas were activated distinctly by the task of simultaneous smelling an incense outdoor and putting their hands together regardless of whether they had the habit of putting their hands together in their daily life. From our experiments, the cortisol value in saliva for the stress and the specific mirror neuron theories. we conclude that the simultaneous new specific effects both the smelling an incense outdoor and the imitating the behavior of putting the hands together can be considered to increase the activities of these areas in the human brain due to mutual interactions, reciprocal connections, or alternative actions.

## **Acknowledgements**

We thank Mr. Ippei Torige, Mr. Kimiyoshi Yoshino, and Mr. Masaru Yamamoto in Nippon Kodo Co. Ltd. for expert help during the experiments in subject's attendance and in the preparations of incense odorants.


This study was supported by the Grants for the Alzheimer's Disease in Osaka Research Association and the Awards of Osaka-Gas for the Research of Alzheimer's Disease in Japan.

## **Author details**

Mitsuo Tonoike\* and Takuto Hayashi  
Department of Medical Engineering, Faculty of Health and Science,  
Aino University, Ibaraki, Osaka, Japan

\*Address all correspondence to: gah00161@nifty.ne.jp

## **IntechOpen**

© 2018 The Author(s). Licensee IntechOpen. This chapter is distributed under the terms of the Creative Commons Attribution License (<http://creativecommons.org/licenses/by/3.0>), which permits unrestricted use, distribution, and reproduction in any medium, provided the original work is properly cited. 

## References

- [1] Takagi SF. Human Olfaction. Tokyo, Japan: University of Tokyo Press; 1989
- [2] Takagi SF. Olfactory frontal cortex and multiple olfactory processing in primates. In: Peters A, Ones EG, editors. *Cerebral Cortex*. Vol. 9. New York: Plenum; 1991. pp. 133-152
- [3] Sobel N, Pranhakaran V, Desmond JE, Glover GH, Goode RL, Sullivan EV, et al. Sniffing and smelling: Separate subsystems in the human olfactory cortex. *Nature*. 1998;**392**:282-286
- [4] Zatorre RJ, Jones-Gotman M, Evans AC, Meyer E. Functional localization and lateralization of human olfactory cortex. *Nature*. 1992;**360**:339-340
- [5] Tonoike M, Yamaguchi M, Kaetsu I, Kida H, Seo R, Koizuka I. Ipsilateral dominance of human olfactory activated centers estimated from event-related magnetic fields measured by 122-channel whole-head neuromagnetometer using odorant stimuli synchronized with respirations. In: Murphy C, editor. *Olfaction and Taste XII*. Vol. 855. New York: New York Academy of Sciences; 1998. pp. 579-590
- [6] Tonoike M, Yamaguchi M, Hamada T, Kaetsu I, Koizuka I, Seo R. Odorant perception and active olfaction: A study of olfactory magnetic fields evoked by odorant pulse stimuli synchronized with respiratory cycle. *Proceedings of 20th Annual International Conference IEEE/EMBS'98*. 1998;**20**(4):2213-2216
- [7] Iacoboni M, Woods RP, Brass M, et al. Cortical mechanisms of human imitation. *Science*. 1999;**286**:2526-2528
- [8] Rizzolatti G, Fadiga L, Fogassi L, Gallese V. From mirror neurons to imitation: Facts and speculations. In: Meltzoff AN, Prinz W, editors. *The Imitative Mind. Development, Evolution, and Brain Bases*. Cambridge: Cambridge University Press; 2002. pp. 247-266
- [9] Arbib M. The Mirror System Hypothesis. *Linking Language to Theory of Mind*. 2005. Retrieved 2006-02-17
- [10] Ramachandran VS, Vilayanur S. Mirror neurons and imitation learning as the driving force behind “the great leap forward” in human evolution. 2005. [http://www.edge.org/3rd\\_culture/ramachandran/ramachandran\\_p1.html](http://www.edge.org/3rd_culture/ramachandran/ramachandran_p1.html) [Accessed: June 15th, 2005]
- [11] Rizzolatti G, Fogassi L, Gallese V. Neurophysiological mechanisms underlying the understanding and imitation of action. *Nature Reviews Neuroscience*. 2001;**2**:661-670
- [12] Rizzolatti G, Craighero L. The mirror neuron system. *Annual Reviews of Neuroscience*. 2004;**27**:169-192
- [13] Raiche ME, MacLeod AM, Snyder AZ, et al. A default mode of brain function. *Proceedings of the National Academy of Sciences USA*. 2001;**98**:676-682
- [14] Cherkassky VL, Kana RK, Keller TA, Just MA. Functional connectivity in a baseline resting-state network in autism. *Neuroreport*. 2006;**17**(16):1687-1690
- [15] Gusnard DA, Raiche ME. Searching for a baseline: Functional imaging and the resting human brain. *Nature Reviews Neuroscience*. 2001;**2**: 685-694
- [16] Xu X, Yuan H, Lei X. Activation and connectivity within the default mode network contribute independently to future-oriented thought. *Scientific Reports*. 2016;**6**:21001. DOI: 10.1038/srep21001

- [17] Maresh EL, Allen JP, Coan JA. Increased default mode network activity in socially anxious individuals during reward processing. *Biology of Mood & Anxiety Disorders*. 2014;**4**:7. DOI: 10.1186/2045-5380-4-7
- [18] John A, Friston KJ. Unified segmentation. *NeuroImage*. 2005;**26**:839-851
- [19] Taulu S, Kajola M, Simola J. The signal space separation method. In: 14th Conference of the International Society for Brain Electromagnetic Topography; Santa Fe, NM
- [20] Taulu S, Simola J, Kajola M. Applications of the signal space separation method. *IEEE Transactions on Signal Processing*. 2005;**53**:3359-3372
- [21] Taulu S, Simola J. Spatiotemporal signal space separation method for rejecting nearby interference in MEG measurements. *Physics in Medicine and Biology*. 2006;**51**(7):1759-1768
- [22] Uutela K, Taulu S, Hamalainen M. Detecting and correcting for head movements. *NeuroImage*. 2001;**14**:1424-1431
- [23] Tonoike M, Yamaguchi M, Kaetsu I, Kida H, Seo R, Koizuka I. Ipsilateral dominance of human olfactory activated centers estimated from event-related magnetic fields measured by 122-channel whole-head neuromagnetometer using stimuli synchronized with respirations. In: Murphy C, editor. *Olfaction and Taste XII*. Vol. 855. New York: New York Academy of Sciences; 1998. pp. 579-590
- [24] Williamson S, Kaufman L. Biomagnetism. *Journal of Magnetism and Magnetic Materials*. 1981;**22**:129
- [25] Uusitalo MA, Ilmoniemi RJ. Signal-space projection method. *Medical & Biological Engineering*. 1997;**32**:35-42
- [26] Uutela K, Hamalainen M, Salmelin R. Global optimization in the localization of neuromagnetic sources. *IEEE Transactions on Biomedical Engineering*. 1998;**45**(6):716-723
- [27] Uutela K, Hamalainen M, Salmelin R. Visualization of magnetoencephalographic data using minimum current estimates. *NeuroImage*. 1999;**10**(2):173-180
- [28] Kiebel SJ, Daunizeau J, Friston KJ. A hierarchy of time-scales and the brain. *PLOS Computational Biology*. 2008;**4**(11):1-12, 4e1000209
- [29] Kiebel SJ, Garrido MI, Moran R, Chen CC, Friston KJ. Dynamic causal modeling for EEG and MEG. *Human Brain Mapping*. 2009;**30**:1866-1876
- [30] Sanja JG, Susac A, Grilj V, et al. Size matters: MEG empirical and simulation study on source localization of the earliest visual activity in the occipital cortex. *Medical & Biological Engineering & Computing*. 2011;**49**(5):545-554
- [31] Sanja JG, Aine Cheryl J, Stephen Julia M, Adair John C, Knoefel Janice E, Selma S. Modulatory role of the prefrontal generator within the auditory M50 network. *NeuroImage*. 2014;**92**:120-131
- [32] Sanja JG, Aine Cheryl J, Stephen Julia M, Adair John C, Knoefel Janice E, Selma S. MEG biomarker of Alzheimer's disease: Absence of a prefrontal generator during auditory sensory gating. *Human Brain Mapping*. 2017;**38**:5180-5194
- [33] Darvas F, Pantazis D, Kucukaltun-Yildirim E, Leahy RM. Mapping human brain function with MEG and EEG: Methods and validation. *NeuroImage*. 2004;**23**(suppl.1):S289-S229
- [34] Hamalainen M, Sarvas J. Feasibility of the homogenous head model in

the interpretation of neuromagnetic fields. *Physics in Medicine and Biology*. 1987;**32**:91-97

[35] Hamalainen M, Hari R, Ilmoniemi RJ, Knuutila JET, Lounasmaa OV. Magnetoencephalography-theory, instrumentation, and application to noninvasive studies of the working human brain. *Reviews of Modern Physics*. 1993;**65**:413-497

[36] Hamalainen M, Ilmoniemi RJ. Interpreting magnetic fields of the brain: Minimum norm estimates. *Medical and Biological Engineering and Computing*. 1994;**32**(1):35-42

[37] Cuffin BN. A comparison of moving dipole inverse solution using EEG's and MEG's. *IEEE Transactions on Biomedical Engineering*. 1985;**32**(11):905-910

[38] Scherg M, Von Cramon D. Evoked dipole source potentials of the human auditory cortex. *Electroencephalography and Clinical Neurophysiology*. 1986;**65**(5):344-360

[39] Ilmoniemi RJ. Neuromagnetism: Theory, techniques, and measurement [PhD thesis]. Helsinki Univ. of Technology; 1985

[40] Sarvas J. Basic mathematical and electromagnetic concepts of the biomagnetic inverse problem. *Physics in Medicine and Biology*. 1987;**32**(1):11-22

[41] Ioannides A, Liu LC, Kwapien J, Drozd S, Streit M. Coupling of regional activations in human brain during an object and face affect recognition task. *Human Brain Mapping*. 2000;**11**:77-92

[42] Tonoike M, Nishimura K, Tobinaga Y. Detection of thinking in human by magnetoencephalography, world congress of medical physics and biological engineering. In: *IFMBE Proceedings*. Vol. 14. 2006. pp. 2617-2621

[43] Nishimura K, Tobinaga Y, Tonoike M. Detection of neural activity associated with thinking in frontal lobe by magnetoencephalography. *Progress of Theoretical Physics*. 2002;**173**(Suppl):332-341

[44] Haueisen J, Ramon C, Eiselt M, Brauer H, Nowak N. Influence of tissue resistivities on neuromagnetic fields and electric potentials studied with a finite element model of the head. *IEEE Transactions on Biomedical Engineering*. 1997;**44**(8):727-735

[45] Dapretto M. Understanding emotions in others: Mirror neuron dysfunction in children with autism spectrum disorders. *Nature Neuroscience*. 2006;**9**(1):28-30

[46] Bastiaansen JACJ, Thioux M, Keysers C. Evidence for mirror systems in emotions. *Philosophical Transactions of the Royal Society Biological Science*. 2009;**364**:2391-2404

[47] Oberman LM, Hubbard EM, McCleery JP, Altschuler EL, Ramachandran VS, Pineda JA. EEG evidence for mirror neuron dysfunction in autism spectral disorders. *Brain Research. Cognitive Brain Research*. 2005;**24**(2):190-198

[48] Oberman LM, Pineda JA, Ramachandran VS. The human mirror neuron system: A link between action observation and social skills. *SCAN*. 2007;**2**:62-66

[49] Kiebel SJ, Friston KJ. Free energy and dendritic self-organization. *Frontiers in System Neuroscience*. 2011;**5**:1-13. DOI: 10.3389/fnsys.2011.00080

[50] Fadiga L, Fogassi L, Pavesi G, Rizzolatti G. Motor facilitation during action observing: A magnetic stimulation study. *Journal of Neurophysiology*. 1995;**73**:2608-2611

- [51] Gallese V, Goldman A. Mirror neurons and the simulation theory of mindreading. *Trends in Cognitive Sciences*. 1998;**2**:493-501
- [52] McClure SM, Li J, Tomlin D, et al. Neural correlates of behavioral preference for culturally familiar drinks. *Neuron*. 2004;**44**:379-387
- [53] Mukamel R, Ekstrom AD, Kaplan J, Jacoboni M, Fried I. Single-neuron responses in humans during execution and observation of actions. *Current Biology*. 2010;**20**(8):750-756
- [54] Hari R, Forss N, Avikainen S, et al. Activation of human primary motor cortex during action observation: A Neuromagnetic study. *Proceedings of the National Academy of Sciences of United States of America*. 1998;**95**(25):15061-15065
- [55] Yarita H, Iino M, Tanabe T, Kogure S, Takagi SF. A trans-thalamic olfactory pathway to orbitofrontal cortex in the monkey. *Journal of Neurophysiology*. 1980;**45**:69-85
- [56] Tanabe T, Yarita H, Iino M, Ooshima Y, Takagi SF. An olfactory projection area in orbitofrontal cortex of the monkey. *Journal of Neurophysiology*. 1975;**38**:1269-1283
- [57] Seubert J, Gregory KK, Chamberland J, Dessirier JM, Lundstrom JN. Odor valence linearly modulates attractiveness, but not age assessment, of invariant facial features in a memory-based rating task. *PLoS One*. 2014;**9**:e98347. DOI: 10.1371/journal.pone.0098347
- [58] Tonoike M, Yoshida T, Sakuma H, Wang L-Q. fMRI measurement of integrative effects of visual and chemical senses stimuli in humans. *Journal of Integrative Neuroscience*. 2013;**12**(3):369-384
- [59] Tonoike M. Odor perception: The mechanism of how odor is perceived, human olfactory displays and interfaces: Odor sensing and presentation. In: IGI Global Disseminator and Knowledge. 2013. pp. 44-59
- [60] Zhou W, Jiang Y, He S, Chen D. Olfaction modulates visual perception in binocular rivalry. *Current Biology*. 2010;**20**:1356-1358
- [61] Calvert GA, Campbell R, Braer MJ. Evidence from functional magnetic resonance imaging of crossmodal binding in the human heteromodal cortex. *Current Biology: CB*. 2000;**10**:649-657
- [62] Calvert GA. Crossmodal processing in the human brain: Insights from functional neuroimaging studies. *Cerebral Cortex*. 2011;**11**:1110-1123
- [63] Davis MH. Measuring individual differences in empathy: Evidence for a multidimensional approach. *Journal of Personality & Social Psychology*. 1983;**44**:113-126
- [64] Simpson JR, Snyder AZ, Gusnard DA, Raichle ME. Emotional-induced changes in human medial prefrontal cortex: 1. During cognitive task performance. *Proceedings of the National Academy of Sciences of the United States of America*. 2001;**98**:683-687
- [65] Buccino G, Binkofski F, Fink GR, Fadiga L, Fogassi L, Gallese V. Action observation activates premotor and parietal areas in a somatotopic manner: An fMRI study. *European Journal of Neuroscience*. 2001;**13**:400-404
- [66] Cherkassky VL, Kana RK, Keller TA, Just MA. Functional connectivity in a baseline resting-state network in autism. *Neuroreport*. 2006;**17**(16):1787-1690



# Neuroimaging Reveals Heterogeneous Neural Correlates of Reading Deficit in Individuals with Dyslexia Consistent with a Multiple Deficit Model

*Agnieszka A. Reid*

## Abstract

Neuroimaging has become a powerful way of studying in vivo brain function and structure. The aim here is to comprehensively review Reid's fMRI study which is the first to use a multiple case approach to investigate individual differences among 18 participants with dyslexia (DPs) and 16 control participants (CPs) and to directly test the predictions of the main dyslexia theories on reading deficit. The results show that the neural correlates of reading deficit for all DPs (except one) are consistent with more than one theory, supporting a multiple deficit model. Striking individual differences between DPs were found; even if the neural correlates of reading deficit in two DPs were consistent with the same theory, the affected brain areas could differ. To make progress, research on causes of reading deficit in dyslexia would need to (1) focus on the multiple deficit model, (2) use neuroimaging to test a further refined set of brain areas (including areas hypothesised by other dyslexia theories) in longitudinal designs, (3) control the effects of co-occurring neurodevelopmental disorders, (4) use high-field MRI (including diffusion techniques), multiband fMRI and MEG with optically pumped magnetometers, (5) progress imaging genetics and (6) pursue neuroimaging intergenerational transmission of brain circuitry.

**Keywords:** dyslexia, MRI, fMRI, neuroimaging, individual differences, a multiple case study, co-occurring neurodevelopmental disorders, reading disorder, imaging genetics, multiple deficit model

## 1. Introduction

### 1.1 A brief summary of neuroimaging methods and neuroimaging research on the biomarkers of neurological, neuropsychiatric and neurodevelopmental disorders

There are six main neuroimaging methods: magnetic resonance imaging (MRI), diffusion tensor imaging (DTI), functional magnetic resonance imaging (fMRI), electroencephalography (EEG), magnetoencephalography (MEG) and positron emission tomography (PET). MRI and DTI enable investigation of brain structure,

whereas fMRI, EEG, MEG and PET enable research into brain function. MRI produces high-resolution images of the brain, with clearly distinguishable grey and white matter, ventricles and fibre tracts. DTI is a method which is mainly used to investigate the anatomical structure of the axon tracts and can provide information on the between-regional anatomical connectivity in the brain. An MRI scanner is used to perform DTI which measures the motion and density of the water in the axons. fMRI uses magnetic resonance imaging to measure brain activity by measuring the ratio of oxygenated to deoxygenated haemoglobin, and this value is referred to as the blood oxygen level-dependent (BOLD) effect; brain activity is usually measured in an experimental task, relative to a control task. EEG is an electrophysiological method for recording global electrical activity of the brain. In order to ask questions on how brain activity is modulated in response to a particular task, an event-related potential (ERP) needs to be extracted from the global EEG signal. MEG is a technique which allows the mapping of brain activity by recording the magnetic fields created by the electrical currents of the brain, using very sensitive magnetometers. Finally, PET measures metabolic activity in the brain by monitoring the distribution of a radioactive tracer. As with fMRI, PET relies on the fact that local blood flow increases in active brain areas. Unlike MEG and EEG, fMRI and PET do not directly measure neural events but metabolic changes which are correlated with neural activity. The neuroimaging techniques differ with respect to critical variables in brain mapping, such as spatial and temporal resolution. Spatial resolution is the ability to distinguish two separate objects that are situated close to one another, whereas temporal resolution is the ability to detect two events that happen in close temporal proximity [1]. ERP and MEG have relatively good temporal resolution of milliseconds (0.01 s) but relatively poorer spatial resolution (10 mm). Structural MRI has relatively good spatial resolution; brain structures much smaller than 1 mm can be resolved with this method, including subcortical structures, such as the superior colliculus. DTI's spatial resolution has been improving, and high-spatial-resolution DTI imaging has been reported with a resolution of 1 mm [2]. fMRI is characterised by relatively good temporal resolution of seconds to hundreds of milliseconds and spatial resolution of 4–5 mm. PET has relatively lower spatial (5–10 mm) and temporal (60–1000 s) resolutions [1]. It should be emphasised here that the neuroimaging methods introduced above are subject to steady improvement, with regard to their spatial and temporal resolution and other characteristics; furthermore new neuroimaging methods are being developed. For instance, three more recent neuroimaging methods need to be mentioned here: diffusion kurtosis imaging (DKI) [3], a neuroimaging method that provides independent and additional information (to that acquired with DTI) which indicates the complexity of the microstructural environment of the imaged tissue, neurite orientation dispersion and density imaging (NODDI) [4] (see Section 3.4) and magnetic field correlation imaging (MFC) [5], a neuroimaging technique used for the quantitative assessment of iron within the brain. For more details on neuroimaging methods, see [6–9].

Neuroimaging has become a popular and powerful way of studying *in vivo* brain function and structure in health and disease. One important branch of neuroimaging is the search for a biomarker in neurological, neuropsychiatric and neurodevelopmental disorders (including dyslexia). For instance, promising strides here have been made using various neuroimaging techniques in Alzheimer's disease (MRI [10], fMRI [11], PET [12] and MEG [13]), schizophrenia (PET [14], EEG [15] and MEG [16]), attention deficit hyperactivity disorder (ADHD) (MEG and structural MRI [17], DKI [18], MRI and MFC [19]) and dyslexia (MEG and structural MRI [17], structural MRI [20], ERPs [21, 22], MEG [23] and fMRI [24]). It should be noted that some of the above cited papers explicitly claim the search for neuroimaging biomarkers, while others do not,

but the results reported can be considered as potential candidates for neuroimaging biomarkers. However, an obstacle to the development of neuroimaging biomarkers in neurodevelopmental disorders, such as dyslexia and ADHD, is sample heterogeneity, due to the phenotypic and aetiological complexity and co-occurrence of other disorders. Therefore, it is likely that no single neuroimaging biomarker (or even multiple biomarkers from the same domain) may be sufficient for reliable and accurate diagnosis of these disorders and there needs to be a shift towards identifying sets of biomarkers, possibly from different domains. The serious problem of sample heterogeneity which is associated with neurodevelopmental disorders was the main reason behind adopting a different approach in Reid's [25] fMRI study reviewed in this chapter.

## **1.2. Dyslexia and the most researched causal theories of this disorder**

'Percy F ... has always been a bright and intelligent boy, quick at games, and in no way inferior to others of his age. His great difficulty has been – and is now – his inability to learn to read. This inability is so remarkable, and so pronounced, that I have no doubt it is due to some congenital defect' [26, p.1378].

This chapter reviews the first fMRI study [25] which used a multiple case approach to investigate reading deficit in participants with similar difficulties to Percy F's struggles described 122 years ago. Such difficulties are nowadays defined as developmental dyslexia (henceforth dyslexia). The above example is only given to illustrate the profound and puzzling literacy difficulties experienced by individuals with dyslexia and not to discuss Morgan's [26] interpretation of reading difficulties as congenital word blindness. It should also be emphasised that despite such profound difficulties when learning to read, most individuals with dyslexia reach a reasonable level of reading ability, becoming compensated DPs.

Dyslexia is one of the most prevalent neurodevelopmental disorders—it affects from 5 to 17.5% of the English-speaking population [27]. DPs exhibit difficulties in learning to read, despite sociocultural opportunities, a scholarly education, adequate conventional instruction and intelligence, as well as intact sensory abilities [28]. It has been demonstrated [29] that the rates of reading disability are higher in boys than in girls. Untreated dyslexia is likely to have a serious impact on the life of an individual, including learning ability, self-esteem, mental health, relationships, social participation, employment and economic status. The vast majority of research on dyslexia has been conducted in English (an unrepresentative language in terms of grapheme-to-phoneme correspondence). More recent research across different languages indicates that dyslexia also occurs in other languages, including languages with an orthographic transparency higher than English [30–32]. Dyslexia is characterised by a strong heritable component [33]. Most research on dyslexia has focused on deficits; however, some publications have explored positive aspects of dyslexia [34]. There is now considerable evidence that dyslexia co-occurs more frequently than by chance with other neurodevelopmental disorders, such as ADHD and developmental coordination disorder (DCD). About 20–42% of reading disabled children also meets the criteria for ADHD [35, 36]. Furthermore, there is growing evidence that some reading impaired individuals exhibit motor difficulties [37, 38]. The prevalence of dyslexia and DCD co-occurrence are relatively high, for example, 63 and 60% in samples in [36] and [38], respectively.

There are three main, most researched causal theories of dyslexia, and each theory postulates a different and single underlying cause of literacy difficulties in dyslexia. A short description of each theory is included below, but the detailed review of these theories is beyond the scope of this chapter; interested readers are referred to the references and to Reid's publication [25]. According to the

phonological deficit theory (PDT) [39–41], phonological deficit is the underlying cause of dyslexia. This means that DPs have a specific impairment in the representation and processing of speech sounds (phonemes) [41] or a deficit in accessing intact phonological representations [42]. According to the PDT, the phonological deficit leads to poor grapheme-to-phoneme conversion and this in turn leads to poor reading. It is claimed that the phonological deficit also manifests itself on the behavioural level by difficulties in phonological fluency [32, 40], phonological awareness [40, 43] and verbal short-term memory [44, 45]. The deficit postulated by the PDT was specified on the biological level as the left (L) perisylvian region abnormality [46] and recently as the L temporoparietal abnormality and L frontal abnormality [47].

The visual magnocellular deficit theory (MDT) [48–50] claims that the underlying cause of literacy problems in dyslexia is not language specific but a more general impairment of the visual magnocellular system with spared parvocellular system. Magnocellular neurons are defined at the level of the retinal ganglion cell which have specific projections to the lateral geniculate nucleus (LGN) in the thalamus. The results in support of the MDT include reduced contrast sensitivity [51], unsteady binocular fixation [48] and a significantly higher threshold for the perception of coherent movement in random-dot kinematograms in DPs than in CPs [52]. The MDT claims that the visual magnocellular system impairment in dyslexia has a genetic origin. According to Stein [48], the clearest genetic result is for linkage to the region on the short arm of chromosome 6 which helps to control the production of antibodies (see also [53, 54] for recent studies showing association between motion deficit and the *DCDC2* gene). The magnocellular system is hypothesised to play an important role in reading and orthographic and phonological representations [48]. First, it subserves the process of image stabilisation and/or letter localisation in words during reading [55]. Second, it affects orthographic knowledge, through reading skill. Third, it affects phonological representations through orthographic representations [48]. For the most recent version of the MDT, see [56].

According to the cerebellar deficit theory (CDT), the underlying cause of dyslexia is a cerebellar impairment. Cerebellar dysfunction has been linked to problems in (1) motor skills, (2) perception and production in timing tasks, (3) automatization of motor skill and (4) classical conditioning of the eye-blink response. Dyslexia research has shown that DPs indeed exhibit deficits over a range of functions which rely on cerebellar processing, such as motor skills, including balancing [57], eye-blink conditioning [58] and time estimation [59]. Nicolson et al. [60] put forward a hypothetical ontogenetic causal chain according to which cerebellar deficit could lead to reading difficulties in dyslexia by two routes. The major route claims that cerebellar impairment leads to mild articulatory problems, which lead to an impoverished representation of the phonological characteristics of speech. In turn, this causes difficulties in phonological awareness and subsequently results in difficulties with learning to read. Furthermore, reduced articulation speed leads to reduced working memory. The second route claims that difficulties in reading acquisition stem from a cerebellar deficit which causes problems with automatising skills and knowledge, leading to problems with (1) automatic grapheme-to-phoneme conversion, (2) automatic word recognition, (3) automatic verbal working memory and (4) automatic awareness of the orthographic regularities. Motor problems (also caused by cerebellar impairment) lead to dysgraphia (writing impairment). Additionally, balance deficits are also caused by cerebellar deficit. However, these motor difficulties (except for the articulatory difficulties) and problems with balance do not lead to reading difficulties, but the underlying cerebellar deficit [60].

## **2. The first neuroimaging study to use a multiple case approach to investigate individual differences among DPs**

Most neuroimaging (and behavioural) studies which have been formulated within the main theories of dyslexia have shortcomings (for a review of studies, see [25]). First, they have used group comparisons which can cloud the less frequent differences between DPs and controls (CPs). Second, they mostly investigated a single underlying cause, hypothesised by one theory. Third, the majority of them concentrated on finding a deficit without empirically showing its relationship with reading deficit, which defines dyslexia. For instance, significantly lower BOLD signal in DPs (vs. CPs) was reported [61] in the R cerebellar cortex when learning a new sequence of finger presses and interpreted as support for the CDT. Another study [62] revealed lack of fMRI activation in V5/MT in DPs in contrast to CPs (while participants viewed a coherently moving, low-contrast, random-dot stimulus), and the results were interpreted as being in agreement with the MDT. However, a demonstration of a significant between-group difference on these variables does not show that there is a relationship with reading, even if DPs had a documented reading deficit, and their reading scores significantly differed from the CPs. This is because a given variable may be a correlate or biological marker of dyslexia, which is independent of any reading deficit [63].

The goal of Reid's study [25] was to shed more light on the neural correlates of reading deficit in dyslexia and address the above criticisms: First, by choosing a multiple case study to investigate individual differences among DPs. Second, by contrasting the hypotheses based on each of the main theories, on the neural correlates of the reading impairment, in individual DP (vs. CP), thereby detecting differences which otherwise would have been obscured in the between-group comparison, due to heterogeneity among DPs. The behavioural studies suggest that there are subtypes of dyslexia [32, 40, 64–68], but they cannot be investigated by focusing on one theory. Third, by focusing on a reading task using fMRI - which provides an opportunity to more directly investigate the relationship between the predictions of a given theory and the neural correlates of reading impairment in dyslexia.

### **2.1 Hypotheses**

First, if, as hypothesised by the PDT, the neural correlates of reading deficit in DPs lie within the phonological network, then DPs should show abnormal activation in all or some areas within this network. As the descriptive terms for phonological deficit on the biological level (L perisylvian, L temporoparietal and L frontal regions) were not detailed enough to thoroughly test the PDT on the neural level, a literature review was undertaken [25] and showed that phonological processing (operationalised as phonological awareness, naming and short-term memory) involves many brain areas but it is still unclear what role each area plays in phonological processing. Broadly speaking, the phonological processing network (also validated with the broader literature review presented in [25]) included the following L hemisphere areas: the inferior frontal gyrus (BA44/45)—Broca's area, Wernicke's area (BA22), the middle temporal gyrus (BA21), the insula, inferior parietal lobule (including the angular gyrus (BA39) and the supramarginal gyrus (BA40)), the precentral gyrus PMC (premotor cortex) (BA6), the fusiform gyrus (BA19/37) and the posterior fusiform gyrus. The role of the L posterior fusiform gyrus is unclear, with some researchers advocating its involvement exclusively in orthographic processing [69] and other investigators [70] in mapping orthography onto phonology. The above listed areas were used to test the PDT. To detect abnormality in the neural correlates of the reading impairment of a given DP, not

all the areas involved in phonological processing needed to exhibit atypical activation, because individuals might have differed in the neural implementation of the phonological network and/or in the presence of areas with atypical activation. The PDT also predicts that DPs should not show abnormal activations in the magnocellular system and the cerebellum, as predicted by the MDT and CDT, respectively.

Second, if, as predicted by the MDT, reading impairment in dyslexia is due to magnocellular abnormality, then DPs should show significantly lower activation in the V5/MT. The neuroimaging research on the MDT [62, 71] focused on the V5/MT area because it receives the input predominantly from the magnocellular stream [72]. The involvement of V5/MT in reading was demonstrated in a study by Liederman et al. [55] which showed that a virtual lesion of V5/MT, created by repetitive transcranial magnetic stimulation (rTMS) during reading in CPs, resulted in visual but not phonological errors. Furthermore, there may also be differences between CPs and DPs in other areas within the magnocellular system. In the study reported in [25], three areas in both hemispheres were investigated: the V5/MT, V1 and V2. This is because of (1) significant correlations between fMRI activation in these areas (under low mean luminance moving grating conditions), and reading performance were reported [73] and (2) V1 and V2 could be more reliably localised than the remaining motion-sensitive areas, using available cytoarchitectonic maps [74, 75]. Hypoactivation in L and right (R) V1 and/or in V2 was interpreted as supporting the MDT only if discovered jointly with underactivation in the V5/MT. The V5/MT receives input predominantly from the magnocellular stream [72], but V1 and V2 consist of partially separated magno and parvo cell inputs. Therefore, the underactivation of V1 and V2 may reflect underactivation of either parvo cells or magno cells or a combination of these. Hypoactivation in V1 and/or V2, with no underactivation in the V5/MT, was interpreted as a visual but not a magnocellular deficit. A hypothetical visual deficit theory (VDT) was put forward, and it was argued that in DPs who exhibited underactivation in V1 and/or V2, without hypoactivation of V5/MT, hypoactivation is in agreement with the VDT but not with the MDT.

Third, given, that according to the CDT, the underlying cause of dyslexia is a cerebellar impairment, one would predict that the neural correlates of reading problems in DPs are localised within the cerebellum and therefore DPs should show atypical activation during reading in some regions of the cerebellum. However, the CDT does not specify which cerebellar areas should be affected. As the research reported in [25] investigated reading, the focus there was mainly on the cerebellar language areas. Probably the most reliable results regarding the language areas in the cerebellum come from the meta-analysis by Stoodley and Schmahmann [76]. The areas include the R lobule VI (Hem), R and L Crus I (Hem), R Crus II (Hem), R Vermal lobule VIIAt (R Vermal lobule VI) and L lobule VI (Hem). These areas were selected to test the CDT in DPs' reading. Additionally, some areas were also included, either because they were shown to significantly differ in DPs and CPs (R Vermal lobule VI [20], the L and R Crus II and the paramedian R and L lobule (VIIB) [77]) or because they were activated during silent reading in CPs (L and R Crus I, L and R Crus II, L and R lobule VI and L and R lobule VIIB [78]). Most of these areas overlapped with Stoodley and Schmahmann's [76] regions.

Finally, it needs to be stated that the MDT and CDT also make additional predictions. The MDT postulates that the magnocellular system is important in the acquisition of accurate visual representations of the written, orthographic forms of words and that this is essential to grasp their structure at the phonemic level. Therefore, it has been hypothesised [49] that a deficient magnocellular system could be the underlying cause of deficient phonological representations and therefore of a phonological deficit. Hence it is possible that the hypoactivation in phonological areas (coupled with the hypoactivation in the V5/MT) in DPs during reading is also consistent with

the MDT (and with the PDT, as discussed above). However, the methods used in [25] do not allow for teasing apart whether the hypoactivation in phonological areas (co-occurring with hypoactivation in magnocellular areas) is 'purely phonological' or has been influenced by magnocellular malfunctioning. The hypoactivation in DPs in phonological areas in the presence (but not in the absence) of the hypoactivation of magnocellular areas is interpreted here as being consistent with the MDT (and with the PDT, as specified above). Moving to the CDT, it predicts that a phonological deficit (in phonological awareness and in reading) can be caused by a cerebellar impairment. Therefore it is possible that the hypoactivation in phonological areas (coupled with the hypoactivation in cerebellar areas) in DPs during reading, in Reid's study, may also be consistent with the CDT. However, the methodology used in [25] does not allow for teasing apart these effects. The hypoactivation in DPs in phonological areas in the presence (but not in the absence) of the hypoactivation of cerebellar areas was interpreted in [25] as being consistent with the CDT (and with the PDT, as specified above). It is important to keep in mind, however, that interpreting hypoactivation within the phonological areas as being also consistent with the MDT and CDT holds only if one takes the perspective of the MDT or CDT, respectively. In contrast, from the theoretical perspective of the PDT, such interpretations do not hold.

## 2.2 Participants

Thirty-eight adult native English speakers from three UK universities took part in Reid's study [25]. They were all right handed, with normal hearing, normal or corrected to normal vision, without clinical ADHD (defined as a score < 70 on the ADHD D index on Conners' scales [79]), without clinical DCD (as defined in DSM-IV [80]) or any other known sensory, neurological, psychiatric or neurodevelopmental disorders. There were indications that DP8 and DP15 may be 'at risk' of clinical DCD (They were the only DPs who responded 'yes' to the question on whether their DCD difficulties significantly interfered with their everyday life). DP8 and DP15 were included in Reid's study [25], but a DCD measure obtained from a questionnaire (based on DSM-IV, Adult DCD Checklist (DANDA—Developmental Adult Neuro-Diversity Association) and questions devised by A. Reid (see [25] for details) was used as a covariate in the fMRI analysis. Furthermore, DP8's and DP15's fMRI data were additionally analysed for possible DCD effects. Four participants were excluded from the analysis (1 CP did not provide a dyslexia diagnosis and 3 DPs because their fMRI data could not be salvaged by the recommended techniques [8]). Eighteen individual DPs and 16 CPs (treated as a control group) were entered into an fMRI multiple case analysis. All DPs (6 males and 12 females; mean age 21.28 years (SD = 3.3)) reported a history of persistent literacy difficulties (mainly with reading) and had a formal diagnosis of dyslexia. Twelve DPs (66.7%) disclosed that literacy problems occurred in one or more of their first-degree relatives. CPs (5 males and 11 females; mean age 21.38 years (SD = 6.03)) had no literacy problems or any other known sensory, neurological, psychiatric or neurodevelopmental disorders. Although the DP and CP groups were matched on years of education, age, handedness, verbal IQ, performance IQ and full scale IQ, this was not always the case in the multiple fMRI case analyses which compared every individual DP to CPs. Hence additionally, age, handedness and FSIQ were used as covariates in these analyses. For more details on participants and other aspects of the study, see [25].

## 2.3 Materials, stimuli and fMRI task

The participants were tested using a broad battery of behavioural measures (see [25] for details). The fMRI reading task reported in Reid [25] had three conditions.

Condition 1 consisted of 100 English words (high familiarity, imageability and concreteness, two-syllable, five to seven letters, with regular spelling selected from the MRC psycholinguistic database [81]); Condition 2 contained 100 pseudowords created by the substitution of consonants in the onset or middle of words from Condition 1. Condition 3 (the control condition) consisted of a fixation cross. The fMRI experiment had an event-related design [82] with stimuli from all conditions randomly intermixed. Each stimulus was displayed for 1000 milliseconds, with an interstimulus interval (ISI) of 3000 milliseconds and a stimulus onset asynchrony (SOA) of 4000 milliseconds. The focus in Reid's [25] communication was on word reading which involved the contrast of Conditions 1 and 3.

## 2.4 fMRI data acquisition

The MRI and fMRI data were acquired at the Aston University MRI Research Centre using a 3 T Trio Siemens scanner equipped with echo planar imaging and a standard eight-channel head coil. A high-resolution structural MRI image was acquired first, followed by fMRI data acquisition during the reading task. For fMRI data, 44 ( $3 \times 3 \times 3$  mm) slices, covering the whole brain, were acquired every 3 sec (TR = 3000 ms, TE = 30, flip angle = 90, FOVread = 192, FOVphase = 100) for a total of 404 volumes. In the scanner the participants were asked to silently read words and to keep their gaze fixed on the '+' sign shown in the centre of the field of view on the screen. They were asked to read every item carefully because there would be a posttest after the fMRI experiment. The posttest scores were summarised in *d Prime* and entered as covariates into the second-level neuroimaging analysis. To monitor participants' vigilance, they were required to press a response button (with their left index finger) when a black star (displayed during ISI) became red. This occurred on 10% of trials.

## 2.5 Data preprocessing

SPM5 was used to analyse (and preprocess) the fMRI data. The preprocessing involved realignment, slice timing correction, coregistration, segmentation, normalisation and smoothing [83]. Usually, realignment is run first and slice timing correction second; however, because each volume was acquired in slices in an interleaved fashion, starting from the bottom slice, the order of these two steps was swapped (John Ashburner, email communication, June 4, 2007). The slice timing correction was applied to correct the differences in slice acquisition times. The 'realign' function was used to remove confounds which can arise in the fMRI data from changes in signal intensity over time due to head motion. Realignment parameters were saved for each participant for each session and entered into the design matrix as covariates. A coregistration function was used to coregister the functional (MRI) and the structural (MRI) data so as to maximise their mutual information. A segmentation function was used to segment the structural image according to tissue probability, using default maps, creating grey and white matter images and a bias-field corrected structural image. The data were pooled into the same anatomical space using a spatial normalisation function to put the MRI images into a standard space defined by template images (corresponding to the space defined by the International Consortium for Brain Mapping (ICBM), NIH P-20 project). The data were smoothed with an 8-mm Gaussian kernel.

## 2.6 Data analysis

In the first-level analysis, the word condition was explicitly modelled. The control condition was implicitly modelled [84]. To avoid confounding the BOLD response



due to the 'Star' stimulus and 'Button Press', they were included in the design matrix as regressors. The shape of the canonical haemodynamic response function (HRF) (SPM5) was used to model the experimental haemodynamic response. Further inclusion of the dispersion and time derivatives was necessary to account for variations in the voxel-to-voxel and subject-to-subject responses, especially in the experiment that involved the DPs characterised by heterogeneity with respect to behavioural and neuroimaging findings. The time derivative allows for the variation in the peak response of plus or minus 1 second, whereas the dispersion derivative allows for the variation in the width of the response by a similar amount [83]. A t-contrast (Word>Fixation Cross) was tested in the first-level analysis. The second-level analysis focused on comparison of a given individual DP and the CPs (treated as a group). Data analysis in the second level involved a two-sample t-test. Two contrasts were tested: CPs > DP (hypoactivation) and DP > CPs (hyperactivation). A number of DPs showed elevated (but non-'clinical') scores on the ADHD and DCD measures in comparison to the CPs; hence these scores were entered into the second-level analysis as covariates. Participants' age, handedness, FSIQ and d Prime scores were also entered into the second-level analysis as covariates, as discussed above.

## 2.7 ROI analysis (mask)

There is growing evidence that different brain regions, such as BA44 and BA45 are characterised by high inter-participant structural variability [85]. Bearing this in mind, a mask for the ROI analysis was prepared mainly using cytoarchitectonic areas (see note for **Table 1**). The ROI mask consisted of 31 areas. Twenty-nine areas were created as individual ROIs in the AT (V1.8) [86], and two areas (not available in AT (V1.8)) were created as individual ROIs in MarsBar (version 0.43) [87]. The ROIs created in MarsBar were coregistered to the ROIs created in the AT (V1.8). All ROIs were combined (and binarised) into one mask using SPM5. The 31 ROI mask was coregistered in SPM5 (using the resliced option) to the fMRI data before running the ROI analysis. As DPs are usually characterised by considerable heterogeneity, activation in a brain area was considered as supporting a given hypothesis when the probability that a given voxel belonged to that area was 10% or higher [88].

## 2.8 Results and discussion

The multiple case analysis of DPs' performance on psychometric tests revealed marked heterogeneity among DPs, and this was in line with the previous findings [32, 40, 64–68] (see [25] for details). The neuroimaging results for underactivation in each individual DP, as compared to CPs (CPs > DPs) during word reading relative to the control condition, are shown in **Table 1** and **Figure 1** (see also Appendix B **Table 1** to **18** for MNI coordinates of the BOLD [25]). Hypoactivation is usually assumed to reflect a functional disruption in a system [89]. In the context of the dyslexia theories, hypoactivation in the hypothesised brain areas was interpreted as lending support for these theories. The contrast DP > CPs revealed brain areas which were hyperactivated by a given individual DP (vs. CPs) during word reading, relative to the control condition. Hyperactivation is usually interpreted as a correlate of a compensatory mechanism [89]. Because the dyslexia theories are concerned with a deficit and not compensatory mechanisms, hyperactivation of the brain areas associated with these main theories was not interpreted as evidence of support for them. An inspection of **Table 1** and **Figure 1** reveals that all individuals with dyslexia exhibited heterogeneous and complex patterns of hypoactivation which involved the areas predicted by the dyslexia theories. Five DPs showed overactivation; see text below.

ROI/DP	1	2	3	4	5	6	7	8	9	10	11	12	13	14	15	16	17	18
L area 44	+		+	✓	✓	+			+		+			+	+	+		
L area 45			+															
L area Ig1																		
L area Ig2																		
L area Id1																		
L area 6	+		+	✓			✓		+					+	+	+		+
L IPC PFop																		
L IPC L PFt																		
L IPC PF	+	✓	+	✓										+				+
L IPC PFm			+		✓		✓			+				+		+		+
L IPC PFcm	+																	
L IPC PGa															+			
L IPC PGp	+		+	✓		+		✓	+					+	+		✓	
L area TE3	+			✓										+				+
L MTG	+		+	✓										+		+		+
L FG	+			✓							+	+				+		+
L hOC5																		
R hOC5	+																	
L area 17									+									
R area 17								✓	+						+			
L area 18			+						+	+				+				+
R area 18			+	✓			✓	✓	+	+				+		+		+
L Lob. VIIa Cr.I		+	+		+	+	✓	+	+	+	+		✓	+	+	+		+
R Lob. VIIa Cr.I		+	+		+	+	✓	+	+	+	+		✓	+	+	+		+

ROI/DP	1	2	3	4	5	6	7	8	9	10	11	12	13	14	15	16	17	18
L Lob. VIIa Cr.II	+					✓					+	+					+	
R Lob. VIIa Cr.II	+	+	+	+	+	✓	+	+	+	+	+	✓	+	+	+	+	✓	+
L Lob. VI					+		✓	✓							+			+
R Lob. VI				+			✓	✓	+	+	+	+	+	+		+		
R Lob. VI (Ver.)													+	+				
L Lob. VIIb				✓														
R Lob. VIIIb																		

Note: 1-18, a unique number for every participant with dyslexia; the presence of underactivation within ROI in the individual DP is denoted by '+', (p < .05 FDR, corrected for multiple comparisons) and '✓' (p < .001, uncorrected for multiple comparisons); 31 ROI included in the mask, L area 44 and L area 45 [90] (equivalent to Broca's area L BA44 and L BA45), L areas Ig1, Ig2, Id1 (the posterior insula) [91], L area 6 (the premotor cortex, equivalent to L BA6) [92], L IPC PFP, L IPC L PFT, L IPC PF, L IPC PFm and L IPC PFCm (inferior parietal lobule, these areas approximately cover the region of L BA40 on the supramarginal gyrus with extension into the depth of the Sylvian fissure [93]); L IPC PGa and IPC PGP [94] (inferior parietal cortex, these areas are located approximately at the position of the angular gyrus (BA39), L area TE3 in the lateral part of the superior temporal gyrus, perhaps homologous to BA22 (Wernicke's area) [95], the L middle temporal gyrus (L MTGL), and the L fusiform gyrus (L FG) [96], the L hOC5 and R hOC5 [75] (equivalent to L and R V1 and V2) and nine cerebellar regions (L Lobule VIIa Crus I (Hem), R Lobule VIIa Crus I (Hem), R Lobule VIIa Crus II (Hem), L Lobule VIIa Crus II (Hem), R Lobule VIIa Crus II (Hem), L Lobule VI (Hem), R Lobule VI (Hem), R Lobule VI (Vermis), L Lobule VIIIb (Hem) and R Lobule VIIIb (Hem) [97]; Lob. denotes lobule; all lobules are hemispheric, except one (R Lob. VI (Ver.)) which is vermal.

**Table 1.**  
 Brain areas (ROI) underactivated in individual DPs (CIPs > DPs).

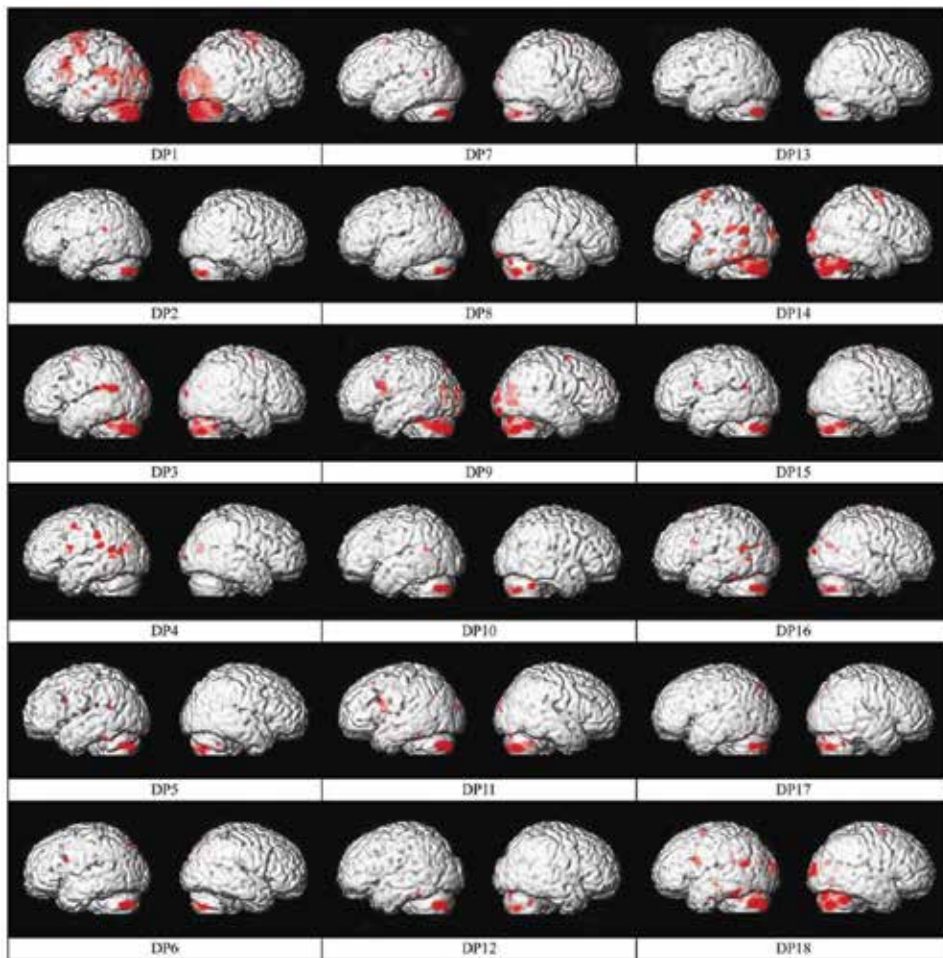


**Figure 1.**

*Clusters of underactivation (CPs > DP) for individual DPs. Underactivation is superimposed on a volume-rendered brain (a spatially normalised anatomical image for an individual DP). Cluster size threshold  $k \geq 6$ . An ROI mask was applied; see Section 2.7 and note for Table 1.*

The main goal of the research reported in [25] was to shed more light on the underlying reading impairment (which defines dyslexia) in adult DPs, as hypothesised by the PDT, MDT and CDT, with special focus on individual differences among DPs. When the hypotheses based on the three main theories of dyslexia were contrasted in the same DPs, the neural correlates of word reading deficit were consistent with the PDT in 17 cases (94.4%), with the CDT in 18 cases (100%) and in 1 case (5.5%) with the MDT. Furthermore, the reading deficit of 10 cases (56%) was consistent with the VDT but not with the MDT.

A more detailed inspection of the neuroimaging results for reading revealed that when hypotheses based on the three main theories are tested in individual DPs, DPs showed complex and heterogeneous patterns of underactivation in the brain regions predicted by the dyslexia theories. For instance, DP1 showed hypoactivation in eight areas predicted by the PDT (L area 6 (BA6), L area 44 (BA44), L middle temporal gyrus (BA21), L fusiform gyrus (BA19/37), L TE 3 (part of BA22), L IPC (PF) (BA40), L IPC (PFcm) (BA40) and L IPC (PGp) (BA39)), one area hypothesised by the MDT (R hOC5 (V5/MT)) and three areas predicted by the CDT (R Lobule VIIa Crus I (Hem), L Lobule VIIa Crus II (Hem) and R Lobule VIIa Crus II (Hem)). DP10 exhibited hypoactivation in one area hypothesised by the PDT (L IPC

(PFm) (BA40)) and four areas predicted by the CDT (L Lobule VIIa Crus I (Hem), R Lobule VIIa Crus I (Hem), R Lobule VIIa Crus II (Hem) and R Lobule VI (Hem)). In contrast, DP13 hypoactivated only areas predicted by the CDT (L Lobule VIIa Crus I (Hem), R Lobule VIIa Crus I (Hem) and R Lobule VIIa Crus II (Hem)) (see **Table 1** and **Figure 1** for the other cases).

Moreover, the neuroimaging data exhibited a high degree of individual differences. Even if the neural correlates of reading disorder in two DPs were consistent with the same theory, the neural correlates in those DPs could differ. For instance, within the framework of the PDT, DP6 showed hypoactivation in the L area 44 (BA44) and L IPC (PGp) (BA39); DP10 exhibited hypoactivation in L IPC (PFm) (BA40), whereas DP12 hypoactivated L FG (fusiform gyrus). This is also the case for the neural correlates of reading deficit hypothesised by the CDT. For instance, DP1 showed hypoactivation in R Lobule VIIa Crus I (Hem), L Lobule VIIa Crus II (Hem) and R Lobule VIIa Crus II (Hem); DP14 hypoactivated L Lobule VIIa Crus I (Hem), R Lobule VIIa Crus I (Hem), R Lobule VIIa Crus II (Hem), R Lobule VI (Hem) and R Lobule VI (Vermis), whereas DP4 showed hypoactivation only in L Lobule VIIb (Hem). The traditional approach, based on group comparison where only between-group differences (DPs vs. CPs) were tested, could not reveal the individual differences among DPs as shown in [25].

The results revealed considerable individual differences in patterns of hypoactivation within the reading network among DPs, which are unexpected in the context of the between-group comparison studies, which have dominated neuroimaging research on dyslexia. Nevertheless, they are perhaps less surprising if one considers the fact that reading is a relatively new (less than 6000 years old) cultural invention in human evolutionary history. It requires areas which evolved for vision, language and associative learning. Reading acquisition is an exercise in brain plasticity; the goal of which is to create an efficient reading network which enables the unimpaired reader to get from visual precept to meaning in approximately 250 milliseconds [98]. As in the ontogenetic development of an individual, a number of brain regions need to be 'adapted' for reading; it is perhaps not surprising that in different DPs, different components may be deficient.

Five (28%) DPs in the study [25] exhibited hyperactivation. Similar to the patterns of underactivation, overactivation differed in different DPs. DP4 exhibited overactivation in L area 6, L insula (Ig2), L IPC (PFm), L IPC (PGa), L area 17, R area 17, L area 18 and R area 18, R Lobule VIIa Crus I (Hem) and L Lobule VI (Hem). DP5 hyperactivated L area 17 and R area 18. DP8 overactivated L insula (Id1) and L area 18. DP13 show hyperactivation in L area 6, L middle temporal gyrus and L area 17. Finally, DP17 exhibited overactivation in L fusiform gyrus, insula (Id1) and L Lobule VIIb (Hem). All results for ROI analyses at  $p < 0.001$  (uncorrected for multiple comparisons), except for DP4's results at  $p < 0.05$  (FDR). Overactivation in some DPs in the areas hypothesised to show underactivation in DPs by the PDT indicates that a compensatory network is not limited to the frontal regions, as suggested by a number of studies based on group comparisons (for instance, see [89]), but involves brain regions distributed across the phonological reading network. Cerebellar and secondary and/or primary visual areas were overactivated in two and four DPs, respectively, suggesting the existence of a potential compensatory network within these brain regions.

An important common characteristic of the dyslexia theories (the PDT, MDT and CDT) investigated in [25] is the assumption that a single underlying deficit is necessary and sufficient to cause symptoms of dyslexia: phonological, or visual magnocellular, or cerebellar, respectively. As mentioned above, one of the limitations of research on dyslexia is that it has mostly investigated one theory in a given sample of DPs. The findings reported in [25] reveal that if one investigates

individual DPs, comparing the predictions of all the main dyslexia theories, the neural correlates of reading for all DPs (except one DP) were in agreement with the hypotheses based on more than one theory. In the sample reported in [25], the neuroimaging results for one case (5.6%) were in agreement with the PDT, MDT and CDT and for another case with only the CDT. The results for six cases (33.3%) were in agreement with the PDT and CDT and the findings for 10 cases (55.6%) with the PDT, CDT and VDT. The results for all, but one DP, supported a multiple deficit model.

Supporters of the PDT may argue that the neural correlates of reading in all cases (except for DP13) are in agreement with the core deficit, as hypothesised by the PDT and that the hypoactivation in the cerebellum and/or magnocellular areas in these DPs just co-occurs with dyslexia. As highlighted above, contrary to previous studies, Reid's study [25] investigated the more direct link between reading deficit in DPs and the predictions of the main dyslexia theories on the neural level by using an fMRI reading task. Hence it seems reasonable to interpret the findings of hypoactivation in the areas hypothesised by the PDT and the CDT, in the same DP, as lending support to the claim that reading in a given DP is consistent with the predictions of both theories and therefore both phonological areas and cerebellar areas contribute to the reading impairment in a given DP and the CDT deficit is not just co-occurring with no causal effect on reading deficit (as argued by the protagonists of the PDT). The same reasoning also applies to DPs who exhibited underactivation in both phonological and visual/magnocellular areas.

Taking into consideration the additional predictions of the CDT (discussed above), it might be the case that the underactivation in phonological areas in all DPs (except DP13) is also consistent with the CDT (and with the PDT), but this holds only from the perspective of the CDT and not the perspective of the PDT. Finally, it is also possible that the underactivation in phonological areas in DP1 is also in line with the additional predictions of the MDT (discussed earlier); however, this is true only from the perspective of the MDT and not from the perspective of the PDT (see Section 3.1 for further discussion).

A single deficit model has been dominant for many years in the research on dyslexia and other neurodevelopmental disorders. Each dyslexia theory postulates a different and single underlying cause of dyslexia. However, a single deficit model, although parsimonious and straightforward to test, has limitations. For instance, it cannot explain cases which exhibit a single deficit but do not have a reading disorder. Such cases have been reported in longitudinal studies involving children 'at risk' of dyslexia [99]. Reid et al. [32] also reported cases of adult CPs, who, although exhibiting a phonological deficit, did not have a reading impairment. Furthermore, the single deficit model cannot account for the more frequent than chance co-occurrence of other neurodevelopmental disorders with dyslexia (see below for a further discussion). Therefore, Pennington [100] formulated a multiple deficit model (MMD). The MMD recognises the fact that there are multitudes of environmental and genetic risk factors and that they do not operate independently. It is possible that they are correlated with each other or that they share effects of gene-by-environment interaction, or genes may interact with each other as they are part of the genetic system. The model does not specify the causal connections between the levels of analyses, including feedback loops from the behavioural level to the neural system level (or even to the aetiology level). The strength and existence of causal connections need to be resolved empirically [100]. Multidisciplinary research on the underlying causes of reading disorder in dyslexia within the MMD holds significant promise.

### **3. Future directions**

#### **3.1 Neuroimaging studies testing a further refined set of brain areas (including areas hypothesised by other dyslexia theories) in longitudinal designs**

Research on the brain areas involved in language processing and reading, including those areas hypothesised by the main theories of dyslexia, is active. For instance, there is now growing evidence of the involvement of subcortical brain areas in reading and language skills [101, 102]. Also new research has been reported for the MDT. For instance, a high-resolution proton density-weighted MRI study [103] revealed that L LGN (but not R LGN) was significantly smaller in volume and differed in shape *in vivo* in DPs (vs. CPs). These results are consistent with the MDT, and future neuroimaging research testing the MDT needs to include LGN as an ROI in a neuroimaging study on reading deficit in DPs. Furthermore, there are other theories of dyslexia, for instance, the auditory MDT [48] and the low-frequency phase-locking mechanism deficit theory [104]. Further research on the underlying reading deficits in dyslexia, using a refined set of brain areas (including also areas hypothesised by the other theories of dyslexia), is warranted, and it is argued below that longitudinal designs are indispensable here.

The study presented in [25] investigated reading in adult DPs in an fMRI task. Although such studies are valuable as they provide insight into the neural correlates of reading in a mature system, it is possible that the adult neural system may have been significantly or partially altered due to compensatory mechanisms. Given that reading is a learned skill that is acquired through instruction and practice over a relatively long period of time, it is likely that brain-based findings are going to be dynamic, and therefore longitudinal neuroimaging studies, starting with newborns with familial risk of dyslexia, are indispensable in tracking the developmental trajectory of reading deficits in dyslexia. Longitudinal studies may also be successful in testing the additional predictions of the CDT and MDT which could not be resolved in Reid's study [25].

#### **3.2 Controlling the effects of co-occurring neurodevelopmental disorders**

The current research indicates that co-occurrence of neurodevelopmental disorders is most likely more common than cases of 'pure' disorders [36]. A detailed history was taken in Reid's study [25] from participants regarding different disorders, and measures were collected for ADHD and DCD and entered into the fMRI analyses as covariates. This procedure ensured that the results were not confounded by these variables. Furthermore, the supplementary fMRI analyses showed that two DPs (11%) who were identified as possibly being at risk of clinical DCD exhibited underactivation in the areas consistent with DCD, but the underactivated areas for DP8 and DP15 differed (see [25] for details). These findings underscore the co-occurrence of these neurodevelopmental disorders and heterogeneity among participants who are at risk of clinical DCD.

There is growing evidence that dyslexia may co-occur with other disorders, such as specific language impairment (SLI), speech sound disorder (SSD), autism spectrum disorder (ASD), dyscalculia, conduct disorder, oppositional defiant disorder, anxiety, depression and disruptive, impulse-control and conduct disorders (CDs). Currently the relationship between these disorders and dyslexia is unclear [105]. It should be emphasised here that, although some efforts, especially more recently, are made to control the effects of some co-occurring disorders, the effects of some other co-occurring disorders are not controlled for in dyslexia studies. Therefore there is an urgent need for future research on the underlying causes of reading

deficit in dyslexia to control for the effects of the co-occurring disorders either by the exclusion of cases with such disorders or by collecting appropriate data (including genetic data, where available) to be used as covariates in the analyses.

The issue of co-occurring disorders is complex and can be further underscored by an observation that a person with a given neurodevelopmental disorder (e.g. dyslexia) may have first-degree relatives diagnosed with different neurodevelopmental disorders, for example, one with ADHD and another with DCD (Deborah Dewey, personal communication, July 2, 2015). It is currently unclear why this is the case, but it may suggest that genes that affect one neurodevelopmental disorder are also likely to affect other neurodevelopmental disorders [106]. The field of molecular genetics of co-occurring neurodevelopmental disorders is young. However, some findings have already suggested that common single-nucleotide polymorphisms on a number of chromosomes increase susceptibility to both dyslexia and SLI [107]. Research investigating generalist gene hypothesis [106], de novo gene mutations [107] and pleiotropic effects [108], using state-of-the-art molecular technologies, such as high-throughput genotyping and next-generation sequencing of whole genomes, holds the promise of providing important answers here. In summary, molecular genetics of co-occurring neurodevelopmental disorders makes progress in identifying genetic components which increase the susceptibility to more than one neurodevelopmental disorder. The more is known here, the easier it would be to also control the genetic component in experimental work. It must be emphasised that co-occurrence of neurodevelopmental disorders cannot be ignored in the future research on dyslexia because it is a potentially serious confound which is likely to distort results. See, for instance [109, 110], for findings which show that ADHD symptoms mediate deficits in developmental dyslexia.

### **3.3 Using a variety of imaging tools in dyslexia research**

A promising way forward in dyslexia research would be to test individual DPs (or samples of DPs as homogenous, as possible, with respect to behavioural and genetic profiles) using various neuroimaging techniques, in addition to fMRI, which would allow for a fuller characterisation of DPs' neural profiles, including the neural correlates of reading deficit. Some attempts have already been made; for instance, a recent study [111] used structural MRI, diffusion MRI and probabilistic tractography to investigate the structural connections of the visual sensory pathway in dyslexia *in vivo*. The results revealed altered structural connectivity in DPs in the direct pathway between the L LGN and L V5/MT but not between the L LGN and L V1. Another study [112] combined fMRI with multi-voxel pattern analysis and functional and structural connectivity analysis of DTI data in adult DPs. The results revealed that phonetic representations in the L and R auditory cortex were intact, whereas anatomical and functional connections found between these areas and the L inferior frontal gyrus were disrupted, suggesting an access deficit.

Another fruitful way forward would be to ask novel questions using neuroimaging. Pugh et al. magnetic resonance spectroscopy (MRS) study [113] was the first to test the role of multiple metabolites in developing readers. The authors reported an inverse relationship between both glutamate and choline and reading ability, such that higher concentrations of these metabolites were associated with lower reading scores. Given that heightened levels of glutamate can reflect hyperexcitability [114], whereas heightened levels of choline are associated with abnormal white matter organisation [115], the results reported in [113] suggest potential links between abnormal white matter organisation and reading deficit and hyperexcitability and reading deficit in atypical brain development and reading acquisition. The findings reported in [113] are cited (among others) in support of a recently formulated neural noise hypothesis (NNH) of dyslexia (see [116] for details).



Finally, recent MRI advances, such as multiband fMRI [117] and high-field MRI [118], promise to increase the spatial and/or temporal resolution of MRI and fMRI. Also, recent developments of more sophisticated diffusion MRI techniques, such as neurite orientation dispersion and density imaging (NODDI), hold promise of new insights into white matter structure and organisation in DPs (see Section 3.4 for further discussion of this). Furthermore, new developments in MEG also look promising. For instance, advanced preprocessing techniques which enable decomposition of the signal into components with origin inside and outside the head increase the signal-to-noise ratio by approximately 100%, enabling therefore even one-trial measurements with the standard MEG systems (e.g. whole head 306 Elekta or 275 CTF channel systems). Furthermore, optically pumped magnetometers (which allow MEG sensors to get closer to the head) should considerably increase the signal-to-noise ratio of MEG [119]. As the defining characteristic of dyslexia is impaired reading—a skill characterised by extremely rapid and inter-locked processing events—it is likely that MEG (with its relatively high temporal resolution) would play a particularly important role in providing valuable insights into the underlying causes of reading deficit in this neurodevelopmental disorder. In summary, the advances discussed above offer new possibilities in dyslexia research, so that dyslexia endophenotypes can be investigated with higher spatial and temporal resolution, increasing the chance of elucidating the underlying causes of reading disorder in dyslexia, as well as reliable biomarkers for dyslexia.

### 3.4 Imaging genetics

The neuroimaging data undoubtedly provide a description of endophenotypes in dyslexia, but they do not offer an explanation of what causes such endophenotypes. As discussed above, Reid's study [25] contrasted, on the neural level, the explanatory frameworks of the main dyslexia theories, but an explanation at the genetic level was not investigated (as genetic data were not available for the studied DPs). Given findings on dyslexia within the fields of molecular genetics and imaging genetics, it is likely that the heterogeneity among DP's phenotypes and endophenotypes reported in [25] is due in part to dyslexia risk genes.

Imaging genetics offers a bridge between behavioural measures and the brain. Relatively direct connections have been made between (1) brain function and dyslexia risk genes and (2) brain anatomy and dyslexia risk genes [120]. As a full summary of studies on imaging genetics in DPs (and in CPs) is beyond the scope of this chapter, interested readers are referred to the relevant reviews [102, 121]. Findings on brain function and genes associated with dyslexia are briefly summarised first. Cope et al.'s study [122] reported the strongest association between an fMRI activation for a reading task in the L anterior inferior parietal lobe and tandem repeat BV677278 in *DCDC2*. Another fMRI study [123], involving CPs and a reading task, reported that (1) single-nucleotide polymorphisms (SNPs) rs6980093 and rs7799109 (in *FOXP2*) were associated with variations of activation in the L frontal cortex and (2) SNP rs17243157 in the *KIAA0319/TTRAP/THEM2* locus was associated with asymmetry in the functional activation of the superior temporal sulcus. Wilcke et al.'s fMRI study [124] revealed a significant main effect for 'genetic risk' of *FOXP2* variant (rs12533005-G) in a temporoparietal area (significantly lower activation in the 'at risk of dyslexia' group than in the 'non-at-risk' group in the angular and supramarginal gyri). A MEG study [125] reported that DPs with a weakly expressing haplotype of *ROBO1* exhibited defective interaural interaction and the extent of the deficit correlated with the *ROBO1* expression level. Finally, another MEG study [126] reported that about half of DPs exhibited significantly higher levels of variability in their cortical responses to auditory and visual stimuli

in several brain areas of the reading network. A positive and significant relationship between the degree of neural variability in the primary auditory cortex across both DPs and CPs and the number of risk alleles at rs6935076 in *KIAA0319* was found, supporting the link between *KIAA0319* and neural variability.

Moving to studies which focused on brain structure and dyslexia risk genes, four publications need to be mentioned. A voxel-based morphometry (VBM) study [127] showed that participants with high genetic risk variants in *TNFRSF1B* exhibited significantly lower grey matter (GM) probability in Heschl's gyrus/posterior superior temporal sulcus (HG/pSTS) but significantly higher GM probability in pSTS and the converse was true for participants with low genetic risk variants in *TNFRSF1B*. A structural MRI study [128] reported that *DYX1C1*, *DCDC2* and *KIAA0319* contained SNPs that significantly correlated with white matter volume in the L temporoparietal area and that white matter volume influenced reading ability in a general population sample. Finally, two studies need to be briefly discussed here—both using DTI. It should be noted that DTI (and a more sophisticated diffusion MRI techniques, such as NODDI, mentioned above, which provides more specific markers of brain tissue microstructure than standard indices from DTI) could become particularly important neuroimaging techniques in dyslexia research when combined with genetic measures because there is evidence that suggests that some dyslexia risk candidate genes (e.g. *DCDC2*, *KIAA0319*, *DYX1C1*, *FOXP2* and *CNTNAP2*) are involved in neuronal migration (a period in brain development during which young neurons 'look' for their final destination in the brain; this process requires stringent controls that are genetically governed) and/or neurite outgrowth [102]. Such genes (together with the environment and gene-by-environment interaction) may contribute to shaping the brain's white matter structure which can be inferred from the results obtained from MRI diffusion techniques. One of the first studies [129], which combined genetic, DTI (and behavioural) measures, reported that *MRPL19/C2ORF3* was associated with general cognitive ability in DPs and participants with SLI. Also associations between white matter structure measured using DTI and genotypes at the *MRPL19/C2ORF3* (in an independent sample) were found in the posterior corpus callosum and cingulum connecting the temporal, parietal and occipital areas. More recently, a voxel-based DTI study [130] revealed that DPs with a deletion in *DCDC2*/intron 2 compared to CPs exhibited significantly lower fractional anisotropy (FA) in a number of L hemisphere areas (including superior longitudinal fasciculus, arcuate fasciculus, inferior longitudinal fasciculus, optic radiation, corpus callosum, inferior cerebellar pedunculus and two R hemisphere areas (superior longitudinal fasciculus and corpus callosum)), indicating anatomical abnormalities of these white matter structures.

Although imaging genetics is a relatively young field and most findings need to be replicated, endophenotypes uncovered by imaging genetics hold promise for building a link between the behavioural and genetic characteristics of DPs [131]. Currently, however, the imaging genetics results are insufficient to obtain a full picture of the underlying causes of reading deficit in dyslexia. Advancement of imaging genetics in dyslexia needs to proceed in three major ways. First, new hypothesis-driven imaging genetic studies must be designed to investigate the function of neuronal migration (and other) genes and their relationships with well-characterised cognitive and sensory vulnerability and to find connections between such susceptibility variants and neuroanatomical endophenotypes [102]. The integration of specific behavioural, imaging and genetic data may result in the identification of brain areas with gene and behavioural specific effects or with wide-spread effects [102]. Second, although valuable results have emerged from known dyslexia risk genes, they cannot test other genetic impacts on the overall reading deficits in dyslexia. Therefore, sequencing studies and genome-wide association studies (GWAS) are needed, so that new genes associated with risk of dyslexia can

be discovered and their role tested in the neuroimaging studies, providing a fuller picture of phenotypes and endophenotypes in dyslexia [121]. Such attempts have already started; for instance, a GWAS [132] reported that mismatch negativity (MMN) (which reflects automatic speech deviance processing and is abnormal in DPs) was significantly associated with an intergenic SNP on chromosome 4q32.1. This SNP is hypothesised to have a potential effect on the expression of *SLC2A3*—a gene that encodes a neuronal glucose transporter. The results suggest a possible trans-regulation effect on *SLC2A3*, which might cause glucose deficits in DPs and this in turn may account for DPs' attenuated MMN response. Third, as behavioural deficits overlap across neurodevelopmental disorders, it is of importance to include in the imaging genetics genes associated with different co-occurring disorders, including dyslexia. Such attempts have already been reported in dyslexia with respect to, for instance, *FOXP2* [124]—a gene originally associated with developmental verbal dyspraxia and included in imaging genetics in this disorder [133].

### **3.5 Neuroimaging intergenerational transmission of brain circuitry**

Intergenerational transmission is defined as 'the transfer of traits from parents to offspring, including genetic and non-genetic influences. For example, the impact of prenatal effects (e.g. parent nutrition and in utero environment) as well as postnatal rearing effects and other environmental factors could lead to epigenetic or behavioural changes in the offspring, which are thereby intergenerationally transmitted' [134, p. 644]. Intergenerational neuroimaging is a new approach which uses neuroimaging to investigate the relationship of cognitive and neural phenotypes between children and their parents. It holds the promise of shedding light on the ontogeny of complex neurodevelopmental disorders, including dyslexia. One of the major goals of neuroimaging intergenerational transmission of brain circuitry in such disorders is to dissociate the different sources of intergenerational effects on the brain circuitry on dyslexia by contrasting parent–child pairs from natural conception, adoptive families and in vitro fertilisation (IVF). Such designs have a potential in addressing many important questions in dyslexia research, including (1) intergenerational effects on the brain structure and function (including those supporting reading ability) and (2) the impact of gender-specific effects at the prenatal stage (especially important as dyslexia is more prevalent in males [29]), including the effects of prenatal testosterone levels on brain development, epigenetic effects of estrogen on dyslexia risk genes and gender-specific transmission patterns in reading-related brain circuits in individuals who haven't yet learnt to read [135].

## **4. Conclusion**

The results from the first neuroimaging study to use a multiple case approach to investigate individual differences among DPs [25], reviewed here, revealed that DPs are characterised by marked heterogeneity and complexity in the neural correlates of their reading deficit; even if the reading deficit of two DPs was consistent with the same theory, their affected brain areas could differ. The results further show that the neural correlates of reading deficit for all (except one) DPs were consistent with more than one theory, supporting a multiple deficit model. It is suggested that future research on causes of reading deficit in dyslexia, to make significant progress, would need to (1) focus on the multiple deficit model [100], (2) use neuroimaging to test a further refined set of brain areas (including areas hypothesised by other dyslexia theories) in longitudinal designs, (3) control the effects of co-occurring neurodevelopmental disorders, (4) use different imaging tools

(high-field MRI (including diffusion techniques), multiband fMRI and MEG with optically pumped magnetometers), (5) progress imaging genetics and (6) pursue the neuroimaging intergenerational transmission of brain circuitry.

## **Acknowledgements**

**Figure 1** is republished with permission of Nova Science Publishers, Inc., from Reid, A.A., An fMRI multiple case study of the neural correlates of reading deficit in individuals with developmental dyslexia: Theoretical implications, in *Advances in Neuroimaging Research*, 2014; permission conveyed through Copyright Clearance Center, Inc..

The Lord Dowding Fund financed the MRI scanning for Reid's study [25]. Thanks are due to the participants and to Joel Talcott, Liz Wilkinson, Simon Eickhoff, the Aston Neuroimaging Group and the FIL Methods Group for help and advice with various aspects of the study [25].

## **Conflict of interest**


The author declares no conflict of interest.

## **Author details**

Agnieszka A. Reid  
Independent Researcher, Cambridge, UK

\*Address all correspondence to: [agnieszka.reid@virginmedia.com](mailto:agnieszka.reid@virginmedia.com)

## **IntechOpen**

© 2018 The Author(s). Licensee IntechOpen. This chapter is distributed under the terms of the Creative Commons Attribution License (<http://creativecommons.org/licenses/by/3.0>), which permits unrestricted use, distribution, and reproduction in any medium, provided the original work is properly cited. 

## References

- [1] Mazziotta JC. Time and space. In: Toga AW, Mazziotta JC, editors. *Brain Mapping: The Methods*. San Diego, USA: Academic Press; 2002. pp. 33-46
- [2] Kamali A et al. Diffusion tensor tractography of the mammillothalamic tract in the human brain using a high spatial resolution DTI technique. *Scientific Reports*. 2018;**8**(1):5229
- [3] Steven AJ, Zhuo J, Melhem ER. Diffusion kurtosis imaging: An emerging technique for evaluating the microstructural environment of the brain. *American Journal of Roentgenology*. 2014;**202**(1):W26-W33
- [4] Zhang H et al. NODDI: Practical in vivo neurite orientation dispersion and density imaging of the human brain. *NeuroImage*. 2012;**61**(4):1000-1016
- [5] Jensen JH et al. Magnetic field correlation imaging. *Magnetic Resonance in Medicine*. 2006;**55**(6):1350-1361
- [6] Hanson SJ, Bunzl M, editors. *Foundational Issues in Human Brain Mapping*. Kindle Edition. Cambridge, MA: MIT Press; 2010
- [7] Jones DK, editor. *Diffusion MRI. Theory, Methods and Applications*. Oxford: Oxford University Press; 2011
- [8] Poldrack RA, Mumford JA, Nichols TE. *Handbook of Functional MRI Data Analysis*. Cambridge: Cambridge University Press; 2011
- [9] Toga AW, Mazziotta JC, editors. *Brain Mapping: The Methods*. 2nd ed. San Diego, USA: Academic Press; 2002
- [10] Frisoni GB et al. Preliminary evidence of validity of the revised criteria for Alzheimer disease diagnosis: Report of 2 cases. *Alzheimer Disease and Associated Disorders*. 2010;**24**(1):108-114
- [11] Wagner AD. Early detection of Alzheimer's disease: An fMRI marker for people at risk? *Nature Neuroscience*. 2000;**3**(10):973-974
- [12] Nobili F et al. Unawareness of memory deficit in amnesic MCI: FDG-PET findings. *Journal of Alzheimer's Disease*. 2010;**22**(3):993-1003
- [13] Josef Golubic S et al. MEG biomarker of Alzheimer's disease: Absence of a prefrontal generator during auditory sensory gating. *Human Brain Mapping*. 2017;**38**(10):5180-5194
- [14] Bose SK et al. Classification of schizophrenic patients and healthy controls using [18F] fluorodopa PET imaging. *Schizophrenia Research*. 2008;**106**(2-3):148-155
- [15] Taylor JA et al. Auditory prediction errors as individual biomarkers of schizophrenia. *Neuroimage: Clinical*. 2017;**15**:264-273
- [16] Bowyer SM et al. Potential biomarkers of schizophrenia from MEG resting-state functional connectivity networks: Preliminary data. *Journal of Behavioral and Brain Science*. 2015;**5**(01):1-11
- [17] Serrallach B et al. Neural biomarkers for dyslexia, ADHD, and ADD in the auditory cortex of children. *Frontiers in Neuroscience*. 2016;**10**:324
- [18] Adisetiyo V et al. Attention-deficit/hyperactivity disorder without comorbidity is associated with distinct atypical patterns of cerebral microstructural development. *Human Brain Mapping*. 2014;**35**(5):2148-2162

- [19] Adisetiyo V et al. Multimodal MR imaging of brain iron in attention deficit hyperactivity disorder: A noninvasive biomarker that responds to psychostimulant treatment? *Radiology*. 2014;**272**(2):524-532
- [20] Pernet CR et al. Brain classification reveals the right cerebellum as the best biomarker of dyslexia. *BMC Neuroscience*. 2009;**10**:67
- [21] Guttorm TK et al. Newborn event-related potentials predict poorer pre-reading skills in children at risk for dyslexia. *Journal of Learning Disabilities*. 2010;**43**(5):391-401
- [22] Maurer U et al. Impaired tuning of a fast occipito-temporal response for print in dyslexic children learning to read. *Brain*. 2007;**130**(Pt 12):3200-3210
- [23] Salmelin R, Helenius P, Service E. Neurophysiology of fluent and impaired reading: A magnetoencephalographic approach. *Journal of Clinical Neurophysiology*. 2000;**17**(2):163-174
- [24] Perrachione TK et al. Dysfunction of rapid neural adaptation in dyslexia. *Neuron*. 2016;**92**(6):1383-1397
- [25] Reid AA. An fMRI multiple case study of the neural correlates of reading deficit in individuals with developmental dyslexia: Theoretical implications. In: Asher-Hansley V, editor. *Advances in Neuroimaging Research*. New York: Nova Science Publishers; 2014. pp. 1-119
- [26] Morgan P. A case study of congenital word blindness. *British Medical Journal*. 1896;**7**:1378-1379
- [27] Shaywitz SE. Current concepts: Dyslexia. *The New England Journal of Medicine*. 1998;**338**:307-312
- [28] World Health Organization. *The International Classification of Diseases. Classification of Mental and Behavioural Disorders*. Vol. 10. Geneva: World Health Organization Publications; 1993
- [29] Rutter M et al. Sex differences in developmental reading disability: New findings from 4 epidemiological studies. *Journal of the American Medical Association*. 2004;**291**(16):2007-2012
- [30] Goulandris N, editor. *Dyslexia in Different Languages. Cross-Linguistic Comparisons*. London: Whurr; 2003
- [31] Reid AA. Developmental dyslexia: Evidence from Polish. In: Joshi RM, Aaron PG, editors. *Handbook of Orthography and Literacy*. Mahwah: LEA; 2006. pp. 249-274
- [32] Reid AA et al. Cognitive profiles of adult developmental dyslexics: Theoretical implications. *Dyslexia*. 2007;**13**:1-24
- [33] Poelmans G et al. A theoretical molecular network for dyslexia: Integrating available genetic findings. *Molecular Psychiatry*. 2011;**16**(4):365-382
- [34] Nicolson R. *Positive Dyslexia*. Sheffield, UK: Rodin Books; 2015
- [35] Germano E, Gagliano A, Curatolo P. Comorbidity of ADHD and dyslexia. *Developmental Neuropsychology*. 2010;**35**(5):475-493
- [36] Kaplan BJ et al. DCD may not be a discrete disorder. *Human Movement Science*. 1998;**17**:471-490
- [37] Fawcett AJ, Nicholson RI. Persistent deficits in motor skill of children with dyslexia. *Journal of Motor Behaviour*. 1995;**27**:235-240
- [38] Iversen S et al. Motor coordination difficulties in a municipality group and in a clinical sample of poor readers. *Dyslexia*. 2005;**11**(3):217-231
- [39] Frith U. Paradoxes in the definition of dyslexia. *Dyslexia. An International Journal of Research and Practice*. 1999;**5**(4):192-214

- [40] Ramus F et al. Theories of developmental dyslexia: Insights from a multiple case study of dyslexic adults. *Brain*. 2003;**126**(Pt 4):841-865
- [41] Snowling MJ, Caravolas M. Developmental dyslexia. In: Gaskell MG, editor. *The Oxford Handbook of Psycholinguistics*. Oxford: Oxford University Press; 2007. pp. 667-683
- [42] Ramus F, Szenkovits G. What phonological deficit? *The Quarterly Journal of Experimental Psychology*. 2008;**61**:129-141
- [43] Olson R et al. Specific deficits in component reading and language skills: Genetic and environmental influences. *Journal of Learning Disabilities*. 1989;**22**:339-349
- [44] Paulesu E et al. A cultural effect on brain function. *Nature Neuroscience*. 2000;**3**(1):91-96
- [45] Wang S, Gathercole SE. Working memory deficits in children with reading difficulties: Memory span and dual task coordination. *Journal of Experimental Child Psychology*. 2013;**115**(1):188-197
- [46] Frith U. Brain, mind and behaviour in dyslexia. In: Hulme C, Snowling M, editors. *Dyslexia: Biology, Cognition and Intervention*. London: Whurr Publishers Ltd; 1997. pp. 1-19
- [47] Hulme C, Snowling MJ. *Developmental Disorders of Language, Learning and Cognition*. Chichester, UK: Wiley-Blackwell; 2009
- [48] Stein J. The magnocellular theory of developmental dyslexia. *Dyslexia*. 2001;**7**(1):12-36
- [49] Stein J. Visual motion sensitivity and reading. *Neuropsychologia*. 2003;**41**:1785-1793
- [50] Stein J, Walsh V. To see but not to read: The magnocellular theory of dyslexia. *Trends in Neurosciences*. 1997;**20**(4):147-152
- [51] Lovegrove WJ et al. Contrast sensitivity functions and specific reading disability. *Neuropsychologia*. 1982;**20**:309-315
- [52] Hansen PC et al. Are dyslexics' visual deficits limited to measures of dorsal stream function? *Neuroreport*. 2001;**12**(7):1527-1530
- [53] Cicchini GM et al. Strong motion deficits in dyslexia associated with DCDC2 gene alteration. *The Journal of Neuroscience*. 2015;**35**(21):8059-8064
- [54] Gori S et al. The DCDC2 intron 2 deletion impairs illusory motion perception unveiling the selective role of magnocellular-dorsal stream in reading (dis)ability. *Cerebral Cortex*. 2015;**25**(6):1685-1695
- [55] Liederman J et al. The role of motion direction selective extrastriate regions in reading: A transcranial magnetic stimulation study. *Brain and Language*. 2003;**85**(1):140-155
- [56] Stein J. The current status of the magnocellular theory of developmental dyslexia. *Neuropsychologia*. 2018
- [57] Fawcett AJ, Nicolson RI. Performance of dyslexic children on cerebellar and cognitive tests. *Journal of Motor Behavior*. 1999;**31**(1):68-78
- [58] Nicolson RI et al. Eyeblink conditioning indicates cerebellar abnormality in dyslexia. *Experimental Brain Research*. 2002;**143**(1):42-50
- [59] Nicolson RI, Fawcett AJ, Dean P. Time estimation deficits in developmental dyslexia: Evidence of cerebellar involvement. *Proceedings of the Biological Sciences*. 1995;**259**(1354):43-47
- [60] Nicolson RI, Fawcett AJ, Dean P. Developmental dyslexia: The cerebellar deficit hypothesis. *Trends in Neurosciences*. 2001;**24**(9):508-511

- [61] Nicolson RI et al. Association of abnormal cerebellar activation with motor learning difficulties in dyslexic adults. *Lancet*. 1999;**353**(9165):1662-1667
- [62] Eden GF et al. Abnormal processing of visual motion in dyslexia revealed by functional brain imaging. *Nature*. 1996;**382**(6586):66-69
- [63] Frith C, Frith U. A biological marker for dyslexia. *Nature*. 1996;**382**:19-20
- [64] Heim S et al. Cognitive subtypes of dyslexia. *Acta Neurobiologiae Experimentalis (Wars)*. 2008;**68**(1):73-82
- [65] Menghini D et al. Different underlying neurocognitive deficits in developmental dyslexia: A comparative study. *Neuropsychologia*. 2010;**48**(4):863-872
- [66] Snowling MJ. Specific disorders and broader phenotypes: The case of dyslexia. *The Quarterly Journal of Experimental Psychology*. 2008;**61**(1):142-156
- [67] Zoubrinetzky R, Bielle F, Valdois S. New insights on developmental dyslexia subtypes: Heterogeneity of mixed reading profiles. *PLoS One*. 2014;**9**(6):e99337
- [68] Reid AA. Cognitive profiles of individuals with dyslexia: Insights from a large sample study. Paper presented at the 57th Annual Conference of the IDA. Indianapolis, USA; 2006
- [69] Cohen L, Dehaene S. Specialization within the ventral stream: The case for the visual word form area. *NeuroImage*. 2004;**22**(1):466-476
- [70] Price CJ, Devlin JT. The myth of the visual word form area. *NeuroImage*. 2003;**19**(3):473-481
- [71] Vanni S et al. Visual motion activates V5 in dyslexics. *Neuroreport*. 1997;**8**(8):1939-1942
- [72] Watson JDG et al. Area V5 of the human brain: Evidence from a combined study using positron emission tomography and magnetic resonance imaging. *Cerebral Cortex*. 1993;**3**:79-94
- [73] Demb JB, Boynton GM, Heeger DJ. Functional magnetic resonance imaging of early visual pathways in dyslexia. *The Journal of Neuroscience*. 1998;**18**(17):6939-6951
- [74] Amunts K et al. Brodmann's areas 17 and 18 brought into stereotaxic space-where and how variable? *NeuroImage*. 2000;**11**(1):66-84
- [75] Malikovic A et al. Cytoarchitectonic analysis of the human extrastriate cortex in the region of V5/MT+: A probabilistic, stereotaxic map of area hOc5. *Cerebral Cortex*. 2007;**17**(3):562-574
- [76] Stoodley CJ, Schmahmann JD. Functional topography in the human cerebellum: A meta-analysis of neuroimaging studies. *NeuroImage*. 2009;**44**:489-501
- [77] Finch AJ, Nicolson RI, Fawcett AJ. Evidence for a neuroanatomical difference within the olivo-cerebellar pathway of adults with dyslexia. *Cortex*. 2002;**38**(4):529-539
- [78] Fulbright RK et al. The cerebellum's role in reading: A functional MR imaging study. *American Journal of Neuroradiology*. 1999;**20**(10):1925-1930
- [79] Conners CK, Erhardt D, Sparrow EP. *Conners' Adult ADHD Rating Scales (CAARS)*. New York: MHS; 1999
- [80] American Psychiatric Association. *Diagnostic and Statistical Manual of Mental Disorders (DSM-IV)*. Washington, DC: American Psychiatric Association; 1994
- [81] Coltheart M. The MRC psycholinguistic database. *Quarterly Journal of Experimental Psychology*. 1981;**33A**:497-505



- [82] Donaldson DI, Buckner RL. Effective paradigm design. In: Jezzard P, Matthews PM, Smith SM, editors. *Functional MRI. An Introduction to Methods*. Oxford, UK: Oxford University Press; 2001. pp. 177-195
- [83] Friston KJ, Statistics I. Experimental design and statistical parametric mapping. In: Toga AW, Mazziotta JC, editors. *Brain Mapping: The Methods*. San Diego, USA: Academic Press; 2002. pp. 605-631
- [84] Glaser DE. Experimental Design. Talk Given at the Statistical Parametric Mapping Course. London: Wellcome Department of Imaging Neuroscience; 2006
- [85] Amunts K et al. Analysis of neural mechanisms underlying verbal fluency in cytoarchitecturally defined stereotaxic space—the roles of Brodmann areas 44 and 45. *NeuroImage*. 2004;**22**(1):42-56
- [86] Eickhoff SB et al. A new SPM toolbox for combining probabilistic cytoarchitectonic maps and functional imaging data. *NeuroImage*. 2005;**25**(4):1325-1335
- [87] Brett M, et al. Region of interest analysis using an SPM toolbox. In: *Proceedings of the 8th International Conference on Functional Mapping of the Human Brain*; 2002. Available on CD-ROM in *NeuroImage*; Vol 16 No 2: Sendai, Japan
- [88] Heim S et al. Interaction of phonological awareness and ‘magnocellular’ processing during normal and dyslexic reading: Behavioural and fMRI investigations. *Dyslexia*. 2010;**16**(3):258-282
- [89] Shaywitz SE et al. Functional disruption in the organization of the brain for reading in dyslexia. *Proceedings of the National Academy of Sciences of the United States of America*. 1998;**95**(5):2636-2641
- [90] Amunts K et al. Broca’s region revisited: Cytoarchitecture and intersubject variability. *The Journal of Comparative Neurology*. 1999;**412**(2):319-341
- [91] Kurth F et al. Cytoarchitecture and probabilistic maps of the human posterior insular cortex. *Cerebral Cortex*. 2009;**20**: 1448-61
- [92] Geyer S. *The Microstructural Border Between the Motor and the Cognitive Domain in the Human Cerebral Cortex*. Wien: Springer; 2003
- [93] Caspers S et al. The human inferior parietal lobule in stereotaxic space. *Brain Structure and Function*. 2008;**212**(6):481-495
- [94] Caspers S et al. The human inferior parietal cortex: Cytoarchitectonic parcellation and interindividual variability. *NeuroImage*. 2006;**33**(2):430-448
- [95] Morosan P et al. Multimodal architectonic mapping of human superior temporal gyrus. *Anatomy and Embryology*. 2005;**210**:401-406
- [96] Tzourio-Mazoyer N et al. Automated anatomical labeling of activations in SPM using a macroscopic anatomical parcellation of the MNI MRI single-subject brain. *NeuroImage*. 2002;**15**:273-289
- [97] Diedrichsen J et al. A probabilistic MR atlas of the human cerebellum. *NeuroImage*. 2009;**46**(1):39-46
- [98] Pugh KR. Neuroimaging studies of skilled reading and reading disability. Paper presented at the 57th Annual Conference of the IDA. Indianapolis, USA; 2006
- [99] Pennington BF. Using genetics and neuropsychology to understand dyslexia and its comorbidities. Paper presented at the 8th BDA International Conference. Harrogate, UK; 2011

- [100] Pennington BF. From single to multiple deficit models of developmental disorders. *Cognition*. 2006;**101**:385-413
- [101] Krishnan S, Watkins KE, Bishop DV. Neurobiological basis of language learning difficulties. *Trends in Cognitive Sciences*. 2016;**20**(9):701-714
- [102] Mascheretti S et al. Neurogenetics of developmental dyslexia: From genes to behavior through brain neuroimaging and cognitive and sensorial mechanisms. *Translational Psychiatry*. 2017;**7**(1):e987
- [103] Giraldo-Chica M, Hegarty JP, Schneider KA. Morphological differences in the lateral geniculate nucleus associated with dyslexia. *Neuroimage: Clinical*. 2015;**7**:830-836
- [104] Goswami U. A temporal sampling framework for developmental dyslexia. *Trends in Cognitive Sciences*. 2011;**15**(1):3-10
- [105] Hendren RL et al. Recognizing psychiatric comorbidity with reading disorders. *Frontiers in Psychiatry*. 2018;**9**:101
- [106] Plomin R, Kovas Y. Generalist genes and learning disabilities. *Psychological Bulletin*. 2005;**131**(4):592-617
- [107] Deriziotis P, Fisher SE. Speech and language: Translating the genome. *Trends in Genetics*. 2017;**33**(9):642-656
- [108] Mascheretti S et al. Complex effects of dyslexia risk factors account for ADHD traits: Evidence from two independent samples. *Journal of Child Psychology and Psychiatry*. 2017;**58**(1):75-82
- [109] Gooch D, Snowling M, Hulme C. Time perception, phonological skills and executive function in children with dyslexia and/or ADHD symptoms. *Journal of Child Psychology and Psychiatry*. 2011;**52**(2):195-203
- [110] Wimmer H, Mayringer H, Raberger T. Reading and dual-task balancing: Evidence against the automatization deficit explanation of developmental dyslexia. *Journal of Learning Disabilities*. 1999;**32**(5):473-478
- [111] Muller-Axt C, Anwender A, von Kriegstein K. Altered structural connectivity of the left visual thalamus in developmental dyslexia. *Current Biology*. 2017;**27**(23):3692-3698 e4
- [112] Boets B et al. Intact but less accessible phonetic representations in adults with dyslexia. *Science*. 2013;**342**(6163):1251-1254
- [113] Pugh KR et al. Glutamate and choline levels predict individual differences in reading ability in emergent readers. *The Journal of Neuroscience*. 2014;**34**(11):4082-4089
- [114] Carrey N et al. Glutamatergic changes with treatment in attention deficit hyperactivity disorder: A preliminary case series. *Journal of Child and Adolescent Psychopharmacology*. 2002;**12**(4):331-336
- [115] Gass A, Richards TL. Serial proton magnetic resonance spectroscopy of normal-appearing gray and white matter in MS. *Neurology*. 2013;**80**(1):17-18
- [116] Hancock R, Pugh KR, Hoeft F. Neural noise hypothesis of developmental dyslexia. *Trends in Cognitive Sciences*. 2017;**21**(6):434-448
- [117] Todd N et al. Evaluation of 2D multiband EPI imaging for high-resolution, whole-brain, task-based fMRI studies at 3T: Sensitivity and slice leakage artifacts. *NeuroImage*. 2016;**124**(Pt A):32-42
- [118] De Martino F et al. Frequency preference and attention effects across cortical depths in the human primary auditory cortex. *Proceedings of the National Academy of Sciences*

of the United States of America.  
2015;**112**(52):16036-16041

[119] Boto E et al. A new generation of magnetoencephalography: Room temperature measurements using optically-pumped magnetometers. *NeuroImage*. 2017;**149**:404-414

[120] Reid AA. Developmental dyslexia—a critical review of imaging-genetics studies. Poster presented at the 22th Annual Meeting of the OHBM. Geneva, Switzerland; 2016

[121] Eicher JD, Gruen JR. Imaging-genetics in dyslexia: Connecting risk genetic variants to brain neuroimaging and ultimately to reading impairments. *Molecular Genetics and Metabolism*. 2013;**110**(3):201-212

[122] Cope N et al. Variants in the DYX2 locus are associated with altered brain activation in reading-related brain regions in subjects with reading disability. *NeuroImage*. 2012;**63**(1):148-156

[123] Pinel P et al. Genetic variants of FOXP2 and KIAA0319/TTRAP/THEM2 locus are associated with altered brain activation in distinct language-related regions. *The Journal of Neuroscience*. 2012;**32**(3):817-825

[124] Wilcke A et al. Imaging genetics of FOXP2 in dyslexia. *European Journal of Human Genetics*. 2012;**20**(2):224-229

[125] Lamminmaki S et al. Human ROBO1 regulates interaural interaction in auditory pathways. *The Journal of Neuroscience*. 2012;**32**(3):966-971

[126] Centanni TM et al. Increased variability of stimulus-driven cortical responses is associated with genetic variability in children with and without dyslexia. *Developmental Cognitive Neuroscience*. 2018;**34**:7-17

[127] Mannel C et al. Working-memory endophenotype and dyslexia-associated

genetic variant predict dyslexia phenotype. *Cortex*. 2015;**71**:291-305

[128] Darki F et al. Three dyslexia susceptibility genes, DYX1C1, DCDC2, and KIAA0319, affect temporo-parietal white matter structure. *Biological Psychiatry*. 2012;**72**(8):671-676

[129] Scerri TS et al. The dyslexia candidate locus on 2p12 is associated with general cognitive ability and white matter structure. *PLoS One*. 2012;**7**(11):e50321

[130] Marino C et al. The DCDC2/ intron 2 deletion and white matter disorganization: Focus on developmental dyslexia. *Cortex*. 2014;**57**:227-243

[131] Carrion-Castillo A, Franke B, Fisher SE. Molecular genetics of dyslexia: An overview. *Dyslexia*. 2013;**19**(4):214-240

[132] Roeske D et al. First genome-wide association scan on neurophysiological endophenotypes points to trans-regulation effects on SLC2A3 in dyslexic children. *Molecular Psychiatry*. 2011;**16**(1):97-107

[133] Liegeois F et al. Language fMRI abnormalities associated with FOXP2 gene mutation. *Nature Neuroscience*. 2003;**6**(11):1230-1237

[134] Ho TC et al. Intergenerational neuroimaging of human brain circuitry. *Trends in Neurosciences*. 2016;**39**(10):644-648

[135] Hoeft F, Hancock R. Intergenerational transmission of reading and reading brain networks. In: Galaburda A, editor. *Dyslexia and Neuroscience*. Brookes Publishing; Baltimore, USA. 2018



---

Section 3

# Structural Imaging

---



# Imaging Tests for Predicting the Presence of Difficult Airway in Head and Neck Cancer Patients Undergoing Otorhinolaryngological Surgery

*Juan Gutiérrez Franchi, S. Merino, P. de la Calle, C. Perrino, M. Represa and P. Moral*

## Abstract

Patients with head and neck cancers represent a challenge for the surgical team from many points of view, but, especially, the surgical moment where greater stress generated corresponds to the perioperative management of the airway, because in many occasions we can face unexpected situations, most of the time, incidental findings can hinder ventilation and endotracheal intubation. Gutierrez et al., in 2018, decided to study four tomography measures and their correlation in anesthesia records with airway management difficulties. Material and methods: A retrospective, observational study was carried out in 104 patients operated by head and neck cancers over a period of 36 months, only in those with access to tomographic records. Four tomographic measurements were considered and were statistically related to the extreme degrees of visualization of the glottis (Cormack III–IV) and the presence of the physical examination of Mallampati III–IV. Results: After performing a multivariate model in the group of extreme degrees of visualization of the glottis, the results were not statistically significant ( $p > 0.05$ ; 95% CI: 0.030–2.31: EPI/PPW, 0.018–1.37 TB/PPW). In the Mallampati III–IV group, in the multivariate model only the VC/PPW showed clinically significant results ( $p < 0.05$ ; 95% CI: 0.104–8.53). Conclusions: Tomographic measurements and the physical examination predictors could represent a useful guide in the prediction of the difficult airway in these patients.

**Keywords:** difficult airway, computed axial tomography, predictors

## 1. Prevalence of head and neck cancers

### 1.1 Prevalence

Head and neck cancers represent 5% of all tumors [1]. The most frequent location is the larynx, followed by the oropharynx, oral cavity, and nasopharynx [2].

Squamous cell carcinomas account for 95% of all malignant tumors of the head and neck, while carcinomas of the salivary glands are almost the remaining 5%. They represent 4% of all malignant neoplasms in the USA. Epidermoid carcinomas of the head and neck can be divided into two different groups according to their pathogenesis, biology, and prognosis. The incidence of cancers related to the environment, mainly caused by tobacco and alcohol, has decreased; however, they are still frequent. An increased incidence of oropharyngeal cancers related to human papillomavirus (OHPV) has been observed. The OHPV currently accounts for about 75% of the oropharyngeal cancers seen in the USA and Europe. OHPV affect a younger population (50–60 years) than cancers of environmental origin (55–65 years). Patients with OHPV are generally also healthier and are not prone to comorbidities or the second neoplasms seen in epidermoid tumors related to environmental factors [3].

The mucosal surfaces of the head and neck are divided into six anatomical regions: the oral cavity, oropharynx, hypopharynx, larynx, nasopharynx, and paranasal sinuses. The anatomical location of an epidermoid carcinoma of the head and neck has important implications, although not well defined, for diagnosis, pathogenesis, dissemination pattern, prognosis, and treatment. Due to intrinsic differences in the biological characteristics of the mucous cells and posterior tumors' origin, tropisms of the carcinogenic viruses could be different lymphatic and anatomic distributions [3] **Figure 1**.

The oropharynx is an osteocartilaginous cavity with a content that extends from the lips to the anterior wall of the first cervical vertebrae and a content that includes the tongue, epiglottis, and hard/soft palate. In Europe and the USA, one of the main causal factors is the human papillomavirus. OHPV are produced almost exclusively by HPV-16, a high-risk type of HPV associated with cervical, anal, and vulvar cancers. Other types of high-risk HPV cause 10–15% of new diagnoses. High-risk types of HPV are transmitted through body fluids that infect the surfaces of the squamous mucosa of the anogenital duct and the oropharynx. Although smoking does not increase the risk of OHPV, HPV is the cause in 50% of smokers with oropharyngeal cancer. Compared to environmental neoplasms, OHPV usually presents initially in a low primary T stage (T1 and T2) and a high nodal stage (N2 and N3) and often represents a cause of cancer of unknown primary origin because the tumors primary are small and difficult to identify [3].

The hypopharynx includes the pyriform sinuses, the lateral and posterior walls of the pharynx, and the posterior surfaces of the larynx. These structures surround the larynx from behind and laterally. It can be difficult to detect tumors in this region because sac bottoms and spaces around the larynx exist. As a result, primary hypopharyngeal tumors may be asymptomatic and, like oropharyngeal tumors, may be detected initially in advanced stages or as a primary tumor of unknown origin. These tumors are related to the consumption of tobacco and alcohol [3].

The larynx includes the vocal cords, the subglottis, and the supraglottic part of the larynx, in addition to the thyroid, cricoid, and arytenoid cartilages. Tumors that originate in the true vocal cords often produce symptoms in early stages and rarely extend beyond the boundaries of the larynx, while subglottic and supraglottic tumors may be relatively asymptomatic and have a much higher risk earlier of spread to the lymph nodes and other regional areas. Laryngeal carcinomas have an intense association with tobacco [3].

The nasopharynx includes the mucosal surfaces and structures of the cavity located behind the nasal passages. Nasopharyngeal carcinomas are frequent on the Pacific coast, North Africa, and the Near East. In some regions of China and Southeast Asia, cancers of the nasopharynx have a frequency similar to



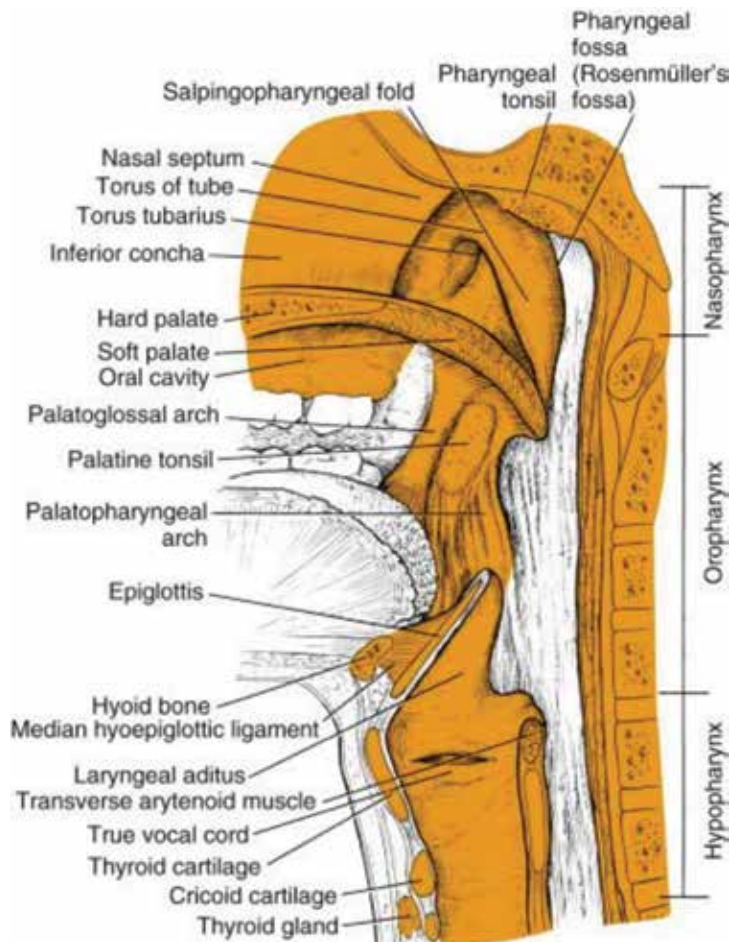


**Figure 1.** Malignant neoplasms of the oropharynx. Retrieved from Parul S, Uli H. Cummings Otolaryngology. January 2, 2015. Páginas 1432.e4-1453.e4. © 2015.

lung cancer. In the USA, approximately 2000 cases occur each year, but this number is increasing in populations with high-risk ethnic origins settling in North America. Nasopharyngeal carcinomas are frequently associated with a latent infection of epithelial tumor cells with EBV, the etiological agent of infectious mononucleosis. Nasopharyngeal carcinomas are also associated with environmental and genetic factors in susceptible populations that have migrated to North America and still have an elevated risk of this disease. Unlike other epidermoid carcinomas of the head and neck, nasopharyngeal carcinomas can appear at an early age, with a maximum incidence evident in adolescents and young adults. Nasopharyngeal carcinomas are divided into three histological types according to the World Health Organization (WHO): the undifferentiated (WHO III) and the non-keratinized (WHO II) have latent infection by EBV in 95% of cases and are the most of the cases in North America and the rest of the world; the well-differentiated form (WHO I) is less frequent and accounts for 5% of cases worldwide, although in North America it represents 15–25% of cancers and is usually associated with traditional risk factors, such as smoking. Nasopharyngeal carcinomas are associated with a high risk of early regional lymph node metastases, prolonged natural evolution, and very high risk of distant dissemination [3].

## **2. Difficult airway**

### **2.1 Prevalence**

In some cases, friable vocal cord tumors, subglottic stenosis, or tongue-based pathologies represent challenges for even the most experienced anesthesiologist. The incidence of difficult intubation in OC population is 7.1%. The American Society of Anesthesiologists defines “Difficult intubation” as the completion of multiple attempts of intubation in the presence or absence of tracheal disease [4].

We know, by difficult airway according to ASA, the clinical situation in which a conventionally trained anesthesiologist has difficulty in ventilating with facial mask, difficulty in tracheal intubation, or both [5]. The intubation failure plus ventilation failure occurs at 0.003%, being the most dramatic situation that can occur [6]. Intubation failure is the inability to place an endotracheal tube. Its incidence is 0.05% in the general population. The estimated incidence of all types of difficulties related to intubation or airway safety is estimated at 1–3% [7].

Currently, there are no generic references for the incidence of difficult intubation, due to the great diversity of material available in terms of video-laryngoscopy, which is nowadays commonly used. The incidence of failed intubation is around 0.05–0.35% [7].

### **2.2 Predictors of difficult airway**

The preoperative recognition in physical examination can help to predict life-threatening situations for our patients. The test of Mallampati is considered the gold standard of the predictors, relating to the structures of the base of the tongue with respect to the visibility of the after pharyngeal structures, on a scale from I to IV, in which III–IV associated with other predictors may suggest difficulty [6]. Lee et al. describe that the modified Mallampati test has a sensitivity to predict difficult intubation of 76% and a specificity of 77% [8]. On the other hand, it is suggested that the Mallampati test in the supine position is a better predictor than in the sitting position [9, 10].

Numerous predictive tests of difficult airway can be mentioned with their different sensitivities and specificities that can improve the predictive power of the Mallampati: hyo- and thyromental distance [sensitivity (S) 88%/65% and specificity (E) 60%/81%, respectively], the bite test (S 88% and E 88%), circumference of the neck in the obese population (S 88.2% and E 83%), and mouth opening (S 26–47% and E 94%). Due to the statistical limitations observed in the studied populations, predictive models that seek to improve the statistical power of these physical examination findings have been developed from multivariate analysis. Mainly they can be mentioned: Wilson (S 75% and E 88%), El-Ganzouri (S 65% and E 94%), Arne (S 94% and E 96%), Karkouti (S 86% and E 96%), and Naguib original (S 81% and E 72%) [8]. Recall that Mallampati plus thyromental distance and sternum distance is the combination of physical tests with greater discriminative power, with a sensitivity of 100% and specificity of 92.7% [11].

### **2.3 Radiology in the difficult airway**

#### *2.3.1 Ultrasonography*

The physical principles of ultrasound consist in the transformation of mechanical energy into electrical and vice versa. The ultrasound wave travels through the tissues undergoing phenomena of scattering, refraction, and reflection, with wave frequencies that oscillate from 2 to 20 MHz and therefore impossible to be heard by the human

ear. The organs of the body have different amounts of water that can help us distinguish the images in the ultrasound monitor. This physical alteration of the wave is known as impedance and is usually measured as the resistance to propagation of sound waves from one medium to another. The greater difference in impedance between two tissues, the easier it will be to distinguish one from the other. The same happens with the air-water interface, and to improve it, we usually place gel in the ultrasound probe to reduce it and optimize the visualization of the tissues. That is why we usually see black (hypoechoic) air in the monitor, solid viscera with high water content in white (hyperechoic), and structures of intermediate echogenicity (isoechoic) [12].

Everything explained previously was not possible without the piezo crystals of the probes. These devices are capable of emitting an electric pulse on their crystals, which is transduced to mechanical energy, generating an “oscillatory” activity in the tissues, and the signal is again received by the probe and transformed into electrical energy giving an image on the monitor. This information is processed in terms of amplitude and time of return of the signal in the ultrasound equipment. Tissues are images interpreted with hypo- (black), iso-, or hyperechoic (white) characteristics in the ultrasound monitor [12].

The resolution of ultrasound devices can be divided into axial, lateral, spatial, and temporal. The axial resolution refers to the ability of the ultrasound probe to define two images. At higher wave frequencies, we will be able to appreciate more superficial structures with greater definition, but not organs that are deeper. The lateral resolution refers to the ability to differentiate two structures perpendicular to the ultrasound probe and depends on the position of the probe with respect to the structure to be evaluated [12].

Spatial resolution is a fixed property of the probe and refers to its ability to solve objects located at the same height or thickness of the ultrasound beam. The number of individual PZT crystals that emit and receive the ultrasound waves and their sensitivity affect the resolution, accuracy, and clarity of the image. The temporal resolution refers to the clarity or resolution of structures in movement [12].

Ultrasounds seem to be beginning to play a role in the perioperative prediction of intubation difficulties. Chou et al. studied hyomandibular distance measured by X-rays and said that it may be increased in patients with difficult airway. The cutoff values described in this study were 33.8 mm in men and 26.4 mm in women. Knowing the limitations of this work, in 2008, it was described that the inability to see the hyoid bone in ultrasound (due to a hypopharyngeal of the base of the tongue or by a short mandibular branch) seems to increase the statistical power in the usefulness of ultrasound in the patient difficult to intubate [13].

Based on the previous study, years later Hui et al. recruited 110 patients that were trained in sublingual ultrasounds after a series of simple instructions. The probability of visualizing the hyoid bone by ultrasound was related in patients with Cormack I and II with a positive probability ratio of 21.6, which suggests that it can become a useful tool to predict difficult airway [14] **Figure 2**.

However, the shape and size of the tongue added to the fact that the patients were not in the sniffing position during the measurements may represent some limitations in the interpretation of the results in this study [14].

### 2.3.2 Computed tomography

The image in computerized axial tomography is an axial and coronal representation of the patient using the physical principles of X-rays. The final reconstruction of the image will generate a series of overlapping structures with attenuations that will depend on the amount of water contained in the tissue under study [15].

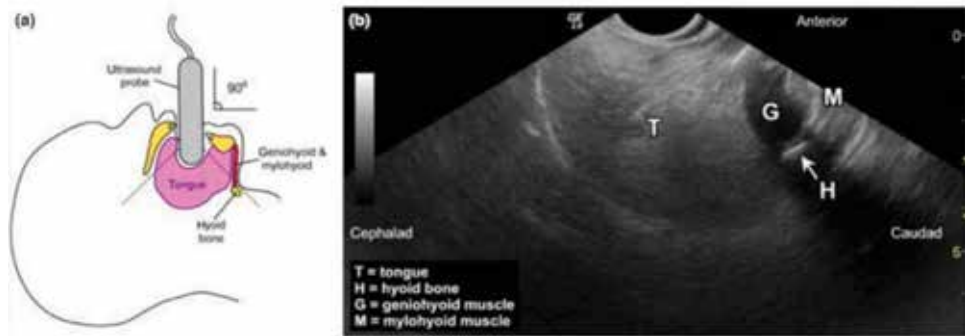


**Figure 2.**

Retrieved from [14]. Sublingual ultrasound of the upper airway. (a) Schematic diagram showing placement of the ultrasound probe perpendicular to the face, as instructed by study participants. Indicated are positions of the tongue, geniohyoid and mylohyoid muscles and hyoid bone. The dashed lines indicate the coverage of the ultrasound beam. (b) Representative ultrasound image showing view of the hyoid bone.

The CT image is produced by the process of reconstruction, digitally combining information from X-ray projections through the patient from many different angles to produce the cross-sectional image. Because the image is digital, it is made up of a group of pixels (shortened from “picture elements”). Each pixel has a gray scale value that is displayed to the viewer. The image is 2D, but it represents a 3D volume of tissue with a finite thickness (usually a very small thickness compared to the field-of-view (FOV) size [ $\approx 2\text{--}5\text{ mm}$ ]). Each pixel is the projection, or 2D representation, of the X-ray attenuation of a voxel (shortened from “volume element”) of physical tissue. The size of the pixels and the thickness of the voxels relate to some important image quality features, such as detail, noise, contrast, accuracy of the attenuation measurement (CT number value), and artifacts. These will be discussed in more detail as they relate to the processes of acquiring and reconstructing CT data [15].

In a CT of a single section of tissue using a single detector, the X-ray beam is collimated to the desired image thickness. The detector array has a number of individual detector elements that each records the intensity of the beam passing through the tissue along the path from the X-ray tube to the element. The system captures a simple projection X-ray through the patient, consisting of a thin strip or row of pixels. It can be thought of as a one-dimensional (1D) radiograph. The scanner then rotates the source and detector to capture additional 1D “strip X-rays” through the same section of the patient, viewed from a number of angles. Each strip radiograph (projection) is stored in the computer memory for later reconstruction [15].

In multislice CT, this operation is performed simultaneously for many arrays of detectors stacked side by side along the z-axis (long axis) of the patient. The X-ray beam collimators can be opened so that a wider section of the patient is irradiated, and each row of detectors can measure a separate transmission signal for the tissue section that lies between the detector row and the tube. The width of tissue that is sampled by each detector row is determined by the physical width of the detector elements along the z-axis [15].

According to X-ray absorption, we use the scale of the Hounsfield units (HU) that allows to stratify the pixels of the measurements according to their densities with respect to water. The advantage of the HU scale is that density differences of 1 part in 1000 (0.1%) can be represented by distinct values. The inherent density resolution of CT scanners is about 0.5%, so the HU scale is sufficient to display all attenuation differences the scanner can measure. Increasing the value of K would not improve on the density resolution of the system [15].

Many authors have tried to apply these imaging tests for the study of airway anatomy. Randell et al. in 1998 in Anesthesiology suggested the possibility of

considering by means of NMR and CT studies parameters such as length of epiglottis, length of tongue, and width thereof, as difficulty markers of the passage of the endotracheal tube during intubation with a fiberoptic bronchoscope [16].

### *2.3.3 Computed magnetic resonance*

Understanding the physics of magnetic resonance is a challenge for many medical specialists, as it involves implicit technical knowledge shared with other professional fields; it may even be harder to understand than the basic principles of tomography and ultrasound. The four main points of the process are:

#### *2.3.3.1 Preparation*

The human being is basically composed of water. Hydrogen molecules contained in water when exposed to a “magnet” can be magnetized. Basically the resonator is a magnet, which confers spin to the hydrogen with a resulting vector that oscillates at a frequency called Larmor that is proportional to the magnetic field surrounding it. This vector is going to align with the said field when it is exposed to 1.5–3.0 T. Magnetization can be manipulated with the use of contrasts such as gadolinium through a process called inversion of the image [17].

#### *2.3.3.2 Excitation*

The “spinning” of the hydrogen molecules generates a radiofrequency pulse in the Larmor spectrum, which is received by a coil (electrical conductor) that is transverse to the tissue magnetization under study and transduced by Faraday thermal induction; the previous really will generate the “magnetic resonance signal.” The signal is attenuated by two processes called relaxation. This usually occurs in two times (T). T<sub>2</sub> represents the loss of coherence of the spin of the hydrogen molecules over time. T<sub>1</sub> represents the time it takes for the vector of the magnetic field to reach equilibrium. The important thing about these last two concepts is that they will determine the resolution of the soft parts during the study [17].

#### *2.3.3.3 Spatial encoding*

The frequency of the spin of the hydrogen molecules with different spatial location differs from each other. The sum of these frequencies generates a resulting vector causing a force called Lorentz force, which is perceived by the coils and will participate in the genesis of the acoustic signal generated during a resonance.

#### *2.3.3.4 Signal acquisition*

The different spatial location of the hydrogen ions and their individual rotation frequency are analyzed by a Fourier transform, which will generate the different pixels of the image and is stored in the magnetic resonance equipment [17].

The application of these concepts to the perioperative management of the airway can be observed. In the work on predictors of difficulty of endotracheal intubation considered from NMR studies conducted by Samra et al. in 40 patients in 1995, no significant differences were found in the 20/21 parameters studied in soft tissue X-ray imaging. NMR is among the difficult intubation groups not anticipated and achieved. It seems that no radiological study alone is able to predict the difficulty in intubation; one of the reasons is that the exposure of the larynx depends on its compressibility. The tongue and the soft tissue consistency of the floor of the mouth, a

situation that cannot be measured with imaging studies, perhaps dynamic studies, could be useful in these cases [18].

#### 2.3.4 Imaging modalities: weaknesses and strengths

In head and neck cancers, tomography through the use of detectors (64 mid-range) can provide dynamic images to assess phonation or oral cavity tumors. In addition, it is a useful rapid test in claustrophobic patients with respiratory problems [19, 20].

Some authors prefer the use of NMR in their institutions, since it is superior in resolution to delimit tumors and bone/cartilaginous parts and perineural invasion and to reach areas such as the base of the tongue that can be difficult to see in nasofibroscopy [21, 22] **Figure 3**.

The 4–7% of head and neck tumors has lung metastases. Many hospital protocols use CT with low levels of radiation to follow these patients and even to determine responses to treatment, tumor biology, and nodal extension. And we cannot forget how important it is in radiotherapy simulation by tomographic tests. So in this group of patients, it seems that the two tests continue to complement each other [23–27].

Currently, it seems that MRI greatly improves the visualization of the bone and cartilage. The importance of this fact is related to staging and treatment of these patients [28–30] but not so in patients on chemotherapy treatment where positron emission tomography remains a better alternative for follow-up at 3 months [31].

CT protocols are less varied than MRI, but the technique still requires optimization and patient cooperation. Many of these patients need a study that ranges from the base of the skull to the chest with a 1–1.5 mm collimation. The use of contrast offers an important advantage in these patients, and, whenever administered at 1 ml/s, it helps to define better vascular structures and squamous cell tumors. The patient is then asked to raise their arms above their head, and the entire chest is scanned. Dental artifact remains a challenge in a patient group who will often have poor dentition. An additional limited CT with angled gantry can be used to mitigate beam hardening if the tumor is obscured [32].

In summary, CT continues to be used in most head and neck cancer patients. The cost of NRM continues to be a limitation for many centers. The tomography as a basis for

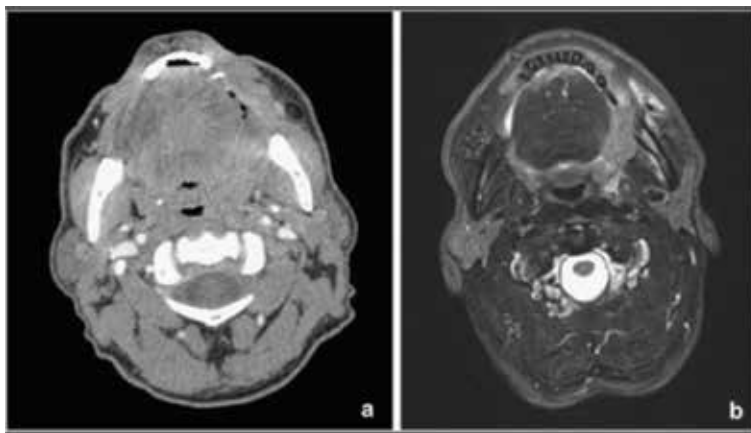


**Figure 3.** Retrieved from [33]. Left oropharyngeal/buccal squamous cell carcinoma on (a) contrast-enhanced computed tomography and (b) T2 axial DIXON-FS magnetic resonance imaging (MRI), showing the benefits of superior contrast resolution in MRI. Head and neck is an area with a difficult anatomy and distortions cause by tumors could compromise imagenologic interpretations. Notice better resolution in image than tomography that could help in staging and surgical decision.

PET and radiotherapy remains a very valuable option in these patients, since it facilitates staging and treatment. It seems that in the future, it is inevitable that the MRI replaces the CT because of its resolution of soft tissue visualization, and therefore it would offer more targeted treatments to this area of such a complex anatomy [33].

### 3. Any place for CT and airway?

Patient intervened for head and neck cancers presents anatomical particularities in the airway, which are probably better described in tests performed routinely in this population as the CT. Comparing the degrees of visualization of the glottis and Mallampati test described in the anesthesia records with four tomographic measurements, the authors of this chapter propose a tool to improve the perioperative management of the airway in this group of patients. A retrospective study was conducted with 104 patients operated for head and neck cancers under general anesthesia and endotracheal intubation in the Otorhinolaryngology department during a period of 36 months. Throughout the selection process, the radiology team reported a number of 15 cases with significant distortion of the airway that are being excluded from the analysis [1].

Based on the findings of the preoperative imaging tests, a multivariate logistic regression analysis was performed, where the dependent variable was the presence of Mallampati III–IV and the extreme degrees of visibility of the glottis (defined as Cormack III–IV). The 89 patients were assigned to the Cormack I–IV and Mallampati I–IV groups in the analysis in equal proportion. A total of four tomographic and clinical factors of difficult airway were introduced into this model. The tomographic predictors considered in the study were the following: distance from the vocal cords to the posterior pharyngeal wall (CVV/PPF) and laryngotracheal angle (Alaring) and distance from the epiglottis to the posterior pharyngeal wall (EPI/PPF) and from the base of the tongue to the posterior pharyngeal wall (BL/PPF). The odds ratio (OR) was 95% with confidence intervals (CI). All the tests were considered statistically significant for all data analyses when  $p < 0.05$  [1] **Figure 4**.

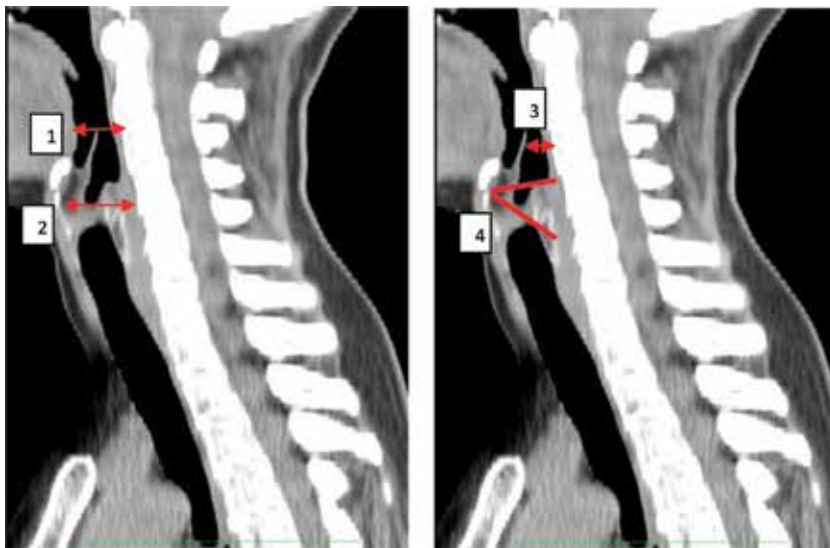


**Figure 4.** Axial CT scan. Measurements made by the Gutiérrez JC et al. [1]. 1. TB/PPW: tongue base distance to posterior pharyngeal wall. 2. VCD/PPW: vocal cords to posterior pharyngeal wall. 3. EPI/PPW epiglottis distance to posterior pharyngeal wall. 4. LTQ: laryngotracheal angle.



The most frequent surgeries performed during the study period were laryngeal microsurgery, total laryngectomy, and laser cordectomy, with percentages of 37.1, 10.1, and 6.7%, respectively.

In the Mallampati III–IV group, the mean in millimeters of distances of CVV/ PFP and BL/PFP was 11.89 and 8.82, respectively. In the Cormack III–IV group, the means of EPI/PFP and BL/PFP were 7 and 10.40 mm. The tomographic predictors EPI/PFP and 177 BL/PFP in Cormack III–IV patients show significant results in the univariate model ( $p < 0.05$ , 95% CI: 0.125–3.84 and 0.654–5.915, respectively), but this situation was not repeated in the multivariate model when the variables were analyzed categorically (95% CI: 0.030–2.31 EPI/PFP, 0.018–1.37 BL/PFP). ROC curve was also assessed during the study, with 71 and 69% being observed for EPI/ PFP and BL/PFP, respectively [1] **Table 1**.

From the tomographic predictors, the CVV/PFP distance in the Mallampati III–IV patients shows significant results in the univariate model ( $p < 0.05$ , 95% CI: 0.032–3.682), a situation that was repeated in the multivariate model with the same distance ( $p < 0.05$ , 95% CI: 0.104–8.53) The diagnostic yield of CVV/PFP was also assessed during the study, with 64% being observed [1].

Although is important to consider that most of the intubations are performed by residents, there is a possibility that the interpretation of the Cormack degree could be altered. On the other hand, were described must take into account the preferences for airway devices according to the experience of each doctor, since this may condition the analysis of the variables. Discerning the differences between device preferences is beyond the scope of this study [1].

Difficult for Cormack		VCD/PPW (mm)	EPI/PPW (mm)	TB/PPW (mm)	°LTQ
I–II degree					
Median		13.20	8.99	13.68	139.81
Minimum		6	3	5	119
Maximum		22	16	21	160
Percentile	25	10.75	7.00	11.00	135.00
	50	13.00	9.00	13.00	141.00
	75	16.00	11.00	17.00	145.25
Standard deviation		3.743	2.785	3.875	9.391
III–IV degree					
Median		12.33	7.00	10.40	141.00
Minimum		6	3	5	122
Maximum		22	11	19	155
Percentile	25	7.00	4.00	6.00	133.00
	50	11.00	8.00	11.00	142.00
	75	16.50	9.00	12.25	149.50
Standard deviation		5.454	2.625	4.195	10.548

*Retrieved from Gutiérrez JC et al. REDAR-913 2018. °LTQ: laryngotracheal angle; EPI/PPW epiglottis distance to posterior pharyngeal wall; TB/PPW: tongue base distance to posterior pharyngeal wall; VCD/PPW: vocal cords distance to posterior pharyngeal parad. Good glottis visualization (Cormack I/II). Extreme degrees of glottis visualization (Cormack III/IV).*

**Table 1.**  
Cormack III/IV and tomographic predictors.



Patients undergoing oncological head and neck surgeries receive preoperative radiotherapy and other diagnostic-therapeutic techniques that were sometimes difficult to relate temporally with the CT evaluated. This fact may condition the interpretation of the imaging tests by the expert radiologist [1].

#### 4. Conclusion

In certain patients, it seems that the role of ultrasonography in the prediction of difficult intubation plays an important role [34]. We cannot forget the importance of the predictors to physical examination, and that their sum complements their statistical power. The particularities of airway management in patients with head and neck cancers are well known, and sometimes supporting us in preoperative imaging tests, in conjunction with the interdisciplinary communication of the surgical team, favors the reduction of unwanted events in the management of the airway.

It is useful in these special populations to anticipate a possible difficult airway. Imaging tests, particularly CT, could help in this regard. Gutiérrez et al. described in the group Mallampati III–IV distance measurement CVV/PPF shows significant statistics in the multivariate model ( $p < 0.05$ , 95% CI: 0.032–3.682). However, obtaining images in a reproducible position that recreates the position that the patient will adopt during intubation and prospective evaluation in a larger population can provide more useful preprocedure information for the anesthetist [1].

Knowing the limitations of difficulty predictors of airway, it seems that techniques are necessary alternatives that support doctors and allow us to foresee life-threatening situations.

#### Author details


Juan Gutiérrez Franchi<sup>1\*</sup>, S. Merino<sup>2</sup>, P. de la Calle<sup>1</sup>, C. Perrino<sup>1</sup>, M. Represa<sup>1</sup> and P. Moral<sup>1</sup>

1 Service of Anesthesiology and Resuscitation, Hospital Clínico San Carlos, Madrid, Spain

2 Radiodiagnosis Service, Hospital Clínico San Carlos, Madrid, Spain

\*Address all correspondence to: [juangutierrezfranchi@gmail.com](mailto:juangutierrezfranchi@gmail.com)

#### IntechOpen

© 2019 The Author(s). Licensee IntechOpen. This chapter is distributed under the terms of the Creative Commons Attribution License (<http://creativecommons.org/licenses/by/3.0>), which permits unrestricted use, distribution, and reproduction in any medium, provided the original work is properly cited. 

## References

- [1] Gutiérrez JC, Merino S, De la Calle P, Perrino C, Represa M, Moral P. Correlation of Preoperative Findings in the Computerized Axial Tomography with the Presence of Via Difficult Airway in Patients Operated Through Otorhinolaryngological Surgery of the Head and Neck. *Rev Esp Anesthesiol Reanim*. 2018 May;**65**(5):252-257. DOI: 10.1016/j.redar.2018.01.013. Epub 2018 Mar 2
- [2] Spanish Society of Medical Oncology. Head and Neck Tumors—O.R.L [consulted 2017]. March 27, 2017. Available at: <http://www.seom.org/es/info-sobre-el-cancer/orl?start=1#content>
- [3] Posner MR. Cáncer de cabeza y cuello. In: Goldman-Cecil. *Tratado de Medicina Interna*. Vol. 190. España: Elsevier; 2017. p. 1297-1303
- [4] Karakus O, Kaya C, Ustun FE, Koksal E, Ustun YB. Predictive value of preoperative tests to estimate difficult intubation in patients undergoing direct laryngoscopy for ear, nose and throat surgery. *Brazilian Journal of Anesthesiology*. 2015;**65**:85-91
- [5] Apfelbaum JL, Hagberg CA, Caplan RA, Blitt CD, Connis RT, Nickinovich DG, et al. Practice guidelines for management of the difficult airway: An updated report by the American Society of Anesthesiologists Task Force on Management of the Difficult Airway. *Anesthesiology*. 2013;**118**:251-270
- [6] Karkouti K, Rose DK, Ferris LE. Inter-observer reliability of ten tests used for predicting difficult tracheal intubation. *Canadian Journal of Anaesthesia*. 1996;**43**:554-559
- [7] Henderson JJ, Popat MT, Latto IP, Pearce AC. Difficult Airway Society. Difficult Airway Society guidelines for management of the unanticipated difficult intubation. *Anaesthesia*. 2004;**59**:675-694
- [8] Lee A, Fan LT, Gin T, Karmakar MK, Ngan Kee WD. A systematic review (meta-analysis) of the accuracy of the Mallampati tests to predict the difficult airway. *Anesthesia and Analgesia*. 2006;**102**:1867-1878
- [9] Bindra A, Prabhakar H, Singh GP, Ali Z, Singhal V. Is the modified Mallampati test performed in supine position a reliable predictor of difficult tracheal intubation? *Journal of Anesthesia*. 2010;**24**:482-485
- [10] Patel B, Khandekar R, Diwan R, Shah A. Validation of modified Mallampati test with addition of thyromental distance and sternomental distance to predict difficult endotracheal intubation in adults. *Indian Journal of Anaesthesia*. 2014;**58**:171-175
- [11] Bhavdip P, Rajiv K, Rashesh D, Ashok S. Validation of modified Mallampati test with addition of thyromental distance and sternomental distance to predict difficult endotracheal intubation in adults. *Indian Journal of Anaesthesia*. 2014 Mar-Apr;**58**(2):171-175. DOI: 10.4103/0019-5049.130821
- [12] Anantham D, Ernst A. Ultrasonography. In: Murray and Nadel's *Textbook of Respiratory Medicine*. Vol. 20. Elsevier; 2016. p. 348.e2-359.e2
- [13] Chou HC, Wu TL. Mandibulohyoid distance in difficult laryngoscopy. *British Journal of Anaesthesia*. 1993;**71**:335-339
- [14] Hui CM, Tsui BC. Sublingual ultrasound as an assessment method for predicting difficult intubation: A pilot study. *Anaesthesia*. 2014;**69**:314-319

- [15] Jordan DW, Haaga JR. Imaging principles in computed tomography. In: CT and MRI of the Whole Body. Vol. 1. Elsevier; 2017. p. 3-30
- [16] Randell T, Hakala P, Kytä J, Kinnunen J. The relevance of clinical and radiological measurements in predicting difficulties in fiberoptic orotracheal intubation in adults. *Anaesthesia*. 1998;**53**(12):1144-1147
- [17] Roth CG, Deshmukh S. Fundamentals of Body MRI, Introduction and Physics of Body MRI. Chapter 12017. Elsevier; 2017. p. 1-44
- [18] Samra S, Schork M, Guinto FA. A study of radiologic imaging techniques and airway grading to predict a difficult endotracheal intubation. *Journal of Clinical Anesthesia*. 1995;**7**(5):373-379
- [19] Wear VV, Allred JW, Mi D, et al. Evaluating 'eee' phonation in multidetector CT of the neck. *AJNR. American Journal of Neuroradiology*. 2009;**30**:1102-1106
- [20] Weissman JL, Carrau RL. Puffed-cheek CT improves evaluation of the oral cavity. *AJNR. American Journal of Neuroradiology*. 2001;**22**:741-744
- [21] Chan AT, Grégoire V, Lefebvre JL, et al. Nasopharyngeal cancer: EHNS-ESMO-ESTRO clinical practice guidelines for diagnosis, treatment and follow-up. *Annals of Oncology*. 2012;**23**:vii83-vii85
- [22] Gregoire V, Lefebvre JL, Licitra L, et al. Squamous cell carcinoma of the head and neck: EHNS-ESMO-ESTRO Clinical Practice Guidelines for diagnosis, treatment and follow-up. *Annals of Oncology*. 2010;**21**:v184-v186
- [23] Leon X, Ferlito A, Myer CM, et al. Second primary tumors in head and neck cancer patients. *Acta Oto-Laryngologica*. 2002;**122**:765-778
- [24] Kim EB, Park Y, Park SJ, et al. Clinical factors related to suspected second primary lung cancer development in patients with head and neck cancer. *Cancer Research and Treatment*. 2008;**40**:178-183
- [25] Kuriakose MA, Loree TR, Rubenfeld A, et al. Simultaneously presenting head and neck and lung cancer: A diagnostic and treatment dilemma. *Laryngoscope*. 2002;**112**:120-123
- [26] Church TR, Black WC. Reduced lung-cancer mortality with low-dose computed tomographic screening. *The New England Journal of Medicine*. 2011;**365**:395-409
- [27] Wender R, Fontham ET, Barrera E, et al. American Cancer Society lung cancer screening guidelines. *CA: A Cancer Journal for Clinicians*. 2013;**63**:107-117
- [28] Becker M, Zbären P, Casselman JW, et al. Neoplastic invasion of laryngeal cartilage: Reassessment of criteria for diagnosis at MR imaging. *Radiology*. 2008;**249**:551-559
- [29] Curtin HD. The 'evil gray': Cancer and cartilage. *Radiology*. 2008;**249**:410-412
- [30] Li B, Bobinski M, Gandour-Edwards R, et al. Overstaging of cartilage invasion by multidetector CT scan for laryngeal cancer and its potential effect on the use of organ preservation with chemoradiation. *The British Journal of Radiology*. 2011;**84**:64-69
- [31] Dixit R, Weissfeld JL, Wilson DO, et al. Incidence of head and neck squamous cell carcinoma among subjects at high risk of lung cancer: Results from the Pittsburgh Lung Screening Study. *Cancer*. 2015;**121**:1431-1435
- [32] Keberle M, Tschammler A, Hahn D. Single-bolus technique for spiral CT

of laryngopharyngeal squamous cell carcinoma: Comparison of different contrast material volumes, flow rates, and start delays. *Radiology*. 2002;224:171-176

[33] Burkill GJ, Evans RM, Raman VV, Connor SE. Modern radiology in the management of head and neck cancer. *Clinical Oncology*. 2016;28(7):440-450. Copyright © 2016 The Royal College of Radiologists

[34] Fristcherova S, Admaus M, Dostalova K, et al. Can difficult intubation be easily and rapidly predicted? *Biomedical Papers of the Medical Faculty of Palacky University in Olomouc*. 2011;155(2):165-172

---

Section 4

# Mind and Brain

---



# Functional Brain Imagery and Jungian Analytical Psychology: An Interesting Dance?

*Leon Petchkovsky, Michael Petchkovsky, Philip Morris, Paul Dickson, Danielle T. Montgomery, Jonathan Dwyer, Patrick Burnett and Kristin Robertson-Gillam*

## Abstract

Jung's original neuroscience research project looked at the neurophysiological responses to the word association test (WAT) in an effort to understand 'complexes', those emotionally laden fixations that bother us all, and can be inferred from certain painful responses in the WAT. He measured breathing rates, skin conductance and electrocardiography, but there was no brain functional imaging technology available at the time. One hundred years later, a wide range of brain functional technologies are available, and this chapter describes two studies in which the WAT was performed under functional magnetic resonance imaging and quantitative electroencephalography conditions. In essence, a complexed response first activates the amygdala (many right-sided). This is followed in the next 3 s by bilateral brain activity in the anterior insula, the supplementary motor area and the dorsal cingulum; the premotor mirror neuron areas, the so-called resonance circuitry, which is central to mindfulness (awareness of self) and empathy (sense of the other), negotiations between self-awareness and the 'internal other', and has been well described by Dan Siegel. But over the following 2 s, activity shifts to the left hemisphere, seemingly the way the brain deals with a complex in the moment, possibly to dull the pain of the complexed response.

**Keywords:** Jungian psychology, complexes, fMRI, QEEG

## 1. Introduction

### 1.1 Jung on the complexes

It is one of life's ironies that Jungian analytical psychology, often regarded as the most starry-eyed of the psychoanalytic methods, had its beginnings, over 100 years ago, in what was essentially Jung's neuroscience research project (Jung [1]) in which he looked at neurophysiological responses to the word association test (WAT), in an effort to understand 'complexes', those emotionally laden fixations that bother us all, and can be inferred from certain painful responses in the WAT.

It is worth going back to Jung's original descriptions:

*[complexes] are psychic entities which are outside the control of the conscious mind... always contain something like a conflict...are the 'sore spots', the bêtes noires, the 'skeletons in the cupboard' which we do not like to remember but still come back to mind unbidden in the most unwelcome fashion....experience shows that complexes are infinitely varied, yet careful comparison reveals a relatively small number of typical primary forms (Jung [1], pp. 528–529).*

Jung's early WAT investigations led him to wonder about the role of complexes across a range of conditions, including psychosis, dissociative disorder and psychological trauma, through to everyday life:

*...the average speed of the reactions and their qualities, was a relatively subsidiary result compared with the way in which the method was disturbed by the autonomous behaviour of the psyche....it was then that I discovered the feeling-toned complexes, which had always been registered before as failures to react (Jung [1], pp. 95).*

## 1.2 A brief history of neuroscience research in analytical psychology

Jung and collaborators at the Burghölzli used the most advanced physiological psychology technology of the times, skin conductance (SC) or galvanic skin response (GSR), electrocardiography (ECG) and plethysmographic spirometry (measurement of breath rate and depth), to track the neurophysiological changes that accompanied complexed responses when patients performed the WAT.

When a person hears a word read-out from a standard list, and is asked to respond as quickly as possible with the first word that comes to mind, most responses tend to be bland and neutral. However, every so often there are long pauses, often with unusual behavioural and semantic features (the so-called complex indicators), and physiological disturbances (heart rate, breathing rate, skin conductance). Such responses typically organise around themes. From these responses, a 'map' of psychological 'hot spots' can be built. Jung called these affect-bound thematic nodes the 'complexes'. But more importantly, both he and Freud viewed complexed reactions as evidence of 'repression', a state in which the subject's experience collides with an internal opposition, generating internal conflict.

## 2. Functional brain imaging methods

Almost 100 years after Jung's research, there is now a range of brain imaging technologies which include functional magnetic resonance imaging (fMRI), QEEG, near-infrared spectroscopy (NIRS), positron emission tomography (PET), single-photon emission computed tomography (SPECT) and magnetoencephalography (MEG). The contributions of NIRS, PET and SPECT to anything of direct relevance to psychoanalytic practice have been modest for various reasons. The two most productive functional imaging modalities, in terms of giving deep insights into psychodynamic brain functions, are fMRI and QEEG.

### 2.1 MRI and fMRI

It takes 1–2 s for blood flow in an activated brain region to increase. More haemoglobin in its oxygenated form arrives in that area, and because it has different



magnetic properties to the deoxygenated form, this can be detected by the MRI scanner as magnetic signal variations, the so-called blood-oxygen-level dependent (BOLD) response. This allows functional maps to be constructed, with spatial resolutions as good as 1 cm<sup>3</sup>.

But temporal resolution is relatively poor, around 2 s. Since the early 1990s, fMRI has come to dominate brain mapping research because it does not require subjects to undergo surgery, be exposed to ionizing radiation or to take in radioactive substances.

## 2.2 Quantitative electroencephalography (QEEG)

The EEG is a collection of electrical signal patterns originating in the brain, recorded from a set of scalp electrodes. The so-called 10/20 placement is the most common electrode placement. Nineteen electrodes are applied to specific scalp sites, with a set of reference electrodes at each ear. QEEG differs from regular EEG because a range of algorithms have been developed over the last two decades to process the data and extract patterns that cannot be easily accessed visually from the 'resting' or 'background' EEG. The technology also allows one to administer a standard range of auditory and visual tasks and stimuli, which in turn generate EEG response patterns, the so-called event-related potentials (ERPs). This allows a closer look at the brain in action (see 'Event-Related Potentials (ERPs)' section) (see also Kropotov [2] and Thatcher [3]).

QEEG spatial resolution can be displayed by the low-resolution electromagnetic tomography (LORETA) process and technology developed by Pascual-Marqui et al. [4], based at the KEY Institute for Brain-Mind Research, University Hospital of Psychiatry Zurich, Switzerland, which is impressive (circa 1–2 cm<sup>3</sup>) but not as good as that of fMRI (1–6 mm). In his 1999 paper, Pascual-Marqui [5] reviews and compares several 'inverse problem' resolution methods and finds that the LORETA method is the most accurate. However, EEG temporal resolution is much better than that of fMRI in the millisecond range, and with fMRI, the initial 2-s poststimulus are unavailable, because it takes that long for the blood oxygenated signal to manifest in the brain, and from then on, temporal resolution of about 500 ms is about the best that can be obtained.

## 3. The fMRI of complexes as elicited by the WAT

This chapter provides a condensed account of our experimental studies. For the reader wanting more details, these are available in Petchkovsky et al. [6, 7]. Jung's word association test was performed under fMRI conditions by 15 normal subjects. Pooled complexed responses were contrasted against pooled neutrals.

### 3.1 Results

The scans were analysed using the Statistical Parametric Mapping program (see SPM-5 2009 url, 8). The complexed responses revealed a very strong pattern of bilaterally symmetrical activity in each hemisphere. Statistical significance of the results was well above the SPM-5 family-wise error (FWE) and false discovery rate (FDR) thresholds, described in SPM-5 2009 [8] with Z-scores ranging from 4.90 to 5.66, i.e. four or more standard deviations above the baseline expectation (a result with a Z-score of 3.9 or above has less than 1 chance in 10,000 of being accidental).

The initial left and right hemisphere symmetry of the generic complex response is well captured in this Drishti image, as developed by Limaye [9]. In each hemisphere, we can see the interactive pattern between mirror neuron sites (premotor mirror

neuron area and supplementary motor area), the conflict-monitoring cingulate gyrus and the anterior insula which tracks internal states but also communicates with midbrain limbic areas like the amygdala (to do with emotions). The BOLD responses accompanying 'complexed' activity are the strongest in the first 3 s (see **Figure 2**).

### 3.2 Complex versus neutral

One striking feature of the 'complexed' response pattern displayed above is the high level of interhemispheric symmetry in the first 3 s.

### 3.3 The complexed activation pattern

The complexed response pattern (see both **Figures 1** and **2**) includes [1] premotor mirror neuron areas that track 'otherness' (Brodmann area 9 and 44), [2] anterior insula on both sides (mediating proprioceptive and emotional self-awareness but also emotional empathy) and [3] dorsal cingulate gyrus (conflict-monitoring and self-monitoring processes, including conscious reflection about the 'other').

These are the sites described by Siegel and colleagues in 2007 and 2011 [10, 11] as the 'resonance circuitry'. This serves both mindfulness (awareness of self) and empathy (sense of the other).

But our findings also show an interhemispheric dialogue. The left hemisphere over-rides the right within 3 s.

We can now add two further findings to this study:

1. Along with all the other findings, there was a very strong BOLD response seen in the first 3 s in the right dorsolateral prefrontal cortex RDLPFC; 7 voxels at 54,749.  $Z = 5.06!$  At that time that we could not find any research literature relating to the significance of this site. Since then, it has emerged that RDLPFC, in connection with the insula, is involved in salience, a state in which the attention is grabbed and shifted from default mode network activity, as it is when we activate a complex (see Sridharan et al. [12] and Goulden et al. [13]). RDLPFC is also active in fear-driven inhibitory responses (see Shackman et al. [14]). This correlates well with the increased response time in a complexed response.
2. The anterior insula interacts with both dorsal cingulate gyrus and mirror neuron areas and in turn influences reciprocally, midbrain limbic areas like the amygdala.

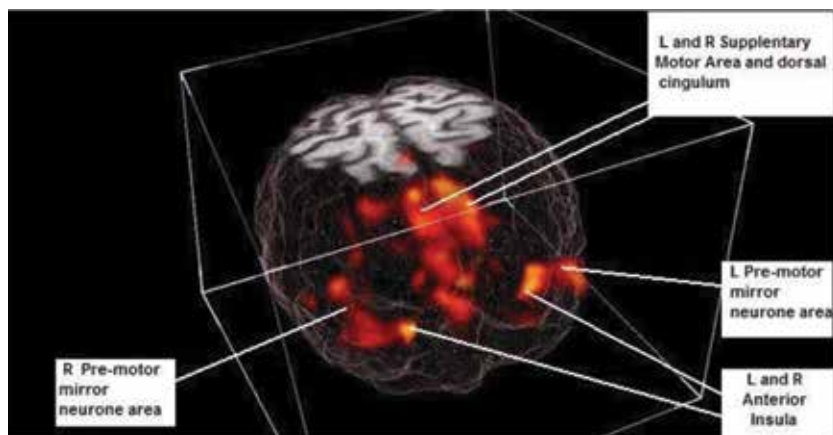


**Figure 1.**  
*The generic complexed response.*

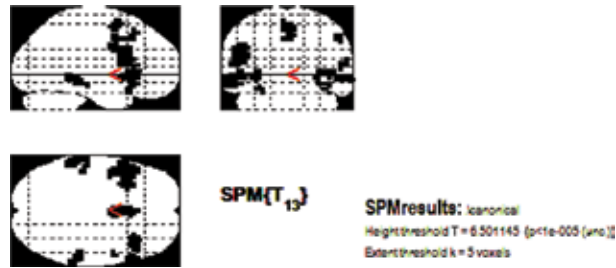


**Figure 2.**  
First 3 s. Complex vs. neutral responses. SPM-5 images showing sagittal, coronal and transverse sections.

The interaction between the DCG and insula is very marked in states of social rejection and experiences of object loss. An easily readable overview of various studies that explore this interaction between the cingulate and insula is available in the December 1, 2012 issue of the *New Scientist* (see [15]). Interestingly, these two sites are also activated in states of physical pain, as described by Slavich et al. [16].

### 3.4 Complexed activity over time

Although fMRI temporal resolution is poor (around 2 s), spatial resolution is high (better than 1 mm<sup>3</sup>). We can compensate somewhat by taking 2 s blocs overlapping by 1 s (as we have done in **Figure 3**), but we cannot break down the first 2 s to smaller time frames. The *much* higher temporal resolution of QEEG (milliseconds) helps us investigate the very earliest events, and we mention some preliminary findings further on in this text.

In the first 2 s, the activity is symmetrical. Presumably, a process of ‘internal conflict’ is active in each hemisphere, across a range of circuits (the ‘resonance circuits’) that mediate various aspects of ‘self’ and ‘others’ within each hemisphere. But soon after, the activity shifts to the left hemisphere.

When we analyse the data in 2-s fragments from the beginning, we see that the left hemispheric activity quickly becomes more prominent and right hemispheric much less so; until by the fifth second, only the left activity raises above FWE or FDR thresholds (see **Figure 3**).

The low temporal resolution of the BOLD fMRI response (some 2 s) does not allow us to make more detailed inferences about the very first 2 s. However, even within these limitations, we can say that the sequential patterns seen above suggest that in the initial 3 s, negotiation between sites subserving ‘self-’ awareness (medial sites like dorsal cingulum) and ‘other’ awareness (lateral prefrontal sites) occurs *within each* hemisphere and results in lateral prefrontal predominance (compare front to back activity in the ‘transverse section’ 0–2 with 1–3 and 2–4 s).

Also note that the medial prefrontal (SMA and dorsal cingulum) activity within *each* hemisphere, while strongest in the first 2 s, begins to fade relative to dorsolateral prefrontal activity. Compare the first ‘transverse section’ with the subsequent ones, and note how activity shifts to the left hemisphere and diminishes in the right one. Negotiation *between* left and right hemispheres results in left hemispheric hegemony. What is happening?

### 3.5 The ‘resonance circuits’

The ‘resonance circuitry’ pattern is the one that corresponds most strongly. Details of the literature review can be found in our Petchkovsky et al. [6].

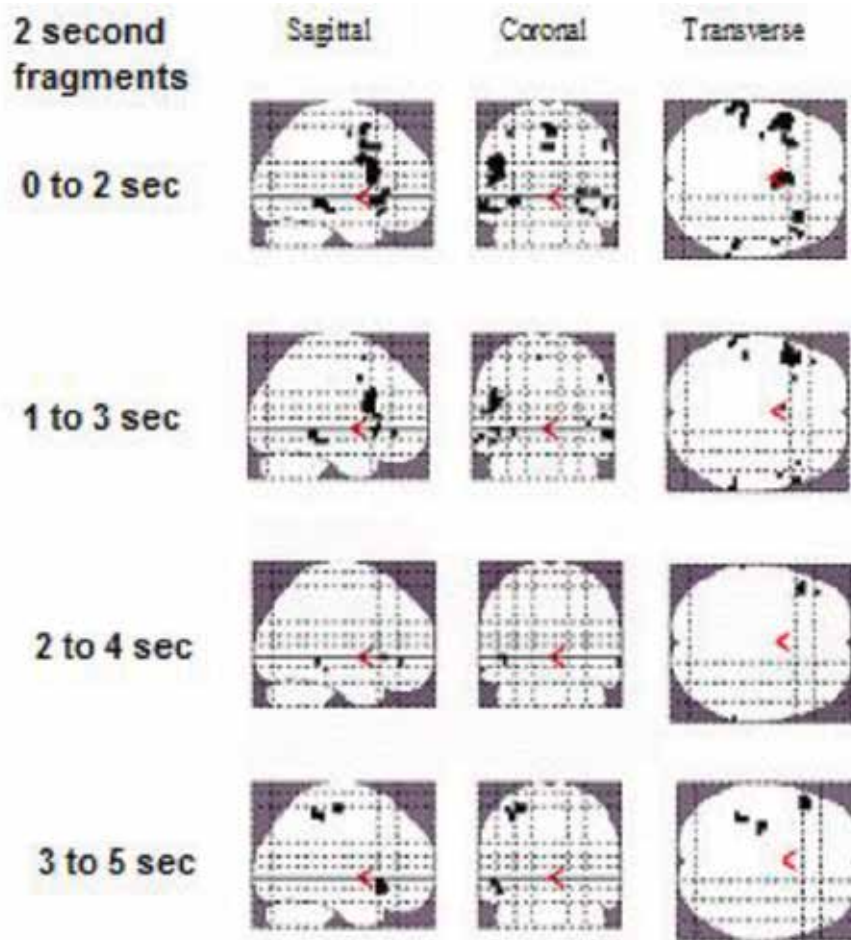


**Figure 3.** Complexed versus neutral. SPM images, sagittal, Coronal and transverse, showing BOLD activity over the first 5 s.

Our findings suggest that what is being accessed is some representation of the ‘internal other’ which seems in conflict with the self. There is a sense in which all representations of ‘otherness’ have to be internal of course, since even mirror neuron activity is actually embedded in the observer’s circuitry.

Why does the ‘generic’ complex response initially show bilateral symmetry and then ‘resolve’ in left hemispheric dominance? We think this is actually a ‘pseudo-resolution’, the way the brain deals with a complex in the moment, possibly to dull the pain of the complexed response (as opposed to a real psychotherapeutic resolution, in which both left and right hemispheric experiences are tolerated, despite the pain, and worked with and hopefully come to a ‘transcendent function’ resolution). McGilchrist [17] argues that each hemisphere has its own distinctive mode of awareness or consciousness. In the first 2–3 years of life, the right hemisphere develops, processing incoming data (including proprioceptive ‘body field’) holistically and emotionally, mediating highly affect-loaded attachment and threat patterns. In the third year, left hemisphere circuitry begins to develop. Its process is linear, organised around language, logic and abstractions. In the affective domain, the left hemisphere is more curious, exploratory and danger-denying (the subject as predator). McGilchrist asserts that optimal mind states have to do with good inter-hemispheric communication, because a third more integrative mode of awareness

becomes possible. Pettigrew's [18] research on right versus left hemispheric function is also worth reading as a complement to the above.

## 4. Implications for psychotherapy

### 4.1 Mindfulness and empathy

The resonance circuits mediate mindfulness (awareness of self-concept and self-process) and empathy (awareness of the other, including the internal other). Much good psychotherapy involves establishing new patterns of relatedness especially in the domain of 'implicit relational knowing' as Lyons-Ruth points out [19].

### 4.2 Psychotherapy strategy: to resolve or tolerate the tension of internal conflict?

Although our fMRI findings suggest that the complex 'pseudo resolves' the conflict through the left brain dominance, there is also a deeper therapeutic opportunity (bringing awareness and compassion to work with the tension of opposites). The complex may continue to 'pseudo resolve' the tension in this fashion forever, unless the 'holding of the tension of opposites' that Jung recommended for psychotherapy can be done in a nurturing environment, leading to the emergence of a 'transcendent function' mediatory product beyond the terms of the original conflict.

In 1977, the Jungian Analyst Rossi [20] wrote that 'just as the cerebral hemispheres are in a continuous process of balancing and integrating each other's functions on a neurophysiological level, Jung describes a similar regulation.' Not all conflicts can be reduced to the left vs. right brain. Our findings also show that in the first 3 or so seconds, *within each* hemisphere, patterns associated with negotiations between the internal self and internal other can be seen.

## 5. QEEG findings in the WAT responses

A new research project, the QEEG responses to the WAT (eight subjects thus far), is also being worked on, but we need at least another six to eight subjects for a reliable pilot study. However, QEEG allows us to look in detail at the first 500 ms that are unavailable to fMRI, because of QEEG's much better time resolution (milliseconds). We are releasing a 'preview' here (**Figure 4**).

We noted in our preliminary examination of the QEEG results that within the first 60 ms, complexed responses begin to manifest as activity in the right middle temporal region. LORETA imaging struggles to locate amygdalar activity precisely, because it is so deep in the brain, but amygdalar activation can be inferred because right middle temporal activity is typically seen when the right hemispheric amygdala is activated by a stressful event, (in this case, the complexed response to a painful stimulus word). But from 150 ms onwards, there is an activation of the default mode network (DMN, anterior cingulate and precuneus), which mediates a background sense of self.

We suspected, in our published fMRI study, that the right amygdala and DMN had to be involved. The QEEG findings confirm this, allowing us to see what could not be detected by fMRI. Amygdalar and DMN activity predominate only in the very earliest phase of the response.

However, from about 1000 ms onwards, QEEG findings are very similar to what was found in the fMRI study. The left hemispheric activity (probably defensive in nature) gradually predominates over right over the next 3 s.

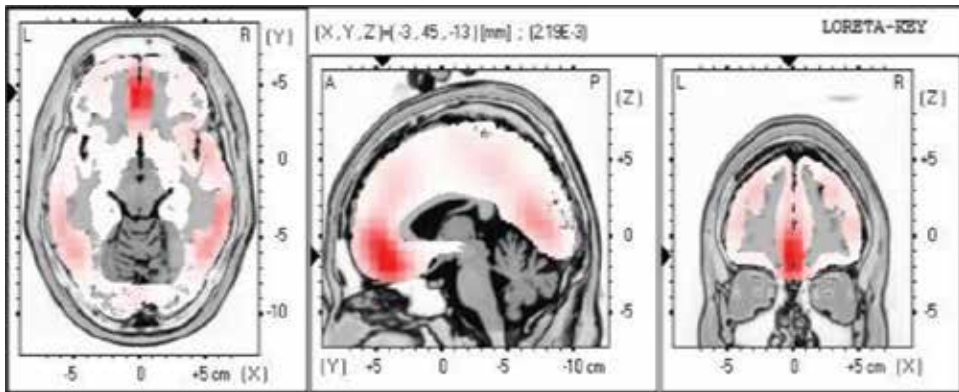


**Figure 4.** The first 200 ms. EEG LORETA image of DMN activity smeared within the first 200 ms of the complexed response. See activation of the cingulate gyrus, precuneus and angular gyrus.

This study sets the basis for further research:

- i. QEEG studies (with their finer temporal resolution) of specific as opposed to generic complexed responses in normal subjects
- ii. QEEG and fMRI studies of complexed responses in other conditions, like schizophrenia, PTSD, developmental trauma disorders and disorders of self-organisation

### 5.1 A clinical example illustrating the usefulness of QEEG in psychotherapy efficacy research

We finish this discussion with an example of how brain functional imaging can facilitate the understanding and tracking of a psychotherapy process. While it is true that Jung encouraged the use of a range of creative techniques, including singing, the following account is not specific to Jungian therapy alone.

A group of 32 treatment-resistant outpatients suffering from chronic depression with anxiety/agitated features were offered an intensive 8-week-long music therapy programme involving choir work by my music therapist colleague Robertson-Gillam et al. [21]. QEEGs were performed before and after, using the Mitsar WinEEG program. This included the visual cognitive performance task (VCPT), which we used to elicit event-related potentials, indicators of brain function. The VCPT task is a GoNoGo task. The three types of visual stimuli presented in this task are pictures with animals, pictures with plants and pictures with peoples. The subject presses a button when an animal picture follows a previous animal picture but refrains if the first animal picture is followed by a plant or if one plant picture follows another. Every so often however, a plant picture is followed by a picture of a human and a bell-like noise. This is the so-called 'novel' stimulus. The component of the ERP wave response to this is called P3a or P3Nov wave. The patients had abnormally high responses to the novel stimuli during QEEG acquisition. This correlated with their hypervigilance and excessive responses to stress.

After 8 weeks of the music therapy, their P3a or novelty response had returned to normal (see (a) and (b) in the diagram). It was also possible to get a 3-D image of the location of the abnormal activity in the mid-cingulate gyrus region (see LORETA image (c)) (Figure 5).



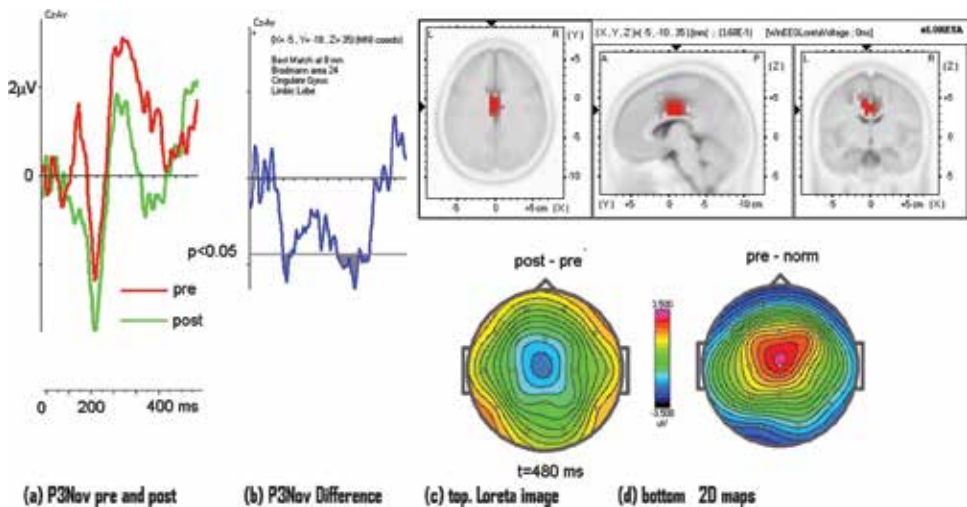


**Figure 5.**  
 QEEG P3a response normalization in a depressive group.

Individual QEEG patterns are extremely constant, usually with very little change over decades, as noted by QEEG neuroscientist Kropotov [2–4]. The rapid change we see here tells us that something major has occurred in the way the patients’ brain processes life events.

## 5.2 Schizophrenia and WAT and fMRI and QEEG

Our very preliminary QEEG findings in three schizophrenic patients doing the WAT suggest that for them, in a complexed response, the right insular/cingulate activity persists for several seconds, accompanied by the right temporal activity (auditory hallucinatory processes?). This matches the patient’s experience. QEEG and fMRI studies of responses to the WAT, with sufficient subject numbers (both normal and patients with schizophrenia), are desperately needed. This will deepen our understanding and opens up a range of important assessments and diagnostic possibilities.

## 6. Conclusion

Science and the transcendental are seemingly incompatible. But they represent two of the deepest currents of human existence. The combination of these two perspectives makes analytical psychological so worthwhile. This field stands to benefit enormously from further engagement with neuroscience and especially its active research components.

## Acknowledgements

We thank the Wesley Hospital fMRI Unit and especially A/Prof. Greig de Zubicaray and Dr. Katie McMahon of the Centre for Advanced Imaging, University of Queensland, for their help. We also thank the Grants Committee of the International Association of Analytical Psychology for their kind moral and financial support.

## **Author details**

Leon Petchkovsky<sup>1,2\*</sup>, Michael Petchkovsky<sup>2</sup>, Philip Morris<sup>2,3</sup>, Paul Dickson<sup>2</sup>, Danielle T. Montgomery<sup>2</sup>, Jonathan Dwyer<sup>2</sup>, Patrick Burnett<sup>2</sup> and Kristin Robertson-Gillam<sup>4</sup>

1 Department of Psychiatry, University of Queensland, Australia

2 Pinniger Clinic, Robina, Queensland, Australia

3 Department of Psychiatry, Bond University, Robina, Queensland, Australia

4 University of Western Sydney, Australia

\*Address all correspondence to: [leon.petchkovsky@gmail.com](mailto:leon.petchkovsky@gmail.com)

## **IntechOpen**

---

© 2018 The Author(s). Licensee IntechOpen. This chapter is distributed under the terms of the Creative Commons Attribution License (<http://creativecommons.org/licenses/by/3.0>), which permits unrestricted use, distribution, and reproduction in any medium, provided the original work is properly cited. 



## References

- [1] Jung CG. *Collected Works*. Vol. 6 *Psychological Types*. London: Routledge and Kegan Paul; 1971. pp. 528-529
- [2] Kropotov J. *Quantitative EEG, Event Related Potentials and Neurotherapy*. Cambridge, Massachusetts: Elsevier, Academic press; 2009
- [3] Thatcher R. *Handbook of Quantitative Electroencephalography and EEG Biofeedback*. 2016. Hardcover ISBN: 978-0-9854692-0-7; eBook ISBN: 978-0-9854692-1-4 Applied Neuroscience research Institute. Largo, Florida, US.
- [4] Pascual-Marqui RD, Lehmann D, et al. Low resolution electromagnetic tomography: A new method for localizing electrical activity in the brain. *International Journal of Psychophysiology*. 1994;**18**:49-65
- [5] Pascual-Marqui RD. Review of methods for solving the EEG inverse problem. *International Journal of Bioelectromagnetism*. 1999;**1**(1):75-86. Printed Issue ISSN: 1457-7857; Internet Issue ISSN: 1456-7865. Available from: <http://www.tut.fi/ijbem>. Author's version. Page 1 of 13
- [6] Petchkovsky L, Petchkovsky M, Morris P, Dickson P, Montgomery D, Dwyer J, et al. Using fMRI responses of subjects performing Jung's Word Association Test to develop a functional model of the complexed response; implications for theory, diagnosis, treatment, outcome measures, and further research. *The Journal of Analytical Psychology*. 2013; Jun;**58**(3):409-431. DOI: 10.1111/1468-5922.12021
- [7] Petchkovsky L. Advances in functional brain imaging technology and developmental neuro-psychology: Their applications in the Jungian analytic domain. *Journal of Analytical Psychology*. 2017;**62**(3):415-433
- [8] SPM5. Wellcome Department of Imaging Neuroscience. Institute of Neurology, University College London. 2009. Available from: <http://www.fil.ion.ac.uk>
- [9] Limaye A. Drishti-Volume Exploration and Presentation Tool, Poster Presentation, Vis Baltimore. 2006. Available from: <http://anusf.anu.edu.au/Vizlab/drishti/downloads.shtml>. Drishti homepage: <http://anusf.anu.edu.au/Vizlab/drishti/index.shtml>
- [10] Siegel D. *Mindsight: The New Science of Personal Transformation*. NY: Bantam Books; 2011. pp. 59-63
- [11] Siegel D. *The Mindful Brain: Reflection and Attunement in the Cultivation of Well-Being*. New York: W. W. Norton & Company; 2007. See especially Appendix III
- [12] Sridharan D, Levitin DJ, Menon V. A critical role for the right fronto-insular cortex in switching between central-executive and default-mode networks. *Proceedings of the National Academy of Sciences*. 2008;**105**(34):12569-12574
- [13] Goulden N, Khusnulina A, Davis NJ, Bracewell RM, Bodke AL, McNulty JP, et al. The salience network is responsible for switching between the default mode network and the central executive network: Replication from DCM. *NeuroImage*. 2014;**99**(1):180-190
- [14] Shackman AJ, Mcmenamin BW, Maxwell JS, Greischar LL, Davidson RJ. Right dorsolateral prefrontal cortical activity and behavioral inhibition. *Psychological Science*. 2009;**20**(12):1500-1506
- [15] Raffensperger L. Words can never hurt me. *New Scientist*. Nov 28, 2012:37-39

- [16] Slavich GM, Baldwin MW, Eisenberger NI, Taylor SE. Neural sensitivity to social rejection is associated with inflammatory responses to social stress. *Proceedings of the National Academy of Sciences of the United States of America*. 2010;**107**(33):14817-14822
- [17] McGilchrist I. *The Master and His Emissary: The Divided Brain and the Making of the Western World*. USA: Yale University; 2009
- [18] Pettigrew JD. Searching for the switch: Neural bases of perceptual rivalry alternations. *Brain and Mind*. 2001;**2**:84-115. Press ISBN: 0-300-14878-X
- [19] Lyons-Ruth K. Implicit relational knowing: Its role in development and psychoanalytic treatment. *Infant Mental Health Journal*. 1998;**19**(3):282-289
- [20] Rossi E. The cerebral hemispheres in analytical psychology. *The Journal of Analytical Psychology*. 1977;**22**(1): 32-58. See especially p. 45
- [21] Robertson-Gillam K, Petchkovsky L, Kropotov J. Using QEEG parameters (asymmetry, coherence, and P3a novelty response) to track improvement in depression. *Advances in Mental Health*. 2013;**11**(3):257-267





*Edited by Sanja Josef Golubic*

Neuroimaging provides a valuable noninvasive window into the human neural system and is used in fundamental and clinical research. Imaging techniques are essential for understanding spontaneous neural activity and brain mechanisms engaged in the processing of external inputs, memory formation, and cognition. Modern imaging modalities make it possible to visualize memory processes within the brain and to create images of its structure and function. Scientists and technologists are joining forces to pave the way for improving imaging technologies and methods, data analysis, and the application of imaging to investigate the wide spectra of neurological diseases, neuropsychological disorders, and aging. Imaging techniques are essential for the identification of biological markers of the earliest stages of neurodegenerative diseases and the development of new therapies. This book intends to provide the reader with a short overview of the current achievements in the state-of-the-art imaging modality methods, their highlights, and limitations in neuroscience research and clinical applications. The current state of in-vivo neuroimaging methods in the context of the understanding and diagnosis of mental disorders and relation to the mind is also discussed in a modern compact format, featuring the latest and most relevant research results.

Published in London, UK

© 2019 IntechOpen  
© Joel Filipe / Unsplash

**IntechOpen**

ISBN 978-1-83962-108-6



9 781839 621086

